OBSERVABILITY ANALYSIS FOR SPACE SITUATIONAL AWARENESS

A Dissertation

Submitted to the Faculty

of

Purdue University

by

Alex M. Friedman

In Partial Fulfillment of the

Requirements for the Degree

of

Doctor of Philosophy

May 2020

Purdue University

West Lafayette, Indiana

THE PURDUE UNIVERSITY GRADUATE SCHOOL
STATEMENT OF DISSERTATION APPROVAL

Dr. Carolin Frueh, Chair

School of Aeronautics and Astronautics

Dr. Daniel DeLaurentis

School of Aeronautics and Astronautics

Dr. Kathleen Howell

School of Aeronautics and Astronautics

Dr. Shaoshuai Mou

School of Aeronautics and Astronautics

Dr. Kyle DeMars

Texas A&M University, Department of Aerospace Engineering

Approved by:

Dr. Gregory Blaisdell

Associate Head of Gambaro Graduate Program of Aeronautics and Astronautics

ACKNOWLEDGMENTS

I would first like to express my deepest appreciation to Dr. Carolin Frueh. She created an excellent environment for pursuing my research interests, and I could not have asked for a better advisor to guide me through this pursuit. I would also like to extend sincere thanks to my committee members, Dr. Daniel DeLaurentis, Dr. Kathleen Howell, Dr. Shaoshuai Mou, and Dr. Kyle DeMars, for their valuable conversations and comments on my dissertation and research. Funding of this work was provided by the Air Force Office of Scientific Research, the Indiana Space Grant Consortium, and the Department of Defense Science, Mathematics And Research for Transformation Scholarship-for-Service Program.

Many thanks to the members of the Space Information Dynamics group for the feedback and collaboration during my time at Purdue, and thanks to New Mexico Skies for help with the Purdue Optical Ground Station. I would also like to thank Dr. Emmanuel Delande for the insightful converstations during visits to Purdue.

I would like to thank my family and friends for their encouragement over the years. I am thankful for my parents and sister who helped me accomplish a major goal and who supported me throughout my life, and for my friends who were always there to provide a much-needed break. Finally, I am thankful for Katie, who was a constant source of encouragement, who made sure I celebrated every accomplishment, and who helped me push through every hardship. For that I am deeply indebted.

TABLE OF CONTENTS

Page

LIST OF TABLES

Table Page

LIST OF FIGURES

Figure Page

Figure Page

Figure Page

Figure Page

Figure Page

Figure Page

Figure Page

Figure Page

Figure Page

ABBREVIATIONS

AIUB	Astronomical Institute at the University of Bern
AMR	Area-to-Mass Ratio
AU	Astronomical Unit
BRDF	Bi-directional Reflection Distribution Function
CCD	Charged Coupled Device
CF	Consider Filter
ECI	Earth Centered Inertial
ECEF	Earth Centered Earth Fixed
EGI	Extended Gaussian Image
EKF	Extended Kalman Filter
ESA	European Space Agency
GEO	Geosynchronous Earth Orbit or Geostationary Earth Orbit
GPS	Global Position System
HAMR	High Area-to-Mass Ratio
KF	Kalman Filter
INS	Inertial Navigation Systems
IOD	Initial Orbit Determination
LCI	Light Curve Inversion
LEO	Low Earth Orbit
LS	Least Squares
LUMVE	Linear, Unbiased, Minimum Variance Estimate
MC	Monte Carlo
MEO	Medium Earth Orbit
MJD	Modified Julian Date
NASA	National Aeronautics and Space Administration

ODE	Ordinary Differential Equation
POGS	Purdue Optical Ground Station
RSO	Resident Space Object
SGP4	Simplified General Perturbations 4
SKF	Schmidt-Kalman Filter
SRP	Solar Radiation Pressure
SSA	Space Situational Awareness
SSN	Space Surveillance Network
STM	State Transition Matrix
SVD	Singular Value Decomposition
UDL	Unified Data Library
USSTRATCOM	U.S. Strategic Command

ABSTRACT

Friedman, Alex M. PhD, Purdue University, May 2020. Observability Analysis for Space Situational Awareness. Major Professor: Carolin Frueh.

Space operations from the dawn of the Space Age have resulted in a large, and growing, resident space object population. However, the availability of sensor resources is limited, which presents a challenge to Space Situational Awareness applications. When direct communication with an object is not possible, whether that is due to a lack of access for active satellites or due to the object being characterized as debris, the only independent information source for learning about the resident space object population comes from measurements. Optical measurements are often a cost-effective method for obtaining information about resident space objects.

This work uses observability analysis to investigate the relationship between desired resident space object characteristics and the information resulting from ground-based optical measurements. Observability is a concept developed in modern control theory for evaluating whether the information contained within measurements is sufficient to describe the dynamical progression of a system over time. In this work, observability is applied to Space Situational Awareness applications to determine what object characteristic information can be recovered from ground-based optical measurements and under which conditions these determinations are possible. In addition, the constraints and limitations of applying observability to Space Situational Awareness applications are assessed and quantified.

1. INTRODUCTION

Many definitions of Space Situational Awareness (SSA) exist, and these definitions vary in scope and focus [1]. However, an overarching aim for SSA is to ensure the sustainable use of near-Earth space. Moreover, sustainable use of near-Earth space consists of

> understanding and maintaining awareness of the Earth orbital population, the space environment, and possible threats,

as defined by the European Space Policy Institute [2]. The Earth orbital population, otherwise referred to as the resident space object (RSO) population, consists of natural and human-made objects. Some definitions of SSA are restricted to awareness of human-made objects only. Beyond natural objects, the RSO population is composed of operational satellite assets and debris objects. Of the total number of objects launched to near-Earth space from the beginning of the Space Age in 1957 to present day, only a small fraction is operational satellites, and the remaining fraction of the RSO population is characterized as orbital debris. The International Academy of Astronautics defines orbital debris as

> any [hu]man-made object, which is non-functional with no reasonable expectation of assuming or resuming its intended function, or any other function for which it is or can be expected to be authorized, including fragments and parts thereof [3, 4].

Therefore, orbital debris consists of not only fragments separated from satellites or from satellite collisions, but also satellites which are no longer operational and mission-related objects. The current U.S. Strategic Command (USSTRATCOM) RSO catalog contains approximately 23,000 objects, consisting of both operational

satellites and orbital debris [5]. However, this catalog is restricted to objects of ten centimeters in diameter or larger in Low Earth Orbit (LEO) and one meter in diameter or larger in Geosynchronous Earth Orbit (GEO) [6]. Also, it is known that even within these size restrictions the catalog is incomplete. The addition of the Space Fence is anticipated to track up to 200,000 objects of one centimeter in diameter or larger in LEO [7]. If objects of one millimeter in diameter or greater could be included in a space object catalog, National Aeronautics and Space Administration (NASA) and European Space Agency (ESA) estimate that the number of objects in such a catalog would be on the order of 100 million. However, current sensor capabilities limit the generation of such a catalog, especially in higher altitudes [8, 9]. Although small objects may not initially appear threatening, the potentially large relative velocity differences between objects in orbit can lead to mission-ending collisions or catastrophic events [10, 11]. In addition to the large number of debris objects in the RSO population, increased capabilities of small satellites have led to plans for massive LEO satellite constellations, which will drastically increase the current number of operational satellites [12]. As the overall RSO population increases due to larger numbers of operational satellites and debris objects, the sustainable use of near-Earth space will only become more challenging.

In order to avoid collisions in the growing population of RSOs for ensuring continued, sustainable use of near-Earth space, precise tracking and prediction of object locations are required. The catalog of space objects distributed by USSTRATCOM is generated from the U.S. Space Surveillance Network (SSN), which is a collection of optical and radar sensors spread around the surface of the Earth [6]. In addition, many other government and commercial entities operate their own space surveillance networks. Nevertheless, even with the large increase in the number of tracked RSOs from the Space Fence and other space surveillance networks, the size of the RSO population exceeds the tracking capabilities of these sensor networks [13]. Additionally, these sensor networks all have differing amounts of inherent noise and capabilities, resulting in varying measurement uncertainties and heterogeneous data sets. There-

fore, the relationship between the required knowledge of RSOs and the sensor specific observations of these objects needs to be understood and clarified, which can then aid in numerous tasks, such as sensor tasking.

The information for each object resulting from optical sensors and radar sensors is primarily in the form of angle and range measurements, respectively. However, predicting the future locations of objects requires state information, typically consisting of position and velocity. Moreover, obtaining object characteristic information, such as shape or reflectivity properties, is important for precise orbit propagation and object identification because an orbit can be perturbed significantly as a result of these characteristics [14]. Achieving efficient and sustainable operations in near-Earth space requires an in-depth knowledge of which measurements are necessary for desired state information, when such measurements should be acquired, and how varying measurement accuracy can be incorporated.

The relationship between measurements and state information is fundamental to the evaluation of control systems. Kalman originally developed observability to define conditions under which the optimal regulator problem has a solution [15]. In general, observability is a method for ensuring that the measurements of a system are sufficient for computing the state. As a result of the early work by Kalman, many methods have been developed for analyzing observability of control systems. Ogata [16], Friedland [17], Gajic [18], and Bay [19] provide a detailed overview of linear observability methods. For linear, time-varying systems a common test computes an observability Gramian or observability matrix for evaluating the observability. When the observability matrix is non-singular, a system is observable. Many applications of observability focus on implementation of linear observability methods, but nonlinear observability methods have also been developed [20–22].

The original observability formulation from Kalman defined observability as a binary criteria for a system, i.e. the system is either observable or it is not. However, Kalman posed an open question for whether observability could be expanded for use as a quantitative measure [15]. Brown expanded upon this by developing the

degree of observability concept [23]. Brown's work on degree of observability was expanded further by Ablin [24] and extended to stochastic systems by Ham [25]. Many additional measures of observability have been developed, and many works have evaluated the applicability of each observability measure [26–34]. For example, the condition number [28, 35, 36], the determinant [37], and the pseudo-inverse [38] of the observability matrix are a few of the measures implemented for quantifying observability of a system.

In addition to extension of observability for use as a quantitative measure, deterministic observability methods have been extended to include state and measurement uncertainties. This extension is often referred to as stochastic observability. Within the field of stochastic observability, a distinction must be made between analysis methods which focus on system model matrices [36, 39–42] versus analysis methods which focus on the covariance matrix of state estimation errors [25, 34, 43–48]. The term stochastic observability has been applied to both types of analysis methods, but the latter are more accurately described by the term estimability, which was first coined by Baram & Kailath [44]. In addition, these applications of observability and estimability are often implemented to predict and evaluate estimation accuracy and performance. The form of the stochastic observability matrix is equal to the information matrix in the linear, unbiased, minimum variance estimate [49, 50]. In addition, several works have evaluated the relationship between observability and estimation through connection of the stochastic observability matrix and the Information Form of the Kalman Filter [32, 51–53]. Furthermore, Dianetti, Weisman, & Crassidis implemented observability for informing a Schmidt-Kalman Filter [42].

As a general control system concept, observability has been applied to many aerospace applications. Within SSA applications, observability has been applied extensively to Inertial Navigation Systems (INS) and Global Positioning Systems (GPS) [28, 33, 37, 46, 48, 54–64]. Beyond INS and GPS applications, analysis of observability has focused on attitude [26, 62, 65, 66], bearings-only navigation [61, 67–70], and coupled position-attitude determination [64, 71]. Moreover, observability has

been applied for determining space object characteristics [42, 72]. The observability analysis in the work by Linares & Crassidis [72] primarily focuses on attitude and shape model parameters. Dianetti, Weisman, & Crassidis implement observability in a Schmidt-Kalman Filter to determine when consider parameters should be estimated [42]. However, the work by Dianetti, Weisman, & Crassidis primarily focuses on the development of a multiple model adaptive estimator. To inform the Schmidt-Kalman Filter, Dianetti, Weisman, & Crassidis defined a single, fixed value based on the singular values of the observability matrix.

In the previous works, the validity of applying the linear observability measure to the problem of SSA has not been shown nor tested. Furthermore, an unproven inference had been drawn between observability and Schmidt-Kalman Filter performance. The previous SSA works have not used a realistic scenario including measurement noise and the influence of *a priori* information within observability analysis. In addition, a direct connection of observability and the required conditions for allowing shape characterization is absent.

In this work, an in-depth analysis of observability is conducted for determining RSO characteristics with optical measurements. Rather than implement observability purely as a tool for evaluating when state variables can be estimated, observability is investigated to gain a deeper understanding of how the knowledge from optical measurements is transformed when determining object characteristics. Furthermore, many works do not estimate object reflectivity and shape variables as separate, solve-for parameters because of the coupled nature in the solar radiation pressure perturbation. However, in this work observability analysis is implemented to determine specific conditions when the reflectivity coefficient and area-to-mass ratio can be determined as separate parameters. Moreover, the connection of observability and estimation in this work applies specifically to the orbit problem for evaluating object characteristics and determining whether observability can be a predictor of estimation performance. When implementing observability in a Schmidt-Kalman Filter, the rank of the observability matrix is used dynamically to insert and remove consider parameters from

the estimation. Also, estimability methods inform the filter of which consider parameters should be estimated first. In addition, observability is applied in a novel way for aiding in sensor tasking and for determining efficient measurement collection strategies for a light curve inversion process. Portions of the work presented in this dissertation have been published in [73–80].

1.1 Research Questions

This work seeks to address the aforementioned challenges facing SSA with observability analysis. As a general control system concept, observability determines whether the knowledge contained within a set of measurements is sufficient for resolving desired state knowledge. This analysis considers the following questions.

1. How can linearized observability be utilized for the nonlinear orbit problem?
2. Can observability be used to evaluate whether optical measurements contain sufficient knowledge to determine position and velocity as well as additional object characteristics?
3. Is observability a predictor of estimation performance when applied to the orbit problem, and what are the conditions thereof?
4. Can observability be implemented as a measure to aid in efficient sensor tasking, and how does measurement uncertainty impact sensor tasking decisions?
5. Is observability able to determine when measurements sufficiently sample a system for performing light curve inversion, and can observability aid in efficient data collection for object shape characterization?

1.2 Outline of Dissertation

Linear observability methods are adopted in this work for answering these research questions. The relationship between angles-only measurements and a state with ob-

ject characteristics is explored through simulations of observability and estimation of the orbit problem. In addition, the sampling of the observer-object-Sun geometry in the light curve inversion problem is evaluated with simulations of realistic object attitude dynamics and observation constraints.

Chapter 2 introduces the background information required for the simulations and analysis performed in the subsequent chapters. Fundamentals of observability, the orbit problem with and without perturbations, ground-based optical observations and sensors, adaptation of the observability matrix for the orbit problem, estimation methods, and the light curve inversion process are introduced. In addition, previous work on observability for SSA is discussed where applicable.

Chapter 3 expands upon the deterministic observability matrix with the inclusion of state and measurement uncertainties. Moreover, the stochastic observability matrix is compared with the Information Form of the Kalman Filter. Next, several simulations are performed to analyze the observability of the orbit problem. First, the impact of measurement noise and propagation method on the time to become observable is explored. Next, solar radiation pressure (SRP) parameters are included in a state vector consisting of position and velocity to determine the observability of object characteristics. The system including SRP perturbations is investigated further by comparing deterministic and stochastic observability results to estimation methods. In addition, a Monte Carlo approach is implemented for evaluating what orbit problem estimation results can be guaranteed with observability analysis. Next, the use of observability as a measure for sensor tasking is evaluated. Finally, observability is analyzed for a system with multiple observers, each with differing measurement uncertainties.

Chapter 4 analyzes the orbit problem with SRP perturbations in a different approach than observability. Instead of using the dynamic and measurement model matrices, estimability methods are implemented for evaluation of the relative estimation performance of state variables, including position, velocity, and SRP parameters. In addition, the knowledge gained from estimability of the orbit problem and

the stochastic observability matrix rank are used to inform a Schmidt-Kalman Filter with the SRP parameters. Comparisons of the state estimation errors with and without the observability-estimability informed Schmidt-Kalman Filter are shown.

Chapter 5 applies observability to the light curve inversion process for determining when an Extended Gaussian Image (EGI) has been sufficient sampled for EGI minimization. An analogous observability Gramian to the common control system observability Gramian is derived and implemented. Methods for evaluating and visualizing the observability of the EGI minimization are developed for Low Earth Orbit (LEO), Medium Earth Orbit (MEO), and Geosynchronous Earth Orbit (GEO) systems. Next, constraints are applied to the observability analysis for determining realistic, efficient measurement strategies for light curve inversion. Finally, observability is conducted with knowledge of the mapping between the EGI and the original object to evaluate the impact of an error in solar panel deployment on the system geometry.

Chapter 6 presents the conclusions drawn from analysis of observability for SSA. In addition, recommendations for future areas of research are given.

2. BACKGROUND

In order to analyze observability for Space Situational Awareness (SSA) applications, several concepts must be introduced first. This chapter presents background materials on the fundamentals of observability, the orbit problem, ground-based optical observations, estimation methods, and light curve inversion.

2.1 Observability Fundamentals

The history of control theory can be divided into two major periods of development, each of which has an associated domain in which most methods focus [17]. The classical control theory period is defined by development of theories, from the early 1940s to the late 1950s, which are characterized by analysis focusing on the frequency-domain of control systems. Control theory development with emphasis on the frequency-domain has continued past this classical control theory period, but modern control theory became a major research area in the late 1950s and early 1960s. Modern control theory is characterized by analysis focusing on the time-domain of control systems, and more specifically, the state-space representation of control systems. A more thorough history of control theory, with additional references, can be found in the work of Friedland [17].

As the name implies, the state-space representation of a control system uses the concept of a state to describe a dynamical system. The state of a system contains physical quantities which are necessary for describing the dynamical progression of the system over time [17]. In actual, physical systems, noise and system inputs confound the ability of the states to exactly define the evolution of the system, but in general, the states of a system completely describe the dynamics. The states of a system are often not or not directly measurable quantities for physical systems.

For example, a simplified description of an orbit around the Earth requires a state consisting of position and velocity, but measurements of an object in orbit typically consist of angles or range from an observer to the object in orbit. In order to define the state of an orbit system, the relationship between the measurements and states must be known. In general, observability analysis explores this relationship between the measurements and states of a system.

The concept of observability was originally introduced by one of the pioneers of state-space modern control theory, Rudolph E. Kalman [15]. In the work by Kalman, the main existence theorem states that the optimal regulator problem has a solution if and only if the state dynamics are completely controllable and completely observable. The optimal regulator problem defined by Kalman seeks to find a control for a system which minimizes a performance index. Kalman also introduced the principal of duality, which determines that the optimal regulator problem is the Wiener filtering problem of the dual system. The principal of duality provides the connection of controllability and observability. If a system is completely observable, then the dual system is completely controllable. The reverse is also true. As a result, control theory analysis typically investigates controllability or observability.

A system is said to be observable if the initial state can be determined with a finite set of measurements. Kalman uses the term complete observability to describe a system where the state at any arbitrary time can be determined with a finite set of measurements [15]. After Kalman's initial definition of observability was posed, many similar definitions have been formulated for adaptation of observability to specific classes of systems [16–20,81]. In a general sense, observability determines whether the knowledge contained within the measurements of a system is sufficient for computing the states.

The test for observability from Kalman is binary in nature, i.e. a system is either observable or it is not observable. However, Kalman speculated that observability could find use as a measure of control system performance. Quantification of observability as a measure for a system has been studied extensively. Brown [23] and

Ablin [24] began to answer the question of how observable a system is through development of a degree of observability. Various tests for observability as a binary criteria and observability as a numeric measure have been developed [16–20, 26–38, 81]. Next, the mathematical formulation of observability is presented, beginning with a general nonlinear state-space control system representation.

2.1.1 State-Space Control System Representation

In the state-space representation of a control system, the dynamics are defined by a first-order ordinary differential equation (ODE) of the state. For a general nonlinear system with a state defined by $\mathbf{x}(t) = [x_1,\ x_2,\ \ldots,\ x_n]^T$, the state ODE is given by

$$\dot{\mathbf{x}}(t) = \mathbf{f}(t, \mathbf{x}(t), \mathbf{u}(t)), \tag{2.1}$$

where $\mathbf{f}(t, \mathbf{x}(t), \mathbf{u}(t))$ is a nonlinear model of the system dynamics, which is a function of time, the state, and the inputs, $\mathbf{u}(t)$. The state consists of n variables, and the state ODE initial condition is defined by the state at time t_0. The state-space system representation models the relationship between the state and output of a system.

$$\mathbf{z}(t) = \mathbf{h}(t, \mathbf{x}(t)) + \boldsymbol{\nu}(t), \tag{2.2}$$

where $\mathbf{z}(t) = [z_1,\ z_2,\ \ldots,\ z_r]^T$ is the output defined by r measurements, $\mathbf{h}(t, \mathbf{x}(t))$ is a nonlinear model of the output as a function of time and the state at time t, and $\boldsymbol{\nu}(t)$ is the continuous-time measurement noise. The dimension of the input is equal to the dimension of the state, n, and the dimension of the measurement noise is equal to the dimension of the output, r.

Most real, physical systems are nonlinear in nature. Hermann [20] and Casti [21] use Lie derivatives, which is a generalization of the directional derivative, for determining the observability of nonlinear systems. Linear methods are often preferred for application to linearized nonlinear systems due to computational efficiency and ease of implementation [61, 63, 67–70]. Although linear observability methods are most often applied to nonlinear systems which have been linearized, observability analysis

methods have been developed for the true nonlinear system. Casti [21] and Sontag [22] show how the observability of a linearized system is a sufficient condition for observability of the nonlinear system in the neighborhood of the linearization. The observability of the linearized system is not a necessary condition for observability of the nonlinear system because of the influence of the input, $\mathbf{u}(t)$, on nonlinear observability. In a linear system, observability does not depend on the control input, so the input can be assumed to be zero, as shown by Ogata [16]. However, Casti discusses how the input is important for nonlinear observability, and thus, observability of the linearized system is not a necessary condition for nonlinear observability [21].

Linear observability methods are studied in this work for SSA due to the computational efficiency and ease of implementation of the methods. In addition, the systems within SSA applications are commonly linearized for analysis. Two methods exist for linearizing the nonlinear state-space equations. State and output deviations from a reference can be used for the linearization, as in [14, 49, 50, 81, 82], or the Jacobian of the nonlinear state and measurement model can be computed, as in [50]. Implementing the Jacobian linearization method from Montenbruck & Gill, the linearized, continuous-time state-space equations are given as

$$\dot{\mathbf{x}}(t) = \mathbf{A}(t)\ \mathbf{x}(t), \tag{2.3}$$

$$\mathbf{z}(t) = \widetilde{\mathbf{H}}(t)\ \mathbf{x}(t) + \boldsymbol{\nu}(t), \tag{2.4}$$

where $\mathbf{A}(t)$ is the Jacobian of the nonlinear state dynamics model in Equation 2.1, and $\widetilde{\mathbf{H}}(t)$ is the Jacobian of the nonlinear measurement model in Equation 2.2. Note that the control input $\mathbf{u}(t)$ is assumed to be the zero vector as it will not influence the linear observability analysis. In addition, if the deviation linearization method was implemented for obtaining the linear state-space equations, $\mathbf{x}(t)$ and $\mathbf{z}(t)$ would represent the deviations in the state and output with respect to a reference.

Discrete-time state-space equations can be defined through a discretization of Equations 2.3 and 2.4. Following the discretization procedure from DeCarlo [83], the discrete-time state-space equations are given by

$$\mathbf{x}(t_k) = \mathbf{\Phi}(t_k, t_0)\ \mathbf{x}(t_0), \tag{2.5}$$

$$\mathbf{z}(t_k) = \widetilde{\mathbf{H}}(t_k)\ \mathbf{x}(t_k) + \boldsymbol{\nu}(t_k), \tag{2.6}$$

where $\mathbf{\Phi}(t_k, t_0)$ is the state transition matrix (STM), which transforms the state from t_0 to t_k. The STM is a linear mapping of the state, which can be numerically determined by solving the STM ODE in Equation 2.7.

$$\dot{\mathbf{\Phi}}(t_k, t_0) = \mathbf{A}(t_k)\ \mathbf{\Phi}(t_k, t_0), \qquad \mathbf{\Phi}(t_0, t_0) = I_{n\times n}. \tag{2.7}$$

A derivation of the STM is presented by Friedland [17]. Next, the observability Gramian is derived with the state-spaced control system representation.

2.1.2 Observability Gramian

The output equations of the continuous-time and discrete-time systems, Equations 2.4 and 2.6, show the relationship between the measurements and states of a system. However, in most cases, the linearized measurement model is non-singular and there is measurement noise, so direct calculation of the state from the measurements is not possible. Therefore, the output equation is manipulated to define the initial state in terms of the measurements, and as a result, the observability Gramian is obtained. A derivation of the observability Gramian follows for the discrete-time system. The observability Gramian in the discrete-time system is commonly referred to as the observability matrix. An analogous derivation exists for the continuous-time observability Gramian, and details of both derivations can be found in the works of Friedland [17], Ogata [16], Gajic [18], and Bay [19]. In addition, the derivation is performed for the deterministic system, i.e. the measurement noise is not present in the output equation. The stochastic observability matrix, including measurement noise, is derived in Section 3.1.1.

The derivation of the deterministic observability matrix begins by substituting Equation 2.5 into Equation 2.6.

$$\mathbf{z}(t_k) = \widetilde{\mathbf{H}}(t_k)\ \mathbf{\Phi}(t_k, t_0)\ \mathbf{x}(t_0), \tag{2.8}$$

Next, measurements from time t_0 to time t_m are accumulated, resulting in

$$\begin{bmatrix} \mathbf{z}(t_0) \\ \mathbf{z}(t_1) \\ \vdots \\ \mathbf{z}(t_m) \end{bmatrix} = \begin{bmatrix} \mathbf{H}(t_0) \\ \mathbf{H}(t_1) \\ \vdots \\ \mathbf{H}(t_m) \end{bmatrix} \mathbf{x}(t_0) \qquad \text{or} \qquad \bar{\mathbf{z}} = \bar{\mathbf{H}}\ \mathbf{x}(t_0), \tag{2.9}$$

where $\mathbf{H}(t_k) = \widetilde{\mathbf{H}}(t_k)\ \mathbf{\Phi}(t_k, t_0)$. The $\bar{\mathbf{H}}$ matrix is not likely to be a square matrix, and the required number of measurements, m, for computing the initial state is not known. The initial state is solved for by first multiplying both sides of Equation 2.9 on the left by $\bar{\mathbf{H}}^T$.

$$\bar{\mathbf{H}}^T\ \bar{\mathbf{z}} = \bar{\mathbf{H}}^T\ \bar{\mathbf{H}}\ \mathbf{x}(t_0). \tag{2.10}$$

Finally, the initial state can be determined by taking the inverse of $\bar{\mathbf{H}}^T\ \bar{\mathbf{H}}$, resulting in

$$\mathbf{x}(t_0) = (\bar{\mathbf{H}}^T\ \bar{\mathbf{H}})^{-1}\ \bar{\mathbf{H}}^T\ \bar{\mathbf{z}}. \tag{2.11}$$

Equation 2.11 relies upon the assumption that $\bar{\mathbf{H}}^T\ \bar{\mathbf{H}}$ is invertible. Observability defines whether sufficient knowledge of the initial state is contained within the measurements of a system. In the discrete-time state-space system, observability depends on the invertibility $\bar{\mathbf{H}}^T\ \bar{\mathbf{H}}$, otherwise known as the observability matrix, $\mathcal{O}(t_0, t_m)$. A common form of the observability matrix is given by

$$\mathcal{O}(t_0, t_m) = \sum_{k=0}^{m} \mathbf{\Phi}(t_k, t_0)^T\ \widetilde{\mathbf{H}}(t_k)^T\ \widetilde{\mathbf{H}}(t_k)\ \mathbf{\Phi}(t_k, t_0), \tag{2.12}$$

Therefore, a discrete-time state-space system is observable if the measurements contain sufficient knowledge of the initial state such that $\mathcal{O}(t_0, t_m)$ is invertible.

This derivation of the discrete-time observability matrix is shown for a time-varying system. Simplified time-invariant observability matrix forms exist, but the

applications of interest in this work are time-varying. Similar derivations of the observability matrix are provided by Ogata [16], Gajic [18], and Bay [19]. Following a similar procedure, the analogous continuous-time observability Gramian is defined by

$$\mathcal{O}(t_0, t_m) = \int_{t_0}^{t_m} \mathbf{\Phi}(\tau, t_0)^T \ \mathbf{H}(\tau)^T \ \mathbf{H}(\tau) \ \mathbf{\Phi}(\tau, t_0) \ dt. \tag{2.13}$$

Typically the continuous-time matrix in Equation 2.13 is called the observability Gramian and the discrete-time matrix in Equation 2.12 is called the observability matrix. Next, the different conditions for observability and measures of observability are introduced.

2.1.3 Conditions for Numerical Evaluation of Observability

For discrete, time-varying, linear systems, the common test for observability involves the observability matrix. The observability matrix is defined within the computation of the initial state vector from measurements in a control system in Equation 2.11. As part of the computation of the initial state vector, the observability matrix is assumed to be invertible. Therefore, a system is observable, if the observability matrix is non-singular.

There are many equivalent conditions for determining whether a matrix has an inverse [84]. Common equivalent conditions used with observability analysis are matrix rank, column linear independence, eigenvalues, singular values, and determinant. For a square matrix with $n \times n$ rows and columns, a matrix is invertible when the rank is equal to n. Equivalently, if the determinant is not equal to zero, then the matrix is invertible. In addition, if all of the eigenvalues are nonzero, then the matrix is invertible. Many of the equivalent conditions for matrix invertibility can be evaluated for determining system observability. In this work, matrix rank through singular value decomposition and column linear independence are explored for analyzing observability.

In observability literature, many different methods are implemented for analyzing the observability of a system. These methods can be separated by methods which determine a binary observability result and methods which determine a quantitative measure for observability. The original definition of observability from Kalman focused on the binary criteria for observability, i.e. whether a system observable for not. A common test for this binary criteria is the observability matrix rank test for determining invertibility. If the observability matrix is full rank, i.e. the rank equals n for a square $n \times n$ matrix, then a system is observable, and if the observability matrix is rank deficient, then the system is not observable. Within the introductory work of observability, Kalman raised an open question of whether observability could be extended beyond the binary full rank criteria, as a numeric measure for control system performance [15]. Quantifying observability through a numeric measure has been explored in many works within the field of state-space modern control theory [19, 24, 26–33, 35, 37, 51, 60, 74–76, 85–87]. Some examples of measures of observability are the observability matrix determinant, condition number, and singular values.

When linear observability methods are applied to linearized, time-varying systems, analytical results can be challenging to achieve due to the linearized dynamics and time-varying nature of the system. Therefore, observability analysis and measures of observability are often computed numerically. Numerical determination of matrix rank can be computed with several methods, the most commonly used methods are eigenvalue decomposition or singular value decomposition. For a system to be full rank, the eigenvalues or singular values must be nonzero, and the rank of a matrix is equal to the number of nonzero eigenvalues or singular values. An advantage of implementing singular values over eigenvalues for determining matrix rank is that singular values are always greater than or equal to zero [88].

The singular values of a matrix are determined through singular value decomposition (SVD), which decomposes a matrix, square or rectangular, into several components. For example, a matrix $\mathbf{A}$ is decomposed with SVD as

$$\mathbf{A} = \mathbf{U}\ \mathbf{S}\ \mathbf{V}^T, \tag{2.14}$$

where $\mathbf{U}, \mathbf{V}$ are orthogonal matrices and $\mathbf{S}$ is a diagonal matrix containing the singular values. Restating the binary condition for observability, if the singular values of the observability matrix are strictly positive, then a system is observable for a given analysis time.

Numerical error, specifically rounding error, presents a challenge of implementing this test for observability numerically. Due to numerical error accumulation over time and precision limits, differentiating a number from zero is not well defined. The machine epsilon, ε, is used to define a tolerance in Equation 2.15 for computing matrix rank with singular values.

$$tol = \max(\mathbf{s}) \times \max(\text{size}(\mathcal{O}(t_0, t_m))) \times \varepsilon, \tag{2.15}$$

where $\mathbf{s}$ are the singular values of the observability matrix. Equation 2.15 is one of many representations of numerical error approximation when computing matrix rank using floating point arithmetic [89].

The ε represents the smallest value that can be added to one, where the resulting summation can still be differentiated from one using floating point arithmetic. For a double precision computer, $\varepsilon = 2^{-53} = 1.11e-16$, and the minimum floating point number which can be stored is 2^{-1074}. The machine epsilon specifies the spacing between two floating point numbers. The spacing between a value of one and the adjacent floating point number is ε, but this spacing also depends on the floating point number being evaluated. Higham defines the spacing between a floating point number, x, and an adjacent number by $\beta^{-1}\ \varepsilon\ |x|$, where β is the base for the precision of the computer, which is often two [90]. For example, the spacing between 10^{-30} and the next adjacent number to 10^{-30} on a computer with double precision is defined

by $2^{-1} \times 2^{-53} \times 10^{-30} = 5.55 \times 10^{-47}$. For determining the rank of a matrix with singular values, the tolerance in Equation 2.15 approximates the rounding error and computes the spacing between two values near the scale of the largest singular value of the observability matrix.

When the observability matrix has singular values which are below the tolerance line, the observability cannot be determined numerically due to rounding errors. This distinction of not being able to determine the observability due to numerical errors and deeming a system unobservable is important when evaluating observability numerically. Even though understanding of a system may enable stating that a system is unobservable given certain measurements and states, evaluation of the system numerically will not prove that said system is unobservable. The cause for singular values of the observability matrix being below the tolerance line cannot be distinguished between a lack of knowledge in the measurements and numerical rounding errors. Although this distinction is minute, it is important to make for accurate representation of numerical observability results. Through understanding of system dynamics, comments on unobservability may be made, but these comments should be made with thorough understanding of the dynamics and not based on the singular values of the observability matrix alone.

The singular values of the observability matrix and the observability matrix rank change over time as more measurements are added to the system. Therefore, these quantities can be used as measures of observability, in addition to the full rank criteria [29, 53]. The observability matrix does not contain measurements, but the observability matrix is evaluated at each measurement time step and the model defining the measurement-state relationship, the linearized measurement matrix, is a component of the observability matrix. As the analysis time increases, which is directly related to the time of each measurement, information is added to the system. When singular values move from below to above the tolerance line, the rank of the observability matrix increases, indicating the measurements provide more knowledge of the state. Note that the relationship between the singular values and the state variables of the

system is not one-to-one. As a singular value moves above the tolerance line, this does not correspond to a single state becoming observable. Systems may exist where the singular value and state relationship is one-to-one, but in general this is not true.

The condition number of a matrix, which is the ratio of the largest singular value to the smallest singular value, is sometimes used with the observability matrix to give a measure of the system observability. The condition number attempts to determine how ill-conditioned a matrix is, i.e. how close the matrix is to not being invertible [91]. Therefore, the condition number is purely a relative measure and cannot give a binary result of observability. Furthermore, the condition number of the observability matrix is implemented with the notion that a smaller condition number indicates the system has strong observability and a larger condition number indicates the system has poor observability. The criteria for small or large condition numbers is not well defined, and the notion of small or large condition numbers will change depending on the system of interest.

Because the condition number does not have a clearly defined criteria for measuring observability, it is not implemented in this work for evaluating whether a system is observable or not. Analysis of the singular values compared to the tolerance line is implemented in this work to provide more information about the system observability beyond the binary criteria of observable or not. This analysis of the singular values of the observability matrix is not necessarily a measure of observability, but it does provide more insight into the observability than a binary result. In addition to comparing the singular values of the observability matrix to the tolerance line, some of the results implement a different measure for analysis of observability. The ratio of the smallest singular value of the observability matrix to the tolerance line is implemented in Section 3.8 for comparing different observability analysis cases. This ratio is related to the inverse of the matrix condition number; however, with the addition of the other components of the tolerance line, an estimation of the numerical rounding error is also considered. When this ratio of the smallest singular value to the tolerance line is implemented, the criteria for observability is given by whether

this ratio is greater than one. Comparison of different observability cases with this ratio as a measure of observability is explored in more detail in Section 3.8.

Finally, when the observability of the light curve inversion problem is explored in Chapter 5, the equivalent condition of matrix observability which depends on the linear independence of the columns of a matrix is exploited as an observability measure. Section 5.1 derives the observability Gramian for the light curve inversion problem. Due to the linear nature of this problem as it has been defined, the linear independence of the columns of the observability matrix are used to determine how specific surface normal directions of an object become observable. More in-depth discussion and results implementing this observability measure are given in Section 5.4.

2.2 The Orbit Problem

The works of Kepler and Newton are fundamental to governing the motion of objects in orbit. Johannes Kepler developed laws of planetary motion after acquiring the extensive astronomical observations from Tycho Brahe, after his untimely death [92, 93]. These laws of planetary motion describe how planetary bodies move in an orbit, but not the dynamical explanation of why bodies move in this way. Sir Isaac Newton developed the laws of motion and the law of universal gravitation which give the mathematical basis for the motion of orbiting bodies [14, 49]. Therefore, this background focuses on Newton's contributions. Newton's laws of motion and law of gravitation are implemented for deriving the two-body equations of motion.

2.2.1 Two-Body Equations of Motion

Newton's universal law of gravitation defines the force between two point masses as

$$F = \frac{GM_1M_2}{d^2}, \tag{2.16}$$

where F is the force on each body, G is the universal gravitation constant, M_i is the mass of each body, and d is the distance between the two bodies [49]. Applying Newton's second law of motion and defining the relative vector relationship between the position of the Earth and a resident space object (RSO), the equations of motion for an RSO with respect to the Earth are defined as

$$\ddot{\mathbf{r}}_{\oplus\text{RSO}} = -\frac{G(m_{\oplus} + m_{\text{RSO}})}{r^2}\hat{\mathbf{r}}_{\oplus\text{RSO}}, \tag{2.17}$$

where $m_{\oplus}$ is the mass of the Earth, m_{RSO} is the mass of an RSO, and $\mathbf{r}_{\oplus\text{RSO}}$ is the position vector from the Earth to an RSO. The mass of the Earth is many orders of magnitude larger than the mass of an RSO, so the acceleration of an RSO due to the Earth is can be reduced to

$$\ddot{\mathbf{r}} = -\frac{\mu}{r^3}\mathbf{r}, \tag{2.18}$$

where $\mu = G\ m_{\oplus}$ is the universal gravitational constant. In Equation 2.18, the position unit vector has been replaced with the equivalent position vector divided by the magnitude of the position vector. In addition, the subscripts are removed for simplicity and for agreement with commonly displayed forms of the two-body equations of motion [14, 49, 50]. The nonlinear equations of motion in this section are converted to the state-space control system representation and linearized in Section 2.4 to develop the observability matrix for the orbit problem.

Several assumptions were made for the derivation of the two-body equations of motion in Equation 2.18. First, the mass of the RSO is assumed to be negligible. Next, the coordinate system used in the derivation of the relative motion of an RSO with respect to the Earth is assumed to be inertial. The Earth is not actually inertially fixed, but for problems focused on the motion of a body around the Earth, this inertial assumption is common. In order to apply Newton's laws, the two bodies must be point masses, so the assumption must be made that the bodies are spherically symmetric with uniform density. Finally, the equations of motion defined by Equation 2.18 describe a system where no forces other than the gravitational force from the central body act on the RSO [14].

2.2.2 Perturbed Orbital Motion

For precisely describing the orbit of RSOs, the assumptions of the two-body model can be too restrictive. The shape of the Earth is not a sphere with uniform density, but an oblate spheroid. The Earth is not a truly inertial frame for an object orbiting the Earth. In addition, other forces in addition to the gravitational force from a point mass central body exist.

These forces in addition to the gravitational force from the central body can be conservative or non-conservative. For example, a non-spherical Earth model results in a conservative, perturbative force on an RSO. Forces from other celestial bodies, such as the Sun and the Moon, are also conservative forces on an RSO. Non-conservative forces modify the energy of the system, and some examples are solar radiation pressure (SRP) and atmospheric drag. Montenbruck & Gill present a schematic of the relative impact of various perturbations compared to the acceleration due to the central body, in Figure 3.1 of [50]. The schematic shows how the perturbations on an RSO vary with orbit altitude above the surface of the Earth. For RSOs in low Earth orbit (LEO) atmospheric drag can be one of the largest perturbations depending on the altitude and object size. For objects in geosynchronous Earth orbit (GEO), third-body perturbations and the SRP perturbation can significantly impact orbital motion. Another method for depicting the impact of various perturbations on orbit accuracy has been shown by Beutler [94]. Beutler similarly gives relative accelerations of the perturbations to the central body gravitational acceleration, and also shows how these perturbations manifest in the orbit error after one day.

The equations of motion for an RSO, including the influence of perturbative accelerations, can be defined as

$$\ddot{\mathbf{r}} = -\frac{\mu}{r^3}\mathbf{r} + \sum \mathbf{a}_{\text{perturb}}, \tag{2.19}$$

where $\sum \mathbf{a}_{\text{perturb}}$ represents the perturbing accelerations due to any modeled perturbing forces.

When the assumption of a perfectly spherical Earth is relaxed, the oblateness of the Earth can be modeled with spherical harmonics and a disturbing potential function.

$$\ddot{\mathbf{r}} = \nabla U, \tag{2.20}$$

where ∇ is the gradient operator and U is the potential function. This potential function form of the equations of motion is equivalent to Equation 2.18 when $U = \frac{\mu}{\mathbf{r}}$. The potential function for a non-spherical Earth model is defined by dividing the Earth into a collection of differential masses. The total gravitational potential due to the differential masses acting on an RSO is given by

$$U = G \int_{\oplus} \frac{1}{\rho_q} \mathrm{d}m_q, \tag{2.21}$$

where ρ_q is the relative distance between the differential mass, m_q [14]. The integral is performed over the entire central body. Equation 2.21 can be approximated with Legendre polynomials and spherical harmonics of degree l and order m. A common form of the potential function for a non-spherical Earth model is given by

$$U = \frac{\mu}{r} \sum_{l=2}^{\infty} \sum_{m=0}^{l} \left(\frac{R_{\oplus}}{r} \right)^{l} P_{l,m} \left[\sin \phi_{\mathrm{gc,sat}} \right] \left(C_{l,m} \cos(m\lambda_{\mathrm{sat}}) + S_{l,m} \sin(m\lambda_{\mathrm{sat}}) \right), \tag{2.22}$$

where $R_{\oplus}$ is the radius of the Earth, $P_{l,m}[\cdot]$ are the Legendre polynomials, $\phi_{\mathrm{gc,sat}}$ is the geocentric latitude of the RSO, and λ_{sat} is the longitude of the RSO. The terms $C_{l,m}$ and $S_{l,m}$ are gravitational coefficients in the spherical harmonics formulation [95].

In addition, other celestial bodies perturb the motion of an object in orbit around Earth. The following third-body perturbation models can be included for a variety of celestial bodies, but the most commonly included third-body perturbations are due to the Sun and the Moon. The third-body perturbation due to the Sun is given by

$$\ddot{\mathbf{r}}_{3\mathrm{B}_{\odot}} = -\mu_{\odot} \left(\frac{\mathbf{r} - \mathbf{r}_{\odot}}{|\mathbf{r} - \mathbf{r}_{\odot}|^3} + \frac{\mathbf{r}_{\odot}}{r_{\odot}^3} \right), \tag{2.23}$$

where $\mu_{\odot}$ is the gravitational constant for the Sun and $\mathbf{r}_{\odot}$ is the position of the Sun with respect to the center of the Earth. Similarly, the third-body perturbation due to the Moon is given by

$$\ddot{\mathbf{r}}_{3\mathrm{B}_{\leftmoon}} = -\mu_{\leftmoon} \left(\frac{\mathbf{r} - \mathbf{r}_{\leftmoon}}{|\mathbf{r} - \mathbf{r}_{\leftmoon}|^3} + \frac{\mathbf{r}_{\leftmoon}}{r_{\leftmoon}^3} \right), \tag{2.24}$$

where $\mu_{\leftmoon}$ is the gravitational constant for the Moon and $\mathbf{r}_{\leftmoon}$ is the position of the Moon with respect to the center of the Earth [95]. For any additional celestial bodies, the position vectors and gravitational constant can be substituted in for the corresponding Sun or Moon terms. A general form of the third-body perturbation for n perturbing bodies is given by

$$\ddot{\mathbf{r}}_{3\mathrm{B}} = -\sum_{i=1}^{n} \mu_{3\mathrm{B}_i} \left(\frac{\mathbf{r} - \mathbf{r}_{3\mathrm{B}_i}}{|\mathbf{r} - \mathbf{r}_{3\mathrm{B}_i}|^3} + \frac{\mathbf{r}_{\odot}}{r_{3\mathrm{B}_i}^3} \right). \tag{2.25}$$

The perturbing accelerations of a non-spherical Earth model and other celestial bodies are independent of the RSO mass, area, and attitude. However, non-conservative forces, such as atmospheric drag and SRP, often heavily depend on the object mass, area, and attitude [50]. For example, an object with large solar panels will experience a larger perturbing acceleration from SRP if the solar panel normal vector is aligned with the Sun vector compared to an object with a smaller surface area facing the Sun.

As shown by Montenbruck & Gill, atmospheric drag can be a dominant perturbing force for objects in LEO. The perturbing acceleration due to drag is modeled by

$$\ddot{r}_{\mathrm{drag}} = -\frac{1}{2} C_D \frac{A}{m} \rho(h) v_{rel}^2 \hat{\mathbf{v}}_{rel}, \tag{2.26}$$

where C_D is the drag coefficient, $\rho(h)$ is the function for the air density at a given altitude h, $\mathbf{v}_{rel}$ is the velocity direction relative to the atmosphere. This model of the drag perturbation assumes a spherical object [95].

For objects in GEO, SRP can be a large perturbing force depending on the area-to-mass ratio (AMR) of an object and material reflectivity characteristics. The SRP perturbation models the acceleration due to reflection of a light source off an object. The so-called cannonball model, which approximates an object as a sphere, is often applied as a first approximation for SRP. The SRP perturbation cannonball model is defined by

$$\mathbf{a}_{\mathrm{SRP,sphere}} = -\frac{A}{m}\, C\, (\mathrm{AU})^2 \frac{E}{c} \frac{\mathbf{s}}{|\mathbf{s}|^3}, \tag{2.27}$$

$$C = \frac{1}{4} + \frac{1}{9} C_d, \tag{2.28}$$

where A is the surface area, m is the mass, C_d is the diffuse coefficient, E is the solar constant, c is the speed of light, AU is the astronomical unit, and $\mathbf{s} = \mathbf{r} - \mathbf{r}_\odot$ is the Sun-object vector. The diffuse coefficient is a component of a Lambertian-Specular reflection model and represents how light reflects off an object in a diffuse manner [95].

If an object is a flat plate or is modeled as a composition of many flat facets, the perturbing acceleration due to each flat face is modeled by

$$\mathbf{a}_{\text{SRP,flat}} = \frac{A}{m}\,\frac{E}{c}\frac{(\text{AU})^2}{|\mathbf{s}|^2}\,\mathbf{s}\cdot\mathbf{n}[(1-C_s)\mathbf{s} + 2(C_s\mathbf{s}\cdot\mathbf{n} + \frac{1}{3}C_d)\mathbf{n}], \tag{2.29}$$

where $\mathbf{n}$ is the outward surface normal vector of the flat plate or facet and C_s is the specular reflection coefficient. The SRP perturbation for a flat plate is constrained by

$$0 < \arccos(\hat{\mathbf{s}}\cdot\hat{\mathbf{n}}) < \frac{\pi}{2}, \tag{2.30}$$

which represents the fact that the surface normal vector and the Sun-object vector must be in the same hemi-sphere to perturb the flat plate or facet [95].

This work predominately focuses on perturbation of the two-body motion with SRP. In a small portion of the work, propagation is performed with the Simplified General Perturbations 4 (SGP4) propagation model. The SGP4 propagator includes perturbations from a non-uniform Earth model with zonal harmonics up to degree five and an analytical drag model. Further details on the development and implementation of SGP4 can be found in [6, 14, 96].

2.3 Ground-based Optical Observations

Ground-based optical observations are considered in this study of observability analysis for SSA. Although ground-based observers have to contend with atmospheric effects, the relatively low cost of establishing new observation systems and the ease of access to hardware for maintenance often make ground-based observation systems advantageous compared to spaced-based systems [97].

2.3.1 Coordinate Systems

In Section 2.2, the equations of motion for an object in orbit around Earth were derived with respect to an inertial frame, which is commonly defined as the Earth Centered Inertial (ECI) reference frame. The ECI reference frame is defined by the $\hat{i}$-axis in the direction of the vernal equinox, the $\hat{k}$-axis is aligned with the rotation axis of the Earth, and the $\hat{j}$-axis completes the right-handed coordinate system [14].

While propagation of the equations of motion for an RSO typically occurs in the ECI reference frame, ground-based observations are obtained from an observer on the surface of the Earth. The frame of the observer differs from the ECI frame in two ways. First, the Earth rotates compared to an inertial frame. Second, the observer reference frame is centered on the surface of the Earth rather than the Earth center. In order to explore the relationship between ground-based optical observations and the state of an RSO with observability analysis, the relationship between the ECI reference frame and the reference frame of the observer must be defined.

A ground-based observer is fixed to the surface of the Earth and rotates with the Earth. As a result, the position of the observer is defined with respect to the Earth Centered, Earth Fixed (ECEF) coordinate frame. The ECEF coordinate frame is defined by the $\hat{e}_1$ axis directed toward the Greenwich meridian from the center of the Earth, the $\hat{e}_3$ axis is aligned with the rotation axis of the Earth, and the $\hat{e}_2$ axis completes the right-handed coordinate system [14]. The ECI and ECEF coordinate frames both share the rotation axis of the Earth as a coordinate axis. Therefore, a position vector for an observer in the ECEF coordinate frame is rotated to the ECI coordinate frame with a rotation about the rotation axis of the Earth. The angle of rotation between these two coordinate systems is defined by the Greenwich Mean Sidereal Time (GMST), θ. For example, the position of a ground station in the ECEF coordinate frame, $\mathbf{r}_{\text{gs}}^{\text{ECEF}}$, is rotated to the ECI coordinate frame by

$$\mathbf{r}_{\text{gs}}^{\text{ECI}} = \mathbf{R}_3(\theta)\ \mathbf{r}_{\text{gs}}^{\text{ECEF}}, \tag{2.31}$$

where $\mathbf{R}_3(\theta)$ is the rotation about the $\hat{e}_3$ axis by the GMST. The GMST determines the angle between the Greenwich meridian and the vernal equinox.

The rotation of an observer position vector from the ECEF coordinate frame to the ECI coordinate frame assumes an inertially fixed rotation axis for the Earth. However, the rotation axis of the Earth is perturbed by the gravitational force of other planets and the Moon. The perturbed motion of Earth's rotation axis is defined by components of gyroscopic motion, precession and nutation. The period of precession and nutation are approximately 26,000 years and 18.6 years, respectively [14]. The impact of these effects is often assumed negligible for short time scales. However, for precise orbit determination, corrections for precession and nutation should be considered. In this work, precession and nutation corrections are applied when SGP4 is implemented for propagation. Montenbruck & Gill provide a thorough derivation and discussion of the precession and nutation corrections to the rotation axis of the Earth [50]. Using these corrections with Equation 2.31 results in a more precise observer position in ECI coordinates.

2.3.2 Right Ascension and Declination Measurements

The ground-based optical observations implemented in this work consists of right ascension, α, and declination, δ, angles. These angles are defined for an observer located with latitude ϕ and GMST θ by

$$\alpha = \arctan\left(\frac{\rho_y}{\rho_x}\right), \tag{2.32}$$

$$\delta = \arctan\left(\frac{\rho_z}{\sqrt{\rho_x^2 + \rho_y^2}}\right), \tag{2.33}$$

where,

$$\rho_x = x - R_\oplus \cos\phi \cos\theta, \tag{2.34}$$

$$\rho_y = y - R_\oplus \cos\phi \sin\theta, \tag{2.35}$$

$$\rho_z = z - R_\oplus \sin\phi. \tag{2.36}$$

The x, y, and z variables are components of the object position in the ECI coordinate frame, and $R_\oplus$ is the radius of the Earth. The right ascension and declination measurements are defined with the relative position vector from the observer to the object, $\rho = [\rho_x,\ \rho_y,\ \rho_z]^T$ in the ECI coordinate frame. Therefore, the state and measurements are now both defined in the ECI coordinate frame.

Note that these angles are often called topocentric right ascension and declination because they are defined with the relative position vector from the observer, or topocenter, to the object. This terminology differentiates the right ascension and declination angles which are defined with respect to the geocenter and are often used in astronomy. More information on common coordinate systems and other types of measurements used in astrodynamics is provided by Vallado [14].

2.3.3 Optical Sensors and Measurement Noise Estimation

In real, physical systems, the right ascension and declination angles in Equations 2.32 and 2.33 are obtained from optical measurements, such as from a ground-based telescope. A common type of optical sensor used in a full telescope setup is the Charged Couple Device (CCD), which determines the electron counts due to photons from various light sources impinging upon the sensor. The noise estimation performed in this work uses observations taken with a CCD. Detail on the CCD sensor and relevant equations are given in the work of Sanson & Frueh [98].

In any physical system, noise is inherent. Sources of noise in the CCD measurement can be separated into noise sources which are internal to the CCD sensor and noise due to external light sources. Two common sources of internal noise are dark noise resulting from extra undesirable electron emissions, and read-out noise resulting from flaws in the CCD. External noise is modeled by various background light sources, e.g. noise effects from the Sun, the Moon, zodiac light, stars, and galactic light. Details on the background light sources is provided in [99]. The internal and

external noise sources in a CCD both contribute to uncertainty in the right ascension and declination measurements.

Uncertainty quantification methods from Sanson & Frueh are implemented in this work to estimate realistic uncertainties in right ascension and declination measurements. The methods from Sanson & Frueh quantify the uncertainty in pixel position of an observation based on a Gaussian fit of a background corrected image and the inversion of the Fisher Information Matrix [98, 100]. These methods quantify the lower limit of the uncertainty in pixel position. Figure 2.1 depicts an observation of a GEO satellite from the Purdue Optical Ground Station (POGS). The satellite is a streak in the image because the optical telescope is moving with the stars, thus the satellite is moving through the frame. Images of this type are used in the following uncertainty quantification.

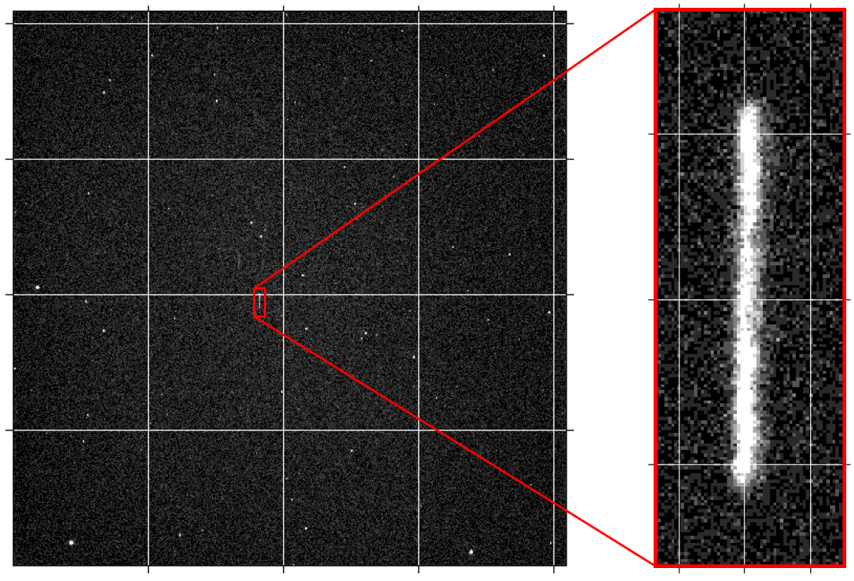

Figure 2.1. Image of a GEO satellite from POGS, taken in sidereal tracking mode resulting in a streaked satellite observation.

For quantification of the pixel position uncertainty in an observation with a satellite streak, parameters for a two-dimensional Gaussian are estimated with the following model

$$f = A \ \exp\left[-\frac{1}{2}\left(c_1(x-x_0)^2 + 2c_3(x-x_0)(y-y_0) + c_2(y-y_0)^2\right)\right], \tag{2.37}$$

where A defines the amplitude of the Gaussian fit, c_1 and c_2 define the size of the fitted Gaussian in the x and y axes, c_3 orients the Gaussian with respect to the x and y axes, and x_0 and y_0 locate the center of the Gaussian in the image. Once the parameters defining the two-dimensional Gaussian are estimated, the inverse of the Fisher Information Matrix, which is calculated to determine the pixel position uncertainties, is shown in Equation 2.38.

$$\begin{aligned}\mathbf{K}_{x_0,y_0} = &\frac{\delta_x\delta_y}{(\mathrm{SNR})^2\sqrt{D}\pi^{\frac{3}{2}}} \times \\ &\times \begin{bmatrix} 2c_2(\sqrt{\pi} + 2\sqrt{\frac{D}{c_2}}ad_a + 2\sqrt{\frac{D}{c_1}}\rho^2 bd_b) & -2c_3(\sqrt{\pi} + 2\sqrt{\frac{D}{c_2}}ad_a + 2\sqrt{\frac{D}{c_1}}\rho^2 bd_b) \\ -2c_3(\sqrt{\pi} + 2\sqrt{\frac{D}{c_2}}ad_a + 2\sqrt{\frac{D}{c_1}}\rho^2 bd_b) & 2c_1(\sqrt{\pi} + 2\sqrt{\frac{D}{c_1}}bd_b + 2\sqrt{\frac{D}{c_2}}\rho^2 ad_a) \end{bmatrix},\end{aligned} \tag{2.38}$$

Equation 2.38 also requires parameters of the CCD and parameters of the signal truncation. In Equation 2.38, δ_x and δ_y are the pixel scales in the x and y directions, $\mathrm{SNR} = \frac{A\delta_x\delta_y}{\sigma}$ is the signal-to-noise ratio, σ is the standard deviation of the background subtracted signal, $D = c_1c_2 - c_3^2$ is the determinant, $\rho = \frac{c_3}{\sqrt{c_1c_2}}$ is a correlation factor between the x and y axes, a and b are image truncation parameters in the x and y directions, $d_a = \exp(-\frac{Da^2}{c_2}D)$, and $d_b = \exp(-\frac{Db^2}{c_1}D)$. Details on the derivation of the pixel position uncertainty quantification for space object observation are given in the works of Sanson & Frueh [98, 100].

Right ascension and declination angle measurements are implemented throughout this work. The uncertainties in pixel position, given by the diagonal in Equation 2.38, are transformed from the pixel position space to the right ascension-declination space. The astronomical position of the image is determined by detecting the catalog stars in the image in a process often called plate solving [101]. The transformation from pixel

coordinates to right ascension-declination coordinates is computed during the plate solving process. Next, this transformation matrix rotates the inverse of the Fisher Information Matrix, $\mathbf{K}_{x_0,y_0}$, from the pixel space into the right ascension-declination space with covariance rotation methods from Vallado and Alfano [102].

When this method for quantifying the right ascension and declination uncertainty is implemented for a single image instead of the true mean of the distribution, a small bias may be introduced. Therefore, the uncertainties from a set of seven comparable images are averaged to overcome the potential small bias from determining the uncertainty from a single measurement. Specific right ascension and declination measurement uncertainties and SNR averages are presented and implemented in Section 3.6.3.

2.3.4 Apparent Magnitude Light Curve Measurements

Light curves, which are defined by the apparent magnitude of an object over time, are another measurement type implemented in this work. The apparent magnitude of an object is a measure of the irradiance received by a sensor relative to the irradiance from a light source. The apparent magnitude is influenced by the geometry among the observer, object, and Sun. In addition, the attitude of the object will influence how light from the Sun is reflected towards the observer.

The magnitude and irradiance of the Sun are often used in apparent magnitude calculations, as shown by

$$\text{mag} = \text{mag}_{\odot} - 2.5 \log_{10} \left(\frac{I_{\text{sensor}}}{I_{\odot}} \right), \tag{2.39}$$

where $\text{mag}_{\odot} = -26.74$ is the apparent magnitude of the Sun at 1 AU, I_{sensor} is the irradiance received by a sensor, and $I_{\odot}$ is the irradiance emmitted by the Sun at 1 AU [99]. The ratio of the irradiance values can be expanded to explain how Equation 2.39 captures the brightness of an object which is illuminated by the Sun.

$$\frac{I_{\text{sensor}}}{I_{\odot}} = \left(\frac{I_{\text{obj}_{\text{in}}}}{I_{\odot}} \right) \left(\frac{I_{\text{obj}_{\text{ex}}}}{I_{\text{obj}_{\text{in}}}} \right) \left(\frac{I_{\text{sensor}}}{I_{\text{obj}_{\text{ex}}}} \right). \tag{2.40}$$

The first fraction in Equation 2.40 corrects for differences between the Sun-object distance and 1 AU. This term is necessary because the magnitude and irradiance of the Sun are based on the value at 1 AU. The second fraction describes how the incident irradiance, $I_{\mathrm{obj}_{\mathrm{in}}}$, is reflected towards the observer as a result of the bi-directional reflection distribution function (BRDF). The BRDF models diffuse and specular reflection properties of a material. The final fraction corrects for differences in the irradiance emitted from the object, $I_{\mathrm{obj}_{\mathrm{ex}}}$, compared to irradiance received by the sensor. A detailed explanation of reflectance and optical radiation measurements can be found in the works of Nicodemus [103, 104].

In this work, light curve measurements are implemented in the observability of the light curve inversion problem in Section 2.7. Observability is applied to light curve inversion for determining when the observer-object-Sun geometry and attitude of the object have been sufficiently sampled for performing light curve inversion. Evaluating the sampling of the light curve geometry will improve the efficiency of generating measurements for light curve inversion and thus, object characteristic determination.

2.3.5 Sensor Tasking

As discussed in Chapter 1, observing a rapidly growing population of RSOs is a challenge for existing sensor networks. Therefore, efficient collection of observations is important for maintaining a catalog of the orbit information for as many RSOs as possible. A sensor tasking problem for SSA has been formulated by Frueh, Fiedler, & Herzog [13]. Moreover, Little & Frueh have developed optimization strategies for solving the sensor tasking problem [105]. A detailed explanation of the problem formulation and application of various optimization strategies for solving the sensor tasking problem can be found in [106].

Within the sensor tasking problem formulation, a weight can be specified for indicating the importance of viewing a particular RSO. If observations of an object have not been obtained for many days, propagation errors resulting from the inability

to exactly model the true orbital dynamics may become large. Therefore, this weight parameter could be set to a large value to increase the importance of observing this object in the optimizer. Manual definition of this weight for each object is not feasible for the entire RSO population. In this work, observability is evaluated as a theory-based method for determining the weight parameter which indicates the importance of viewing an object. Section 3.8 explores how the singular values of the observability matrix can be used as a measure for the sensor tasking problem. Performing the sensor tasking optimization itself is beyond the scope of this work.

2.4 Observability Matrix for the Orbit Problem

Observability has been extensively researched for Global Position Systems (GPS) and Inertial Navigation Systems (INS) [28, 33, 37, 46, 48, 54–64], but few works have looked at observability for SSA applications outside of GPS and INS [36, 42, 53, 66, 72, 107]. In this section the observability matrix is derived for the orbit problem.

The equations of motion for a system are required to be first-order ODEs for representation in the state-space form. Moreover, the observability matrix as derived in Section 2.1.2 starts from a linearized, discrete-time state-space system. However, the equations of motion for the orbit problem in Equation 2.18 are nonlinear, second-order ODEs. Therefore, they must be manipulated to be used in the observability matrix. The equations of motion are converted to a state-space representation by first reducing the three second-order ODEs to six first-order ODEs. Next, the nonlinear, first-order ODEs are linearized to obtain the state-space representation of the orbit problem. The observability matrix for the linearized orbit problem is completed by computing the STM and linearized measurement matrix. Finally, this process is repeated for a state vector extended beyond position and velocity with SRP parameters.

2.4.1 State-Space Representation of the Orbit Problem

For propagation of an orbit with a two-body model, a state consists of variables which capture the position and velocity of an orbit. These state variables can be Cartesian position and velocity components or they can be some other representation of the orbit, such as orbital elements. An orbit can be represented in many different ways, but this work focuses on a state consisting of Cartesian position and velocity. The reduction of the three second-order ODEs to six first-order ODEs begins with the following state definition.

$$\mathbf{x} = \begin{bmatrix} \mathbf{r} \\ \mathbf{v} \end{bmatrix} = \begin{bmatrix} x_1 \\ x_2 \\ x_3 \\ x_4 \\ x_5 \\ x_6 \end{bmatrix}, \tag{2.41}$$

where $\mathbf{r}$ is the position vector and $\mathbf{v}$ is the velocity vector, each with three components. Because the time derivative of the position vector is the velocity vector, the following relations exist for the x_i components of the state vector

$$\dot{x}_1 = x_4, \quad \dot{x}_2 = x_5, \quad \dot{x}_3 = x_6. \tag{2.42}$$

With this state vector, the nonlinear state-space equation, Equation 2.1, becomes

$$\dot{\mathbf{x}} = \begin{bmatrix} \dot{\mathbf{r}} \\ \dot{\mathbf{v}} \end{bmatrix} = \begin{bmatrix} \mathbf{v} \\ \mathbf{a} \end{bmatrix}, \tag{2.43}$$

where **a** is the acceleration vector. Next, the relationships among the state variables from Equation 2.42 and the equations of motion from Equation 2.18 are substituted into Equation 2.43, resulting in

$$\dot{\mathbf{x}} = \begin{bmatrix} \dot{x}_1 \\ \dot{x}_2 \\ \dot{x}_3 \\ \dot{x}_4 \\ \dot{x}_5 \\ \dot{x}_6 \end{bmatrix} = \begin{bmatrix} x_4 \\ x_5 \\ x_6 \\ -\frac{\mu}{r^2} x_1 \\ -\frac{\mu}{r^2} x_2 \\ -\frac{\mu}{r^2} x_3 \end{bmatrix}. \tag{2.44}$$

Equation 2.44 is the first-order ODE representation of the nonlinear orbit problem equations of motion. For use with linear observability methods, the system must be linearized, as shown in the following section.

2.4.2 State Transition Matrix

The next step in obtaining the linearized, discrete-time state-space equations for the orbit problem is the derivation of the $\mathbf{A}(t_k)$ for the STM ODE in Equation 2.7. The $\mathbf{A}(t_k)$ is defined by the Jacobian of the nonlinear dynamics with respect to the state vector, otherwise stated as

$$\mathbf{A}(t_k) = \frac{\partial \mathbf{f}(t_k, \mathbf{x}(t_k))}{\partial \mathbf{x}(t_k)}. \tag{2.45}$$

When the partial derivatives are performed with the state variables in Equation 2.44, the linearized dynamics are defined by

$$\mathbf{A}(t_k) = \begin{bmatrix} \mathbf{0}_{3\times3} & \mathbf{I}_{3\times3} \\ \mathbf{G}_{\text{grav}}(t_k) & \mathbf{0}_{3\times3} \end{bmatrix}, \tag{2.46}$$

where $\mathbf{0}_{3\times3}$ is a zero matrix with three rows and three columns and $\mathbf{I}_{3\times3}$ is the identity matrix of dimension three. In addition, $\mathbf{G}_{\text{grav}}(t_k)$ is the Jacobian of the gravitational accelerations due to the Earth with respect to the position components,

$$\mathbf{G}_{\text{grav}}(t_k) = \frac{\mu}{|\mathbf{r}|^5} \left(3\ \mathbf{r}\ \mathbf{r}^T - |\mathbf{r}|^2\ \mathbf{I}_{3\times3} \right). \tag{2.47}$$

This form of the $\mathbf{A}(t_k)$ matrix is implemented in the STM ODE of Equation 2.7 to determine the STM which transforms the state from t_0 to t_k. Next, the output equation, Equation 2.6, is derived for the orbit problem by linearizing the nonlinear measurement model.

2.4.3 Measurement Matrix

The measurement matrix in the discrete-time observability matrix is defined with a similar linearization procedure as the state dynamics. The Jacobian of the nonlinear measurement model in Equation 2.2 with respect to the state vector is given by

$$\widetilde{\mathbf{H}}(t_k) = \frac{\partial \mathbf{h}(t, \mathbf{x}(t))}{\partial \mathbf{x}(t_k)}. \tag{2.48}$$

For the orbit problem, the measurement vector is composed of right ascension and declination angles, as defined in Equations 2.32 and 2.33. The partial derivatives of the measurement vector with respect to the state vector are defined by

$$\widetilde{\mathbf{H}}(t_k) = \begin{bmatrix} -\frac{\rho_y}{\rho_x^2+\rho_y^2} & \frac{\rho_x}{\rho_x^2+\rho_y^2} & 0 & 0 & 0 & 0 \\ \frac{\rho_x \ \rho_z}{(\rho_x^2+\rho_y^2+\rho_z^2)\sqrt{\rho_x^2+\rho_y^2}} & -\frac{\rho_y \ \rho_z}{(\rho_x^2+\rho_y^2+\rho_z^2)\sqrt{\rho_x^2+\rho_y^2}} & \frac{\sqrt{\rho_x^2+\rho_y^2}}{(\rho_x^2+\rho_y^2+\rho_z^2)} & 0 & 0 & 0 \end{bmatrix}. \tag{2.49}$$

This completes the derivation of the components of the discrete-time observability matrix in Equation 2.12 for a state consisting of Cartesian position and velocity modeled with two-body dynamics and measurements consisting of right ascension and declination angles.

2.4.4 State Extension Beyond Position and Velocity

The previous derivation defined components of the observability matrix for the orbit problem with a state consisting of position and velocity only. In this section, the state is extended with additional parameters to improve the understanding of how object characteristics are obtained from angles-only measurements. More specifically, two SRP perturbation parameters, area-to-mass ratio, AMR, and the reflectivity

coefficient, C, are added to the state vector for observability of the orbit problem. In addition, the SRP perturbation, $\mathbf{a}_{\text{SRP}}$, is included in the orbit problem equations of motion. The extended state and equations of motion are now defined as

$$\mathbf{x} = \begin{bmatrix} \mathbf{r} \\ \mathbf{v} \\ \text{AMR} \\ C \end{bmatrix}, \qquad \ddot{\mathbf{r}} = -\frac{\mu}{|\mathbf{r}|^3}\,\mathbf{r} + \mathbf{a}_{\text{SRP}}. \tag{2.50}$$

In Equation 2.50, the SRP perturbing acceleration can be modeled with the cannonball model in Equation 2.27 or the flat plate model in Equation 2.29. The latter model can be applied to a faceted 3D geometry to include the SRP perturbing acceleration for a more complex shape.

Following a similar procedure to Sections 2.4.2 and 2.4.3, the STM and linearized measurement matrix are derived for the new state vector, which is extended with AMR and C. The first-order state vector ODEs are now defined as

$$\dot{\mathbf{x}} = \begin{bmatrix} \dot{x}_1 \\ \dot{x}_2 \\ \dot{x}_3 \\ \dot{x}_4 \\ \dot{x}_5 \\ \dot{x}_6 \\ \dot{x}_7 \\ \dot{x}_8 \end{bmatrix} = \begin{bmatrix} x_4 \\ x_5 \\ x_6 \\ -\frac{\mu}{r^2}x_1 + \mathbf{a}_{\text{SRP}_{x_1}} \\ -\frac{\mu}{r^2}x_2 + \mathbf{a}_{\text{SRP}_{x_2}} \\ -\frac{\mu}{r^2}x_3 + \mathbf{a}_{\text{SRP}_{x_3}} \\ \dot{x}_7 \\ \dot{x}_8 \end{bmatrix}. \tag{2.51}$$

where $\mathbf{a}_{\text{SRP}_{x_1}}$, $\mathbf{a}_{\text{SRP}_{x_2}}$, and $\mathbf{a}_{\text{SRP}_{x_3}}$ are the x_1, x_2, and x_3 position components of the SRP perturbing acceleration.

The AMR of a debris object could vary with time if the object is not rigid. For example, orbital debris composed of multilayer insulation (MLI) will change shape over time because the object is not rigid. In addition, materials properties have been shown to change with time due to the harsh space environment, and the materials

which are illuminated on an object with a complex geometry could change over time, resulting in a change in the reflectivity properties [108,109]. In this work, time-varying AMR and C models are defined by

$$\text{AMR} = \text{AMR}_o + \alpha_{\text{AMR}} \cos(\omega_{\text{AMR}}\ t), \tag{2.52}$$

$$C = C_o + \alpha_C \cos(\omega_C\ t), \tag{2.53}$$

where α defines the amplitude of the oscillations and ω defines the frequency of the oscillations. The specific values of α and ω used in this work are defined in Section 3.6.3 when the time-varying AMR and C models are implemented.

The derivation of the STM and linearized measurement matrix is continued with AMR and C models which are time-varying, for generality. The Jacobian of the nonlinear equations of motion in Equation 2.50 with respect to the extended state vector becomes

$$\mathbf{A}(t_k) = \begin{bmatrix} \mathbf{0}_{3\times3} & \mathbf{I}_{3\times3} & \mathbf{0}_{3\times1} & \mathbf{0}_{3\times1} \\ \mathbf{G}_{\text{tot}}(t_k) & \mathbf{0}_{3\times3} & \frac{\partial \mathbf{a}_{\text{SRP}}}{\partial x_7} & \frac{\partial \mathbf{a}_{\text{SRP}}}{\partial x_8} \\ \mathbf{0}_{2\times3} & \mathbf{0}_{2\times3} & \mathbf{0}_{2\times1} & \mathbf{0}_{2\times1} \end{bmatrix}, \tag{2.54}$$

where $\mathbf{G}_{\text{tot}}(t_k) = \mathbf{G}_{\text{grav}}(t_k) + \mathbf{G}_{\text{SRP}}(t_k)$, and

$$\mathbf{G}_{\text{SRP}}(t_k) = -\frac{A}{m}\ C\ (\text{AU})^2 \frac{E}{c} \frac{1}{|\mathbf{s}|^5} \left(3\ \mathbf{s}\ \mathbf{s}^T - |\mathbf{s}|^2\ \mathbf{I}_{3\times3}\right). \tag{2.55}$$

The partial derivatives of the SRP perturbing acceleration with respect to the AMR and C equal

$$\frac{\partial \mathbf{a}_{\text{SRP}}}{\partial x_7} = \frac{\partial \mathbf{a}_{\text{SRP}}}{\partial \text{AMR}} = \frac{\mathbf{a}_{\text{SRP}}}{\text{AMR}}, \quad \frac{\partial \mathbf{a}_{\text{SRP}}}{\partial x_8} = \frac{\partial \mathbf{a}_{\text{SRP}}}{\partial C} = \frac{\mathbf{a}_{\text{SRP}}}{C}. \tag{2.56}$$

If the state is extended beyond position and velocity with only one SRP variable, the row and column corresponding to the SRP variable which is not included in the state is removed from Equation 2.54. In addition, Section 3.6 explores the impact of the combined variable AMR$\cdot C$ on observability of the orbit problem. For a state vector extended by this combined SRP variable, the partial derivative of the SRP perturbing acceleration with respect to this state variable is defined as

$$\frac{\partial \mathbf{a}_{\text{SRP}}}{\partial x_7} = \frac{\partial \mathbf{a}_{\text{SRP}}}{\partial (\text{AMR} \cdot C)} = \frac{\mathbf{a}_{\text{SRP}}}{(\text{AMR} \cdot C)}, \tag{2.57}$$

for Equation 2.54.

The extension of the linearized measurement matrix is simply completed by adding extra columns of zeros equal to the number of SRP variables by which the state is extended. For example, if only AMR is included as an extra state variable, the linearized measurement matrix has an extra column of zeros. The right ascension and declination measurements do not explicitly depend on the SRP parameters, so the partial derivatives of the measurements with respect to the SRP state variables are equal to zero. The impact of extended state SRP variables on the observability of the orbit problem is analyzed in Chapter 3.

2.5 Estimation Methods

This work implements three estimation methods: nonlinear batch least squares, the Extended Kalman Filter (EKF), and the Schmidt-Kalman Filter (SKF). The details of these estimation methods are presented in the following.

2.5.1 Nonlinear Batch Least Squares

The nonlinear batch least squares estimator follows the iterative process in Tapley, Schutz & Born [49]. The linear, unbiased, minimum variance estimate (LUMVE) is employed in the iterative batch process with and without *a priori* information. First, the LUMVE without *a priori* is presented, where the estimate of $\mathbf{x}$ is computed with the information matrix, $\mathbf{\Lambda}$, and the normal matrix, $\mathbf{N}$,

$$\mathbf{\Lambda}\ \hat{\mathbf{x}}_k = \mathbf{N}, \tag{2.58}$$

$$\mathbf{\Lambda} = \bar{\mathbf{H}}^T\ \mathbf{R}^{-1}\bar{\mathbf{H}} \tag{2.59}$$

$$\mathbf{N} = \bar{\mathbf{H}}^T\ \mathbf{R}^{-1}\ \bar{\mathbf{z}}. \tag{2.60}$$

Note that $\mathbf{x}$ in the LUMVE formulation is a deviation from the reference or nominal state. In Equation 2.58, the state estimate $\hat{\mathbf{x}}_k$ can be determined at any time and $\mathbf{R}$

is the covariance of the measurement noise. Recall from Equation 2.9, $\bar{\mathbf{z}}$ is a vector of the measurements at multiple times. Typically, the initial state is estimated in the LUMVE, but the state which is estimated depends on the mapping of the linearized measurement matrix, $\widetilde{\mathbf{H}}$, by the STM, $\mathbf{\Phi}$. This mapping occurs in $\bar{\mathbf{H}}$, which is equal to

$$\bar{\mathbf{H}} = \begin{bmatrix} \widetilde{\mathbf{H}}(t_1)\ \mathbf{\Phi}(t_k, t_1) \\ \widetilde{\mathbf{H}}(t_2)\ \mathbf{\Phi}(t_k, t_2) \\ \vdots \\ \widetilde{\mathbf{H}}(t_i)\ \mathbf{\Phi}(t_k, t_i) \end{bmatrix}, \tag{2.61}$$

where $\widetilde{\mathbf{H}}(t_i)$ is the linearized measurement matrix at some time t_i, and t_k is the time for the state to be estimated. Next, *a priori* information is included in the LUMVE by augmenting the $\mathbf{R}$, $\bar{\mathbf{H}}$, and $\bar{\mathbf{z}}$ matrices as

$$\mathbf{R} = \begin{bmatrix} \mathbf{R} & \mathbf{0} \\ \mathbf{0} & \mathbf{P}_k \end{bmatrix}, \quad \bar{\mathbf{z}} = \begin{bmatrix} \bar{\mathbf{z}} \\ \mathbf{x}_k \end{bmatrix}, \quad \bar{\mathbf{H}} = \begin{bmatrix} \bar{\mathbf{H}} \\ \mathbf{I} \end{bmatrix} \tag{2.62}$$

In Equation 2.62, $\mathbf{R}$ is augmented with the covariance of the *a priori* state estimate, $\mathbf{P}_k$, and $\bar{\mathbf{z}}$ is augmented with the *a priori* state estimate $\mathbf{x}_k$. The matrix $\bar{\mathbf{H}}$ is augmented with the identity matrix to maintain dimensional consistency in the LUMVE formulation. Typically, the *a priori* state estimate and the covariance of the *a priori* estimate are defined by an initial orbit determination process, thus $k = 0$. However, *a priori* estimates from different times can be used. When these augmented matrices are used in the LUMVE formulation, the estimate of the state is given by

$$\mathbf{\Lambda}\ \hat{\mathbf{x}}_k = \mathbf{N} \tag{2.63}$$

$$\mathbf{\Lambda} = \mathbf{P}_k^{-1} + \bar{\mathbf{H}}^T\ \mathbf{R}^{-1}\bar{\mathbf{H}} \tag{2.64}$$

$$\mathbf{N} = \mathbf{P}_k^{-1}\ \mathbf{x}_k + \bar{\mathbf{H}}^T\ \mathbf{R}^{-1}\ \bar{\mathbf{z}}. \tag{2.65}$$

The information matrix, $\mathbf{\Lambda}$, and the normal matrix, $\mathbf{N}$ now contain the *a priori* state information. This concludes the formulation of LUMVE, and this formulation is used in an iterative procedure for the nonlinear batch least squares. Chapter 3 discusses

similarities between the LUMVE and the stochastic observability matrix. In addition, stochastic observability results are compared to state estimation with the nonlinear batch least squares.

2.5.2 Extended Kalman Filter

Next, the required equations for the EKF are defined. The EKF is an extension to the Kalman Filter for application to nonlinear systems by linearization of the nonlinear state and measurement models [14, 49, 110]. The dynamical model and the measurement model implemented in the EKF are given by

$$\dot{\mathbf{x}}(t) = \mathbf{f}(\mathbf{x}(t)) + \mathbf{M}(t)\ \mathbf{w}(t), \tag{2.66}$$

$$\mathbf{z}_k = \mathbf{h}(\mathbf{x}_k) + \mathbf{L}_k\ \boldsymbol{\nu}_k, \tag{2.67}$$

where $\mathbf{f}(\mathbf{x}(t))$ is a nonlinear model of the state dynamics and $\mathbf{w}(t)$ is a white noise process for the state dynamics defined by

$$\mathrm{E}\{\mathbf{w}(t)\} = \mathbf{0}, \quad \mathrm{E}\{\mathbf{w}(t)\ \mathbf{w}(\tau)^T\} = \mathbf{Q}_s(t)\delta(t-\tau). \tag{2.68}$$

The white noise, $\mathbf{w}(t)$, is zero-mean, $\mathbf{Q}_s(t)$ is the process noise power spectral density, and δ is the Dirac delta function. In Equation 2.68, $\mathrm{E}\{\cdot\}$ is the expectation operator, $\mathbf{z}_k$ defines the measurements at time t_k, and $\mathbf{h}(\mathbf{x}_k)$ is the nonlinear measurement model given the state at time t_k. Also, $\boldsymbol{\nu}_k$ defines the measurement noise which is assumed to be a zero-mean white noise process with covariance $\mathbf{R}_k$, i.e.

$$\mathrm{E}\{\boldsymbol{\nu}_k\} = \mathbf{0}, \quad \mathrm{E}\{\boldsymbol{\nu}_k\ \boldsymbol{\nu}_l^T\} = \mathbf{R}_k\delta_{kl}. \tag{2.69}$$

Finally, the $\mathbf{M}(t)$ and the $\mathbf{L}_k$ matrices map the noise to the state and measurement dynamics.

Next, the mean, $\mathbf{m}$, and covariance, $\mathbf{P}$, for initializing the EKF are defined by

$$\mathbf{m}_0 = \mathrm{E}\{\mathbf{x}_0\}, \tag{2.70}$$

$$\mathbf{P}_0 = \mathrm{E}\{(\mathbf{x}_0 - \mathbf{m}_0)(\mathbf{x}_0 - \mathbf{m}_0)^T\}. \tag{2.71}$$

The EKF requires an initial state and covariance for performing the estimation. The mean and covariance are propagated with the numerical integration of the following ODEs.

$$\dot{\mathbf{m}}(t) = \mathbf{f}(\mathbf{m}(t)), \tag{2.72}$$

$$\dot{\mathbf{P}}(t) = \mathbf{F}(t)\ \mathbf{P}(t) + \mathbf{P}(t)\ \mathbf{F}(t)^T + \mathbf{M}(t)\ \mathbf{Q}_s(t)\ \mathbf{M}(t)^T, \tag{2.73}$$

where $\mathbf{F}(t)$ is the Jacobian of the nonlinear dynamics evaluated at $\mathbf{m}(t)$. As measurements are acquired in a system, the Kalman gain, $\mathbf{K}_k$, is computed with

$$\hat{\mathbf{z}}_k = \mathbf{h}(\mathbf{m}_k^-), \tag{2.74}$$

$$\mathbf{W}_k = \mathbf{H}(\mathbf{m}_k^-)\ \mathbf{P}_k^-\ \mathbf{H}(\mathbf{m}_k^-)^T + \mathbf{L}_k\ \mathbf{R}_k\ \mathbf{L}_k^T, \tag{2.75}$$

$$\mathbf{C}_k = \mathbf{P}_k^-\ \mathbf{H}(\mathbf{m}_k^-)^T, \tag{2.76}$$

$$\mathbf{K}_k = \mathbf{C}_k\ \mathbf{W}_k^{-1}, \tag{2.77}$$

where $\hat{\mathbf{z}}_k$ is the expected measurement evaluated with mean state at time t_k prior to the measurement update in the nonlinear measurement model, $\mathbf{W}_k$ is the residual or innovation covariance, and $\mathbf{C}_k$ is the cross-covaraince.

Finally, the measurement update of the mean and covariance estimates for the EKF is given by

$$\mathbf{m}_k^+ = \mathbf{m}_k^- + \mathbf{K}_k\ (\mathbf{z}_k - \hat{\mathbf{z}}_k), \tag{2.78}$$

$$\mathbf{P}_k^+ = \mathbf{P}_k^- - \mathbf{C}_k\ \mathbf{K}_k^T - \mathbf{K}_k\ \mathbf{C}_k^T + \mathbf{K}_k\ \mathbf{W}_k\ \mathbf{K}_k^T. \tag{2.79}$$

In Equations 2.74 through 2.79, the superscript $-$ represents the mean and covariance prior to the measurement update. Similarly, the $+$ represents the mean and covariance after the measurement update. The *a priori* mean state is updated with the Kalman gain and the error in the expected measurement, $\mathbf{z}_k - \hat{\mathbf{z}}_k$. This measurement error is often referred to as the innovation or the residual. The *a posteriori* covariance is computed by updating the *a priori* covariance with the Kalman gain, cross covariance, and innovation covariance matrices. A detailed derivation of the EKF can be found in [14, 49, 110]. The EKF is implemented in Chapters 3 and 4 for investigation of observability and estimability of the orbit problem.

2.5.3 Schmidt-Kalman Filter

The Schmidt-Kalman Filter, or Consider Filter (CF), is a modification of the KF which seeks to improve estimation performance by designating some state variables as consider parameters [111, 112]. The consider parameters are components of the state vector, but these parameters are not estimated initially. When the observability of the system has improved, consider parameters are changed to be additional solve-for parameters within the state vector. Schmidt developed the CF for real-time systems with unobservable biases, and the CF is well suited for systems with low observability.

The state vector for a CF can be defined by

$$\mathbf{x} = \begin{bmatrix} \mathbf{s} \\ \mathbf{p} \end{bmatrix}, \tag{2.80}$$

where $\mathbf{s}$ is the vector of estimated states and $\mathbf{p}$ is the vector of consider parameters. The dimension of the estimated states and consider parameters is n_s and n_p, respectively. Zanetti & D'Souza demonstrate how the gain calculation step of the CF is simply given by setting the rows of the KF gain which correspond to the consider parameters to zero, i.e.,

$$\mathbf{K}_{\text{CF}} = \begin{bmatrix} \mathbf{K}_s \\ \mathbf{0} \end{bmatrix}, \tag{2.81}$$

where $\mathbf{K}_s$ is the Kalman gain for the estimated states $\mathbf{s}$ given by Equation 2.77 [113]. For the consider parameters, when the switch is made from considering these parameters to estimating them, the corresponding rows of the Kalman gain are no longer zero and the consider parameters will be estimated.

The consider approach to the KF must implement a method for determining when parameters should be considered and when parameters should be estimated. In this work, observability is implemented as a measure for indicating when consider parameters should be estimated. Dianetti also implements observability as a measure for indicating when consider parameters should enter the state estimation [53]. Observability is implemented with the CF because states which are challenging to observe

can be detrimental to the overall estimation. Therefore, the CF may define parameters which are challenging to observe as consider parameters initially to improve the observability of the system. Then, after some time, more difficult to observe states can be estimated, reducing the detrimental impact these variables would have if estimated initially.

The implementation of an observability measure for the CF differs from the work by Dianetti in one significant way. To define when a consider parameter should be estimated, Dianetti selected a specific numeric value for the singular value corresponding to the consider parameter. When the singular value was larger than the selected numeric value, the consider parameter was changed from considered to estimated [53]. However, as discussed in Section 2.1.3, determining which singular values of the observability matrix correspond to the state variables is often not possible. Rather than using a fixed numeric value for defining when consider parameters should be estimated, this work implements the rank of the observability matrix as a measure for the CF. As the rank of the observability matrix increases beyond n_s, consider parameters become estimated in the state. One challenge with this approach is that when multiple consider parameters exist, the observability rank measure does not indicate which parameter to change from considered to estimated. Estimability is implemented in an attempt to inform the CF of which consider parameters should be estimated first.

2.6 Estimability

As introduced in Chapter 1, estimability compares the *a posteriori* and *a priori* state estimation error covariances. The term estimability was first introduced by Baram & Kailath in 1988, who defined a system to be estimable when the *a posteriori* state estimation error covariance is strictly less than the *a priori* state estimation error covariance [44]. Therefore, if the difference between the *a posteriori* state estimation error covariance and the *a priori* state estimation error covariance

is positive definite, than a system is considered estimable [114]. From Baram & Kailath's early work, many methods have been developed for evaluating estimability of a system [23–25,28,43,46,48,57]. Some of the preceding works label this method for estimation performance as stochastic observability. In this work, the term estimability applies to methods which evaluate estimation performance with the *a priori* and *a posteriori* state estimation error covariances. Chapter 4 discusses the distinction and terminology of observability and estimability in more detail.

The estimability method implemented in Chapter 4 of this work for evaluation of relative state estimation performance originates from Ham [25]. Ham's work is a stochastic extension of the work from Brown [23] and Ablin [24]. The methods from Brown and Ablin seek to determine a vector which is "most orthogonal" to what the authors call the observability function [23,24]. Ham refers to the stochastic extension of these methods as stochastic observability. As previously noted, this terminology is considered a misnomer within the scope of this analysis of observability for SSA. Therefore, the term estimability is used throughout the remainder of this work when implementing the methods from Ham.

The estimability methods from Ham analyze the eigenvectors of a normalized state estimation error covariance matrix to indicate "directions" of relative strong or weak estimability. The normalization of the *a posteriori* state estimation error covariance is conducted in two steps. First,

$$\mathbf{P}(t_k)^{N^+} = \frac{n}{tr(\mathbf{P}(t_k)'^+)} \begin{bmatrix} p'^+_{11} & p'^+_{12} & \cdots & p'^+_{1n} \\ p'^+_{21} & p'^+_{22} & \cdots & p'^+_{2n} \\ \vdots & \vdots & \vdots & \vdots \\ p'^+_{n1} & p'^+_{n2} & \cdots & p'^+_{nn} \end{bmatrix}, \tag{2.82}$$

where $\mathbf{P}(t_k)^{N^+}$ is the final normalized state estimation error covariance matrix and n is the number of state variables. In Equation 2.82, tr represents the trace of the $\mathbf{P}(t_k)'^+$ matrix. The scalar multiplier in Equation 2.82 bounds the eigenvalues of the

$\mathbf{P}(t_k)^{N^+}$ matrix between 0 and n. The second normalization step occurs within the definition of $\mathbf{P}(t_k)'^{+}$.

$$\mathbf{P}(t_k)'^{+} = \left(\sqrt{\mathbf{P}(t_0)^-}\right)^{-1} \mathbf{P}(t_k)^{+} \left(\sqrt{\mathbf{P}(t_0)^-}\right)^{-1}$$
$$= \begin{bmatrix} \frac{p_{11}}{p_{11}(t_0)^-} & \frac{p_{12}^+}{\sqrt{p_{11}(t_0)^- p_{22}(t_0)^-}} & \cdots & \frac{p_{1n}^+}{\sqrt{p_{11}(t_0)^- p_{nn}(t_0)^-}} \\ \frac{p_{21}^+}{\sqrt{p_{22}(t_0)^- p_{11}(t_0)^-}} & \frac{p_{22}^+}{p_{22}(t_0)^-} & \cdots & \frac{p_{2n}^+}{\sqrt{p_{22}(t_0)^- p_{nn}(t_0)^-}} \\ \vdots & \vdots & \vdots & \vdots \\ \frac{p_{n1}^+}{\sqrt{p_{nn}(t_0)^- p_{11}(t_0)^-}} & \frac{p_{n2}^+}{\sqrt{p_{nn}(t_0)^- p_{22}(t_0)^-}} & \cdots & \frac{p_{nn}^+}{p_{nn}(t_0)^-} \end{bmatrix}. \quad (2.83)$$

In Equation 2.83, $\mathbf{P}(t_0)^-$ is the *a priori* state estimation error covariance matrix at epoch. Moreover, $\mathbf{P}(t_0)^-$ is assumed to be uncorrelated resulting in a diagonal matrix.

The estimability method from Ham determines the directions of weak and strong relative estimability from the eigenspace of the normalized covariance matrix in Equation 2.82. Eigenvectors associated with eigenvalues close to n indicate states or linear combinations of states with weak relative estimability, and eigenvectors associated with eigenvalues close to zero indicate states or linear combinations of states with strong relative estimability. Chapter 4 evaluates the applicability of the estimability methods from Ham to the orbit problem, and estimability results are implemented for informing the CF.

2.7 Light Curve Inversion

The next application of observability in this work investigates the observability of the light curve inversion process for determining when a system is sufficiently sampled with light curve measurements. Due to the large distances between ground-based observers and RSOs, optical observations of objects are typically non-resolved, i.e. object attitude, material characteristics, and object shape are not explicitly available in the images. An example of a non-resolved image is given in Figure 2.2 from the Purdue Optical Ground Station (POGS).

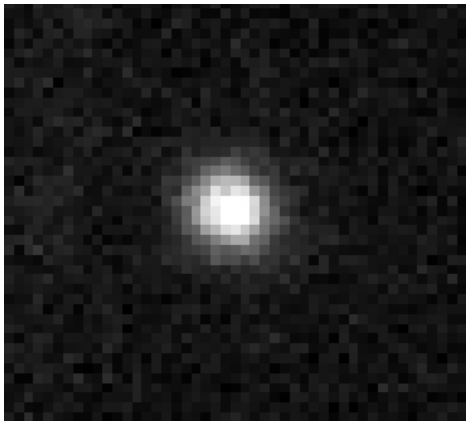

Figure 2.2. Titan 3C transtage rocket body, NORAD ID 9855, International Designator 1977-007C. Image from POGS on February 16, 2020.

Even though shape information is not apparent in the non-resolved images, the apparent brightness of the object changes over time as the system geometry progresses. Variation in the system geometry is attributed to the observer-object-Sun positions, the object attitude, the object BRDF, the object size, the object material properties, the object reflectivity characteristics, atmospheric attenuation, and the CCD sensor noise. Light curves of astronomical objects have a long history of being used for determining target shape and attitude information which is challenging to determine from non-resolved images [115–123]. Furthermore, light curve measurements for SSA applications have been used for determining RSO characteristic information, such as attitude, shape, and reflectivity properties [72, 124–137]. Characteristic properties of RSOs are important for improving perturbation modeling accuracy for more accurate object propagation and identification.

Because the observations are non-resolved, light curve inversion methods are required for extracting desired shape and reflectivity information from the light curve measurements. A prominent method for light curve inversion comes from Kaasalainen et al. and was originally developed for determining asteroid shape and spin models [138]. The light curve inversion techniques from Kaasalainen et al. have been explored for SSA applications [79, 139–142]. Fan & Frueh apply the light curve in-

version process from Kaasalainen et al., depicted in Figure 2.3, for RSO shape and reflectivity information determination [142].

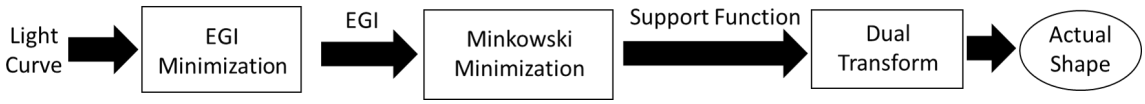

Figure 2.3. Light curve inversion process [142].

The light curve inversion process consists of several steps. First, an Extended Gaussian Image (EGI) is constructed from the light curve measurements. Next, adjacency information is determined with methods initially developed by Minkowski [143, 144]. Finally, Little completed the light curve inversion process by utilizing the adjacency information with the dual transform to construct the original object shape [139–141].

The original concept of the EGI, developed by Gauss, was referred to as a spherical image [145]. Smith applied the spherical image mapping for representation of objects and referred to them as enhanced spherical images [146]. Next, Horn performed in-depth analysis of the EGI for machine vision, which demonstrated that an arbitrary shape can be projected onto a unit sphere [147, 148]. The discrete representation of an EGI for an object defined by a polygon mesh, i.e. a non-smooth polygon with a finite number of flat facets, is described by

$$\text{EGI} = \left\{ A_s = \sum A_i | \mathbf{n}_i = \mathbf{n}_s : 1 \leq s \leq m, 1 \leq i \leq n \right\}, \ \{\mathbf{n}_s : 1 \leq s \leq m\}, \quad (2.84)$$

where n is the number of flat facets on the polygon mesh. Each flat facet has a normal vector $\mathbf{n}_i$ with associated area A_i. The number of EGI normal vectors, $\mathbf{n}_s$, is specified during the construction of the EGI with the integer m. A more detailed explanation of the EGI construction process is described in the early work of Horn [148] for machine vision and the work of Fan & Frueh [142] for the light curve inversion process of Figure 2.3.

Quad-cubed projection is one possible method for defining a sphere in a discrete manner [149]. It is advantageous for discrete representation of a sphere because areas

associated with each normal direction are similar in size. The quad-cubed projection is implemented in this work to define a discrete EGI representation of the unit sphere, and the number of facets on the EGI is given by m from Equation 2.84. For the quad-cubed projection, an integer tessellation number, or the number of facets per row and column on each side of the quad-cubed sphere, is specified to define the total number of facets, m. Examples of EGI representations of objects are given in Figure 2.4.

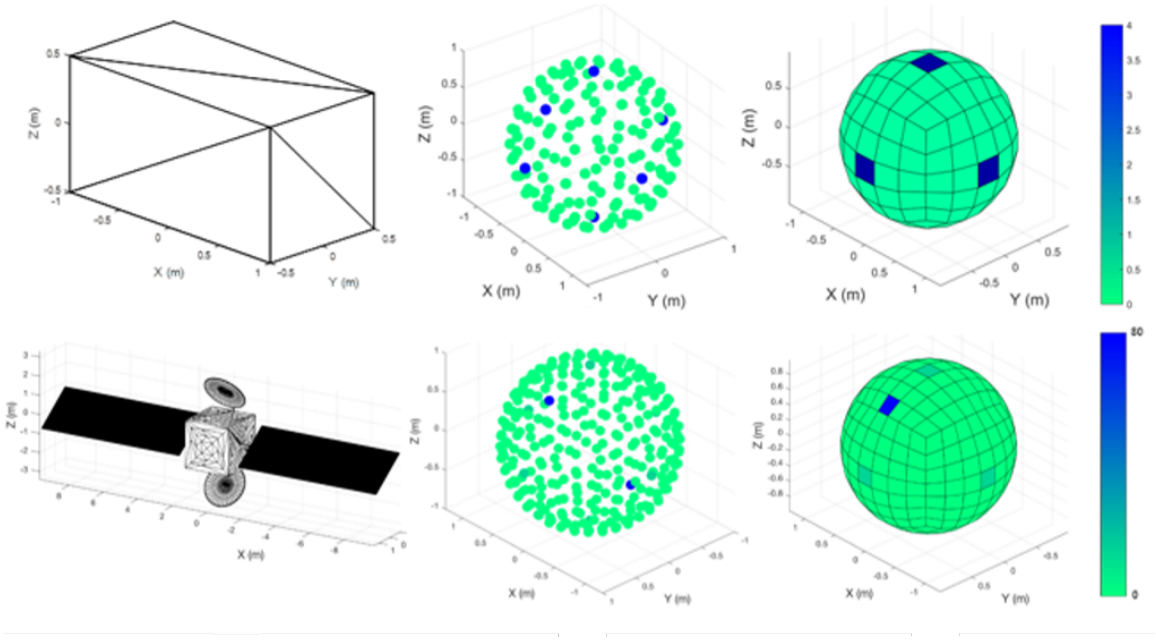

Figure 2.4. Examples of shape representation with an EGI, adapted from Fan & Frueh [142]. The cuboid EGI representation has 150 facets and the ASTRA box-wing satellite EGI representation has 294 facets, corresponding to tessellation numbers of 5 and 7, respectively.

The first column of Figure 2.4 contains the original object shapes. The second and third columns are different representations of the EGI, a dot representation and a facet representation, respectively. Figure 2.4 is adapted from Fan & Frueh [142], which explains the process for defining the EGI dot and facet representations in more detail. The facet representation is used throughout this work. The color of each facet on the EGI represents the associated albedo-area for each surface normal vector. For

example, the cuboid shape in the first row of Figure 2.4 has an EGI representation with all facets given in green except for six of the facets given in blue. The six blue facets define the albedo-areas associated with the six surface normal vectors of the original cuboid shape. As the cuboid is completely represented by the six surface normal vectors, all other EGI surface normal vectors have albedo-areas equal to zero. The ASTRA box-wing satellite EGI depiction in the second row of Figure 2.4 contains many shades of blue and green as there more surface normal vectors with associated albedo-areas which define the original object. Note that the EGI representations of the cuboid and ASTRA box-wing satellite model are generated using the surface normal vectors and associated albedo-areas of the original objects. In addition, for a convex surface, the EGI is unique, but for a non-convex surface the EGI is not unique.

In the light curve inversion process of Figure 2.3, the original object is unknown because the ground-based observations only lead to non-resolved images. Therefore, the EGI minimization step of the light curve inversion process is required to estimate the albedo-area vector associated with the surface normal directions of the EGI faceted sphere. The optimization problem for determining the albedo-area vector can be posed with a linear least squares cost function as follows

$$\begin{aligned} &min \quad J = ||\mathbf{L} - \mathbf{G}\ \mathbf{a}||^2\,, \\ &subject\ to \quad \mathrm{a}_s \geq 0\ \forall \mathrm{a}_s \text{ in } \mathbf{a} = [\mathrm{a}_1, \ldots, \mathrm{a}_m]^T, \end{aligned} \tag{2.85}$$

where $\mathbf{L}$ is a vector of light curve measurements, $\mathbf{G}$ is the reflection matrix, and $\mathbf{a}$ is the albedo-area vector, which contains the albedo-area for each of the facets of the discrete EGI. Note that the albedo-area vector is constrained to be greater than zero as negative albedo-areas are not physically realizable. The reflection matrix is defined for a specific reflection model in Section 5.1. In addition, a detailed analysis of the EGI minimization is conducted in Section 5.1.

After determining the EGI representation of an object from the light curve measurements, the Minkowski problem is solved to determine adjacency information. This

Minkowski minimization step has been extensively studied by Little [139–141]. The cost function for the Minkowski minimization can be posed as

$$min \quad J = \frac{1}{3}\,\widetilde{\mathbf{h}} \cdot \mathbf{a}, \tag{2.86}$$

$$subject\ to \quad \widetilde{\mathbf{h}} \cdot \mathbf{a} = \text{constant}, \tag{2.87}$$

where $\widetilde{\mathbf{h}}$ is the vector of the support, h_s, and the support is the distance of each facet to the center of the object. The tilde over $\mathbf{h}$ indicates that the support vector is defined in the dual space. In addition, the volume of the final inverted shape is constrained with the hyperplane condition in Equation 2.87. Adjacency information is determined by solving the Minkowski minimization for the support. Then, the actual object shape is computed with the dual transform. More detailed descriptions of the Minkowski minimization and dual transform can be found in the work of Fan & Frueh [142].

The EGI minimization step within the light curve inversion process is the only step where the light curve measurements are directly utilized, as shown in Equation 2.85. The Minkowski minimization step estimates the support vector, and as the measurements for this system are non-resolved, the distance between the object and observer are significantly larger than the support distances. Therefore, the observability of the Minkowski minimization cannot be determined due to the significant differences in scale between the support and observer-object distance. Because light curve measurements are directly used within the EGI minimization step of the light curve inversion process, observability of the EGI minimization is the focus of this work. Chapter 5 evaluates when light curve measurements are sufficient for light curve inversion, through observability of the EGI minimization.

3. OBSERVABILITY OF THE ORBIT PROBLEM

As introduced in Section 2.1, observability is a mathematically rigorous method for exploring the relationship between measurements and states of a control system. This chapter applies observability to the orbit problem for investigating the relationship between optical, angles-only measurements and orbital states. The orbital states of interest contain object information beyond position and velocity to determine the applicability of observability for object characterization. Moreover, analysis of dynamical systems is often conducted without noise initially to understand the fundamental mechanics before addition of noise, but noise can change the relationship between the measurements and states of a system. Therefore, the impact of noise on stochastic observability results is explored for the orbit problem with extended states.

In addition, the connection of observability and estimation is inherent to the definition of observability from Kalman. The requirement of observability for guarantee of an accurate estimate is validated with the extended state orbit problem. This chapter shows that when the observability of a system cannot be determined, an accurate estimate cannot be guaranteed. Furthermore, two observability use cases are presented: observability for sensor tasking optimization and observability for multiple sensor and observation evaluation.

3.1 Stochastic Observability

Stochastic observability can indicate two different types of analysis in the observability and estimation fields. First, stochastic observability, as applied in this work, is the extension of deterministic observability to include measurement and state uncertainties. Multiple methods exist for deriving stochastic observability forms [36, 39, 40, 52, 53]. The specific method applied throughout this work is shown in Sec-

tion 3.1.1. The second form of stochastic observability focuses on analysis of the covariance matrix of state estimation errors. Although the main existence theorem from Kalman defines a relationship between observability and estimation, this work limits stochastic observability to analysis of the state and measurement model matrices with uncertainties as defined in Section 2.4. As noted by Silva, the second form of stochastic observability should be deemed estimability [48]. Chapter 4 analyzes estimability of the orbit problem, and discusses the distinction between stochastic observability and estimability in more depth. For the remainder of this work, stochastic observability refers to the extension of deterministic observability methods to include measurement and state uncertainties.

Sections 3.1.1 and 3.1.2 derive the stochastic observability matrix with measurement and state uncertainties through pre-whitening and Cholesky decomposition. After derivation of the stochastic observability matrix form, the impact of measurement uncertainties on observability of the orbit problem is explored in Section 3.4. Moreover, a comparison of deterministic and stochastic observability for object characterization is conducted in Section 3.6.3.

3.1.1 Measurement Noise Incorporation

The derivation of the stochastic observability matrix begins with incorporation of measurement uncertainties. Frueh introduced the method of pre-whitening for folding measurement noise into the measurement matrix for observability analysis [150], and this method is also used in the work by Geeraert [36]. For both the continuous and discrete systems, the measurement noise in the state-space output equations, Equations 2.4 and 2.6, is assumed to be zero-mean with covariance given by

$$\mathbb{E}[\boldsymbol{\nu}(t)] = 0, \tag{3.1}$$

$$\mathbb{E}[\boldsymbol{\nu}(t)\ \boldsymbol{\nu}(\tau)^T] = \mathbf{R}(t)\ \delta(t-\tau), \tag{3.2}$$

for the continuous-time system, and

$$\mathbb{E}[\boldsymbol{\nu}(t_k)] = 0, \tag{3.3}$$

$$\mathbb{E}[\boldsymbol{\nu}(t_k)\ \boldsymbol{\nu}(t_k)^T] = \mathbf{R}(t_k), \tag{3.4}$$

for the discrete-time system. The $\mathbf{R}(t_k)$ is a covariance matrix for the discrete-time system, but in a continuous-time system, $\mathbf{R}(t)$ is a power spectral density because of the Dirac delta, resulting in different units for $\mathbf{R}(t)$ and $\mathbf{R}(t_k)$. As shown by Gelb, the continuous-time measurement noise is a non-physically realizable process [151]. Although these differences exist between the covariance of the measurement noise for the continuous-time and discrete-time systems, $\mathbf{R}(t_k)$ approaches $\mathbf{R}(t)/\Delta t$ as the discrete-time steps approach zero, $\Delta t \rightarrow 0$. The analysis performed in this work focuses on the discrete-time implementation of observability. Analogous continuous-time observability forms are shown, but derivations are completed using the discrete state space representation. When the continuous-time covariance of the measurement noise is presented, the form will be shortened to $\mathbf{R}(t)$ to simplify notation, instead of the true form given by $\mathbf{R}(t)\ \delta(t-\tau)$.

Pre-whitening, otherwise referred to as decorrelation, is the process of whitening a covariance matrix to identity and simultaneously incorporating the covariance of the measurement noise into the measurement model. The whitening process begins by first decomposing the inverse of a general covariance matrix, or

$$\mathbf{R}^{-1} = \mathbf{L}\ \mathbf{L}^T, \tag{3.5}$$

where $\mathbf{L}$ a lower-triangular matrix. Several methods exist for creating such a decomposition, e.g. eigendecomposition or Cholesky decomposition [152]. The latter method, Cholesky decomposition or Cholesky whitening is implemented in this work. A proof of the whitening of the covariance, $\mathbf{R}$, using the similarity transformation

from Vallado and Alfano is shown below [102]. The covariance is whitened with $\mathbf{W} = \mathbf{L}^T$ [152].

$$\mathbf{W}\ \mathbf{R}\ \mathbf{W}^T = \mathbf{L}^T\ \mathbf{R}\ \mathbf{L} \tag{3.6}$$

$$= \mathbf{L}^T\ (\mathbf{L}\ \mathbf{L}^T)^{-1}\ \mathbf{L} \tag{3.7}$$

$$= \mathbf{L}^T\ \mathbf{L}^{T^{-1}}\ \mathbf{L}^{-1}\ \mathbf{L} \tag{3.8}$$

$$\mathbf{W}\ \mathbf{R}\ \mathbf{W}^T = \mathbf{I}. \tag{3.9}$$

The whitening matrix $\mathbf{W} = \mathbf{L}^T$, defined with Cholesky decomposition, whitened the covariance of the measurement noise to identity. In this work the measurement noise covariance is assumed to be uncorrelated, resulting in a diagonal whitening matrix and $\mathbf{L} = \mathbf{L}^T$. Next, this whitening matrix, $\mathbf{L}^T$, is applied to Equation 2.6 to incorporate measurement noise into the observability matrix. With Cholesky whitening, the output equation is redefined as

$$\mathbf{z}'(t_k) = \mathbf{H}'(t_k)\ \mathbf{x}(t_0) + \mathbf{r}(t_k), \tag{3.10}$$

where,

$$\mathbf{z}'(t_k) = \mathbf{L}^T\ \mathbf{z}(t_k), \tag{3.11}$$

$$\mathbf{H}'(t_k) = \mathbf{L}^T\ \mathbf{H}(t_k)$$

$$= \mathbf{L}^T\ \widetilde{\mathbf{H}}(t_k)\ \mathbf{\Phi}(t_k, t_0), \tag{3.12}$$

$\mathbf{r}(t_k)$ is the whitened measurement noise, resulting in zero-mean and covariance equal to identity. The redefined output equation is used to derive the stochastic observability matrix with covariance of the measurement noise following the same procedure as Section 2.1.2 for deriving the deterministic observability matrix. Measurements at m time steps are collected to form

$$\begin{bmatrix} \mathbf{z}'(t_0) \\ \mathbf{z}'(t_1) \\ \vdots \\ \mathbf{z}'(t_m) \end{bmatrix} = \begin{bmatrix} \mathbf{H}'(t_0) \\ \mathbf{H}'(t_1) \\ \vdots \\ \mathbf{H}'(t_m) \end{bmatrix} \mathbf{x}(t_0) \qquad \text{or} \qquad \bar{\mathbf{z}}' = \bar{\mathbf{H}}'\ \mathbf{x}(t_0). \tag{3.13}$$

Next, the observability matrix with measurement uncertainty is defined by solving for the initial state. Equation 3.16 shows the observability matrix which contains the inverse of the covariance of the measurement noise as a result of pre-whitening with Cholesky decomposition.

$$\widetilde{\mathcal{O}}(t_0, t_m) = \bar{\mathbf{H}}'^T \; \bar{\mathbf{H}}', \tag{3.14}$$

$$= \sum_{k=0}^{m} \mathbf{\Phi}(t_k, t_0)^T \; \widetilde{\mathbf{H}}(t_k)^T \; \mathbf{L}(t_k) \; \mathbf{L}(t_k)^T \; \widetilde{\mathbf{H}}(t_k) \; \mathbf{\Phi}(t_k, t_0), \tag{3.15}$$

applying Equation 3.5, the observability matrix with meaurement uncertainty is given by

$$\widetilde{\mathcal{O}}(t_0, t_m) = \sum_{k=0}^{m} \mathbf{\Phi}(t_k, t_0)^T \; \widetilde{\mathbf{H}}(t_k)^T \; \mathbf{R}(t_k)^{-1} \; \widetilde{\mathbf{H}}(t_k) \; \mathbf{\Phi}(t_k, t_0). \tag{3.16}$$

Note that this form of the observability matrix, using a variety of methods to incorporate the covariance of the measurement noise, is also given by Geeraert [36], Dianetti [53], and Jazwinski [40]. In this work, the tilde on the observability matrix variable, $\widetilde{\mathcal{O}}(t_0, t_m)$, denotes the stochastic observability matrix form. A similar process can be performed for the continuous-time observability Gramian as well, resulting in the following.

$$\widetilde{\mathcal{O}}(t_0, t_m) = \int_{t_0}^{t_m} \mathbf{\Phi}(\tau, t_0)^T \; \widetilde{\mathbf{H}}(\tau)^T \; \mathbf{R}(\tau)^{-1} \; \widetilde{\mathbf{H}}(\tau) \; \mathbf{\Phi}(\tau, t_0) \; \mathrm{d}\tau. \tag{3.17}$$

The observability matrix in Equation 3.16 is also called the information matrix or normal equations matrix within the linear, unbiased, minimum variance estimator [49, 50].

3.1.2 Initial State Covariance Incorporation

In the estimation of nonlinear systems, initial information is required in order to start the iterative estimation process. In linear systems, initial information is optional, but it can lead to faster convergence. In this section, initial state uncertainties are incorporated into the observability matrix. A similar procedure to incorporating

prior information into the linear, unbiased, minimum variance estimator is followed for incorporating the initial state uncertainties. The covariance of the measurement noise is augmented with the covariance of the initial state. In order to maintain dimensional consistency, the $\mathbf{H}(t_k)$ matrix is augmented with the identity matrix of size n.

$$\mathbf{R}(t_k) = \begin{bmatrix} \mathbf{R}(t_k) & \mathbf{0} \\ \mathbf{0} & \mathbf{P}(t_0) \end{bmatrix}, \tag{3.18}$$

$$\mathbf{H}(t_k) = \begin{bmatrix} \mathbf{H}(t_k) \\ I \end{bmatrix}. \tag{3.19}$$

First, Cholesky whitening is applied to Equation 3.18. The covariance of the initial state is also assumed to be uncorrelated, but this assumption is not strictly necessary. The Cholesky whitening of the augmented covariance matrix is given by

$$\mathbf{R}(t_k)^{-1} = \begin{bmatrix} \mathbf{R}(t_k)^{-1} & \mathbf{0} \\ \mathbf{0} & \mathbf{P}(t_0)^{-1} \end{bmatrix} = \mathbf{L}(t_k)\ \mathbf{L}(t_k)^T. \tag{3.20}$$

The inverse of the augmented covariance matrix is defined by the inverse of each matrix component if and only if each matrix is invertible. As the covariance of the initial state is assumed to be uncorrelated, the whitening matrix is diagonal and $\mathbf{L}(t_k) = \mathbf{L}(t_k)^T$. Next, Equations 3.18, 3.19, and 3.20 are used in the same procedure as Equations 3.10 through 3.16 to include measurement and initial state uncertainties in the stochastic observability matrix.

$$\widetilde{\mathcal{O}}(t_0, t_m) = \mathbf{P}(t_0)^{-1} + \sum_{k=0}^{m} \mathbf{\Phi}(t_k, t_0)^T\ \widetilde{\mathbf{H}}(t_k)^T\ \mathbf{R}(t_k)^{-1}\ \widetilde{\mathbf{H}}(t_k)\ \mathbf{\Phi}(t_k, t_0). \tag{3.21}$$

Augmenting the covariance of the measurement noise with initial state uncertainty and performing pre-whitening of the output equation results in the information matrix with *a priori* state information used in the least squares solution [49].

3.2 Information Form of the Kalman Filter

Prior to application of deterministic and stochastic observability analysis to the orbit problem for object characterization and for estimation performance analysis, the

connection of observability and the Kalman Filter (KF) is shown. More specifically, the stochastic observability matrix is contained within the Information Form of the KF, after manipulation for agreement with observability notions. Within the Information Form of the KF, from Tapley, Schutz, and Born [49], the covariance update is defined by

$$\begin{aligned}\mathbf{P}(t_{k+1})^{-1} = \mathbf{\Phi}(t_{k+1},t_k)\ \mathbf{P}(t_k)^{-1}\ \mathbf{\Phi}(t_{k+1},t_k)^T \\ + \mathbf{\Phi}(t_{k+1},t_k)\ \widetilde{\mathbf{H}}(t_k)^T\ \mathbf{R}(t_k)^{-1}\ \widetilde{\mathbf{H}}(t_k)\ \mathbf{\Phi}(t_{k+1},t_k)^T,\end{aligned} \tag{3.22}$$

where $\mathbf{P}(t_{k+1})^{-1}$ is the information matrix at time t_{k+1}, $\mathbf{\Phi}(t_{k+1},t_k)$ is the STM which transforms the state from time t_k to time t_{k+1}, $\widetilde{\mathbf{H}}(t_k)$ is the measurement matrix at time t_k, and $\mathbf{R}(t_k)$ is the covariance matrix of the measurement noise at t_k. Process noise has been removed from Equation 3.22 to aid in the clarity of the connection to the stochastic observability matrix.

As defined in Section 2.1, observability evaluates whether sufficient information about the states exists within the measurements to determine the initial state of a system. In order to show the connection of observability and the Information Form of the KF, the Information Form of the KF is manipulated to reference the initial state, rather than the previous time step as in Equation 3.22. The manipulation of the Information Form of the KF begins with $k = 0$ to solve for the information matrix at $k = 1$, or

$$\begin{aligned}\mathbf{P}(t_1)^{-1} = \mathbf{\Phi}(t_1,t_0)\ \mathbf{P}(t_0)^{-1}\ \mathbf{\Phi}(t_1,t_0)^T \\ + \mathbf{\Phi}(t_1,t_0)\ \widetilde{\mathbf{H}}(t_0)^T\ \mathbf{R}(t_0)^{-1}\ \widetilde{\mathbf{H}}(t_0)\ \mathbf{\Phi}(t_1,t_0)^T.\end{aligned} \tag{3.23}$$

Next, the information at $k = 2$ can be defined as

$$\begin{aligned}\mathbf{P}(t_2)^{-1} = \mathbf{\Phi}(t_2,t_1)\ \mathbf{P}(t_1)^{-1}\ \mathbf{\Phi}(t_2,t_1)^T \\ + \mathbf{\Phi}(t_2,t_1)\ \widetilde{\mathbf{H}}(t_1)^T\ \mathbf{R}(t_1)^{-1}\ \widetilde{\mathbf{H}}(t_1)\ \mathbf{\Phi}(t_2,t_1)^T,\end{aligned} \tag{3.24}$$

and the information matrix at $k = 1$ can be substituted into Equation 3.24, resulting in

$$\begin{aligned}\mathbf{P}(t_2)^{-1} &= \mathbf{\Phi}(t_2,t_0)\ \mathbf{P}(t_0)^{-1}\ \mathbf{\Phi}(t_2,t_0)^T \\ &\quad + \mathbf{\Phi}(t_2,t_0)\ \widetilde{\mathbf{H}}(t_0)^T\ \mathbf{R}(t_0)^{-1}\ \widetilde{\mathbf{H}}(t_0)\ \mathbf{\Phi}(t_2,t_0)^T \\ &\quad + \mathbf{\Phi}(t_2,t_1)\ \widetilde{\mathbf{H}}(t_1)^T\ \mathbf{R}(t_1)^{-1}\ \widetilde{\mathbf{H}}(t_1)\ \mathbf{\Phi}(t_2,t_1)^T \qquad (3.25) \\ &= \mathbf{\Phi}(t_2,t_0)\ \mathbf{P}(t_0)^{-1}\ \mathbf{\Phi}(t_2,t_0)^T \\ &\quad + \sum_{p=0}^{1} \mathbf{\Phi}(t_2,t_p)\ \widetilde{\mathbf{H}}(t_p)^T\ \mathbf{R}(t_p)^{-1}\ \widetilde{\mathbf{H}}(t_p)\ \mathbf{\Phi}(t_2,t_p)^T. \qquad (3.26)\end{aligned}$$

Extending the information matrix to the $k+1$ time step,

$$\begin{aligned}\mathbf{P}(t_{k+1})^{-1} &= \mathbf{\Phi}(t_{k+1},t_0)\ \mathbf{P}(t_0)^{-1}\ \mathbf{\Phi}(t_{k+1},t_0)^T \\ &\quad + \sum_{p=0}^{k} \mathbf{\Phi}(t_{k+1},t_p)\ \widetilde{\mathbf{H}}(t_p)^T\ \mathbf{R}(t_p)^{-1}\ \widetilde{\mathbf{H}}(t_p)\ \mathbf{\Phi}(t_{k+1},t_p)^T. \qquad (3.27)\end{aligned}$$

Equation 3.27 contains the information matrix at time t_{k+1} which is a function of the initial information matrix and the measurements at each previous time step, including the measurement uncertainties. The stochastic observability matrix with state and measurement uncertainties in Equation 3.21 can be obtained by multiplying Equation 3.27 on the left by $\mathbf{\Phi}(t_{k+1},t_0)^T$ and on the right by $\mathbf{\Phi}(t_{k+1},t_0)$.

$$\begin{aligned}\mathbf{\Phi}(t_{k+1},t_0)^T\ \mathbf{P}(t_{k+1})^{-1}\ \mathbf{\Phi}(t_{k+1},t_0) &= \mathbf{\Phi}(t_{k+1},t_0)^T \Big[\mathbf{\Phi}(t_{k+1},t_0)\ \mathbf{P}(t_0)^{-1}\ \mathbf{\Phi}(t_{k+1},t_0)^T \\ &\quad + \sum_{p=0}^{k} \mathbf{\Phi}(t_{k+1},t_p)\ \widetilde{\mathbf{H}}(t_p)^T\ \mathbf{R}(t_p)^{-1}\ \widetilde{\mathbf{H}}(t_p)\ \mathbf{\Phi}(t_{k+1},t_p)^T\Big]\ \mathbf{\Phi}(t_{k+1},t_0).\end{aligned} \qquad (3.28)$$

Applying the following properties of the STM

$$\mathbf{\Phi}(t_k,t_0)^{-1} = \mathbf{\Phi}(t_k,t_0)^T, \qquad (3.29)$$

$$\mathbf{\Phi}(t_k,t_0)^T = \mathbf{\Phi}(t_0,t_k), \qquad (3.30)$$

$$\mathbf{\Phi}(t_2,t_0) = \mathbf{\Phi}(t_2,t_1)\ \mathbf{\Phi}(t_1,t_0), \qquad (3.31)$$

Equation 3.28 becomes

$$\mathbf{\Phi}(t_0, t_{k+1})\ \mathbf{P}(t_{k+1})^{-1}\ \mathbf{\Phi}(t_0, t_{k+1})^T = \mathbf{P}(t_0)^{-1} + \sum_{p=0}^{k} \mathbf{\Phi}(t_0, t_{k+1})\ \mathbf{\Phi}(t_{k+1}, t_p)\ \widetilde{\mathbf{H}}(t_p)^T\ \mathbf{R}(t_p)^{-1}\ \widetilde{\mathbf{H}}(t_p)\ \mathbf{\Phi}(t_p, t_{k+1})\ \mathbf{\Phi}(t_{k+1}, t_0). \quad (3.32)$$

Next, Equation 3.32 is simplified and new variables are substituted in for the indices to match Equation 3.21.

$$\mathbf{\Phi}(t_0, t_{m+1})\ \mathbf{P}(t_{m+1})^{-1}\ \mathbf{\Phi}(t_0, t_{m+1})^T = \mathbf{P}(t_0)^{-1} + \sum_{k=0}^{m} \mathbf{\Phi}(t_k, t_0)^T\ \widetilde{\mathbf{H}}(t_k)^T\ \mathbf{R}(t_k)^{-1}\ \widetilde{\mathbf{H}}(t_k)\ \mathbf{\Phi}(t_k, t_0). \quad (3.33)$$

Equation 3.33 represents the information matrix at a future time, mapped to time t_0. The information matrix in Equation 3.33 is a function of the initial information matrix and the accumulation of the measurements with uncertainty, mapped to time t_0, which is identical to the stochastic observability matrix with state and measurement uncertainties given by Equation 3.21. Similar derivations for the connection of the Information Form of the KF and observability can be found in [32, 51–53].

Kalman's original work on observability makes a statement for the requirement of observability for a solution to the optimal regulator problem [15]. However, the original definition of observability does not define any expectations for estimation results when a system is not observable. Section 3.6.3 explore the connection of observability and estimation further through simulations of stochastic observability, the extended Kalman Filter (EKF), and nonlinear batch Least Squares (LS). In addition, Section 3.7 shows that accurate estimates cannot be guaranteed when the observability of a system cannot be determined.

3.3 Simulation Orbit Definitions

The following sections analyze observability of the orbit problem with simulations of deterministic observablity, stochastic observability, observability with extended states, EKF state estimation, and nonlinear batch LS state estimation. The orbits

of interest for many of the simulations are defined by five low Earth orbit (LEO) objects and five geosynchronous Earth orbit (GEO) objects in Tables 3.1 and 3.2, respectively. For each orbit, the orbital elements are defined and an area-to-mass (AMR) value is assigned. For a typical GPS satellite, the AMR is approximately 0.02 m^2/kg [94], but high area-to-mass ratio (HAMR) objects, with AMR above 1.0 m^2/kg, have been found in GEO-like orbits [108, 153]. A range of AMR values were selected for the five LEO and five GEO objects to explore the impact of AMR on the observability of the orbit problem. For each of the orbit cases, the diffuse coefficient, a component of the solar radiation pressure (SRP) perturbation, is assumed to equal to 0.5. Therefore, the C variable in Equation 2.27, which assumes a cannonball model, is equal to 0.3056.

Table 3.1. Orbital elements and AMR for five LEO objects.

Orbit #	1	2	3	4	5
a [km]	8124.9673	7464.0111	7059.5685	7868.6408	7011.9387
e [-]	1.4686e-1	1.1651e-2	1.3704e-2	2.2336e-3	1.7747e-3
i [deg]	32.8687	28.3284	65.0611	74.0150	39.7500
Ω [deg]	55.8261	302.1046	18.5642	107.5861	28.6732
ω [deg]	53.8800	183.3909	176.8673	260.0122	58.1497
ν [deg]	0.0	0.0	0.0	0.0	0.0
AMR [m^2/kg]	5.00	0.02	1.00	10.0	20.0

Table 3.2. Orbital elements and AMR for five GEO objects.

Orbit #	1	2	3	4	5
a [km]	42170.238	42190.793	42164.796	42166.668	42308.743
e [-]	9.7343e-4	4.9220e-4	1.5716e-3	1.6556e-4	3.1852e-4
i [deg]	35.7448	2.6447	7.4310	0.051497	13.8121
Ω [deg]	359.3036	295.4140	52.7661	123.2611	30.9790
ω [deg]	124.1101	255.2388	114.5845	79.7058	346.1611
ν [deg]	0.0	0.0	0.0	0.0	0.0
AMR [m^2/kg]	5.00	0.02	1.00	10.0	20.0

3.4 Impact of Measurement Noise on Orbit Observability

Section 3.1.1 derived the stochastic observability matrix, consisting of the observability matrix with the inverse of the covariance of the measurement noise. If the measurement noise covariance is assumed to be uncorrelated and time-invariant, a simple relation between the measurement noise variances can be defined. Given two measurement variables, the variances of the measurement noise can be related with

$$\sigma_2^2 = c\ \sigma_1^2, \tag{3.34}$$

where c is a nonzero scalar and is the ratio of the measurement noise variances. Equation 3.16, the stochastic observability matrix with measurement noise, includes the inverse of the measurement noise covariance matrix. Including the above relationship

between two measurement variances, the inverse of the measurement noise covariance can be stated as

$$\mathbf{R}^{-1} = \begin{bmatrix} \frac{1}{\sigma_1^2} & 0 \\ 0 & \frac{1}{\sigma_2^2} \end{bmatrix} \tag{3.35}$$

$$= \begin{bmatrix} \frac{1}{\sigma_1^2} & 0 \\ 0 & \frac{1}{c\ \sigma_1^2} \end{bmatrix} \tag{3.36}$$

$$= \frac{1}{\sigma_1^2} \begin{bmatrix} 1 & 0 \\ 0 & \frac{1}{c} \end{bmatrix}. \tag{3.37}$$

The stochastic observability matrix with the new measurement noise covariance form is reformulated as

$$\widetilde{\mathcal{O}}(t_0, t_m) = \frac{1}{\sigma_1^2} \sum_{k=0}^{m} \mathbf{\Phi}(t_k, t_0)^T\ \widetilde{\mathbf{H}}(t_k)^T \begin{bmatrix} 1 & 0 \\ 0 & \frac{1}{c} \end{bmatrix} \widetilde{\mathbf{H}}(t_k)\ \mathbf{\Phi}(t_k, t_0). \tag{3.38}$$

The stochastic observability matrix is now dependent on one of the measurement noise variances and the ratio of the two measurement noise variances.

As c approaches one, the measurement noise variance values approach an equivalent value, and the only impact the measurement noise has on the observability matrix is the inverse of the first measurement noise variance. Theoretically, scaling the observability matrix by a constant factor of $\frac{1}{\sigma_1^2}$ will not change the observability of a system, when treating observability as a binary criteria. The typical test of observability is the rank of the observability matrix, which is a method for determining whether the observability matrix is invertible or not. An equivalent condition for the non-singularity of the observability matrix is computing the determinant of the matrix. For a non-singular matrix the determinant of the matrix is nonzero. The following property of a matrix determinant is used to show that the observability result will not be theoretically change when the observability matrix is multiplied by

a scalar constant. Given a matrix A with n rows multiplied by a scalar constant c, the determinant of A can be states as follows

$$\det(\mathbf{A}) = c^n \ \det(\mathbf{A}). \tag{3.39}$$

Applying this matrix determinant feature to observability,

$$\det(\widetilde{\mathcal{O}}(t_0, t_m)) = \det(\frac{1}{\sigma_1^2} \ \mathcal{O}(t_0, t_m)) \tag{3.40}$$

$$= \frac{1}{\sigma_1^2} \ \det(\mathcal{O}(t_0, t_m)). \tag{3.41}$$

Substituting in for the observability determinant definition, $\det(\mathcal{O}(t_0, t_m)) \neq 0$, the determinant of the stochastic observability matrix with uncorrelated, time-invariant, and equal measurement noise variances is equivalent to

$$\det(\widetilde{\mathcal{O}}(t_0, t_m)) \neq 0. \tag{3.42}$$

From the above proof, when the measurement noise variances are equal, the observability matrix is scaled by a constant and the observability result will not be theoretically changed. Moreover, numerical evaluation of the observability will not change given the observability test used in this work. The singular values of the observability matrix will all be scaled by the scalar value due to the commutative property for matrices multiplied by scalars. Recalling the definition of a matrix with singular value decomposition,

$$c \ \mathbf{A} = c \ (\mathbf{U} \ \mathbf{S} \ \mathbf{V}^T) = \mathbf{U} \ (c \ \mathbf{S}) \ \mathbf{V}^T. \tag{3.43}$$

The singular values of $c \ \mathbf{A}$ are singular values of the matrix $\mathbf{A}$ multiplied by the scalar c. As the tolerance for determining observability numerically, given by Equation 2.15, is a function of the maximum singular value of the observability matrix, the tolerance will also scale with the constant $\frac{1}{\sigma_1^2}$, and the binary observability result will not change. Methods for determining observability which do not use singular value decomposition and the tolerance defined by Equation 2.15, may have a different numerical result

for the observability matrix multiplied by a scalar due to the numerical error and precision.

When the ratio of the measurement noise variances, c, is not equal to one, the observability matrix will be changed more significantly as the ratio of the measurement noise variances will redistribute how information progresses from the measurements to the states. The ratio of the measurement noise variances will influence the contribution of the measurements for determining the states in a system. The impact of the ratio of measurement noise variances on the time for a system to become observable is explored in more detail for the LEO and GEO objects given in Tables 3.1 and 3.2.

The measurements implemented in this analysis are right ascension, α, and declination, δ. The variance in right ascension is kept fixed at $\sigma_\alpha^2 = 1.0$ arcsec^2, and a range of variances in declination, from 0.01 arcsec^2 to 100.0 arcsec^2, are analyzed for impact on time for a state consisting of Cartesian position and velocity to become observable with angles-only measurements. Stochastic observability analysis was performed multiple times with the fixed right ascension measurement noise variance and different values of declination measurement noise variance defined according to the range of declination variance values.

For each observability result, the time for the system to become observable was defined as the time for the smallest singular value to cross the tolerance line, which is the time when the observability matrix becomes full rank. Figures 3.1 and 3.2 show the LEO and GEO observability results for the range of measurement noise variances. The time for the system to become observable in seconds is plotted against the variance ratio, i.e. $\sigma_\delta^2/\sigma_\alpha^2$, on a log scale. Discussion of the impact of the ratio of the measurement noise variances focuses on the LEO 1 and GEO 4 orbits, and these two objects are highlighted in blue in Figures 3.1 and 3.2.

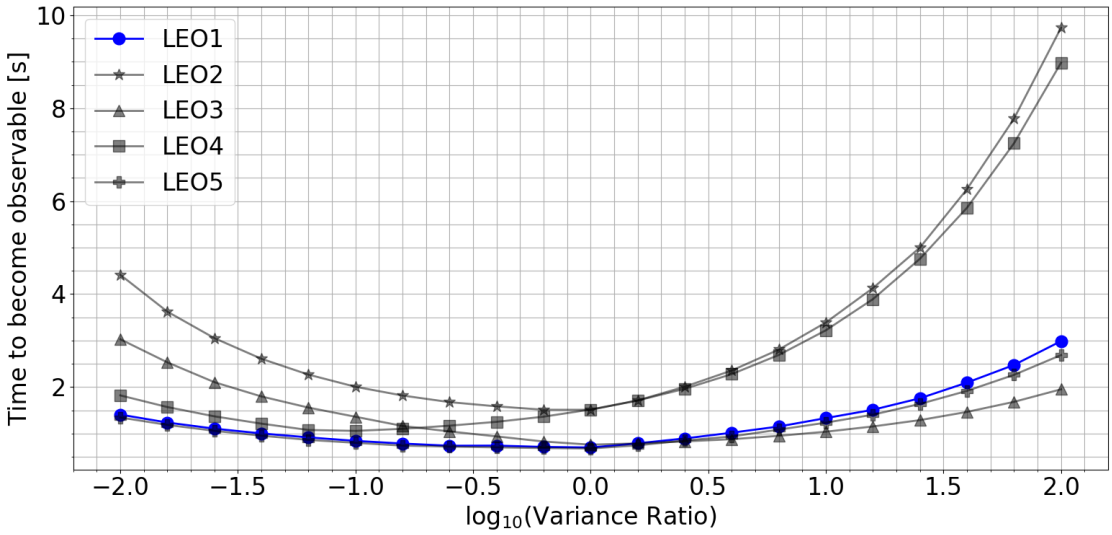

Figure 3.1. LEO observability analysis with a range of declination measurement noise variance ratios.

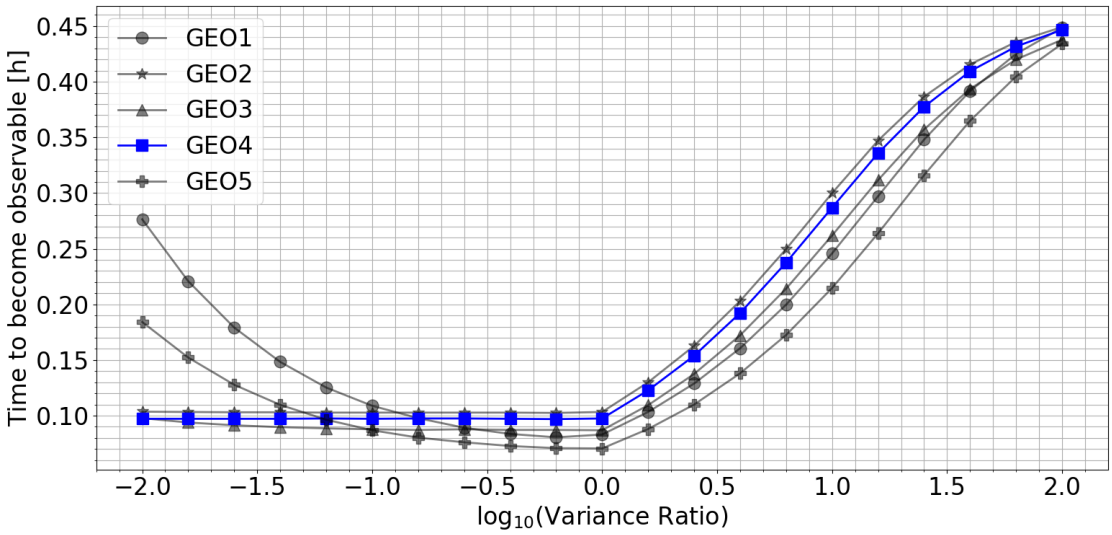

Figure 3.2. GEO observability analysis with a range of declination measurement noise variance ratios.

The trends for both objects are in alignment with understanding of the orbits of the two cases and the ratio of the variances. As shown in Table 3.1, the LEO 1 object is in an inclined orbit, and as shown in Table 3.2, the GEO 4 object is in a nearly circular, equatorial orbit. Because the inclination of both orbits is less than 45° the declination measurement includes more knowledge about the z-components of position and velocity compared to the right ascension measurement. Therefore, as the measurement noise variance on declination is larger than the measurement noise variance on right ascension, $\log(c) > 0$ in Figures 3.1 and 3.2, the time to become observable is expected to increase.

The shape of the time to become observable curve for the LEO 1 object is more parabolic compared to the GEO 4 object due to the higher inclination for the LEO 1 object. Even though large differences in the measurement noise variances increases the time to become observable for both $\sigma_\delta^2 > \sigma_\alpha^2$ and $\sigma_\delta^2 < \sigma_\alpha^2$, the ratio with a larger measurement noise variance in declination compared to right ascension has a longer time to become observable compared to the opposite arrangement. This comparison agrees with the notion that these orbits will depend on the knowledge from the declination measurement more for recovering the z-components of position and velocity.

The trends defined for the LEO 1 object become even more exaggerated for the GEO 4 object. In Figure 3.2, when the measurement noise variance in right ascension is greater than declination, $\log(c) < 0$, there impact on the time for the system to become observable is small. This behavior also exists for the GEO 2 and GEO 3 objects, which have lower inclinations compared to the GEO 1 and GEO 5 objects. For these higher inclination GEO objects, the time to become observable is affected when the measurement noise variance in right ascension is greater than declination.

As the log of the variance ratio decreases, the measurement noise variance in declination decreases because the measurement noise variance in right ascension is kept fixed for this analysis. Therefore, the declination measurement becomes more accurate, thus more representative of the truth, and the time to become observable

does not increase for the GEO 4 object as the knowledge of the z-components of position and velocity are well defined with the declination measurement. However, when the declination measurement has a large noise variance, the time to become observable increases considerably. For an optical sensor system, these results reveal that a timing bias will impact the observability of a low inclination GEO object less than a pixel bias.

This analysis is also performed for the case where the measurement noise variance in declination is kept fixed, and the measurement noise variance in right ascension is varied. The resulting curves of time to become observable versus variance ratio are given in Appendix A.1. Since the right ascension measurement noise variance is now changing, $\log(c) < 0$ corresponds to large right ascension noise variance values and $\log(c) > 0$ corresponds to small right ascension noise variances. In Figures 3.1 and 3.2, $\log(c) < 0$ corresponds to small declination noise variance values and $\log(c) > 0$ corresponds to large declination noise variances. The trends of Figures 3.1 and 3.2 are exactly the same for the fixed declination measurement noise variances in Appendix A.1 except the plots are flipped.

3.5 Impact of Propagation Method and Linearization Reference on Orbit Observability

Before exploring observability of a state extended beyond position and velocity with SRP parameters, the state propagation method for the observability matrix is analyzed. Recall the deterministic, discrete observability matrix equation from Section 2.1.

$$\mathcal{O}(t_0, t_m) = \sum_{k=1}^{m} \mathbf{\Phi}(t_k, t_0)^T \ \widetilde{\mathbf{H}}(t_k)^T \ \widetilde{\mathbf{H}}(t_k) \ \mathbf{\Phi}(t_k, t_0). \tag{3.44}$$

The linearized measurement matrix, $\widetilde{\mathbf{H}}(t_k)$, of Equation 3.44 is evaluated with state at time t_k, as the nonlinear measurement model is linearized about the true state. As observability defines whether or not there is sufficient information in the measurements to determine the state at t_0, the state must be propagated from t_0 to

t_k to evaluate the observability matrix, specifically for evaluation of the linearized measurement matrix.

Two different propagation methods for computing the state at time t_k are evaluated for applicability to observability of the orbit problem. Due to the linearization of the measurement model, the linearized measurement matrix is evaluated at a reference state, or $\widetilde{\mathbf{H}}|_{\mathbf{x}(t_k)*}$, where $|_{\mathbf{x}(t_k)*}$ denotes evaluation of the linearized matrix about the reference state $\mathbf{x}^*$ at time t_k. The first method for propagating the reference uses the STM to transform the state at time t_0 to the state at time t_k, shown in Equation 3.45.

$$\mathbf{x}(t_k)^* = \mathbf{\Phi}(t_k, t_0)\ \mathbf{x}(t_0)^*. \tag{3.45}$$

The second method numerically integrates the nonlinear dynamics to propagate state from time t_0 to t_k. Both propagation methods in this analysis assume a two-body model without perturbations for the state dynamics.

These two methods for propagating the state to time t_k for evaluation of the linearized measurement matrix are implemented for determining the observability of a state consisting of position and velocity with angles-only measurements. The singular values of the observability matrix for each propagation method are shown in Figures 3.3 and 3.4. Analysis of the GEO 4 object is shown here, with a short propagation time shown in Figure 3.3 and a longer propagation time shown in Figure 3.4. Similar analysis is shown in Appendix A.2.1 for the other orbits in Tables 3.1 and 3.2. Additional analytic STM formulations and propagation methods are explored in Appendix A.2.2.

The singular values of the observability matrix in Figures 3.3 and 3.4 are ordered from largest to smallest with corresponding tolerance lines given by the dashed lines of the same color as the singular value curves. As introduced in Section 2.1.3, the tolerance line implemented with the singular values of a matrix is an approximation of the numerical error. The STM propagation method results are represented by the blue curves, and the numerical integration propagation method results are represented by the red curves.

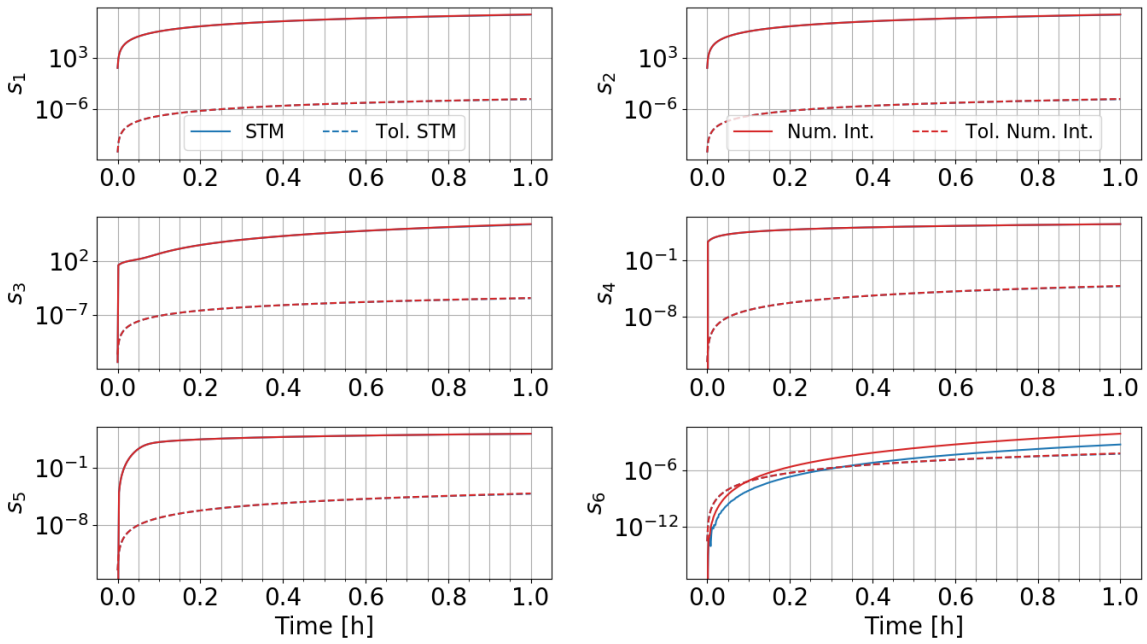

Figure 3.3. Singular values of the observability matrix using the STM propagated state versus the numerically integrated state for the GEO 4 object.

With the shorter propagation time in Figure 3.3, the two propagation methods have singular values which are indistinguishable over the analysis time except for the smallest singular value, s_6. The tolerance lines for the two propagation methods over the short analysis time are also indistinguishable. Note that the time to become observable for this system is different depending on the propagation method selected as the smallest singular values cross the tolerance at different times. When the state is propagated with the two methods for a longer time, larger differences arise in the singular values of the observability matrix as depicted in Figure 3.4. The dashed tolerance lines only correspond to the singular value curves of the same color.

The differences in the observability results exist because of the fundamental differences in what each method represents for observability of the orbit problem. The STM propagation is a linear mapping, so over longer analysis times, the resulting state from this propagation method will not represent the true orbit as accurately. Unlike the EKF, which updates the state estimate and covariance from the previous

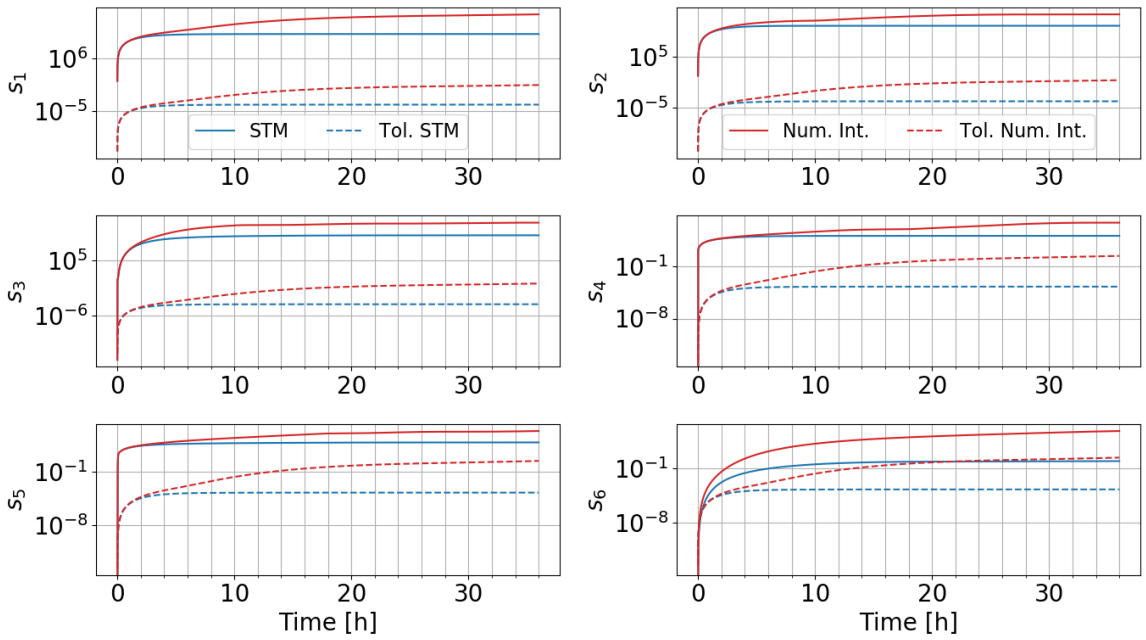

Figure 3.4. Singular values of the observability matrix using the STM propagated state versus the numerically integrated state with a longer analysis time for the GEO 4 object.

time step, thus reducing detrimental effects from linearization, observability is defined for the initial state of a system. As a result the STM in the observability matrix is a transformation from the initial state to the state at time t_k, which is the same state used to evaluate the linearized measurement matrix with the STM propagation method.

The numerical integration method maintains the nonlinear propagation of the state to time t_k for the evaluation of the linearized measurement matrix. Therefore, the linearized measurement matrix is more representative of the true orbit; however, the STM and the linearized measurement matrix then represent different orbits due to the requirements of the STM to transform the state from time t_0 for observability. As this work investigates the applicability of linear observability methods to the nonlinear orbit problem and focuses on observability for informing EKF estimation performance, the numerical integration method is used for propagation of the state to

time t_k for evaluation of the linearized measurement matrix. This method of updating the state through numerical integration is conventional in a sequential filter, such as the EKF.

3.6 Observability of Object Characteristics

The orbit of an object is subject to perturbations, as introduced in Section 2.2.2, and these perturbations can significantly alter the orbit over time. Non-conservative perturbing forces, such as SRP, are often functions of object characteristics. Therefore, extending the state vector beyond position and velocity to include object characteristics provides crucial information for precise orbit propagation of RSOs. Determining which parameters, such as AMR or C in the SRP perturbation, or combinations of parameters are observable is important. In this section, deterministic observability is evaluated for five LEO and five GEO objects, defined in Tables 3.1 and 3.2, with several configurations of extended states including SRP parameters. In addition, the times required for each system to become observable are compared to determine how a state should be configured for achieving observability of object characteristics efficiently.

As introduced in Section 2.1.3, the invertibility of the observability matrix is determined by computation of the matrix rank. Singular value decomposition (SVD) is commonly implemented when determining the rank of matrix numerically. Due to the error inherent in a numerical process, a tolerance is implemented to determine when the singular values are numerically different from zero. The singular values of the observability matrix for a state consisting of position and velocity with angles-only optical measurements are shown in Figure 3.5. The tolerance line, defined as a function of the largest singular value in Equation 2.15, is the black dashed line. The number of singular values in Figure 3.5 is equal to the dimension of the observability matrix. Note that a one-to-one correspondence of singular values to the state variables

is unlikely. The singular values are more likely to correspond to linear combination of the state variables.

When all of the singular values of the observability matrix are greater than the tolerance line, the observability matrix is full rank, and therefore, the system is observable. As discussed in Section 2.1.3, when observability is determined numerically, singular values below the tolerance line do not necessarily indicate a system which is not observable, but the observability cannot be determined because the tolerance line is an estimate of numerical error in the analysis. A system may be theoretically unobservable when singular values remain below the tolerance line, but determining the observability is prevented because of the numerical error in the numerical evaluation method.

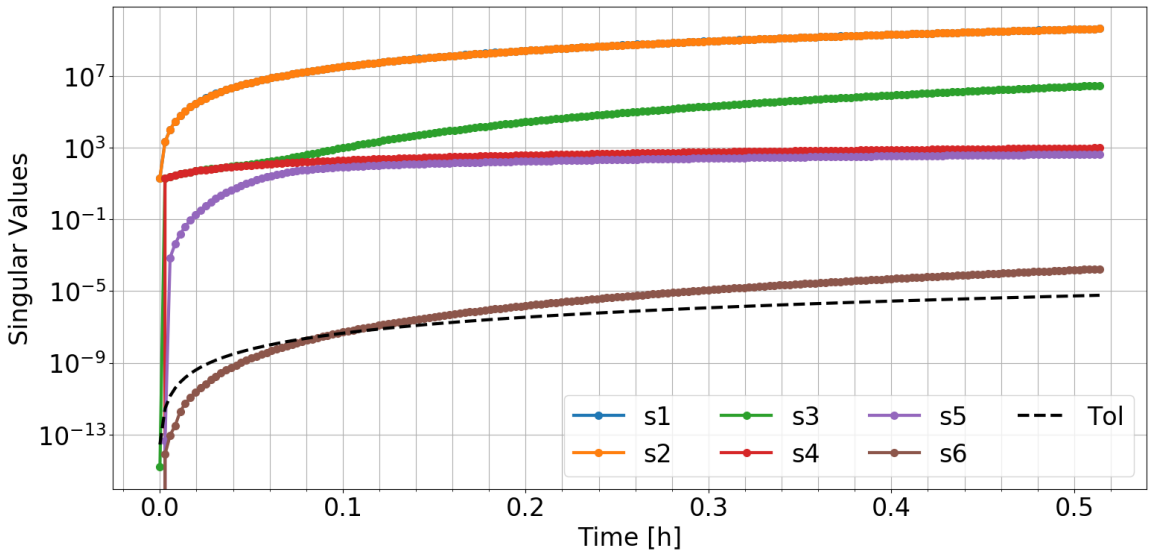

Figure 3.5. Singular values of the observability matrix for a state consisting of position and velocity only for the GEO 4 object.

The rank of the observability matrix over time is another representation of the system observability, which is shown in Figure 3.6. The rank of the observability matrix is computed by determining how many singular values are greater than the

tolerance line in Figure 3.5. Therefore, Figures 3.5 and 3.6 both show the same observability matrix rank information.

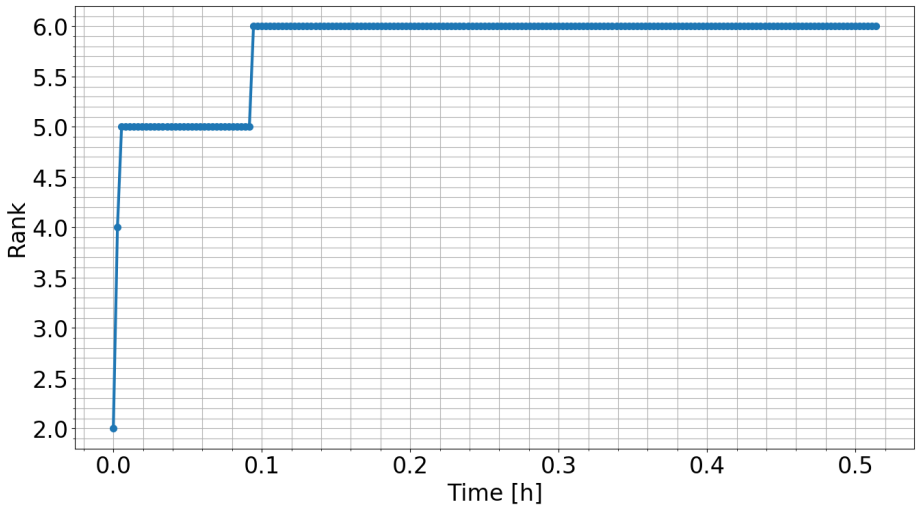

Figure 3.6. Rank of the observability matrix for a state consisting of position and velocity only for the GEO 4 object.

The singular values of the observability matrix above a tolerance line may suggest observability can be a defined as a quantitative measure rather than purely a binary criteria. Therefore, the trends the singular values of the observability matrix exhibit over time provide knowledge of the system observability. However, the time when the smallest singular value crosses the tolerance line can be challenging to see visually. The depiction of the observability with the matrix rank over time shows the time to become observable more clearly than the singular values. For the system given in Figure 3.6, the system becomes observable after approximately 0.1 hours.

3.6.1 Extended State Observability Numerical Challenges

In this work on observability of object characteristics, the time required for the observability matrix to become full rank is the measure of observability implemented for comparing different extended state observability results. Four extended state

vectors, beyond position and velocity, are considered in this analysis of observability: AMR, C, AMR & C, and (AMR $\cdot$ C). The first two extended state cases include one SRP parameter in the state vector in addition to position and velocity. The third state vector includes two extra state variables as separate solve-for parameters, resulting in eight state variables. The final extended state case includes the combined SRP parameter (AMR $\cdot$ C) as these SRP parameters are multiplied within the SRP perturbation implemented in this work. Initially, the state extended by AMR and the state extended by C may be expected to have similar times required to achieve observability. However, the order of magnitude of each SRP parameter has a large impact on the time required to become observable, and the impact initially appears contrary to what may be expected.

The AMR variable, which may realistically range from approximately 0.02 m^2/kg to 100.0 m^2/kg, is much smaller in magnitude compared to C, position, and velocity. In this work, C is assumed to be equal to 0.3056 and is a unit-less parameter. If analysis of observability with a state extended by AMR is conducted with units of km, the size of AMR for a typical GPS object would be defined as 2.0×10^{-8} km^2/kg. The approximate order of magnitude differences of the AMR variable and the position and velocity of LEO and GEO objects are on the order of 10^{11} and 10^{12}, respectively. State vectors with large order of magnitude differences can be challenging for evaluation with numerical methods because of finite precision and numerical error inherent in numerical systems [89].

Due to the large order of magnitude differences between the AMR variable and the position variables, the time to become observable for a state extended by AMR may be expected to be greater than the time to become observable for a state extended by C. However, this expected result is incorrect due to the formulation of the observability matrix, and specifically the STM. As shown in Section 2.4.4, the impact of the extended state variables within the observability matrix occurs with the derivation of the STM. Recall that to define the STM ODE for this nonlinear system, the Jacobian of the dynamics is computed. With a state extended by SRP

parameters and an SRP perturbation on the dynamics, the $\mathbf{A}(t_k)$ matrix of the STM ODE is defined by

$$\mathbf{A}(t_k) = \begin{bmatrix} \mathbf{0}_{3\times3} & \mathbf{I}_{3\times3} & \mathbf{0}_{3\times1} \\ \mathbf{G}_{\text{tot}}(t_k) & \mathbf{0}_{3\times3} & \frac{\partial \mathbf{a}_{\text{SRP}}(t_k)}{\partial \mathbf{x}(7)} \\ \mathbf{0}_{1\times3} & \mathbf{0}_{1\times3} & \mathbf{0}_{1\times1} \end{bmatrix}, \tag{3.46}$$

where $\mathbf{G}_{\text{tot}}(t_k) = \mathbf{G}_{\text{grav}} + \mathbf{G}_{\text{SRP}}$ is the sum of the Jacobians of the equations of motion, when reduced to six first order differential equations. The partial derivatives of the extra state element beyond position and velocity, e.g. AMR or C, are given by $\frac{\partial \mathbf{a}_{\text{SRP}}(t_k)}{\partial \mathbf{x}(7)}$. Moreover, the partial derivative of the SRP perturbing acceleration with respect to AMR or C explain the counter-intuitive extended state observability results. The partial derivatives of the SRP perturbing acceleration with respect to AMR or C are given as

$$\frac{\partial \mathbf{a}_{\text{SRP}}}{\partial \text{AMR}} = \frac{\mathbf{a}_{\text{SRP}}}{\text{AMR}}, \tag{3.47}$$

$$\frac{\partial \mathbf{a}_{\text{SRP}}}{\partial C} = \frac{\mathbf{a}_{\text{SRP}}}{C}. \tag{3.48}$$

The AMR partial derivative, Equation 3.47, does not contain AMR, which results in a much larger partial derivative than it otherwise would be due to the scale of AMR. The C partial derivative still contains AMR, so the scale is orders of magnitude smaller than the other partial derivatives within the $\mathbf{A}(t_k)$ matrix. As a result, observability of a system consisting of a state extended with C is expected to be more challenging to achieve than the state extended with AMR due to the large order of magnitude differences within each state vector.

The impact of AMR on the time to become observable for the state extended with C is explored in more detail by varying AMR for the LEO and GEO objects in Tables 3.1 and 3.2. For each orbit, observability is performed with AMR values ranging from 0.01 m^2/kg to 100.0 m^2/kg and a position and velocity state extended by C. The time to become observable, given by the time where the rank of the observability matrix first becomes seven, is determined for each AMR and object. Figures 3.7 and

3.8 summarize the times to become observable for the LEO and GEO objects versus the range of AMR values.

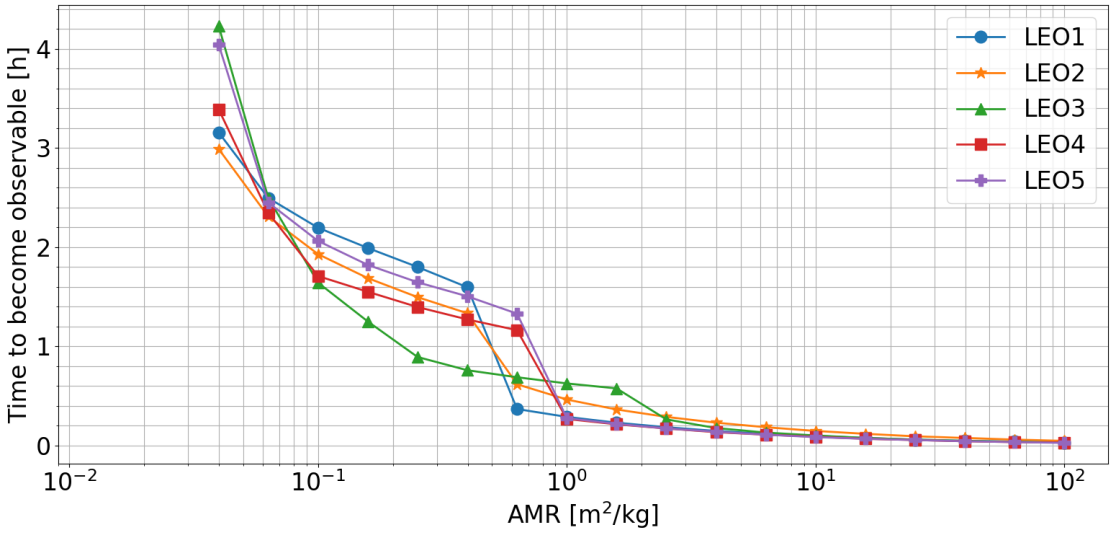

Figure 3.7. Impact of AMR on the time to become observable for a state extended beyond position and velocity with C and the LEO objects of Table 3.1.

For the LEO and GEO objects, the time to become observable is less sensitive to larger AMR values. Conversely, as the AMR values are smaller, given by the left side of Figures 3.7 and 3.8, the impact of the SRP perturbation on the position and velocity is smaller. Therefore, the time to become observable is larger because more measurements are required to determine the relationship between the C variable and the system dynamics. The combined impact of inclination and AMR is also apparent in Figure 3.8. GEO objects 2, 3, and 4 all have inclination less than 10°, and the observability results in Figure 3.8 are similar.

AMR values less than 0.04 m^2/kg do not have associated times to become observable for the LEO objects. The SRP perturbation has a larger affect on GEO objects compared to LEO objects due to distance to the Sun and distance to the central body, Earth in this case. The observability of a system consisting of a state extended beyond position and velocity with C could not be determined for the given

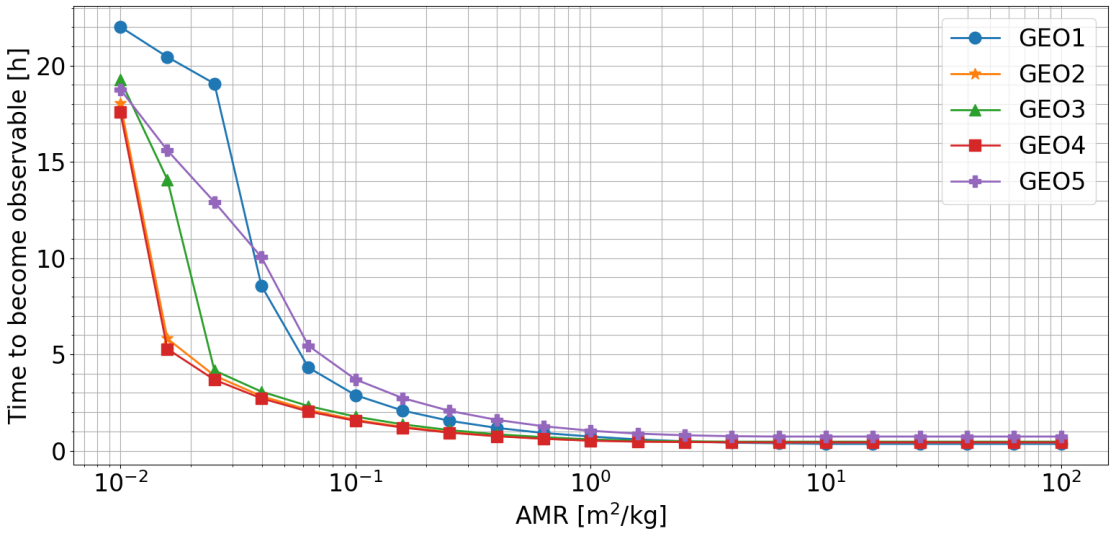

Figure 3.8. Impact of AMR on the time to become observable for a state extended beyond position and velocity with C and the GEO objects of Table 3.1.

LEO objects when AMR is less 0.04 m^2/kg due to the numerical challenges of states which are approximately eleven orders of magnitude different. As the times to become observable can increase significantly for smaller AMR with a state extended beyond position and velocity with C, this extended state case is not included in the following comparisons of observability for different state extensions. However, the following results are replicated in the Appendix A.3 with the extended state case including C.

3.6.2 Extended State Observability with Constant SRP Parameters

Next, the times to become observable for the four extended state cases and the state vector consisting of position and velocity only are compared in Figures 3.10 through 3.13. The observability results are grouped in two ways. Figures 3.10 and 3.11 group the observability results per orbit, and Figures 3.12 and 3.13 show the same observability information, but the results are grouped per extended state case.

For the extended state case with AMR and C as separate, solve-for variables, the observability could not be determined because the eighth singular value is never greater than the tolerance line. Figure 3.9 shows how the eighth singular value of the observability matrix is strictly less than the tolerance line for the GEO 4 object. Note that the singular values are ordered largest, s_1, to smallest, s_8. The s_1 and s_3 singular value curves are not visible because they are nearly identical to the s_2 and s_4 curves.

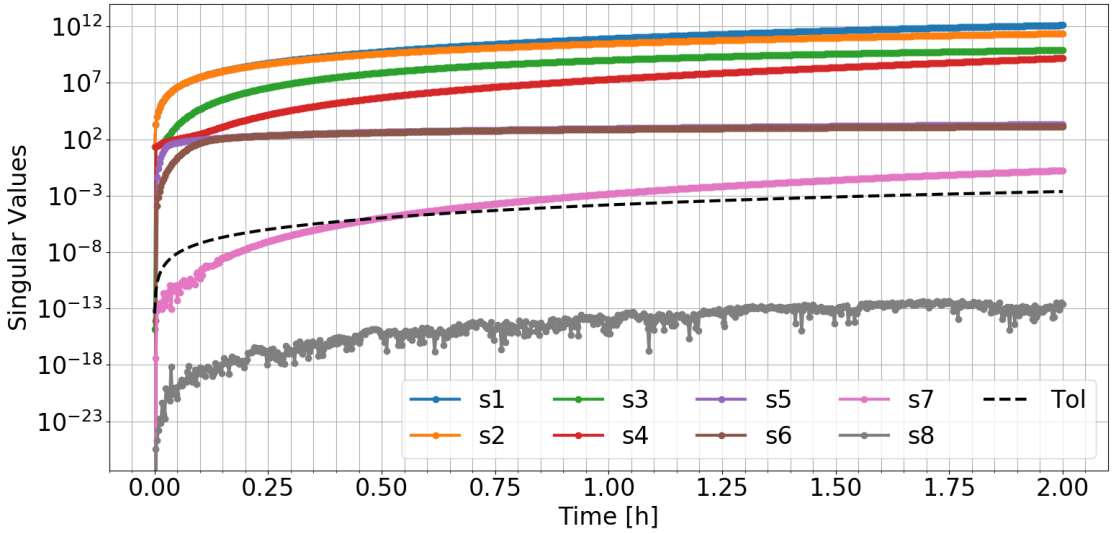

Figure 3.9. Singular values of the observability matrix for the GEO 4 object and the state extended by AMR and C.

Even if the analysis time was extended, the smallest singular value would not progress above the tolerance line for this case with AMR and C as state variables. This behavior is due to the fact that these parameters are both constants in the SRP perturbing acceleration and the angles-only measurements are not sufficient to differentiate between the two states. As the observability of the system cannot be determined when the singular values are not all greater than the tolerance line, the time when the second smallest singular value crosses the tolerance line is shown for

the extended state case with AMR and C as separate variables, as denoted by the s_7 in Figures 3.10 through 3.13.

For the five LEO objects in Figure 3.10 and the five GEO objects in Figure 3.11, the time to become observable increases significantly when the state is extended beyond position and velocity. The AMR and C variables affect the right ascension and declination measurements through perturbations to the position and velocity of the orbit. The scale of the SRP perturbation is approximately six orders of magnitude smaller than the acceleration due to the central body gravitation for a LEO object and approximately four orders of magnitude smaller than the acceleration due to the central body gravitation for a GEO object. Therefore, longer times to become observable are expected when the state is extended beyond position and velocity because of the minimal affect of the AMR and C variables on the right ascension and declination measurements.

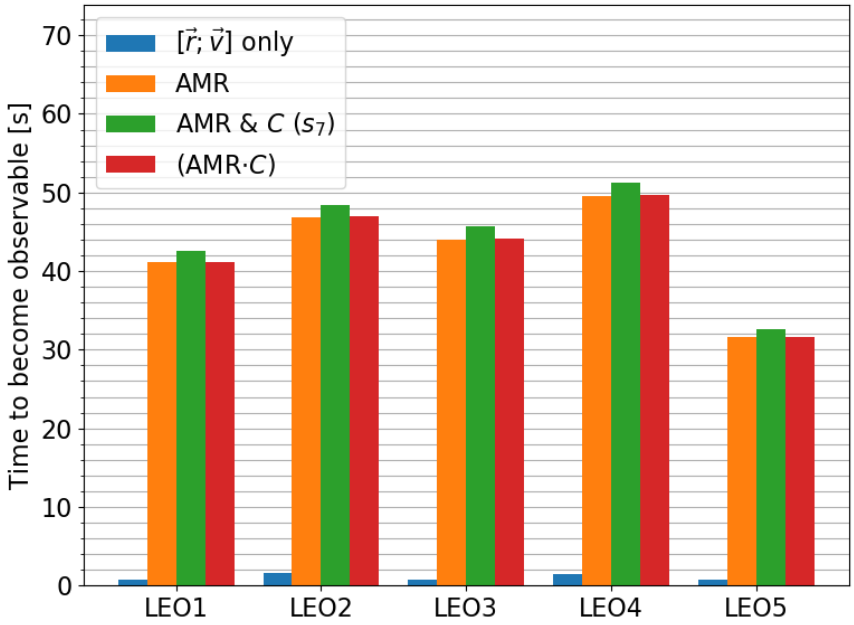

Figure 3.10. Time to become observable for the LEO objects, grouped by orbit.

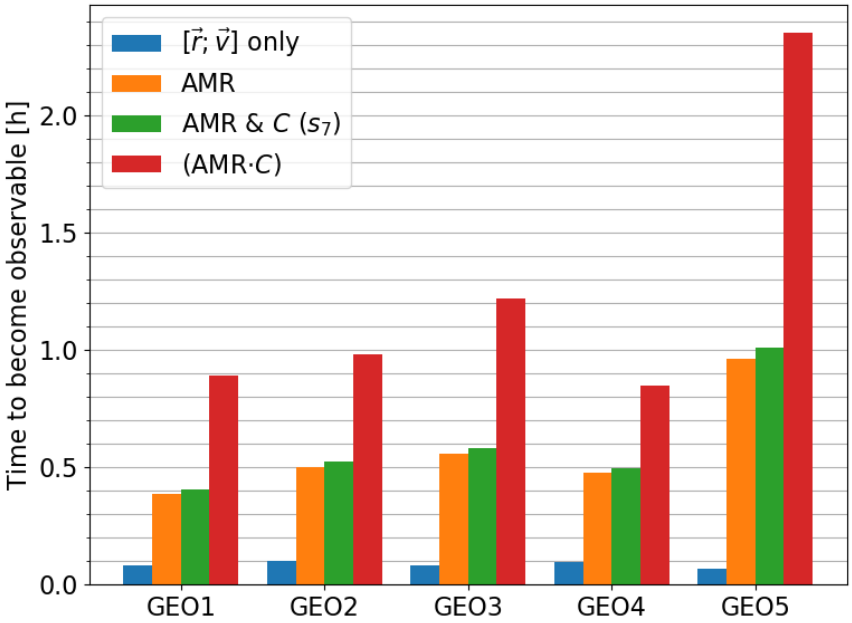

Figure 3.11. Time to become observable for the GEO objects, grouped by orbit.

In addition, the time to become observable is larger for a state extended with the variable (AMR·C) compared to a state extended with AMR. In this work, C is a function of the diffuse coefficient, C_d, and the variable C is defined for the cannonball SRP assumption as $C = \frac{1}{4} + \frac{1}{9}\ C_d$. The diffuse coefficient is bounded between zero and one to maintain energy conservation in a classical Lambertian reflection model, resulting in bounds of 0.250 and 0.361 for C. Therefore, AMR will always be greater than (AMR·C), and the time to become observable will be larger for a state extended by the combined parameter (AMR·C) compared to a state extended by AMR alone. Moreover, this indicates that more measurements would be required to determine the AMR and diffuse coefficient as a combined parameter versus assuming a diffuse coefficient and determining the AMR of an object alone.

Another trend within the times to become observable for a state extended with the variable (AMR·C) compared to a state extended with AMR is the impact of computing the observability of the combined AMR and C variable has a much larger

impact on the time to become observable for the GEO objects compared to the LEO objects. The differences in the times to become observable for these two extended state cases and the LEO objects are on the order of seconds, but the time differences are on the order of half an hour or greater, comparing the same extended state cases for the GEO objects. The SRP perturbation has a larger impact on GEO objects compared to LEO objects, and the affect of SRP parameters will be more significant on the right ascension and declination measurements compared to the affect on the LEO objects. Therefore, reducing the magnitude of the extended state variable through multiplication of C has a larger impact on the time to become observable for a GEO object compared to a LEO object.

Even though the observability of the extended state case with AMR and C as separate, solve-for parameters could not be determined due to numerical error, knowledge of how the observability of the orbit problem is impacted by the addition of extra state parameters can be gained by analyzing the time when the seventh singular value crosses the tolerance line. For all of the LEO and GEO cases, the time for the seventh singular value of the observability matrix for a state extended by AMR and C separately is longer than the time to become observable for a state extended by AMR only. Although a one-to-one correspondence between the singular values of the observability matrix and state variables is unlikely, the singular values of the observability matrix are negatively impacted by extending a state vector with parameters which cannot be differentiated by the measurements.

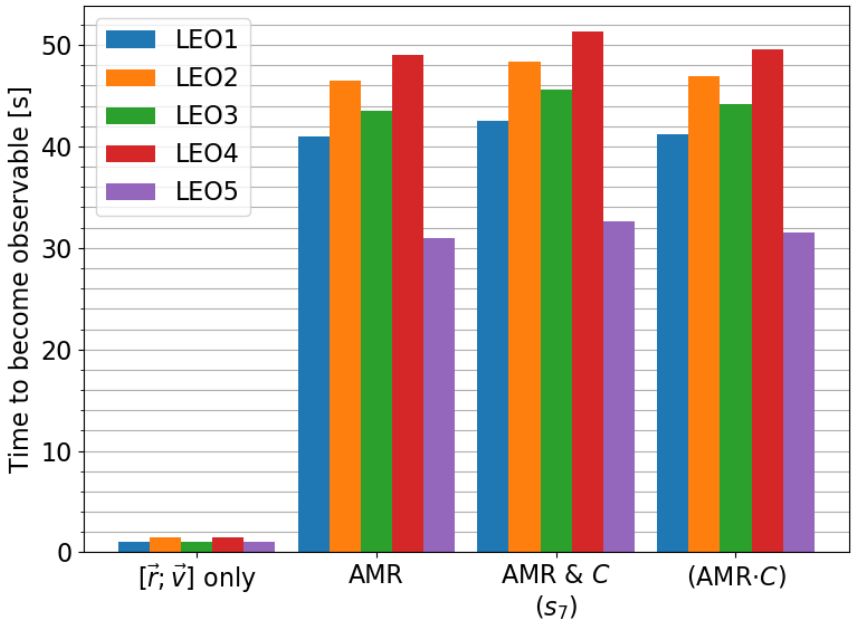

Figure 3.12. Time to become observable for the LEO objects, grouped by extended state case.

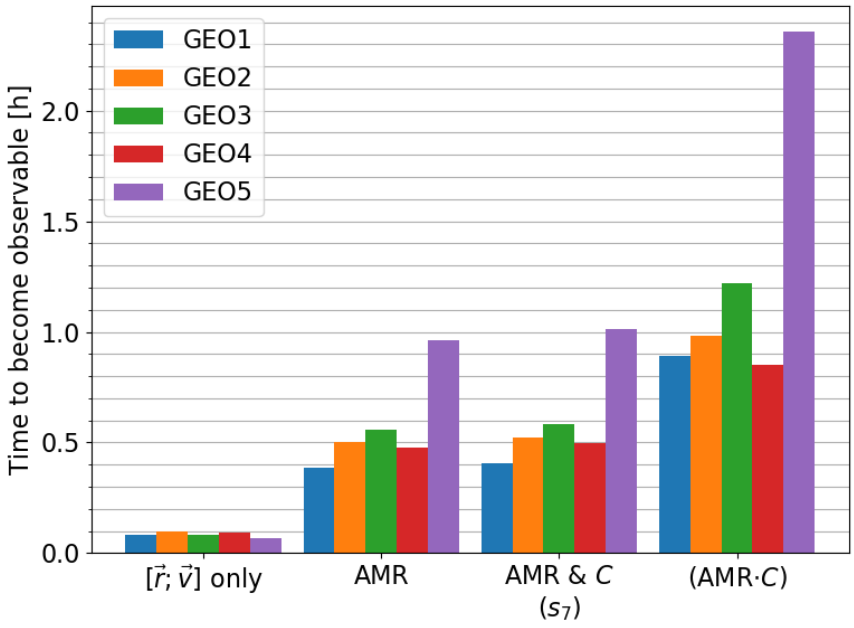

Figure 3.13. Time to become observable for the GEO objects, grouped by extended state case.

3.6.3 Extended State Observability with Time-Varying SRP Parameters

In the previous section, observability analysis was conducted without state and measurement uncertainties, and the position and velocity state vector was extended with SRP parameters, AMR and C. When the state is extended with one of the SRP parameters, defined as constants, the system is observable with the exception of one of the LEO objects. However, when both SRP variables are added as separate, solve-for parameters in the state vector, the observability of the system could not be determined. However, Section 3.4 has shown that measurement noise can impact observability results as the system dynamics are redistributed with the inverse of the covariance of the measurement noise.

As noted in Section 2.2, there are occasions where AMR and the reflectivity properties of an object can change in orbit. When these variables are time-varying, differences in the orbit of an object due to each SRP parameter may become evident in angles-only measurements. Therefore, deterministic and stochastic observability is analyzed with several constant and time-varying configurations of AMR and C to determine whether the AMR and C object characteristics can be observable as separate, solve-for parameters. In addition, the connection of stochastic observability with state and measurement uncertainties and estimation, as shown in Section 3.2, is explored in more detail for each of the AMR and C extended state cases.

Throughout this section, the GEO 4 object in Table 3.2, is used in the simulations of observability and estimation for the four combinations of constant and time-varying

AMR and C variables in Table 3.3. The time-varying models listed in Table 3.3 are modeled by Equations 2.52 and 2.53, with

$$AMR_o = 1.0 \times 10^{-5} \text{ km}^2/\text{kg}, \tag{3.49}$$

$$\alpha_{AMR} = 2.0 \times 10^{-6} \text{ km}^2/\text{kg}, \tag{3.50}$$

$$\omega_{AMR} = 2.778 \times 10^{-4} \text{ Hz}, \tag{3.51}$$

$$C_o = 0.306, \tag{3.52}$$

$$\alpha_C = 0.025, \tag{3.53}$$

$$\omega_C = 5.556 \times 10^{-4} \text{ Hz}. \tag{3.54}$$

In addition, the observer is defined as the Purdue Optical Ground Station (POGS) in New Mexico, USA. The following simulations consist of measurement batches spaced by one hour with six measurements spaced by ten minutes within each batch.

Table 3.3. AMR and C constant and time-varying combinations.

Case #	AMR	C
1	Constant	Constant
2	Time-Varying	Time-Varying
3	Time-Varying	Constant
4	Constant	Time-Varying

As the stochastic observability matrix with state uncertainties, the nonlinear batch least squares estimation with *a priori* information, and the EKF all utilize the covariance of the initial state, realistic initial state uncertainties were generated for this system. In addition, the estimability methods implemented in Chapter 4 require an uncorrelated covariance of the initial state. Details on how the initial state uncertainties in Table 3.4 are discussed in Chapter 4.

The procedure defined in Section 2.3.3 for estimating the pixel uncertainties, and thus the uncertainty in right ascension and declination is implemented to define the

Table 3.4. Initial State Uncertainties.

x [m]	y [m]	z [m]	v_x [m/s]	v_y [m/s]	v_z [m/s]	AMR [m^2/kg]	C [-]
172.527	522.305	51.338	0.0295	0.0388	0.0128	5.809	0.173

covariance of the measurement noise for this analysis. The observations of a GEO object used in the uncertainty quantification and transformation were collected from the POGS, and the resulting average standard deviations of right ascension and declination are estimated as 0.67 arcseconds and 0.045 arcseconds, respectively. Moreover, the images used to estimate the uncertainty in right ascension and declination have an average signal-to-noise ratio of 3.6. Although the right ascension uncertainty is an order of magnitude larger than the declination uncertainty, Section 3.4 has shown that there is minimal impact on the observability for the GEO4 object with this ratio of measurement noise variances. In addition, the measurement uncertainties can be explained by the fact that the images analyzed for the uncertainty quantification are of a GEO object, which has a larger change in right ascension than declination over time.

Deterministic and stochastic observability is analyzed for the extended state analysis cases in Table 3.3. As multiple observability results are compared in this analysis, the rank of the observability matrix over time is presented for clarity of comparison among the different observability methods. In addition, estimation of the same systems is performed with the nonlinear batch least squares and the EKF. The nonlinear batch least squares is performed with and without *a priori* state information.

Constant AMR and C

As Section 3.6 has shown, the deterministic observability cannot be determined for the case where the state vector is extended beyond position and velocity with con-

stant AMR and C as separate state variables. Figure 3.14 shows the deterministic and stochastic observability matrix rank over time. In Figure 3.14, the blue curve represents the deterministic observability matrix, the green curve represents the stochastic observability matrix with measurement uncertainties, and the red curve represents the stochastic observability matrix with state and measurement uncertainties. Recall that a system is considered observable when the rank of the observability matrix is equal to the number of state variables. Therefore, this system, with two SRP parameters included in the state consisting of position and velocity, must reach an observability matrix rank of eight to be observable.

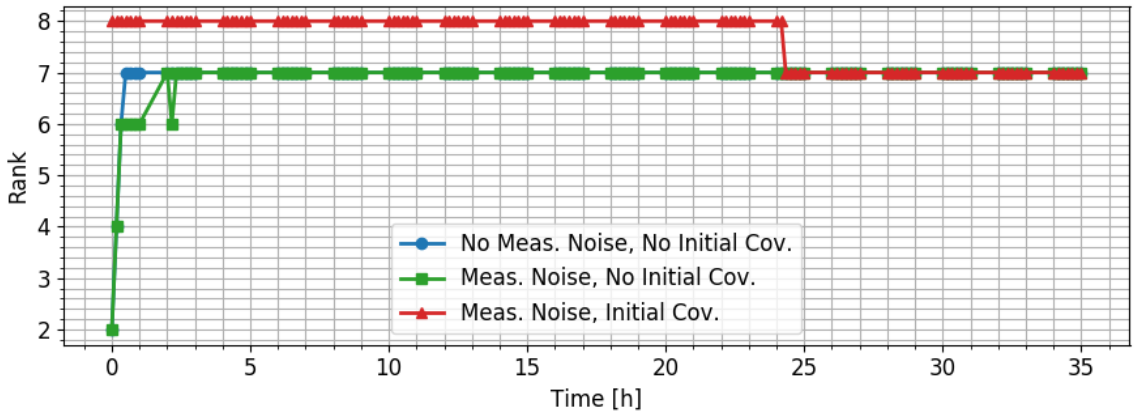

Figure 3.14. Rank of the deterministic and stochastic observability matrices for constant AMR and C.

The deterministic observability results from Section 3.6 are confirmed in Figure 3.14. The rank of the stochastic observability matrix with measurement uncertainty only does not reach a rank of eight as well. The covariance of the measurement noise in the stochastic observability matrix with measurement uncertainties does cause the rank over time to differ from the deterministic observability matrix rank over time due to how the information from the measurements is redistributed to the states with the measurement noise. Of the three observability matrices analyzed, the stochastic observability matrix with initial state and measurement uncertainties does have a

rank equal to the number of state variables during the analysis. This stochastic observability matrix contains information about the states from the beginning of the analysis because of the information matrix at epoch, $\mathbf{P}(t_0)^{-1}$. However, the angles-only measurements for this system do not contain any information on the AMR and C variables separately. Therefore, as the measurements are accumulated over time, the AMR and C information provided by the covariance of the initial state is diluted out of the observability matrix. After approximately 24 hours, the rank of the stochastic observability matrix with initial state and measurement uncertainties reduces from eight to seven, and the observability of the system can no longer be determined.

Next, the connection of the stochastic observability results and estimation is explored. Section 3.2 shows how the observability matrix with initial state and measurement uncertainties exists within the Information Form of the KF. In addition, this form of the stochastic observability matrix is known as the information matrix in the batch LS estimator with *a priori* information. Figure 3.15 shows the state estimation errors for the batch LS with *a priori* state information and the EKF. The LS state estimation errors are given in green and the EKF state estimation errors are given in red. Also, the 3σ bounds, defined by the square root of the state covariance matrix diagonal, for each estimator are shown in the same color as the state estimation errors.

Presentation of the state estimation errors in this manner for the LS estimator is atypical as the LS estimator determines a state estimate at epoch. The LS results are presented in this way to have a similar representation of the state estimation errors as the EKF results. As each measurement is added to the system, the state estimate and covariance are computed by inverting the information matrix in the LS solution. Then the estimated initial state and covariance are propagated to the time of the current measurement. Note that this representation of the system information at the time of the current measurement is equivalent to the stochastic observability matrix with initial state and measurement uncertainties with the exception that the LS information matrix implements the state estimate for evaluation of the STM and

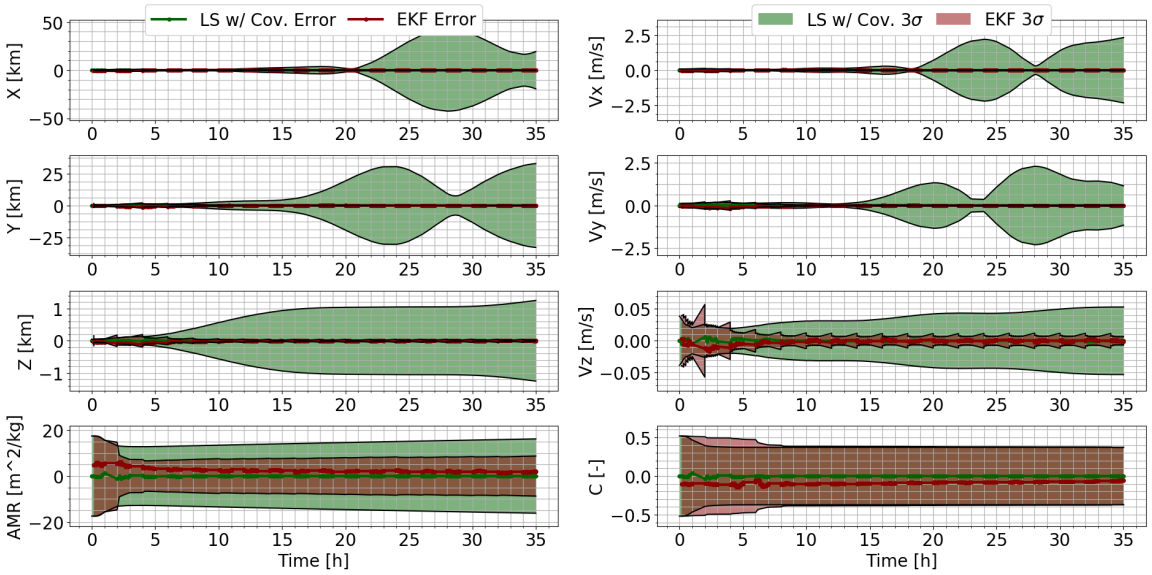

Figure 3.15. State estimation errors using the LS and EKF for the case with constant AMR and C.

measurement matrix whereas the stochastic observability matrix implements the true state.

When AMR and C are both constants, the 3σ bounds for the AMR and C state estimation errors in Figure 3.15 are large for both estimators. The state estimation errors are still within the 3σ bounds, but as discussed with the stochastic observability results of Figure 3.14, the measurements do not contain information about the AMR and C variables to determine them separately. As a result, the 3σ bounds for these constant, extended state variables do not decrease as more measurements are added to the system. There is a small decrease in the 3σ bounds for the AMR and C variables within the first few batches of measurements as the information from the covariance of the initial state has not yet been diluted. In addition, a bias is apparent in the AMR and C state estimation errors. This bias is due to the fact that the measurements only contain information on the combined AMR and C term in the SRP perturbation.

The LS results presented in Figure 3.15 contain *a priori* state information. However, LS estimation can be performed without *a priori* state information, but for this state of constant AMR and C, the LS estimator without *a priori* information does not converge and the estimate is inaccurate. This result agrees with the stochastic observability matrix with measurement uncertainties only. As the measurements are not sufficient for determining the states and no information is provided about the states though the information matrix, the observability of the system cannot be determined. Therefore, the performance of the LS estimator without *a priori* information is expected from the stochastic observability results without covariance of the initial state.

Time-Varying AMR and C

The next extended state case includes AMR and C which are both time-varying, and the time-varying models for both variables are given by Equations 2.52 and 2.53 with variables defined in Equation 3.49 through Equation 3.54. Figure 3.16 shows the deterministic and stochastic observability results for the time-varying AMR and C extended state.

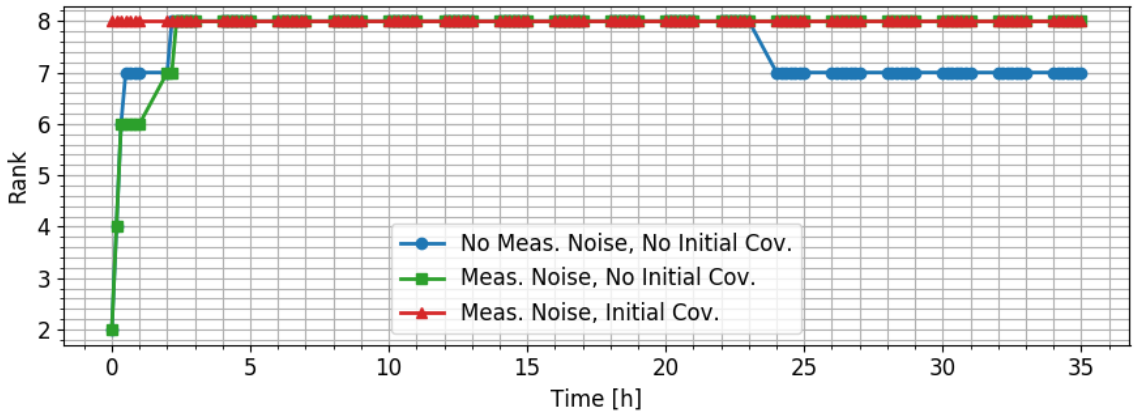

Figure 3.16. Rank of the deterministic and stochastic observability matrices for the case with time-varying AMR and C.

Similar to the previous observability results, the stochastic observability matrix with initial state and measurement uncertainties has a full rank from the first measurements in the analysis. The deterministic observability matrix and the stochastic observability matrix with measurement uncertainties only require approximately two batches of measurements to become observable for this system. As the AMR and C states are time-varying, the SRP perturbation is influenced by each of these variables in a different way. This change is apparent in the deterministic and stochastic observability results as there is sufficient knowledge of the states provided by the measurements for the system to become observable.

The two stochastic observability matrices are full rank for the duration of the analysis. Therefore, an estimator can be expected to perform well as the stochastic observability matrices show an observable system. However, the deterministic observability matrix becomes rank deficient after approximately 23 hours, indicating that in the absence of measurement noise, the observability of the system cannot be determined after some time. Earlier analysis of the impact of the measurement noise on observability in Section 3.4 demonstrated how the time to become observable varies with the covariance of the measurement noise in the observability matrix. For all cases analyzed in that section, the binary observability result, observable or not, was always observable, even though the time to become observable changed. However, in this system with a state extended by time-varying AMR and C, the measurement noise is responsible for the stochastic observability matrix maintaining full rank for the analysis time.

The influence of the measurement noise on this system is verified by Figures 3.17 and 3.18. Figure 3.17 shows deterministic and stochastic observability results with measurement noise on right ascension and declination which are equal, and Figure 3.18 shows deterministic and stochastic observability results with smaller right ascension measurement noise compared to the declination measurement noise. Note that this second case is the opposite of Figure 3.16 which has larger measurement noise on right ascension than declination.

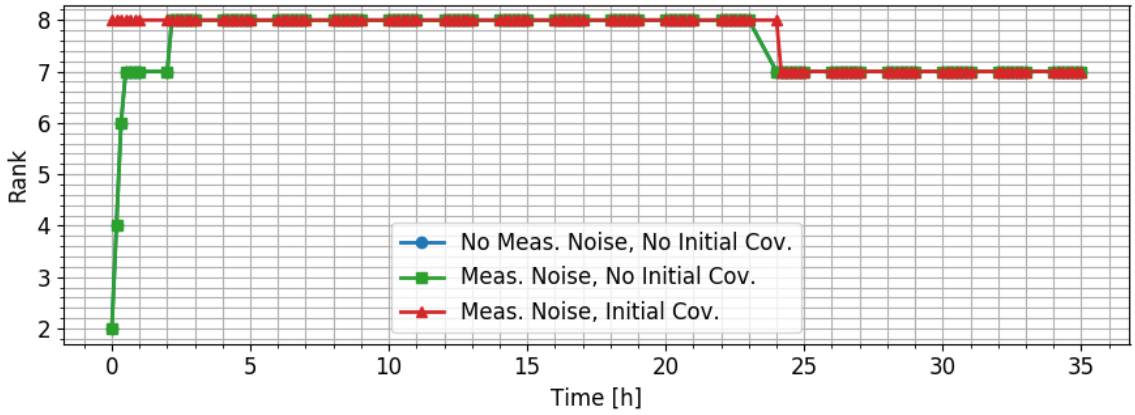

Figure 3.17. Rank of the deterministic and stochastic observability matrices for the case with time-varying AMR and C. Measurement noise on right ascension and declination are equal.

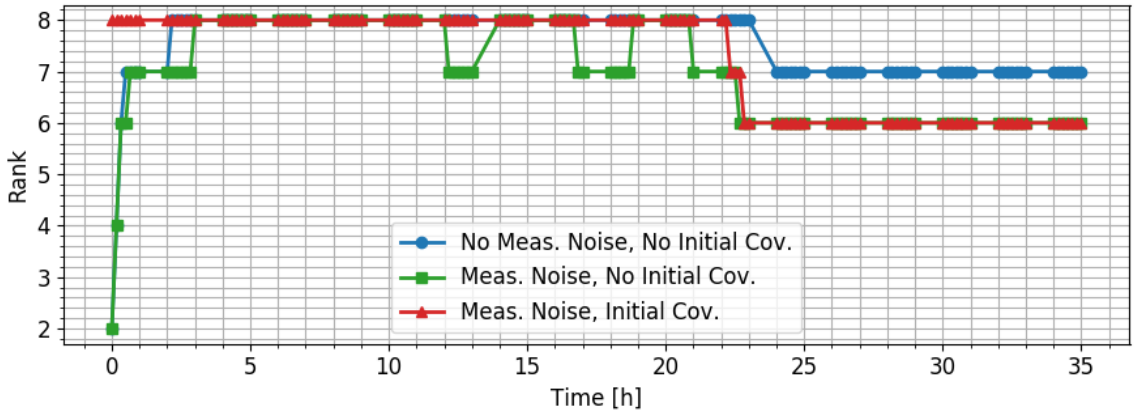

Figure 3.18. Rank of the deterministic and stochastic observability matrices for the case with time-varying AMR and C. Right ascension measurement noise is smaller than declination measurement noise.

When the right ascension measurement noise is equal to the declination measurement noise, the stochastic observability matrix with the covariance of the measurement noise is equal to the deterministic observability matrix scaled by a constant, as shown in Equation 3.38. Therefore, the deterministic observability matrix and the stochastic observability matrix with measurement uncertainties should have the same

matrix rank. Figure 3.17 confirms this behavior, where the rank of the deterministic observability matrix and the rank of the stochastic observability matrix with measurement uncertainties are identical. In addition, the stochastic observability matrix with state and measurement uncertainties becomes rank deficient for this system when the right ascension and declination measurement noise are equal.

When the right ascension measurement noise is smaller than the declination measurement noise, the system is expected to talk a longer time to become observable because for this GEO object, the declination measurements are important for determining the z-components of the state vector, as shown in Figure 3.2. The stochastic observability matrix with measurement uncertainties of Figure 3.18 does take longer than the deterministic observability matrix to achieve full rank. In addition, the detrimental effect of the larger declination measurement noise is evident in Figure 3.18 because both stochastic observability matrices eventually have a rank deficiency of two. These observability results of a state extended beyond position and velocity with time-varying AMR and C show the influence measurement noise can have on observability of a system.

Next, state estimation error results are presented for the time-varying AMR and C extended state case. Figure 3.19 shows the LS and EKF state estimation errors for the extended state case with time-varying AMR and C. Unlike previous estimation results where only the LS results with the initial state covariance was shown, this system is stochastically observable after some time, so the estimation results for the LS without initial state covariance are also shown. The LS state estimation errors without initial state covariance are given in blue, and the LS state estimation errors with initial state covariance are given in green. The EKF state estimation errors and 3σ bounds are given in red.

Initially, the LS estimation without initial state covariance has large state estimation errors and 3σ bounds, outside the limits of the plots in Figure 3.19. As information about the states is not included initially through the covariance of the initial state, the observability of the system cannot be determined. Therefore, the in-

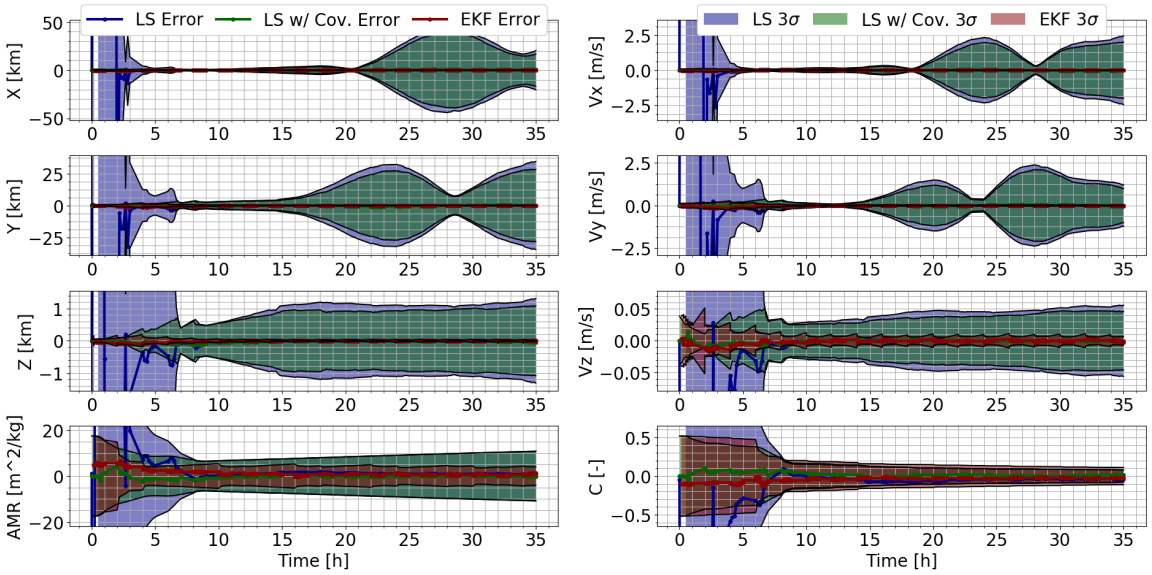

Figure 3.19. State estimation errors using the LS and EKF for the case with time-varying AMR and C.

formation matrix of the nonlinear batch LS is singular, which results in an inaccurate initial state estimate. However, as this system becomes stochastically observable, after several batches of measurements, the state estimation errors and 3σ bounds reduce to be similar to the LS estimation results with initial state covariance.

Comparing the 3σ bounds of Figure 3.19 to the 3σ bounds of the case with constant AMR and C in Figure 3.15, the 3σ bounds of the time-varying AMR and C system reduce over time or are smaller than the corresponding 3σ bounds of the other system. The EKF 3σ bounds for the AMR and C variables in Figure 3.19 continue to reduce throughout the analysis time. Whereas, the EKF 3σ bounds for the AMR and C variables in Figure 3.15 remain constant after the first few batches of measurements. In addition, the C 3σ bounds decrease over time for all of the estimators in Figure 3.19. Moreover, the bias in the AMR and C state estimation errors is removed in this analysis compared to the constant AMR and C estimation results. The impact of stochastic observability on estimation results is seen with a comparison of the time-

varying AMR and C extended state vector to the constant AMR and C extended state vector results.

Time-Varying AMR, Constant C

The final two cases in Table 3.3 contain one constant SRP parameter and one time-varying SRP parameter. The case of a position and velocity state vector extended with time-varying AMR and constant C is presented here. Figure 3.20 shows the rank of the deterministic and stochastic observability matrices over time.

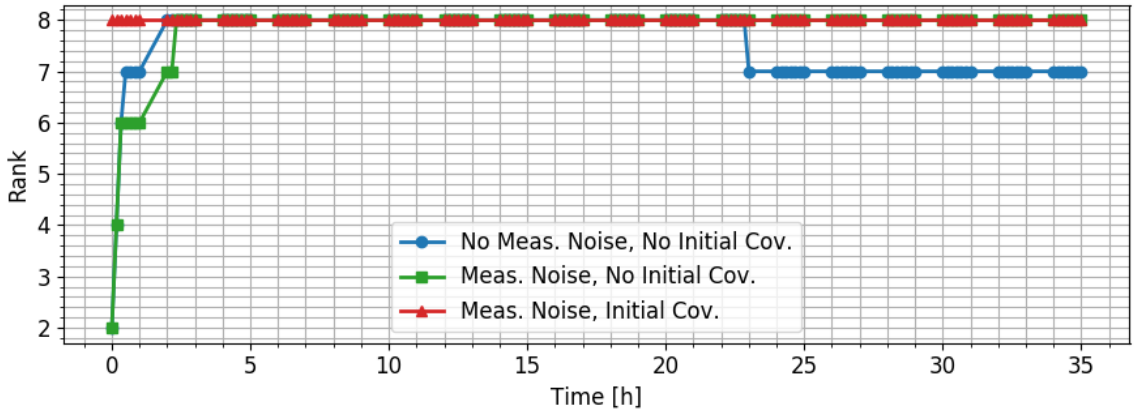

Figure 3.20. Rank of the deterministic and stochastic observability matrices for the case with time-varying AMR and constant C.

The observability results of Figure 3.20 are similar to the time-varying AMR and C case of Figure 3.16, where the stochastic observability matrix is full rank for the duration of the analysis and the deterministic observability matrix becomes rank deficient after approximately 23 hours. The differences between the stochastic and deterministic observability results for this system is explained in the same way as the time-varying AMR and C system, i.e. the measurement noise changes how the measurement information is distributed to the states of the system. As the stochastic observability results indicate an observable system, the estimation performance is expected to be accurate for this system.

Figure 3.21 shows the LS and EKF results for this system with time-varying AMR and C. The LS estimation is performed with and without covariance of the initial state. As expected because of the similar observability results to the time-

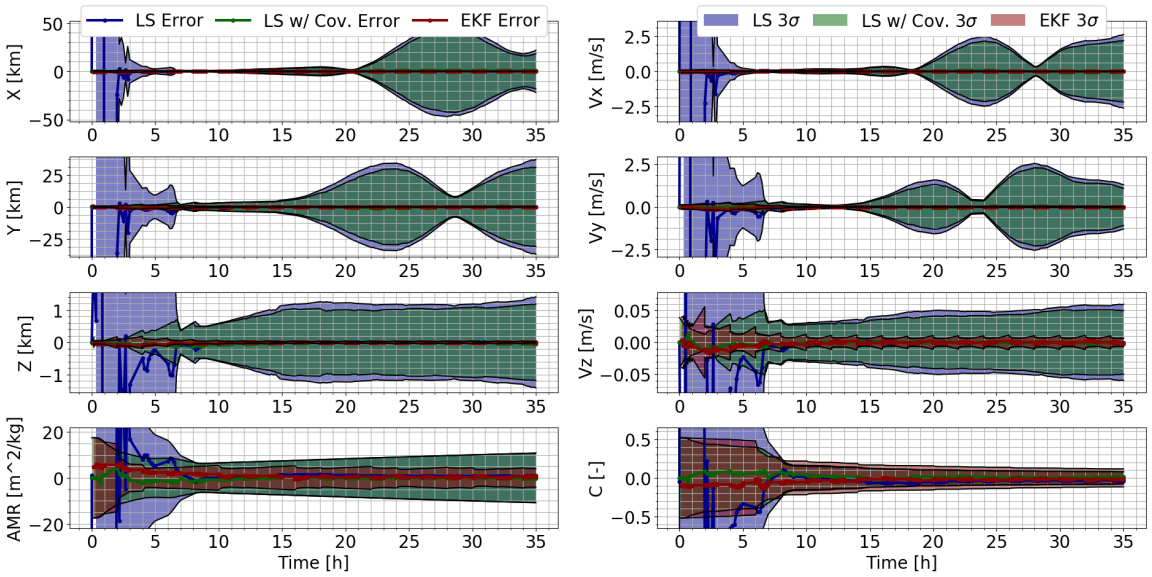

Figure 3.21. State estimation errors using the LS and EKF for the case with time-varying AMR and constant C.

varying AMR and C case, the estimation results of Figure 3.21 reflect the stochastic observability results for this system. The LS estimation errors without initial state covariance are large initially, but as the system becomes observable, the errors reduce to be similar to the LS estimation with initial state covariance. In addition, the 3σ bounds reduce for the C variable and the bias in the state estimation errors of AMR and C is not apparent.

Time-Varying C, Constant AMR

The final case combining time-varying and constant SRP parameters extends the position and velocity state vector with time-varying C and constant AMR. Figure 3.22 shows the deterministic and stochastic observability results for this case.

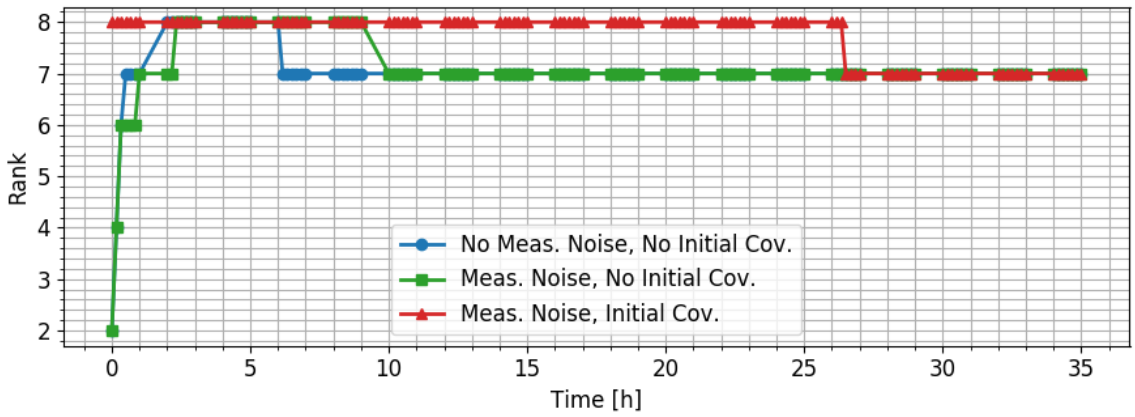

Figure 3.22. Rank of the deterministic and stochastic observability matrices for the case with time-varying C and constant AMR.

The observability of this system at the end of the analysis is similar to the observability of the system consisting of constant AMR and C. The deterministic observability matrix and the stochastic observability matrix with measurement uncertainties are full rank for a few batches of measurements before becoming rank deficient, and the stochastic observability matrix with state and measurement uncertainties is full rank for approximately 26 hours before becoming rank deficient. Note that the deterministic observability matrix and stochastic observability matrix with measurement uncertainties were always rank deficient for the constant AMR and C case.

Next, the LS and EKF estimation results are presented in Figure 3.23 for the case with time-varying C and constant AMR. Because the stochastic observability matrix for this system becomes rank deficient, the LS estimation is only performed with *a priori* information. Therefore, Figure 3.23 is comparable to Figure 3.15, where a bias is present in the state estimation errors, and the 3σ bounds for the AMR and C variables do not continue to decrease after the first few measurement batches.

The differences in the AMR and C cases with one time-varying parameter and one constant parameter are explained by the observability results of Section 3.6.1. Within the STM formulation, the partial derivatives of the dynamics with respect to

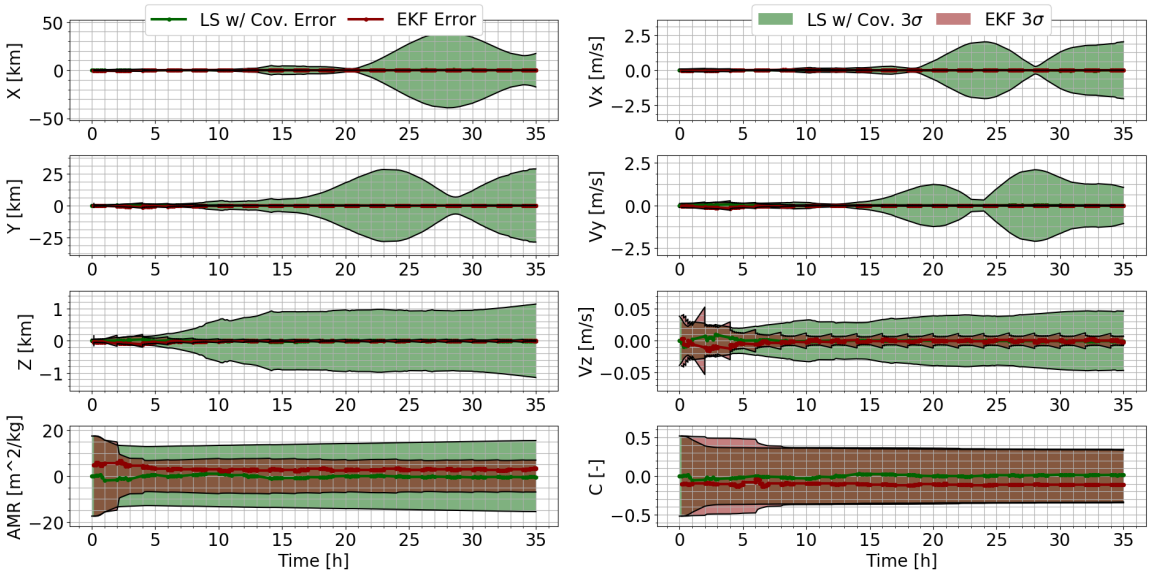

Figure 3.23. State estimation errors using the LS and EKF for the case with time-varying C and constant AMR.

C are many orders of magnitude smaller than the partial derivatives of the dynamics with respect to AMR. Moreover, Section 3.6 showed that observability of a state extended with constant AMR had a smaller time to become observable compared to observability of a state extended with constant C. Therefore, the behavior of the stochastic observability results with one constant SRP parameter and one time-varying SRP parameter are expected. When C is time-varying and AMR is constant, the impact on the STM, and thus the observability matrix, is minor because of the small partial derivative with respect to the C variable. Hence, this extended state case is similar to the case with constant AMR and C. However, the case with time-varying C and constant AMR does become stochastically observable for a short period because the time-varying nature of C does improve the impact of the C partial derivative on the observability. For a similar reason, the case with time-varying AMR and constant C is comparable to the time-varying AMR and C case as the influence of AMR on the system is more evident in the observability as a result of the partial derivative of the dynamics with respect to the AMR variable.

Summary

In this section, the connection of observability and estimation of two SRP parameters as separate, solve-for parameters was explored. The impact of state and measurement uncertainties on observability was evident in deterministic and stochastic observability results which differed. The covariance of the measurement noise redistributes the information from the measurements in the observability matrix. This change in the observability matrix can result in an observable system, even if the deterministic observability matrix is rank deficient. Also, the covariance of the initial state provides information on the state variables which may not necessarily exist within the measurements, as shown in the constant AMR and C extended state case. This analysis has shown that AMR and C can be estimated separately when modeled as time-varying parameters in a state vector extended beyond position and velocity. However, if AMR and C are defined as constants, this analysis and the results of Section 3.6.2 show that estimating a single object characteristic or the combined AMR$\cdot C$ parameter within the SRP perturbation is advantageous for improved estimation performance.

Based on the definition of observability from Kalman, when a system is stochastically observable, accurate estimates can be expected as the measurements contain sufficient information about the states. However, when the stochastic observability matrix is rank deficient, the expected accuracy of estimation results is not clearly defined. In the case of constant AMR and C, the state estimation errors remained within the 3σ bounds, which could be considered a positive estimation result, but a bias existed for the AMR and C variables and the 3σ bounds did not improve with more measurements.

3.7 Observability as a Predictor of Estimation Performance

From Kalman's original definitions, the optimal regulator problem is guaranteed to have a solution for an observable problem. Conversely, this would indicate that

the optimal regulator problem is not guaranteed to have a solution for an unobservable system. As Section 3.6 has shown, determining observability numerically can result in cases where the observability cannot be determined because of numerical error estimates with the tolerance line. As the Kalman Filter and other estimators have become widely used for a variety of applications, estimation is often applied without much consideration of the system observability. Moreover, whether or not a system has been tested for observability, estimation is applied. Unless the estimation fails to converge, an estimation solution, which is likely to appear reasonable, will be produced. However, for the systems presented in the following simulations, this analysis seeks to show that observability should always be considered before performing estimation because an accurate estimation result is not guaranteed for these systems if the observability cannot be determined. Furthermore, the cases presented here demonstrate how an estimation result may appear accurate when evaluating measurement estimation errors, even in the presence of some poorly estimated states.

In order to validate the definition that accurate estimates are not guaranteed for systems which are not observable, a Monte Carlo (MC) analysis is performed with the estimation of two systems, one observable and one where the observability cannot be determined numerically. The observable system consists of a state composed of Cartesian position and velocity components. From previous analysis of the extended state with SRP parameters and knowledge of the system dynamics, when AMR and C are both constant, separate solve-for parameters, the observability cannot be determined numerically with angles-only measurements. The SRP variables cannot be determined separately within the SRP perturbation because the measurements do not help differentiate them and the terms are multiplied in the SRP perturbation. The covariance of the initial state is sampled 10,000 times for each system. The mean and standard deviation, σ used for generating the 10,000 samples are shown in Table 3.5. The mean state in Table 3.5 represents the truth in this analysis. Therefore, the MC analysis implemented in this work samples the state uncertainties only, and there is only one true state compared to the sampled initial state estimates. The

MC sampling for the observable system utilizes the position and velocity uncertainties only. Seven measurement batches with four hours between each batch and each batch consisting of 60 right ascension and declination angle measurements spaced by 20 seconds are implemented for this analysis. The object defined by the mean state in Table 3.5 is the GEO 4 object of Table 3.2.

Table 3.5. Initial State Mean and Standard Deviation.

State	Mean	Standard Deviation
x [km]	-38817.694	0.1
y [km]	-16450.667	0.1
z [km]	37.283	0.1
v_x [km/s]	1.200	0.001
v_y [km/s]	-2.831	0.001
v_z [km/s]	4.939×10^{-4}	0.001
AMR [km^2/kg]	1.0×10^{-5}	5.0×10^{-6}
C [-]	0.3056	0.5

Except otherwise noted, the following results do not include process noise in the EKF. The process noise in the KF is an additive white noise on the state dynamics, but it is often used to compensate for differences between the true dynamics and the modeled dynamics [49]. The true dynamics of these simulations are known exactly. Therefore, the modeled dynamics reflect the true dynamics of the simulated system, and thus, process noise is not required for matching the modeled and true state dynamics. For some of the MC analysis results, additional results are included which have implemented process noise in the MC analysis for comparison to the analysis without process noise.

The observability results for each system are given in Section 3.6, specifically Figure 3.5 for the system with a state consisting of position and velocity and Figure

3.9 for the system with a state extended by two constant SRP parameters. The singular values of the observability matrix are used to show the observability of each system.

In order to evaluate and summarize the MC analysis, several measures are implemented. First, root mean square error (RMSE), given by Equation 3.55, is often used for summarizing the MC performance. However, as Li & Zhao [154] show, RMSE is considered a pessimistic measure of error because large error values tend to dominate the RMSE. If a large number of MC iterations all have low error values, but a few MC iterations have high error values, the RMSE would be large. In addition, Li & Zhao address how the RMSE does not have a physical interpretation when states contain different units.

$$\text{RMSE}(\tilde{\mathbf{x}}) = \sqrt{\frac{1}{M}\sum_{i=1}^{M} ||\tilde{\mathbf{x}}_i||^2}, \tag{3.55}$$

where,

$$||\tilde{\mathbf{x}}_i|| = (\tilde{\mathbf{x}}_i^T \ \tilde{\mathbf{x}}_i)^{\frac{1}{2}}. \tag{3.56}$$

In Equation 3.55, $\tilde{\mathbf{x}}_i = \mathbf{x} - \hat{\mathbf{x}}_i$ is the state estimation error, M is the total number of MC samples, and i is the index for each MC sample. Because the RMSE has potential shortcomings, specifically for systems with states with largely different scales or units, as in the case with a state extended by AMR and C, another measure was defined for summarizing the MC performance. A challenge of this system is the large order of magnitude difference between the position states and the AMR state. The position and velocity of this system could be non-dimensionalized with a characteristic distance and velocity, but a characteristic value does not exist for AMR or C. Therefore, large errors in AMR may not appear in RMSE measures because the overall impact on the position is small. If a goal of the estimation is to determine characteristic parameters such as AMR, RMSE may not be a suitable measure of estimation accuracy when such a large order of magnitude difference exists in the states.

Since the RMSE combines the estimation errors of the different state variables together in a single measure, which could lead to challenges with dimensions, another

measure, called root mean square error per state, was implemented. The RMSE per state keeps the estimation errors separate for each state variable. The measure is similar to RMSE, but there is a different error measure for each state. The form of the measure is given by Equation 3.57.

$$\text{RMSE per state } = \sqrt{\frac{1}{M}\sum_{i=1}^{M}\tilde{\mathbf{x}}_i^2}. \tag{3.57}$$

Note that with this measure, systems may not be as directly comparable for systems with different state variables. Since the average estimation errors for the MC analysis are kept separate, unlike RMSE, the RMSE per state measure is not susceptible to large order of magnitude differences among state variables. If one of the SRP parameters is poorly estimated but the positions are estimated well, then the RMSE per state will reflect this difference and not hide the potential SRP errors in an overall measure.

The next method for summarizing the MC analysis uses the 1σ and 3σ state estimation error bounds. For a one dimensional normal distribution, there is a probability of 0.6827 that a sample is within 1σ of the mean and a probability of 0.997 that a sample is within 3σ of the mean. This is often referred to as the 68-95-99.7 rule, representing the probabilities a sample is within 1σ, 2σ, and 3σ of the mean. When the dimension of the problem increases, the probabilities of a sample being within 1σ and 3σ of the mean change. For higher dimensions, the Mahalanobis distance is used to compute the probabilities [155]. The system in this work has dimensions of six to eight depending on whether the SRP parameters are included in the state with the position and velocity. The percentages for 1σ, 2σ, and 3σ for a range of dimensions are given in Figure 3.24.

The 1σ percentages are given by the blue curve, the 2σ percentages are given by the red curve, and the 3σ percentages are given by the yellow curve. With six dimensions, the 1σ probability is 0.1438 and the 3σ probability is 0.8264. These values are significantly different from the one dimensional probabilities.

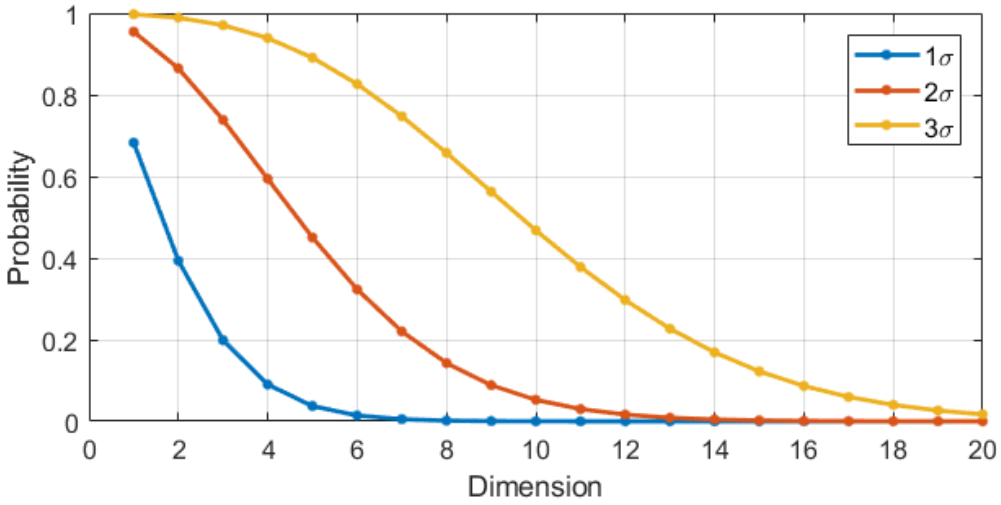

Figure 3.24. 1σ, 2σ, and 3σ probabilities per dimension.

For the EKF, the 1σ and 3σ bounds for the state estimation errors are based on the diagonal of the *a posteriori* state covariance. Therefore, defining the σ bounds in this way assumes uncorrelated states, and the 68-95-99.7 rule applies to each of the states. Given that the initial state covariance is sufficiently sampled for the MC analysis, the samples for each state should abide by the 68-95-99.7 rule. This method of summarizing the MC analysis hypothesizes that an observable system will maintain these percentages for the MC samples throughout the analysis time, but an unobservable system will not due to poor estimation performance. For each MC iteration and time step, the state and measurement estimation error σ bounds in the EKF are calculated from Equations 3.58 and 3.59, respectively.

$$\sigma_{\text{state}} = \sqrt{\text{diag}(P_k^+)}, \tag{3.58}$$

$$\sigma_{\text{meas}} = \sqrt{\text{diag}(W_k)}, \tag{3.59}$$

where,

$$\mathbf{W}_k = \mathbf{H}(\hat{\mathbf{x}}_k^-)\ \mathbf{P}_k^-\ \mathbf{H}(\hat{\mathbf{x}}_k^-)^T + \mathbf{L}_k\ \mathbf{R}_k\ \mathbf{L}_k^T, \tag{3.60}$$

$$\mathbf{C}_k = \mathbf{P}_k^-\ \mathbf{H}(\hat{\mathbf{x}}_k^-)^T, \tag{3.61}$$

$$\mathbf{K}_k = \mathbf{C}_k\ \mathbf{W}_k^{-1}, \tag{3.62}$$

$$\mathbf{P}_k^+ = \mathbf{P}_k^- - \mathbf{C}_k\ \mathbf{K}_k^T - \mathbf{K}_k\ \mathbf{C}_k^T + \mathbf{K}_k\ \mathbf{W}_k\ \mathbf{K}_k^T. \tag{3.63}$$

The EKF matrices defined in Equation 3.58 through Equation 3.59 have been introduced in Section 2.5.2. The σ bounds change for each MC iteration as $\mathbf{W_k}$ and $\mathbf{P_k^+}$ are functions of the estimated state, $\hat{\mathbf{x}}$, at time t_k. Therefore, each MC iteration will compare the state and measurement estimation errors to a different σ value per time step. The method for visualizing the 68-95-99.7 rule for this analysis determines the number of MC samples which are contained within the different σ bounds for each time step. Then, percentages are computed per time step to determine whether the 68-95-99.7 rule is maintained throughout the analysis time.

The previously introduced measures for the MC analysis intuitively follow from the estimation errors and the σ bounds of the estimation errors. Another method for analyzing the MC results is implemented in this work. This additional method may not be as intuitive as the other methods, but it is concise. The final method implemented for analyzing the MC results uses a ratio to depict when the filter is conservative or over-confident [156, 157]. Note that the term smug is sometimes used in the place of over-confident. When a filter is conservative, the state estimation errors may reduce slowly, but the σ bounds of the estimation errors will not condense too rapidly for the measurements to provide sufficient information for estimating the state. When a filter is over-confident, the information supplied by the measurements is not consistent with how well the filter thinks the state is being estimated. Ideally, a filter will be neither conservative nor smug, but because a filter is stochastic in nature, this will not be the case. In general, a conservative filter is advantageous because the confidence in the state uncertainty will not lead to ill-informed decisions based on the estimated state.

This measure for determining whether a filter is conservative or smug will be referred to as the average filter ratio in this work. The average filter ratio is defined by the average of the 1σ bounds in the MC divided by the standard deviation of the distribution of the state estimation errors in the MC. The numerator in the average filter ratio is average confidence bound over the MC iterations, and the denominator measures how the state estimation errors are distributed. When the average filter ratio is greater than one, the filter is conservative, and when the average filter is less than one, the filter is smug. A more detailed explanation is provided for each of the MC implementations that follow.

3.7.1 Observable System

Figure 3.25 through Figure 3.35 show the MC estimation results for the observable orbit problem with a state vector consisting of position and velocity. The singular values of the observability matrix for this system are shown in Figure 3.5. All of the singular values progress above the tolerance line, indicating an observable system. EKF estimation was performed 10,000 times using samples from the mean and the initial state covariance given in Table 3.5. As this system is observable, the estimation results are all expected to produce accurate state estimates.

The RMSE over time for the 10,000 MC iterations is shown in Figure 3.25. Between each measurement batch the RMSE grows as there are no measurements to improve the confidence in the state estimate. After the third batch of measurements, the RMSE does not change as significantly with each new batch of measurements.

As dimensional differences exist between the states in this system, the RMSE per state is computed to determine the RMSE per state in the MC iterations for each state. The RMSE per state over time is shown in Figure 3.26. In this case, the RMSEs per state all reduce with time, but if a velocity state was poorly estimated, the RMSE measure may not identify this issue because of the relative order of magnitude differences between the position and velocity states. This potential challenge of using

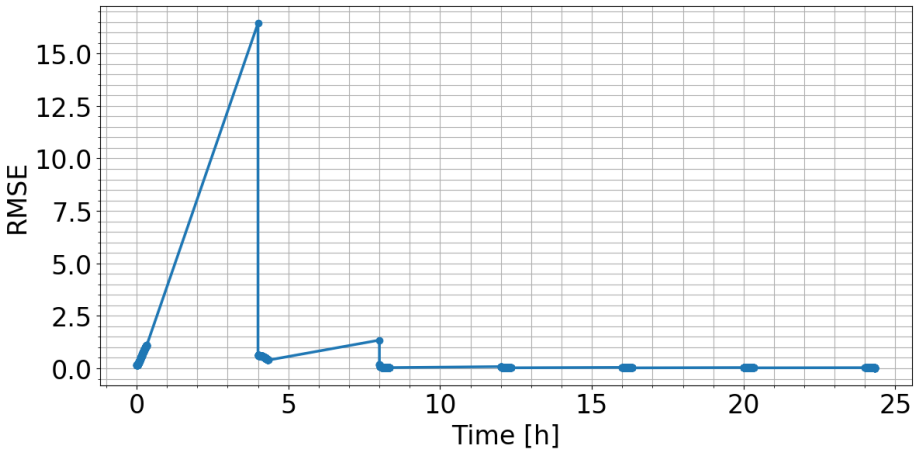

Figure 3.25. Estimated state RMSE for the observable system.

RMSE as a measure for the MC analysis will become more apparent for the system with a state extended with AMR and C.

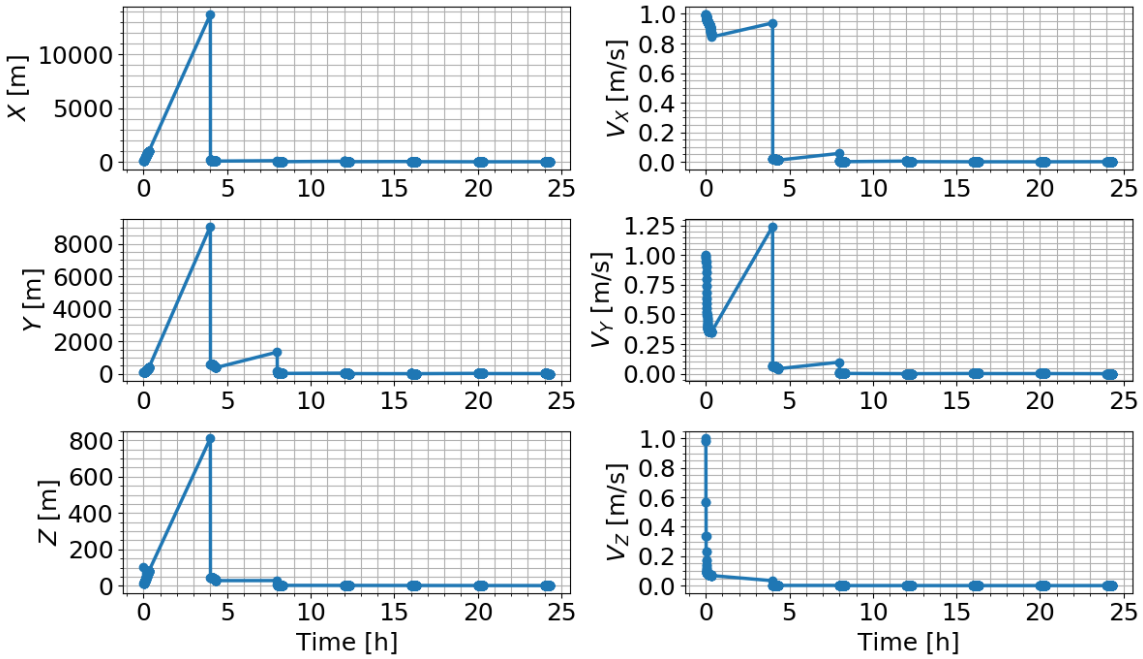

Figure 3.26. RMSE per state for the observable system.

Next, the state estimation errors for all of the MC iterations are shown in Figure 3.27. All of the colored lines represent the state estimation errors for each of the 10,000 MC iterations. The 1σ and 3σ bounds are defined by the black dashed lines. Note that there are 1σ and 3σ bounds for each MC iteration, but the curves are nearly identical, resulting in the appearance of only one line for the 1σ and 3σ bounds. Different σ bounds are defined for each MC iteration because the state and measurement σ bounds, defined in Equation 3.58 through 3.63, are functions of the estimated state.

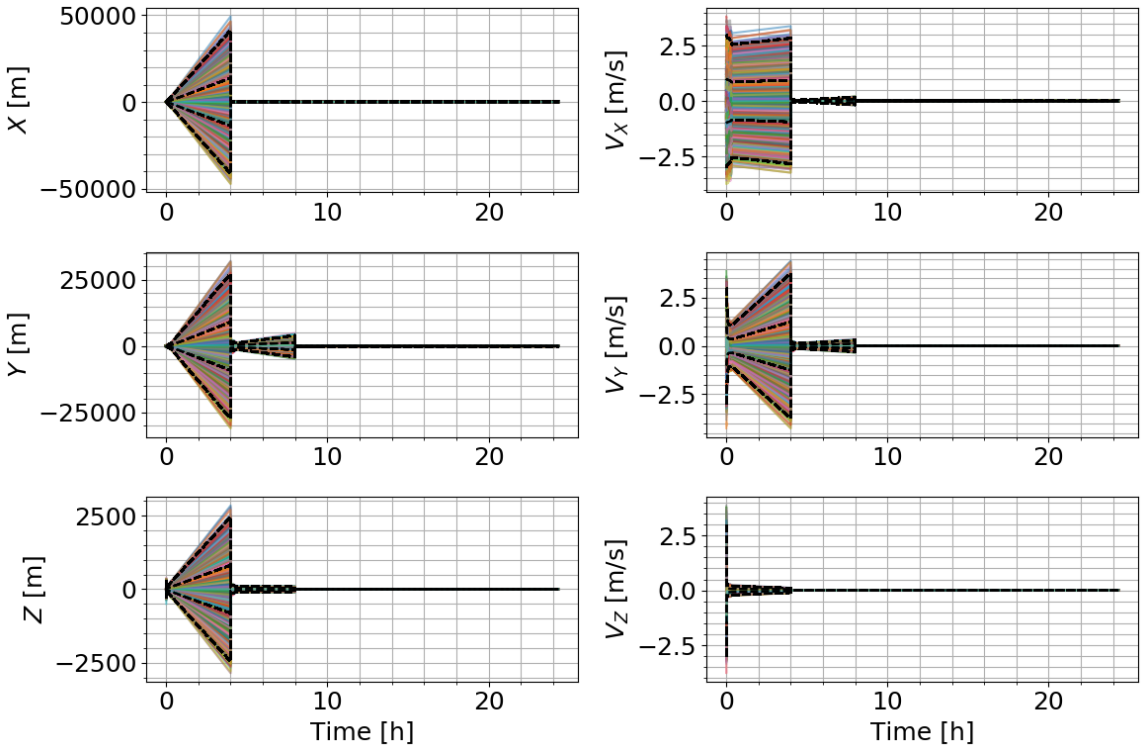

Figure 3.27. State estimation errors for the observable system. All MC runs shown in different colors.

From visual inspection, a few of the MC runs can be seen outside of the 3σ bounds. From the 68-95-99.7 rule this is expected for 10,000 sample points. Throughout the analysis time, only a few of the estimation error curves appear outside of the 3σ bounds.

As the σ bounds vary for each MC iteration, this representation of the state estimation errors may not be indicative of the overall MC results. To more accurately summarize the state estimation error performance for the 10,000 MC points, the percentage of state estimation errors at each time step which are less than or equal to the 1σ and 3σ bounds are shown in Figure 3.28. Two curves, one for each σ bound, are presented for each state. Since the σ bounds are defined by assuming the *a posteriori* covariance is uncorrelated, the percentages for each state are expected to follow the 68-95-99.7 rule.

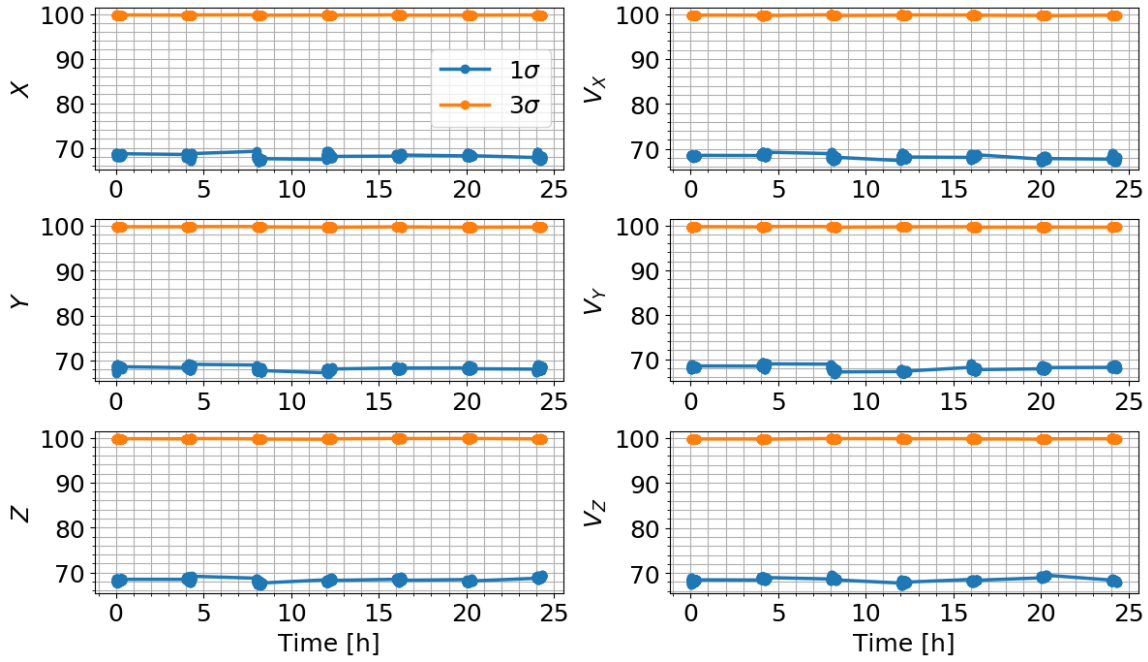

Figure 3.28. Percentage of MC runs within the state estimation error σ bounds for the observable system.

Table 3.6 shows the average percentages over the analysis time for each state and σ bound. For this observable system, the average percentages of MC sample points per state are consistent with the 68-95-99.7 rule. The exact percentages for the 1σ and 3σ bounds are 68.270% and 99.730%, respectively. Performing the same analysis

with a larger number of MC sample points is expected to produce percentages which are closer to the exact values for a normal distribution.

Table 3.6. Percentage of state estimation errors less than or equal to the σ bounds averaged over time for the observable system.

	x	y	z	v_x	v_y	v_z
1σ %	68.106	68.344	67.977	68.199	68.226	68.488
3σ %	99.721	99.747	99.721	99.710	99.720	99.750

For comparison, the same MC analysis is performed with process noise in the EKF. Process noise is white noise on the dynamics of the state in the Kalman Filter, as shown by Equation 2.66, but it is often included or tuned to account for unmodeled dynamics in a system. For this simulated system, the modeled dynamics reflect the true dynamics. Although process noise is not required for this simulated system, it is included to evaluate the impact on the MC estimation results. Figure 3.29 and Table 3.7 show the analogous results to Figure 3.28 and Table 3.6, but with process noise included in the estimation. For this observable system, the addition of process noise does not change the average percentages of MC iterations which are less than the 1σ and 3σ bounds for each state variable.

Table 3.7. Percentage of state estimation errors less than or equal to the σ bounds averaged over time for the observable system with process noise.

	x	y	z	v_x	v_y	v_z
1σ %	68.106	68.344	67.977	68.199	68.226	68.488
3σ %	99.721	99.747	99.721	99.710	99.720	99.750

Next, the average filter ratio is calculated for the observable system. Figure 3.30 depicts the average filter ratio for the MC analysis of the observable system. The

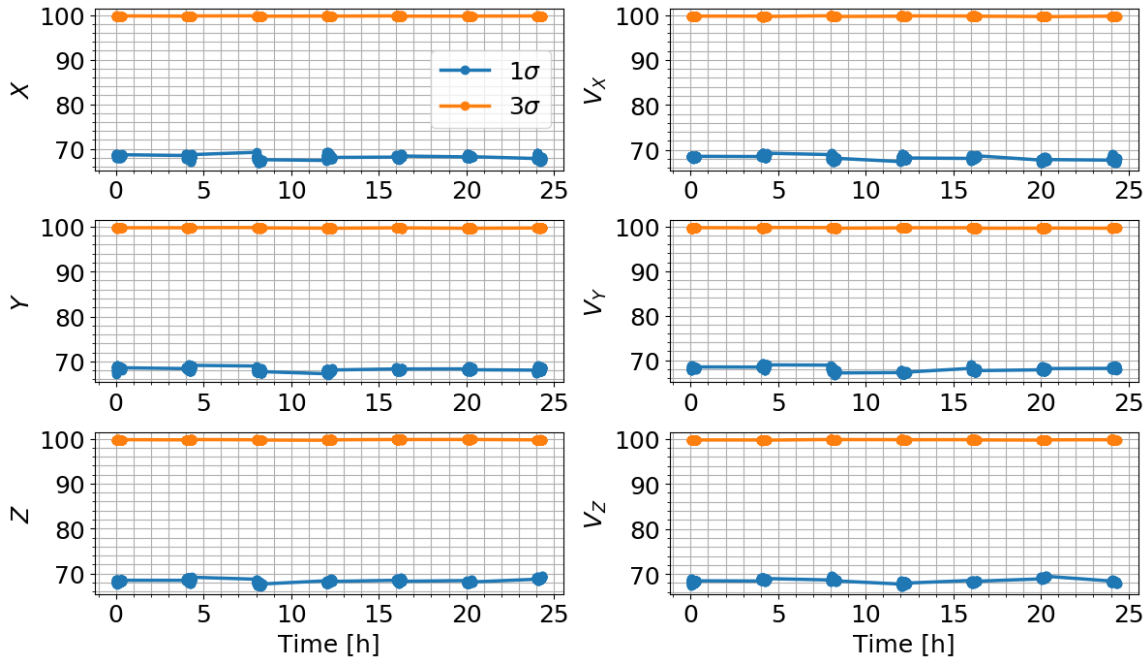

Figure 3.29. Percentage of MC runs within the state estimation error σ bounds for the observable system with process noise.

average filter ratio is split between position and velocity. The position and velocity average filter ratios are defined by first computing the average for the square root of the trace of the state estimation error covariance matrix. The trace of the state estimation error covariance matrix represents the sum of the variances for each of the state variables. Therefore, the average filter ratio is separated into position and velocity by limiting the trace to the respective position and velocity components. The denominator of the average filter ratio is calculated with the covariance of the position and velocity state estimation errors. The square root of the trace of the covariance matrix at each time step completes the components of the average filter ratio.

In Figure 3.30, the average filter ratio for position and velocity is given by the black line. The green region, where the ratio is greater than one, indicates that a filter is conservative. The red region, where the ratio is less than one, indicates that a filter is smug. Because the EKF is a sequential filter, the average filter ratio can move

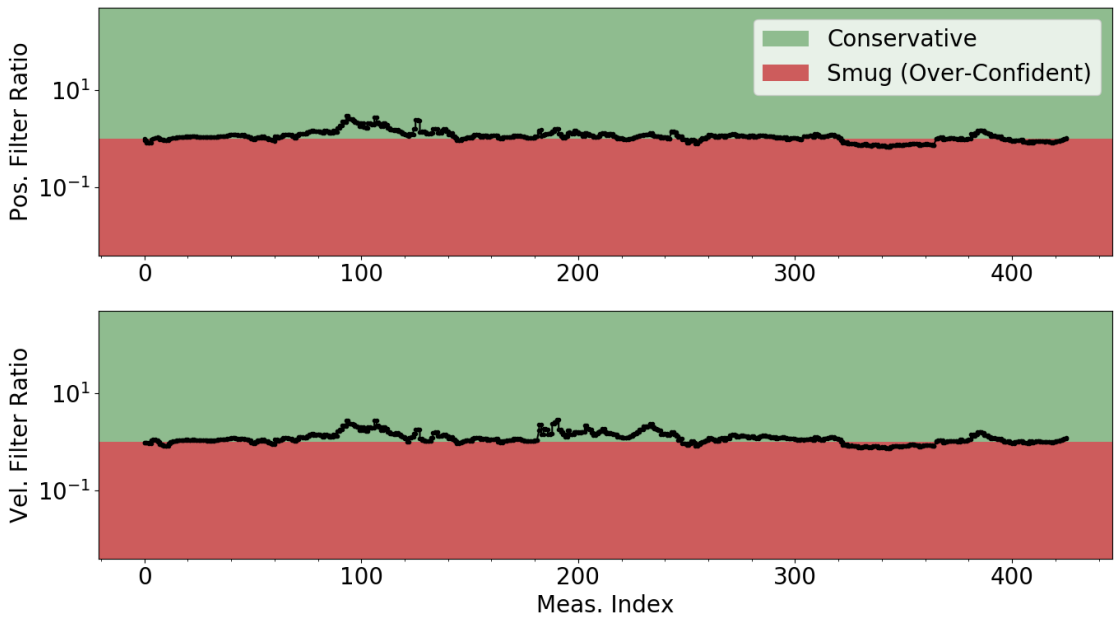

Figure 3.30. Position and velocity average filter ratios for the observable system.

between the conservative and smug regions as the time progresses and measurements are processed. For this observable system, the average filter ratio is nearly one. Note that the y-axis scale of these results is set to reflect the y-axis scale of the unobservable system for comparison. The filter for the observable system is often more conservative than smug. Next, the average filter ratio with process noise is shown in Figure 3.31.

Similar to the percentage plots of the observable system, the average filter ratio is not significantly different when process noise is included. Moreover, the differences between the average filter ratio with and without process noise are on the order of the process noise. The average filter ratio with and without process noise in the EKF indicates that the filter is performing well in terms of conservativeness and smugness. Next, the MC analysis measurement estimation errors are analyzed.

When estimating a state vector with real measurements from an optical telescope, and not simulating the measurements from the truth, some of the performance measures and plots presented thus far cannot be determined because knowledge of the true state is not known. As a result, measurement estimation errors, defined by the

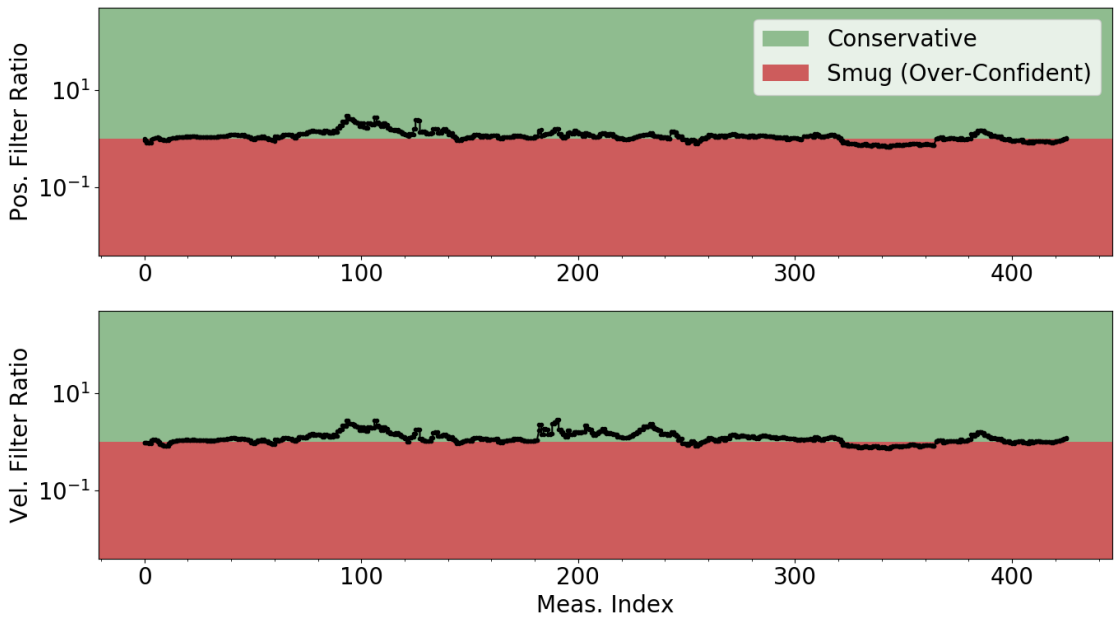

Figure 3.31. Position and velocity average filter ratios for the observable system with process noise.

difference between the acquired measurements and measurements evaluated with the *a priori* estimated state, are implemented for evaluation of estimation performance. Although these simulation use the true state for estimation performance evaluation, the MC analysis is also summarized with the measurement estimation errors to depict estimation evaluation methods which are common when a true state is not known.

The RMSE and the RMSE per measurement in the measurement space are given by Figures 3.32 and 3.33. These measures are computed in a similar way as the state estimation errors, i.e. the difference in the true measurement and the estimated measurement is used in Equations 3.55 and 3.57 instead of the state estimation errors. In this simulation, the true measurements are defined with the nonlinear measurement model evaluated at the true state with added noise sampled from the covariance of the measurement noise. The estimated measurement is computed with the nonlinear measurement model evaluated at the state estimate.

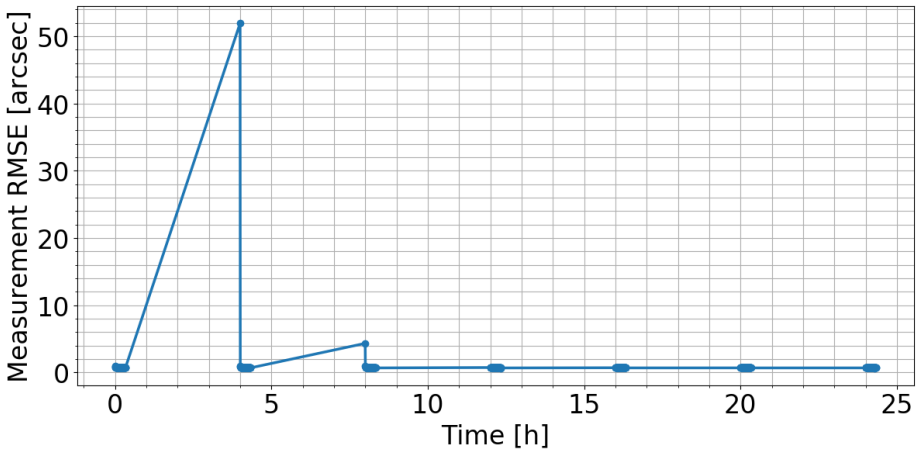

Figure 3.32. Estimated measurement RMSE for the observable system.

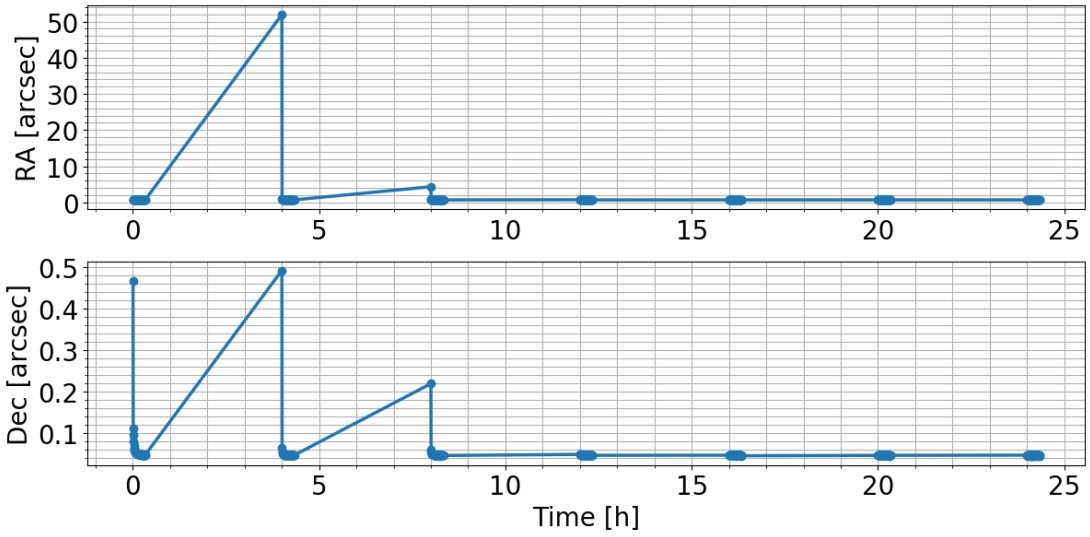

Figure 3.33. RMSE per measurement for the observable system.

Similar to the state estimation RMSE, the measurement estimation RMSE and RMSE per measurement decrease over the analysis time, and between measurement batches the errors increase. As the measurements both have units of arcseconds, the RMSE and RMSE per measurement both have units of arcseconds. For the RMSE per measurement in Figure 3.33, there is a large difference in the RMSE per measurement when comparing right ascension and declination. The covariance of

the measurement noise for this system has an almost order of magnitude difference between the right ascension and declination noise, with the right ascension noise being larger. Although the noise on the right ascension measurement is larger than the noise on the declination measurement, the ratio of the measurement noise variances has a small impact on the time to become observable for this GEO 4 object when the measurement noise on right ascension is larger than declination, as shown in Figure 3.2.

Next, the measurement estimation errors are shown in Figure 3.34. Similar to the state estimation errors, there is little variation in the measurement σ bounds and most of the curves from each MC iteration are contained within the σ bounds.

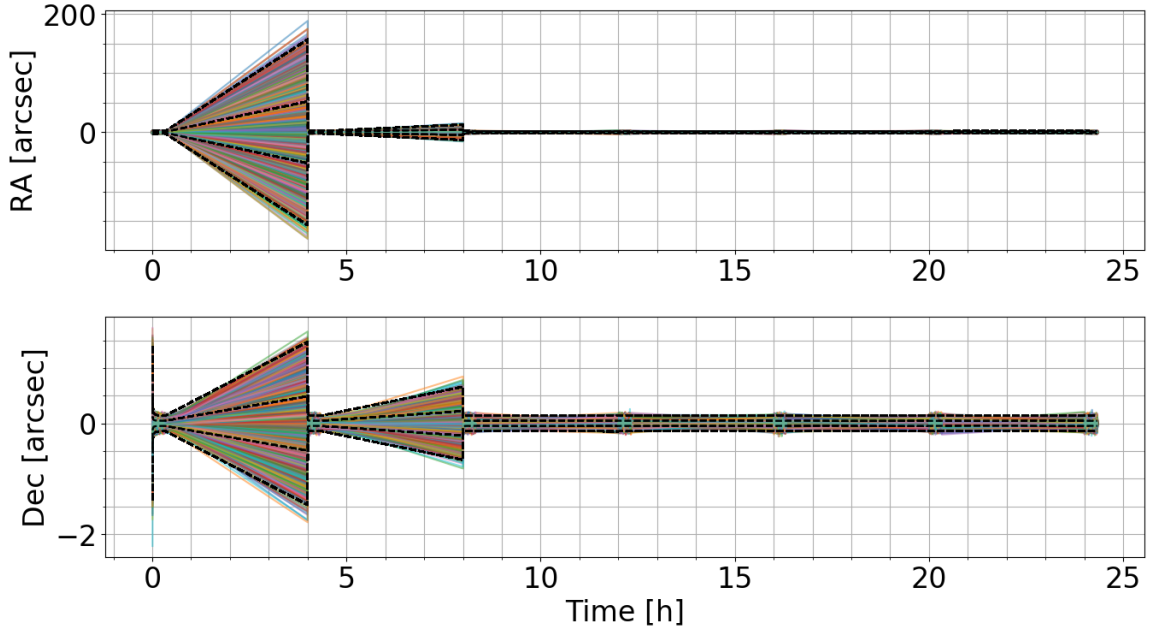

Figure 3.34. Measurement estimation errors for the observable system. All MC runs show in different colors.

As the σ bounds do change with each MC iteration, the measurement estimation errors of Figure 3.34 are summarized in Figure 3.35. For each MC iteration, the mapped estimation errors are compared to the corresponding σ bounds and the percentage of state estimation errors which are within their respective σ bounds are

shown. This analysis is performed at each time step. Once again, the estimation errors in the measurement space show a similar result for the MC analysis of the observable system. The 68-95-99.7 rule also applies for the measurement estimation error percentage plots as the assumption of uncorrelated measurements is also made to define the 1σ and 3σ measurement bounds. Table 3.8 summarizes Figure 3.35, averaging over time.

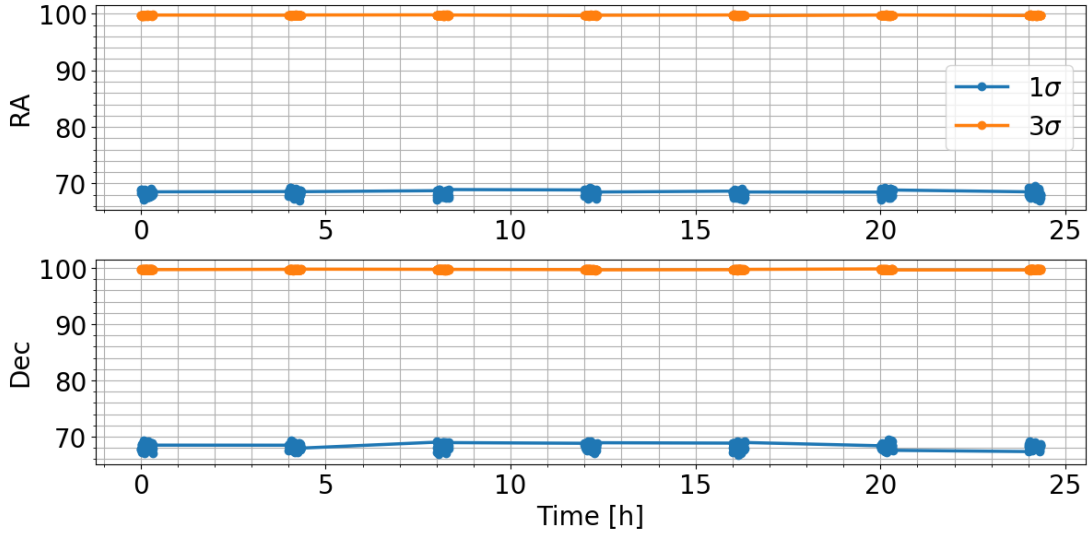

Figure 3.35. Percentage of MC runs within the measurement estimation error σ bounds for the observable system.

Table 3.8. Percentage of measurement estimation errors less than or equal to the σ bounds averaged over time for the observable system.

	Right Ascension	Declination
1σ %	68.238	68.242
3σ %	99.731	99.733

This analysis of the percentage of MC iterations which are within the measurement σ bounds is also conducted with EKF results which include process noise. Figure

3.36 and Table 3.9 show that the addition of process noise in the estimation of the observable system does not impact the percentage of MC iterations which are within the measurement σ bounds.

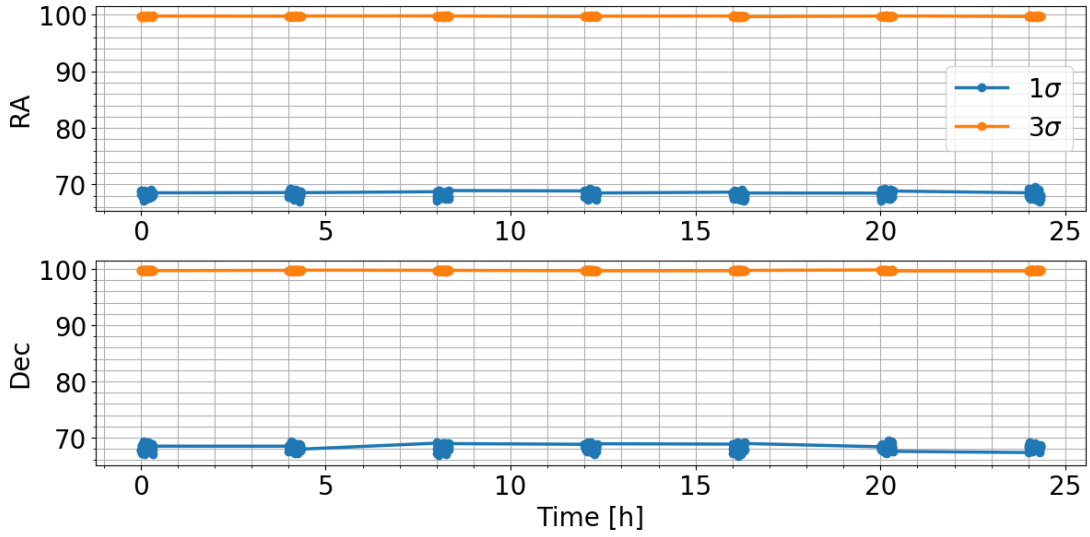

Figure 3.36. Percentage of MC runs within the measurement estimation error σ bounds for the observable system with process noise.

Table 3.9. Percentage of measurement estimation errors less than or equal to the σ bounds averaged over time for the observable system with process noise.

	Right Ascension	Declination
1σ %	68.238	68.242
3σ %	99.731	99.733

Similar conclusions can be drawn from the estimation error analysis in the state space and in the measurement space for the observable system. The preceding analysis showed a statistically significant percentage of the MC iterations accurately estimated the state consisting of position and velocity.

3.7.2 Unobservable System

The same analysis is performed for a system with a state extended beyond position and velocity with AMR and C. The singular values of the observability matrix are shown in Figure 3.9. Recall that the observability of this system cannot be determined numerically as all of the singular values do not progress above the tolerance line. The tolerance line is an approximation of the numerical error in the problem. However, due to the nature of the coupling of constant AMR and C in the SRP perturbation, this system is unobservable because the differences between the AMR and C variables can not be differentiated with optical angles measurements alone.

The initial state covariance in Table 3.5 for this system is sampled 10,000 times for the MC analysis with the EKF. The two metrics, RMSE and RMSE per state, for summarizing the MC analysis are shown in Figures 3.37 and 3.38. Similar to the observable system, the state estimation RMSE curve shows a general decrease in the error for each batch of measurements and an increase in error between measurements. There is an increase in the error for the last batch of measurements. As the following results will demonstrate, the estimation of the AMR and C variables is not accurate for many of the MC iterations. However, the RMSE is only indicative of a poor estimate in the last batch of measurements when the RMSE increases slightly.

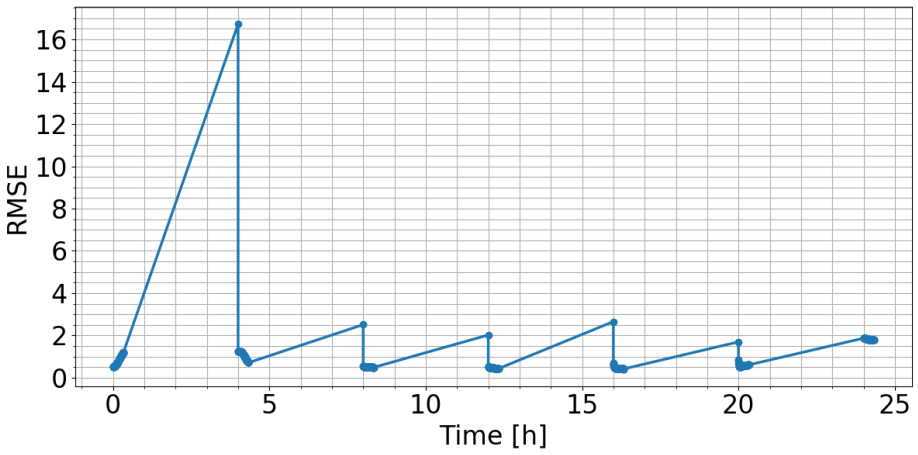

Figure 3.37. Estimated state RMSE for the unobservable system.

Figure 3.38 shows on average for the MC analysis which states are estimated more accurately and which are not. After approximately eight hours in the analysis, the AMR and C states exhibit a large increase in the RMSE per state. In addition, near the end of the analysis time, the x position and velocity have an increase in the RMSE per state. A potential shortcoming of the RMSE and RMSE per state measures is that an average is computed over all of the MC iterations. Therefore, there is no indication of how poorly the states are estimated based on the statistically significant sampling of the initial covariance.

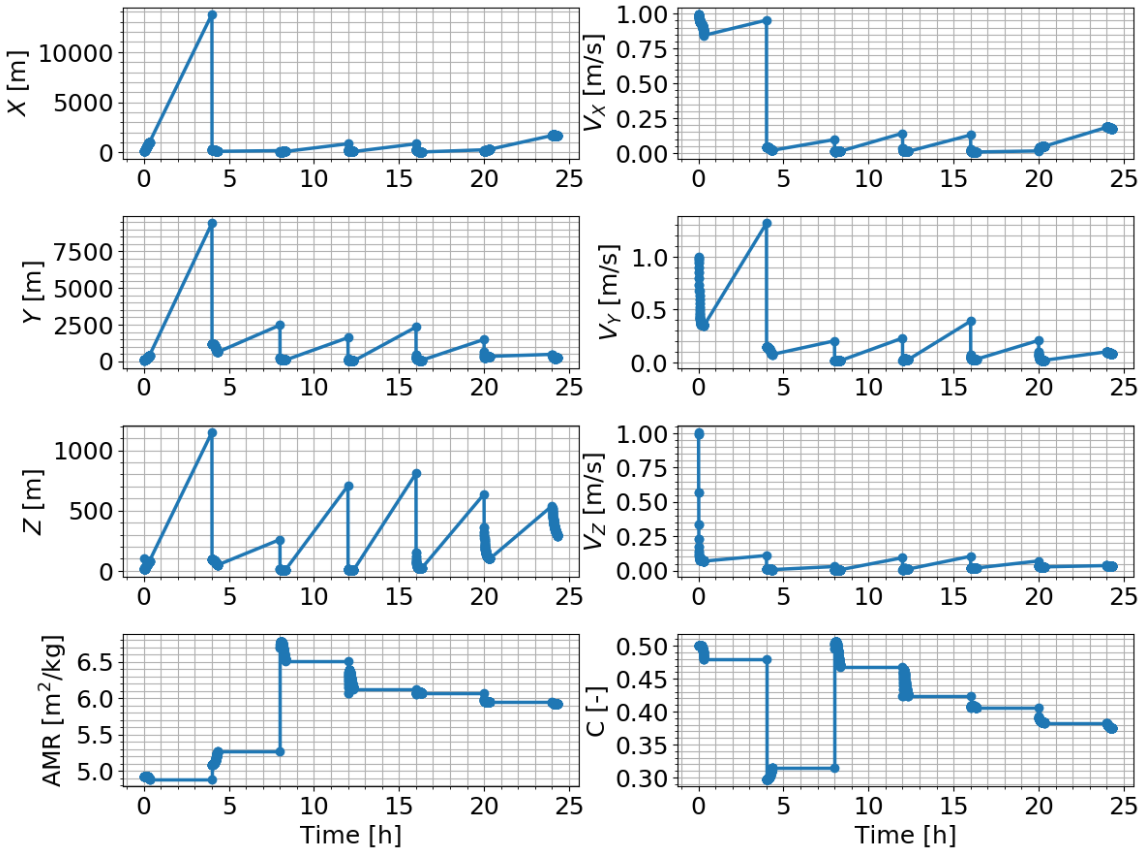

Figure 3.38. RMSE per state for the unobservable system.

Next, the state estimation errors for all of the MC iterations are presented in Figure 3.39. Many of the MC runs can be clearly seen outside of the 3σ bounds in the AMR and C state estimation error plots. Furthermore, some curves can be seen

outside of the position and velocity 3σ bounds. Unlike the observable system state estimation errors, the 1σ and 3σ bounds have visible differences per MC iteration. The large variations in the σ bounds for this system are due to the MC iterations which result in poor estimates of the states because the state estimation error σ bounds are functions of the state estimates, as shown in Equations 3.58 through 3.63.

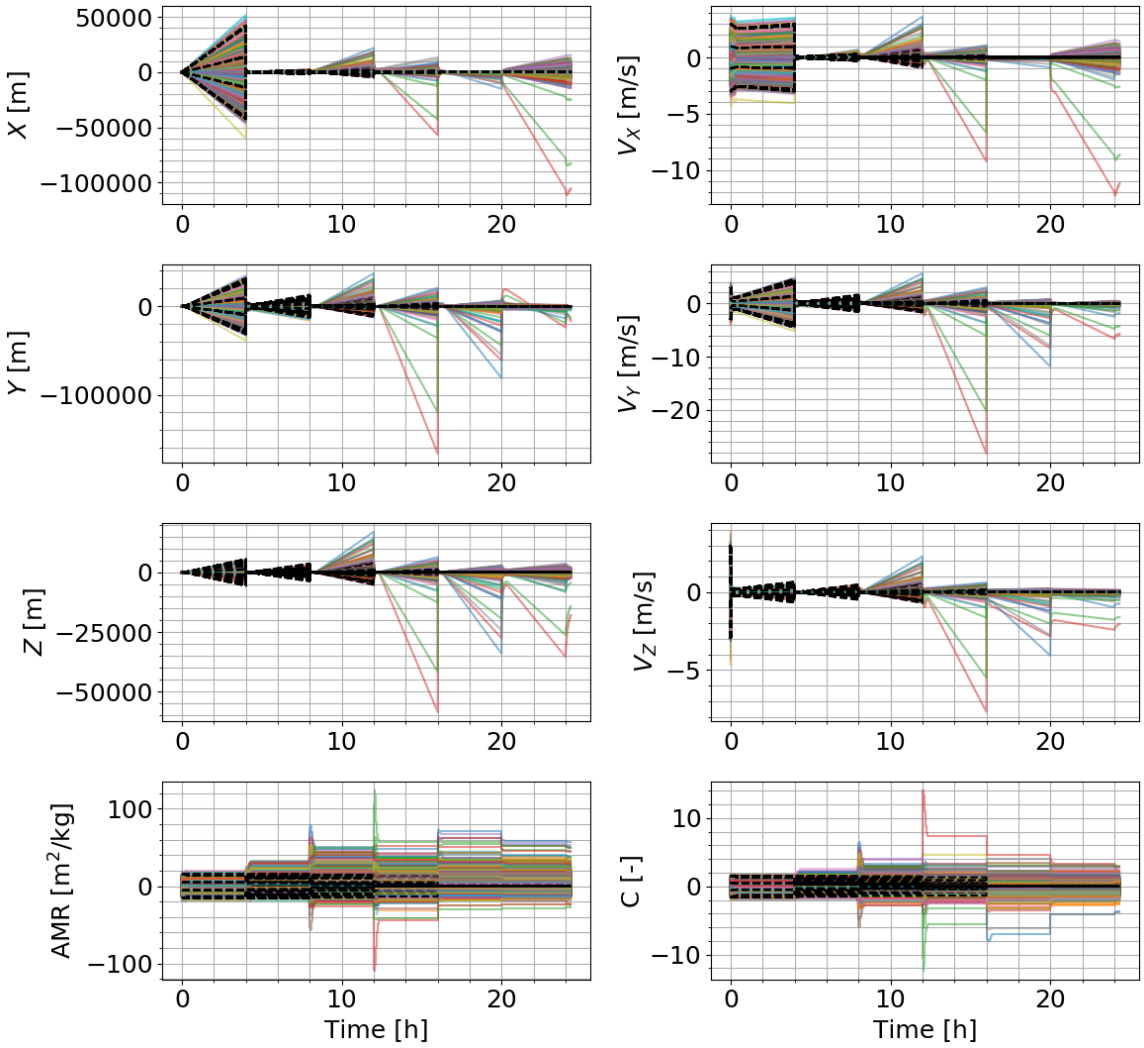

Figure 3.39. State estimation errors for the unobservable system. All MC runs show in different colors.

The large variation in the σ bounds makes evaluation of the performance of each MC iteration difficult through visualization alone. An estimation error curve in Figure 3.39 outside of one of the black dashed lines does not necessarily indicate a poor estimate because the estimation error curve and the σ bound may not correspond to the same MC sample. Therefore, the corresponding state estimation errors and σ bounds are compared for each MC iteration at each time step in Figure 3.40.

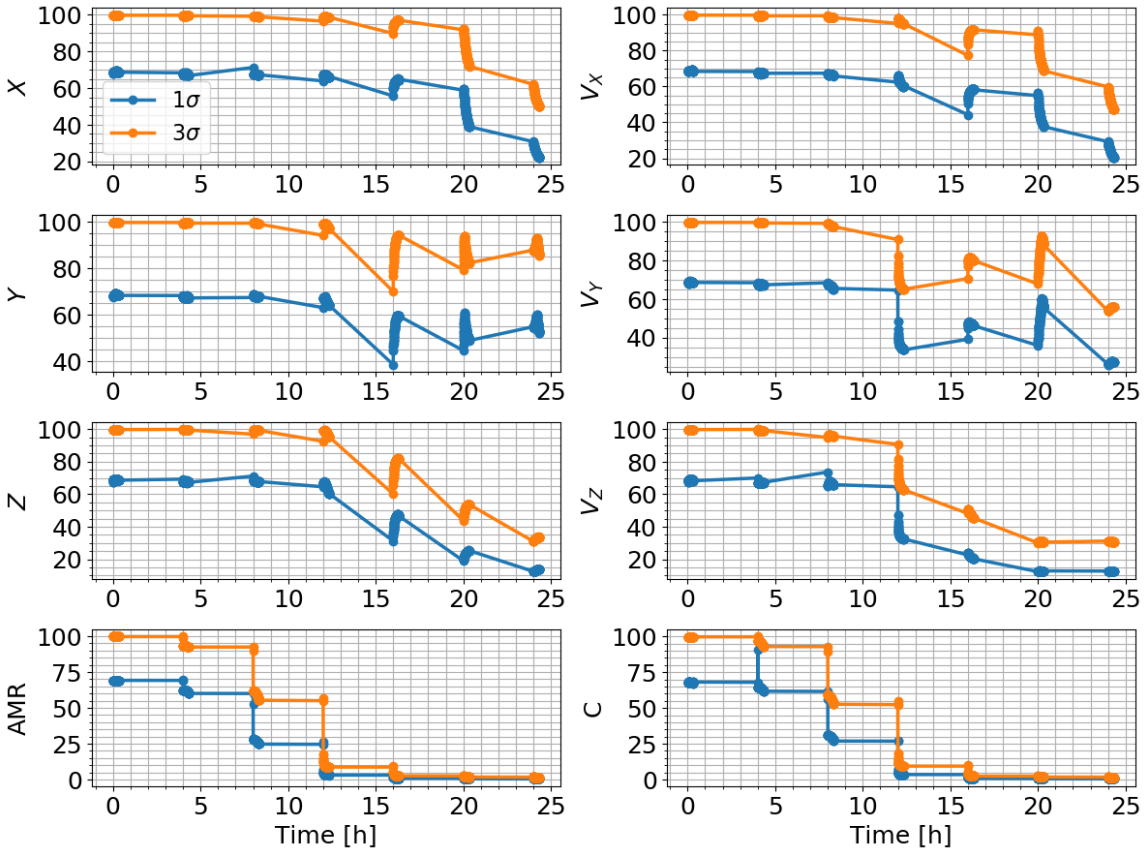

Figure 3.40. Percentage of MC runs within the state estimation error σ bounds for the unobservable system.

After only a couple of measurement batches, the percentage of the MC runs within the 1σ and 3σ bounds for the AMR and C variables are much lower than 68% and 99.7%, respectively. In addition, the position and velocity percentages do not follow the statistically significant σ percentages due to the impact of the poorly estimated

AMR and C. Table 3.10 shows the averages over time for each of the curves in Figure 3.40. When presenting the percentage of the MC samples which remain within the σ bounds for the unobservable system, the poor performance of the estimation becomes clear.

Table 3.10. Percentage of state estimation errors less than or equal to the σ bounds averaged over time for the unobservable system.

	x	y	z	v_x	v_y	v_z	AMR	C
1σ %	57.981	50.057	52.181	62.318	55.497	40.542	23.343	23.911
3σ %	89.613	79.928	83.826	94.819	87.301	67.055	38.474	38.460

Even with the addition of process noise to the EKF, the percentage of the estimation error curves which stay within the σ bounds does not remain at the statistically significant 1σ and 3σ percentages. Figure 3.41 shows the percentage of state estimation errors within the σ bounds when process noise is included in the estimation. The percentages for the AMR and C variables do not go to zero as was the case in Figure 3.40 without process noise, but there is still considerable variation in the estimation errors with respect to the σ bounds. In addition, Table 3.11 shows the averages percentages over time when process noise is included.

Table 3.11. Percentage of state estimation errors less than or equal to the σ bounds averaged over time for the unobservable system with process noise.

	x	y	z	v_x	v_y	v_z	AMR	C
1σ %	69.244	69.684	81.077	68.696	73.701	84.041	40.766	40.325
3σ %	99.486	99.593	99.663	99.509	99.551	99.571	75.440	69.814

The average filter ratio for the unobservable system is shown in Figure 3.42. The position and velocity average filter ratios in Figure 3.42 are near one for approximately

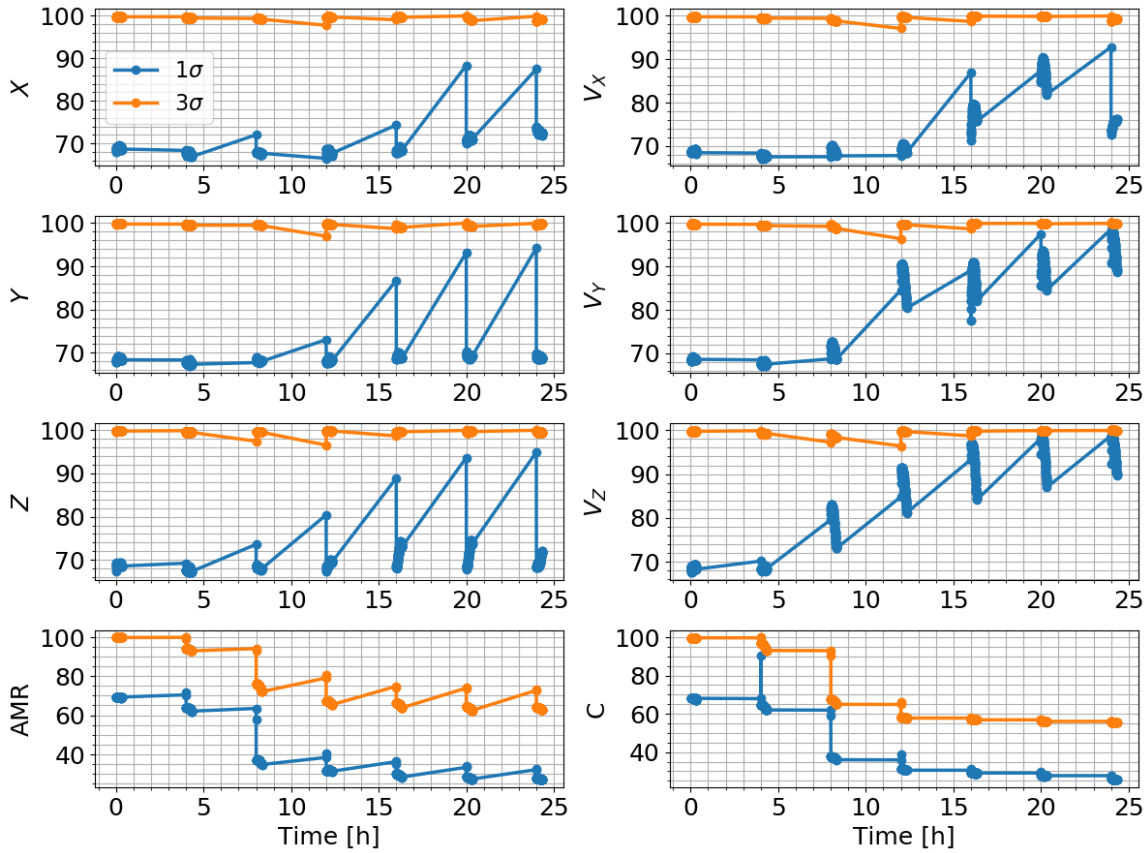

Figure 3.41. Percentage of MC runs within the state estimation error σ bounds for the unobservable system with process noise.

the first half of the analysis. The average filter ratios within the first 50 measurements indicate a filter which is more conservative when compared to the corresponding ratios in the observable system. However, the filter for the unobservable system is smug for the second half of the analysis. This trend is reflected in Figure 3.40. The filter appears to perform well initially, but then the influence of the poorly estimated AMR and C variables causes the σ bounds to be an over-confident representation of the state estimation errors.

When process noise is included in the MC analysis of the unobservable system, the average filter ratio indicates the filter is not as smug compared to when process noise is not included. Figure 3.43 shows the average filter ratio over time for the analysis

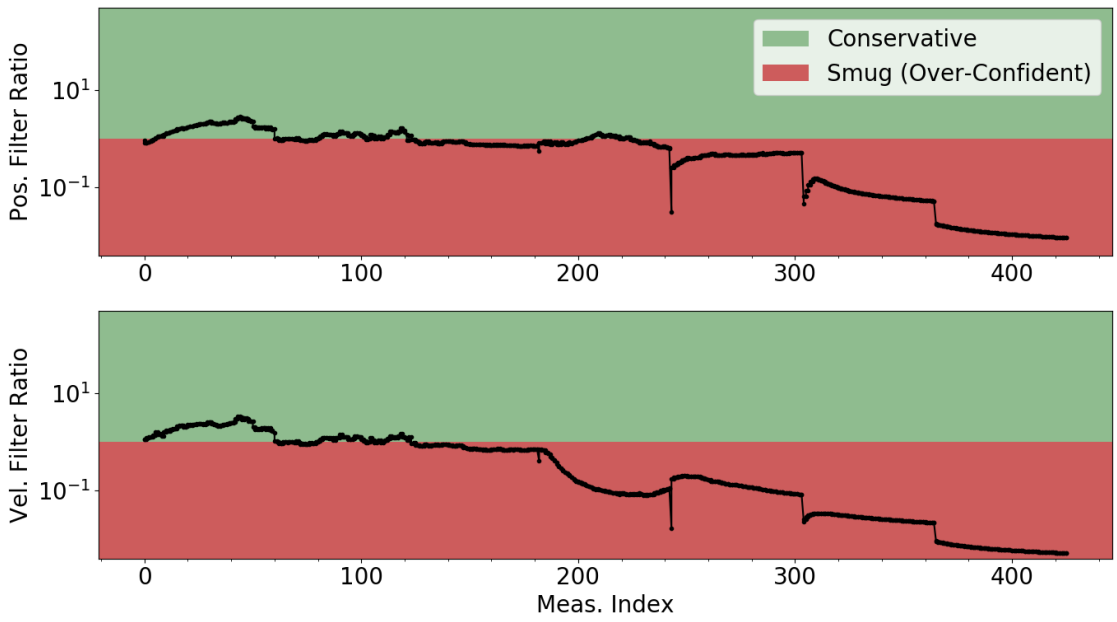

Figure 3.42. Position and velocity average filter ratios for the unobservable system.

with process noise. In a filter, the process noise is commonly manipulated to inflate the covariance to compensate for model mismatch. In this system a model mismatch does not exist, but right ascension and declination measurements are not sufficient for estimating a state containing AMR and C as separate state variables. By including process noise, the filter does not become over-confident in estimating the position and velocity. Moreover, the velocity average filter ratio tends to be conservative after approximately 200 measurements have been processed. This trend is reflected in the plots for the percentage of the MC iterations with state estimation errors within the σ bounds in Figure 3.41. Because the filter is conservative, a larger percentage of the MC iterations have velocity state estimation errors which are within the σ bounds compared to the expected percentage indicated by the 68-95-99.7 rule.

Although the position and velocity average filter ratios appears to indicate that the filter is not over-confident when process noise is included, the average filter ratio for the AMR and C variables indicate a filter which is over-confident. Note that the average filter ratio for the AMR and C variables is the ratio of the standard

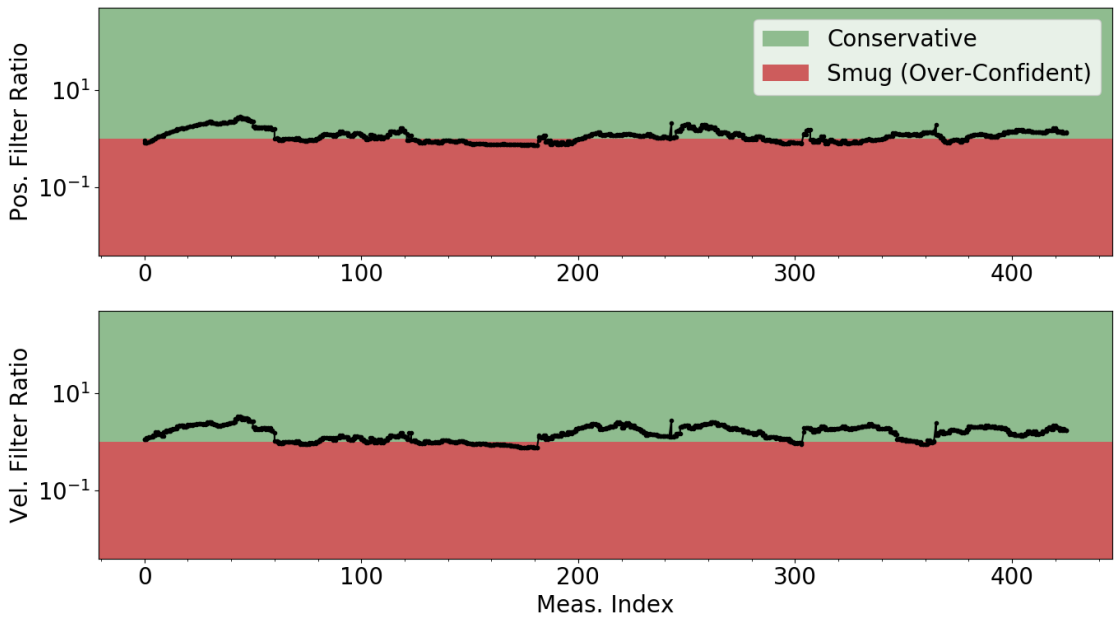

Figure 3.43. Position and velocity average filter ratios for the unobservable system with process noise.

deviation of the 1σ bounds to the standard deviation of the state estimation errors in each variable because multiple state components are not combined as in the position and velocity ratios. Figures 3.44 and 3.45 show the AMR and C average filter ratios over time when process noise is not included in the EKF and when process noise is included in the EKF. In both cases, the filter becomes smug after the first batch of measurements, which consists of 60 measurements. When process noise is included, the AMR and C average filter ratios are closer to one compared to when process noise is not included. However, even if the process noise was increased more to obtain a more conservative filter, this would not necessarily indicate that the AMR and C variables are estimated more accurately. When the average filter ratio is close to one, this indicates that the confidence in the state uncertainty reflects how well the state is estimated. Therefore, the average filter ratios in Figure 3.45, which are closer to one than the average filter ratios of Figure 3.44, indicates that the filter is not as over-confident in the estimation of AMR and C, but as other representations of

the state estimation errors have shown, the AMR and C variables are not accurately estimated.

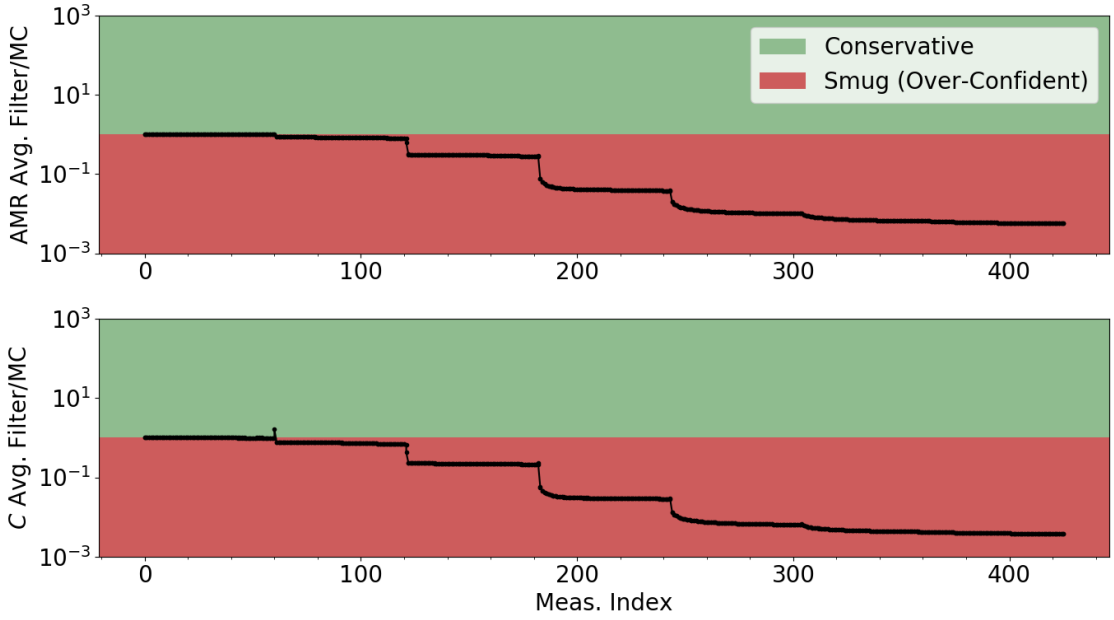

Figure 3.44. AMR and C average filter ratios for the unobservable system.

Next, Figures 3.46 through 3.49 show the evaluation of the MC analysis using the measurement estimation errors only. Similar to the state estimation error RMSE, the measurement estimation error RMSE in Figure 3.46 only has a small indication that the some of the MC iterations result in poor estimates. The last batch of the measurements have a larger RMSE than the previous batch of measurements. However, the general trend of the RMSE decreases with more measurements, which is not an accurate representation of the MC results.

When the MC average measurement estimation errors are split per measurement, the poor estimates for this system become more apparent. The right ascension RMSE does not appear to indicate poor estimation performance, but comparing the declination RMSE to the observable system in Figure 3.33 differences in scale and trend appear. The observable system has a declination RMSE which reduces with each measurement batch and is less than 0.5 arcseconds throughout the analysis. However,

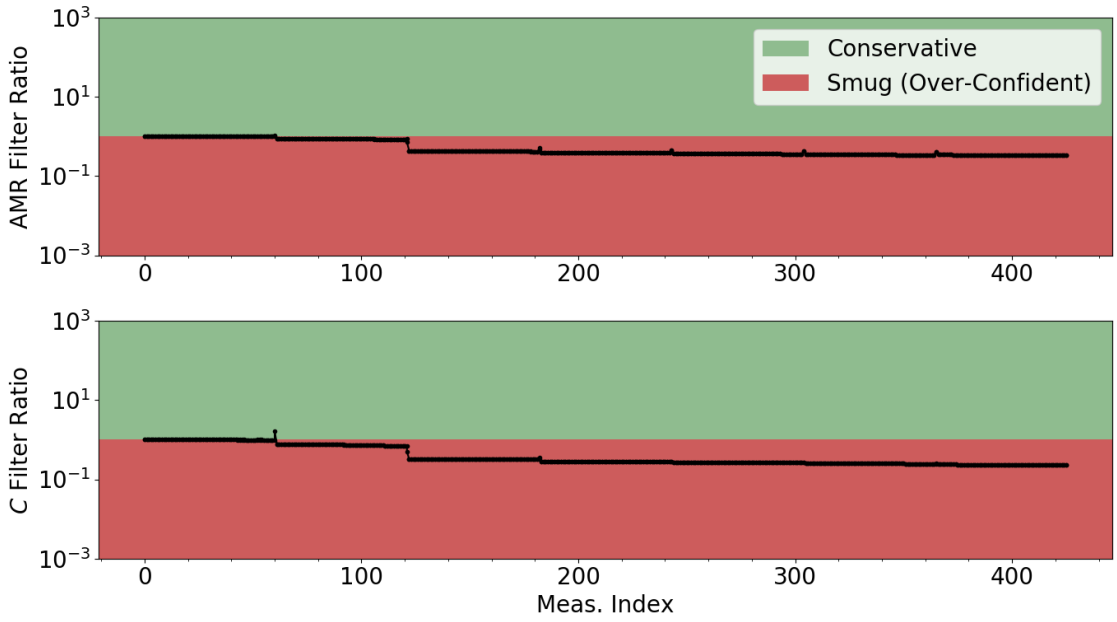

Figure 3.45. AMR and C average filter ratios for the unobservable system.

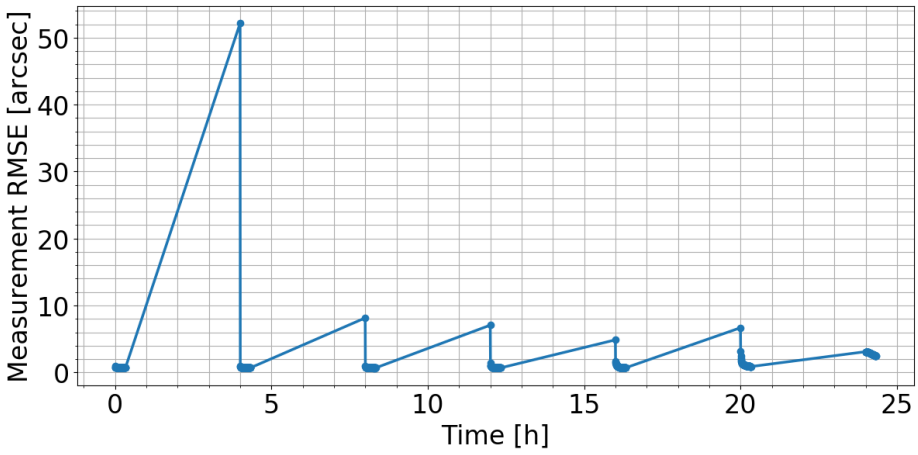

Figure 3.46. Estimated measurement RMSE for the unobservable system.

the declination RMSE for the unobservable system continues to increase significantly between measurement batches throughout the analysis and the error is often greater than 0.5 arcseconds. This representation of the RMSE for the MC results shows that the poorly estimated AMR and C variables have a larger impact on the declination

estimation errors compared to the right ascension estimation errors. Moreover, the importance of the declination measurement relates back to the observability measurement noise analysis in Section 3.4 showing the importance of the declination measurement for the time required for a system to become observable.

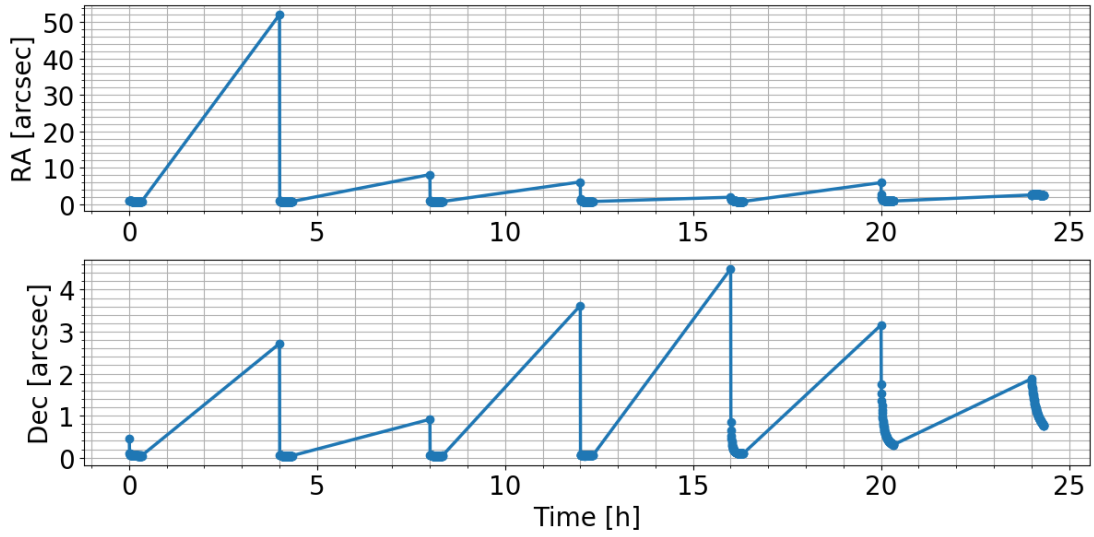

Figure 3.47. RMSE per measurement for the unobservable system.

Similar trends appear for the measurement estimation errors and the percentage of MC iterations which remained within the measurement σ bounds. Figure 3.48 shows the measurement estimation errors for each of the MC iterations and the corresponding σ bounds. The σ bounds have a large variation for each MC iteration, and when comparing the right ascension and declination σ bounds variation, the declination σ bounds appear to vary more.

Figure 3.48 is summarized in Figure 3.49 by counting the number of MC iterations which are less than the corresponding σ bounds for each time step. Compared to the observable system, the percentages within the σ bounds are smaller, i.e. fewer MC iterations follow the 68-95-99.7 rule, for the system with a state extended by AMR and C. In addition, the declination percentages are smaller than the right ascension percentages, reaffirming the notion that the declination measurements have a larger

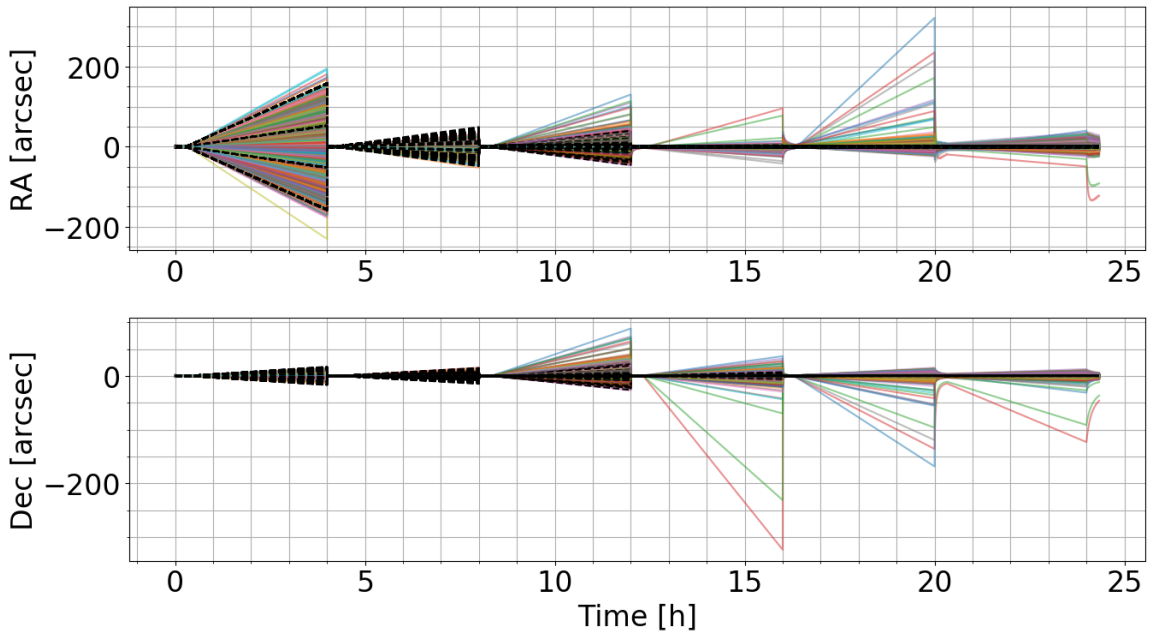

Figure 3.48. Measurement estimation errors for the unobservable system. All MC runs show in different colors.

impact on the system observability than the declination measurements. Also, Table 3.12 averages Figure 3.49 over time.

Table 3.12. Percentage of measurement estimation errors less than or equal to the σ bounds averaged over time for the unobservable system.

	Right Ascension	Declination
1σ %	66.489	60.218
3σ %	98.429	92.895

Figure 3.50 and Table 3.13 show the measurement error percentages which remain within the σ bounds when process noise is included in the estimation. Even though the average values in Table 3.13 show percentages which are consistent with the 1σ

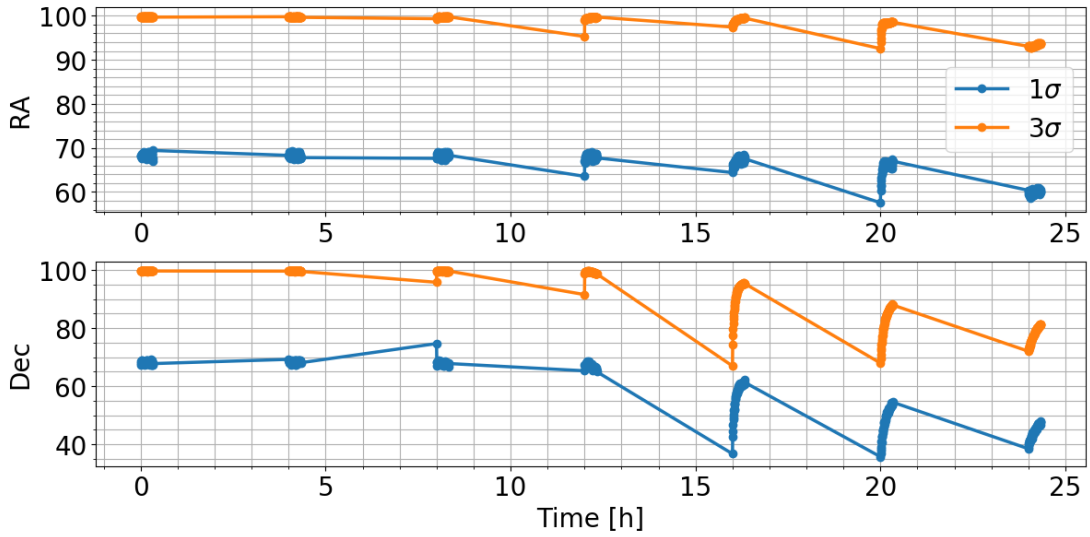

Figure 3.49. Percentage of MC runs within the measurement estimation error σ bounds for the unobservable system.

and 3σ statistically significant values, Figure 3.50 shows that the percentages are not always near the average values throughout the analysis time.

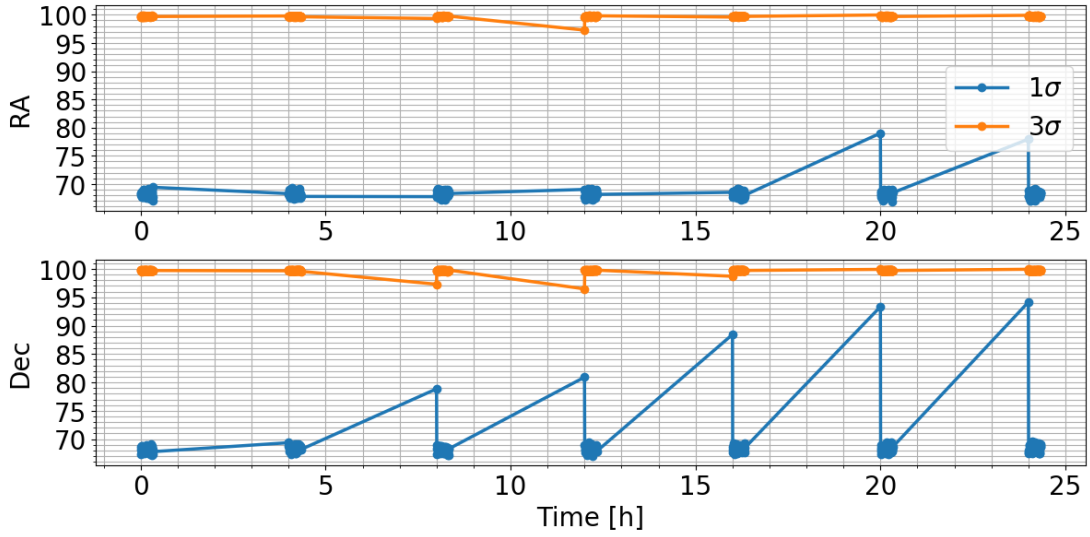

Figure 3.50. Percentage of MC runs within the measurement estimation error σ bounds for the unobservable system with process noise.

Table 3.13. Percentage of measurement estimation errors less than or equal to the σ bounds averaged over time for the unobservable system with process noise.

	Right Ascension	Declination
1σ %	68.315	68.550
3σ %	99.720	99.718

3.7.3 Summary

According to Kalman's initial definition of observability, an observable system has a solution to the optimal regulator problem. The MC analysis of the observable system presented in this section, with a state consisting of position and velocity only, confirms this definition. The percentage of estimation errors within the σ bounds in a MC approach are consistent with the percentages in the 68-95-99.7 rule. In addition, among the MC iterations, the σ bounds show little variation.

A potentially dangerous aspect of estimation is that an estimate can often be produced for any system, whether or not observability has been analyzed. The resulting estimation may not converge, but when the estimation does converge, the estimation could be considered somewhat successful at determining a state estimate. Through the MC estimation analysis, this work has shown that when the orbit problem with an extended state is not observable, estimation accuracy cannot be guaranteed. Figures 3.40 and 3.49 have shown how a percentage of the estimation results in a MC approach for a system which is not observable may produce seemingly accurate estimates within σ bounds. Moreover, measures of estimation performance when the true state is unknown may not clearly show that an estimate is not accurate. For example, the measurement estimation error RMSE and RMSE per measurement of Figures 3.46 and 3.47 appear to have errors which follow a pattern where the error decreases successfully with each measurement batch.

When a true state is not known, the estimation errors in the measurement space are relied upon for determining whether the estimates are accurate. However, order of magnitude differences among states, as is the case with the AMR and C extended state system, may not show poor estimates for some of the states within the measurement estimation errors. The SRP perturbations have an impact on an orbit, but they are small compared to the impact of the central body. Therefore, estimation of AMR and C may be inaccurate but measurement estimation errors may still appear to indicate an accurate estimate. This MC analysis has shown the necessity for determining observability of this system because accurate estimation is not guaranteed if the observability cannot be determined.

3.8 An Observability Use Case: Sensor Tasking Optimization

In order to maintain a catalog for the large and growing RSO population, measurements should contain as much knowledge of the desired state variables as possible. In addition, measurements should be collected efficiently. In this section, observability is investigated for use as a tool in a sensor tasking optimizer. The sensor tasking problem formulation from Frueh, Fiedler, & Herzog [13] contains a weighting parameter for adjusting the importance of obtaining observations for each object. Obtaining frequent observations of the entire RSO population is a challenge because of the size of the RSO population compared to the number of available sensors. In addition, each sensor will have limited windows of observation due to availability of resources, the nature of orbits, and the rotation of Earth. Therefore, the sensor tasking problem posed by Frueh, Fiedler, & Herzog contains a weighting parameter for the importance of acquiring observations of an object. As the time from the last observation of an RSO increases, the uncertainty in the state of the object grows. In order to maintain accurate knowledge of where objects are located and where they will be located in the future, additional observations must be obtained.

In the most general sense, six measurement quantities are required at a minimum to determine an orbit because an orbit is composed of six state quantities. Whether the state vector is composed of Cartesian position and velocity, orbital elements, or some other representation, these six state variables uniquely define an orbit. Many classical initial orbit determination (IOD) methods exist for using a small set of measurements to determine an orbit. Although the measurement quantities implemented in the IOD methods may differ, they all contain six measurement quantities. For example, Gauss' and Laplace's methods for IOD use three astrometric, angles-only observations for determining an orbit. Whereas, Gibbs' and Herrick-Gibbs' methods use three position vectors, calculated from a line-of-sight vector and range, to determine an orbit [14,158]. In this work, observability is analyzed for orbit determination with three astrometric, angles-only observations which are defined by right ascension and declination.

In most classical orbit determination methods, no strict requirements are placed on the spacing between measurements. Theoretically, measurements could be close together and a unique orbit could still be determined. However, in the presence of uncertainties, measurements which are close together may result in an inaccurately determined orbit. The Herrick-Gibbs orbit determination method does maximally bound the spacing of the three position vectors because a Taylor series expansion is implemented in the algorithm. However, in general, these orbit determination methods do not specify how measurements should be spaced for determining an orbit.

This work implements observability analysis for determining how measurements should be spaced for determining an orbit. The relative impact of selecting different measurement spacings on an orbit determination solution is explored with analysis of the observability matrix singular values. In addition, a MC analysis is performed with a nonlinear batch least squares estimator for evaluating how the relative heights of the observability matrix singular values translate to the MC estimation root mean square errors.

3.8.1 Observability Results

Observability is analyzed for a system defined by the GEO 4 object in Table 3.2 and three equally spaced batches of measurements. Each measurement batch consists of 30 measurements spread over one minute of observation. The observability of this system is analyzed by varying the time between the equally spaced batches of measurements. Therefore, observability simulations are performed many times for each measurement batch spacing case. Each observability iteration is summarized by the singular values at the final measurement in the analysis.

Figure 3.51 shows the smallest singular value of the deterministic observability matrix, s_6, versus different measurement batch spacing cases. Each point in Figure 3.51 represents an observability simulation for the measurement spacing defined by the time between measurement batches on the x-axis. Therefore, a measurement batch spacing of one hour would have the first measurement batch at epoch, the second measurement batch one hour from epoch, and a third measurement batch two hours from epoch. Figure 3.51 also contains the value of the tolerance line at the time of the last measurement for each of the observability simulations. Recall that a system is considered observable when the smallest singular value of the observability matrix is greater than the tolerance line.

The observability of this system changes as the time between measurement batches changes. When measurements are spaced by six hours, the system is observable, but when measurement batches are spaced by 12 hours, the system is not observable. The latter result is expected because the GEO4 object has a period which is approximately 24 hours. Therefore, the third batch of measurements does not provide more knowledge of the system geometry compared to the first batch of measurements. This measurement batch spacing behavior resulting in poor system observability is repeated every orbital period, e.g. measurement batches spaced every 24 hours, 36 hours, and so on.

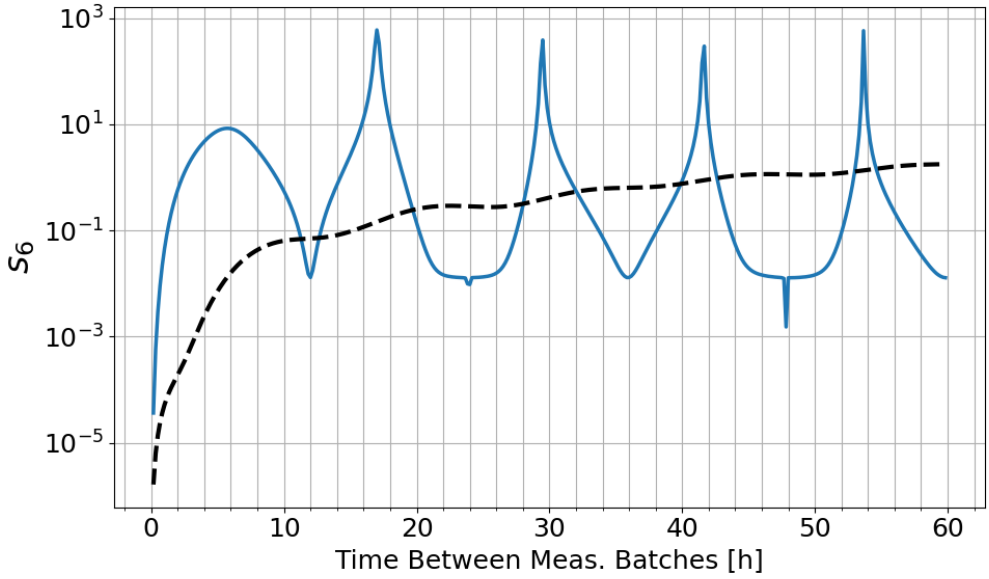

Figure 3.51. Smallest singular value of the deterministic observability matrix versus time between measurement batches.

The preceding observability analysis in this chapter has shown how measurement uncertainty can significantly change the observability results for a system. As expected, this representation of observability is no different. In Figure 3.52, the stochastic observability matrix with measurement uncertainty is analyzed in the same manner as Figure 3.51. The uncertainty in measurement noise is the same as Section 3.6.3, where the standard deviations of the right ascension and declination measurements are 0.67 arcseconds and 0.045 arcseconds, respectively. When measurement uncertainties are included in this analysis of observability, the shape of the observability results change considerably. The measurement batch spacing cases which correspond to an observable system are approximately the same, but instead of sharp peaks like in Figure 3.51, the peaks of the observability results in Figure 3.52 tend to be more rounded. For a telescope operator planning observations for orbit determination, observability results with a more rounded peak are advantageous because a range of potential observation spacings could be selected which will result in a well observed

system. However, it should be noted that this rounding of the peaks is due to the measurement uncertainties and not the orbital dynamics.

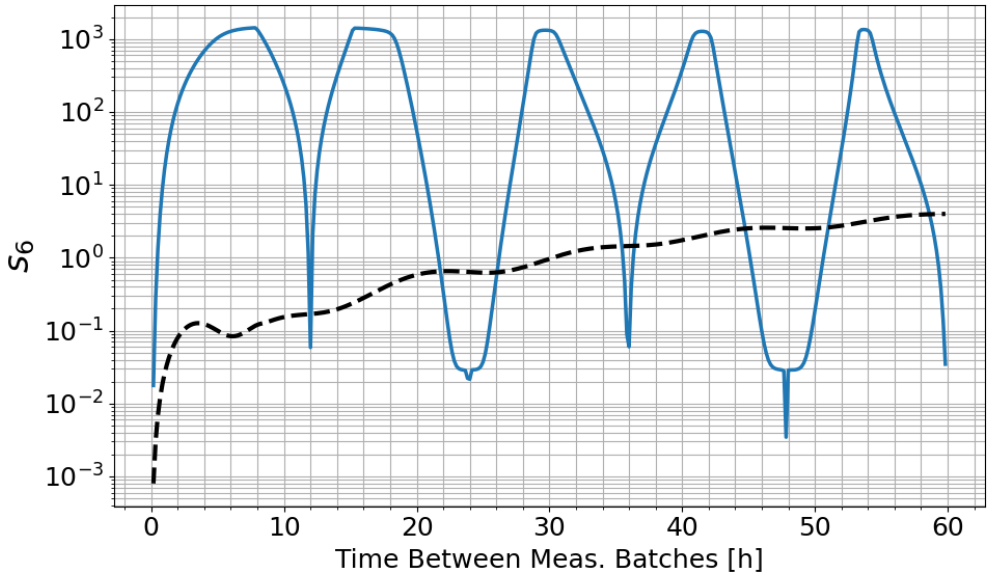

Figure 3.52. Smallest singular value of the stochastic observability matrix with measurement uncertainties versus time between measurement batches.

Next, this work evaluates whether the height of the smallest observability matrix singular values can be used as an indicator of estimation accuracy. Since the tolerance line in Figures 3.51 and 3.52 changes with time, this analysis of the singular value height computes the ratio of the smallest singular value to the tolerance line. The observability results for the deterministic and stochastic systems are shown with this representation in Figures 3.53 and 3.54. The condition for system observability is now defined by a tolerance line at one because the smallest singular value is greater than the numerical error estimate when the ratio of the smallest singular value to the tolerance line is greater than one.

In the deterministic and stochastic systems, the ratio of the smallest singular value to the tolerance decreases as the time between measurement batches increases. Although the tolerance line grows in Figures 3.51 and 3.52 the relative height of the

smallest singular value above the tolerance is not apparent. Therefore, for comparing the impact of different measurement batch spacing cases on the observability of a system, this representation of the observability with the ratio of the smallest singular value to the tolerance is used.

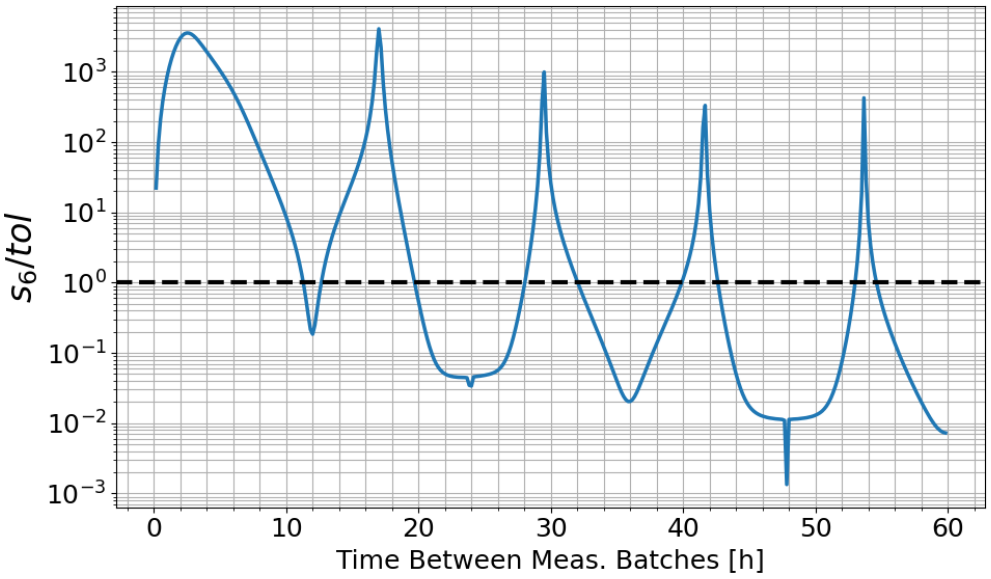

Figure 3.53. Ratio of the smallest singular value of the deterministic observability matrix to the tolerance line versus time between measurement batches.

Another observability representation implemented in this analysis uses the condition number of the observability matrix. The condition number of a matrix is defined by the ratio of the largest singular value to the smallest singular value. Therefore, the condition number of the observability matrix is proportional to the ratio of the smallest singular value to the tolerance line. Recall the definition of the tolerance line introduced in Section 2.1.3.

$$tol = \max(\mathbf{s}) \times \max(\text{size}(\mathcal{O}(t_0, t_m))) \times \varepsilon, \tag{3.64}$$

where $\mathbf{s}$ contains the singular values of the observability matrix, $\mathcal{O}$, and ε is the machine epsilon. In this system, the observability matrix has dimension six by six

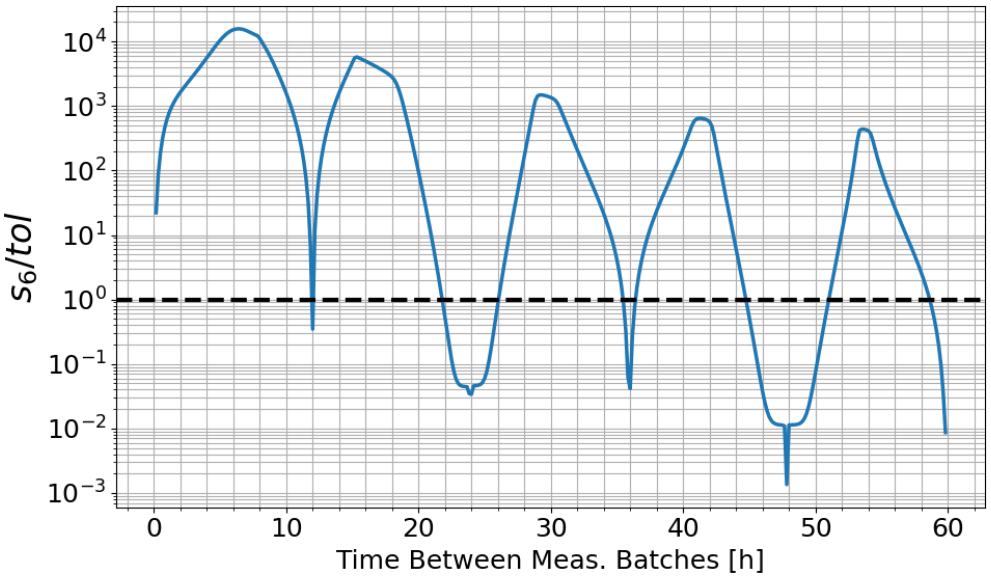

Figure 3.54. Ratio of the smallest singular value of the stochastic observability matrix with measurement uncertainties to the tolerance line versus time between measurement batches.

because of the six state variables. In addition, the smallest singular value is defined by s_6, and the largest singular value is defined by s_1. The ratio of the smallest singular value of the observability matrix to the tolerance is given by

$$\frac{s_6}{tol} = \frac{s_6}{6\varepsilon s_1} = \frac{1}{6\varepsilon \text{cond}(\mathcal{O})}, \tag{3.65}$$

where $\text{cond}(\mathcal{O}) = \frac{s_1}{s_6}$ is the condition number of the observability matrix. The condition number of a matrix indicates how close a matrix is to singularity. The condition number does not specify whether a matrix is singular or not. Therefore, a tolerance is not shown in the observability results represented by the condition number of the observability matrix because a system can not be defined as observable or not with the condition number. However, the condition number is used in this work as a method for comparing the observability results for the different measurement batch spacing cases and for relating to the mean square error (MSE) of a MC analysis.

Figures 3.55 and 3.56 show the condition number of the deterministic and stochastic observability matrix for a range of measurement batch spacing cases. These condition number results are inversely proportional to the singular value-tolerance ratio as defined by Equation 3.65. When the condition number of a matrix is large, a matrix is more ill-conditioned. Therefore, in Figures 3.55 and 3.56 the peaks now indicate measurement spacing cases which may be ill-advised for orbit determination.

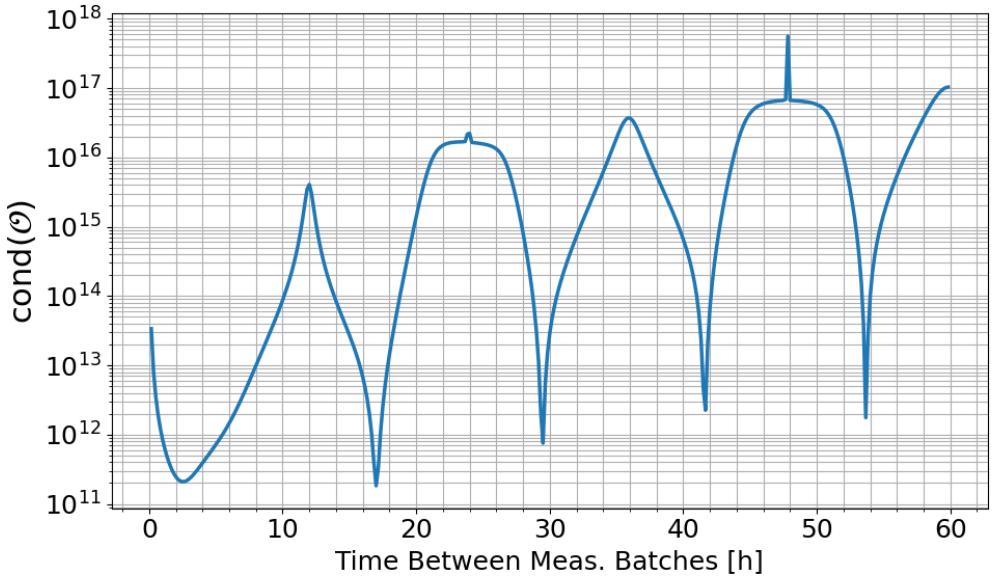

Figure 3.55. Condition number of the deterministic observability matrix versus time between measurement batches.

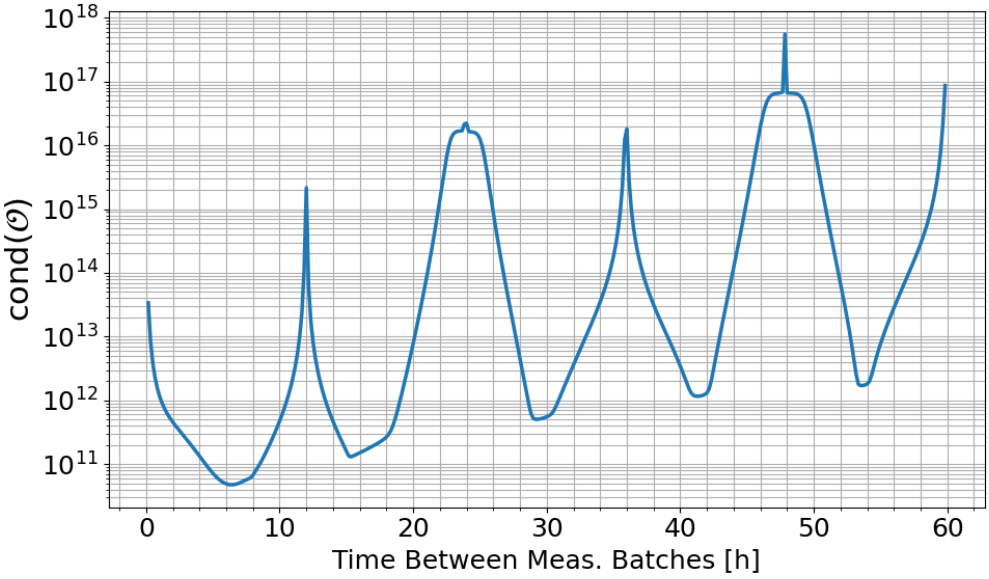

Figure 3.56. Condition number of the stochastic observability matrix with measurement uncertainties versus time between measurement batches.

3.8.2 Comparison of Observability and Nonlinear Batch Least Squares Monte Carlo Analysis

A MC analysis is performed to evaluate the impact of singular value height on the orbit determination accuracy. Similar to the structure of the observability analysis in the previous section, each point in the following simulation represents a different MC simulation for a range of measurement batch spacing cases. In addition, nonlinear batch least squares estimation is implemented in the MC analysis because the observability results in the previous section are representative of the observability matrix singular values at the time of the last measurement. Batch estimation methods use all of the measurements in a system to estimate a single state, rather than sequentially updating the state as in the EKF.

MC analysis is performed for each measurement spacing case given in the observability results of the previous section. Each MC run consists of 1,000 samples of the initial state estimate. The samples are generated from the mean and covariance in

Table 3.14. Note that the mean corresponds to the true initial state of the GEO 4 object for an epoch of 53159.5 Modified Julian Date (MJD). In addition, the nonlinear batch LS estimation implemented in this work follows the iterative estimation process of the linear, unbiased, minimum variance estimate (LUMVE) given by Tapley, Schutz, & Born [49]. This estimation method improves the estimation accuracy by iterating for a fixed number of iterations or until a convergence criteria is achieved. This work limits the number of iterations to five to ensure that the MC analysis is computationally efficient.

Table 3.14. Mean and Standard Deviation for defining the MC samples.

State	Mean	Standard Deviation
x [km]	-38817.694	0.1
y [km]	-16450.667	0.1
z [km]	37.283	0.1
v_x [km/s]	1.200	0.001
v_y [km/s]	-2.831	0.001
v_z [km/s]	4.939×10^{-4}	0.001

Recall the estimate of the initial state in the LUMVE is defined by

$$\hat{\mathbf{x}}(t_0) = \mathbf{x}_{\text{ref}}(t_0) + (\bar{\mathbf{H}}^T\ \bar{\mathbf{H}})^{-1}\ \bar{\mathbf{H}}^T\ \bar{\mathbf{R}}^{-1}\ (\bar{\mathbf{z}} - \bar{\hat{\mathbf{z}}}), \tag{3.66}$$

where,

$$\mathbf{x}_{\text{ref}}(t_0) = \mathbf{m}(t_0), \tag{3.67}$$

$$\bar{\mathbf{H}} = \begin{bmatrix} \mathbf{\Phi}(t_1, t_0)\ \widetilde{\mathbf{H}}(\mathbf{m}(t_1)) \\ \mathbf{\Phi}(t_2, t_0)\ \widetilde{\mathbf{H}}(\mathbf{m}(t_2)) \\ \vdots \\ \mathbf{\Phi}(t_k, t_0)\ \widetilde{\mathbf{H}}(\mathbf{m}(t_k)) \end{bmatrix}, \quad \bar{\mathbf{R}}^{-1} = \begin{bmatrix} \mathbf{R}^{-1} \\ \mathbf{R}^{-1} \\ \vdots \\ \mathbf{R}^{-1} \end{bmatrix}, \tag{3.68}$$

$$\bar{\mathbf{z}} = \begin{bmatrix} \mathbf{z}(t_1) \\ \mathbf{z}(t_2) \\ \vdots \\ \mathbf{z}(t_k) \end{bmatrix} = \begin{bmatrix} \mathbf{h}(\mathbf{x}(t_1)) + \nu(t_1) \\ \mathbf{h}(\mathbf{x}(t_2)) + \nu(t_2) \\ \vdots \\ \mathbf{h}(\mathbf{x}(t_k)) + \nu(t_k) \end{bmatrix}, \quad \bar{\hat{\mathbf{z}}} = \begin{bmatrix} \hat{\mathbf{z}}(t_1) \\ \hat{\mathbf{z}}(t_2) \\ \vdots \\ \hat{\mathbf{z}}(t_k) \end{bmatrix} = \begin{bmatrix} \mathbf{h}(\mathbf{m}(t_1)) \\ \mathbf{h}(\mathbf{m}(t_2)) \\ \vdots \\ \mathbf{h}(\mathbf{m}(t_k)) \end{bmatrix}, \tag{3.69}$$

$\mathbf{x}(t_k)$ is the true state at time t_k, and $\mathbf{m}(t_k)$ is the propagated initial state estimate, i.e. reference state, from t_0 to t_k. The mean square error (MSE) for the MC analysis is defined by

$$\text{MSE} = \frac{1}{M} \sum_{i=1}^{M} (\mathbf{x}(t_0) - \hat{\mathbf{x}}(t_0)_i)^T\ (\mathbf{x}(t_0) - \hat{\mathbf{x}}(t_0)_i), \tag{3.70}$$

where M is the number of MC samples, $\hat{\mathbf{x}}(t_0)_i$ is the estimated initial state after five iterations in the nonlinear batch LS for each MC sample, and $\mathbf{x}(t_0)$ is the true initial state. The following simulation results compare the trends of the MSE to the trends of the observability matrix condition number and the observability matrix singular value-tolerance ratio. As discussed in Section 3.1.1, the LUMVE solution in Equation 3.66 contains the observability matrix $\bar{\mathbf{H}}^T\ \bar{\mathbf{H}}$ evaluated at the reference rather than the true state. Moreover, the inverse of this matrix is used to define estimated initial state. Therefore, the inverse of the MSE will be compared to the observability matrix singular value-tolerance ratio. Furthermore, the MSE will be directly compared to the condition number of the observability matrix because the condition number is inversely proportional to the observability matrix singular value-tolerance ratio.

Figures 3.57 and 3.59 show the MSE for the MC analysis and the condition number of the observability matrix for each measurement batch spacing case. Figures 3.58 and 3.60 show the inverse of the MSE and the observability matrix smallest singular

value to tolerance ratio for each batch spacing case. The stochastic observability matrix with measurement uncertainty is implemented in this analysis because of the stochastic nature of the nonlinear batch LS. The following observability results are equal to the observability results in Figures 3.56 and 3.54.

In each figure, the observability results are given in blue, the position MSEs are given in yellow, and the velocity MSEs are given in green. The MSE curves are scaled to reflect the range of the observability results in Figures 3.57 and 3.58. The scaling of the MSE curves is accomplished with linear interpolation of the MSE values to be contained within the minimum and maximum of the observability matrix results.

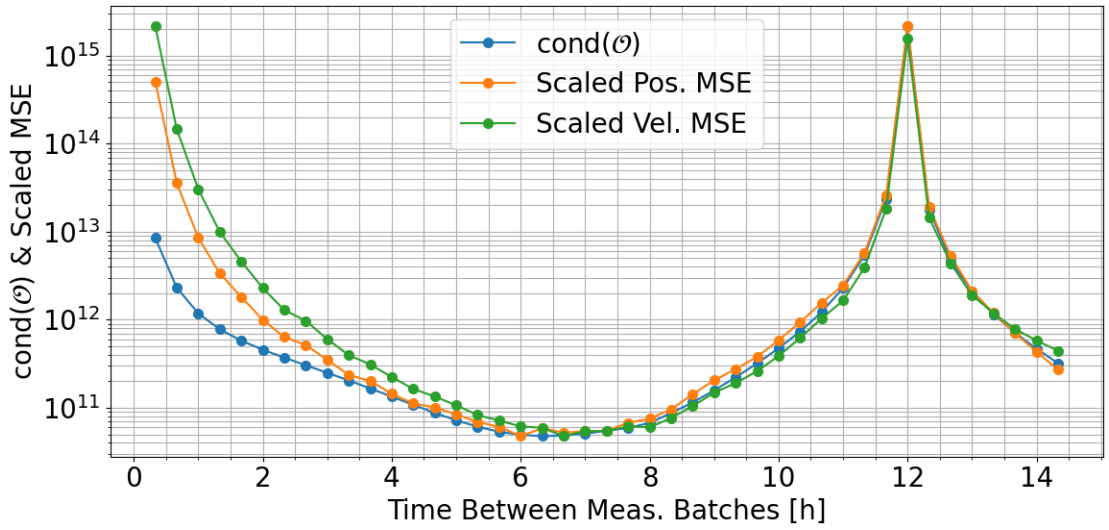

Figure 3.57. Comparison of the scaled nonlinear batch LS MC mean square error to the condition number of the stochastic observability matrix.

In Figures 3.57 and 3.58, the trends in the nonlinear batch LS MC mean square error reflect the trends of the observability results. The position and velocity MSEs have a maximum value when three measurement batches are equally spaced by 12 hours, and the position and velocity MSEs have a minimum value when three measurement batches are equally spaced by approximately 6.333 hours. Because trends of the observability matrix reflect the trends in the MSE, differences in the observability

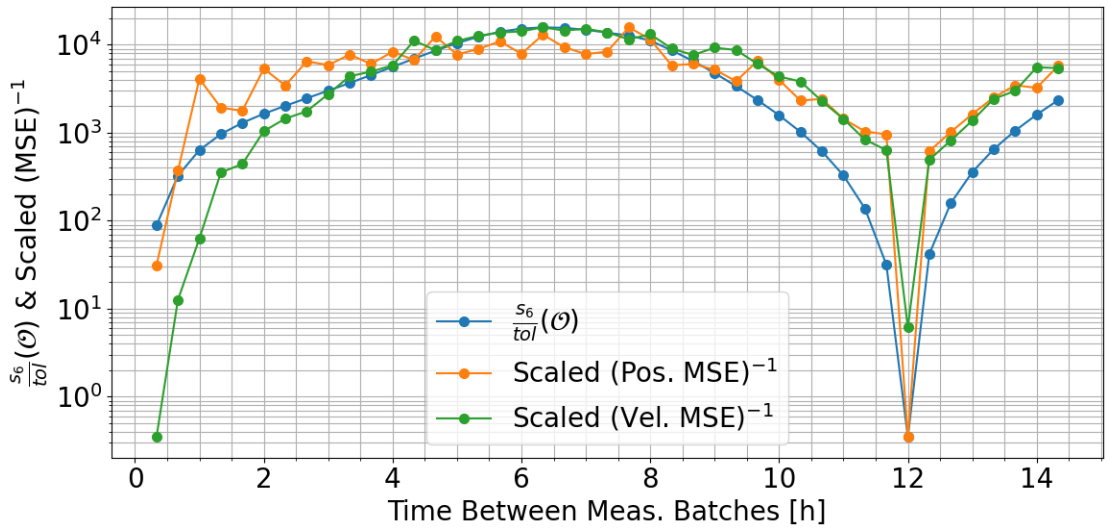

Figure 3.58. Comparison of the scaled nonlinear batch LS MC mean square error to the ratio of the smallest singular value in the observability matrix to the tolerance line.

smallest singular value height for two different measurement spacing cases could be used to determine which measurement spacing case will provide a more accurate orbit estimate. Furthermore, these observability results could be used to identify regions of measurement batch spacing to avoid so the likelihood of less accurate orbit estimates is reduced.

Next, the MSE results which have not been scaled to match the observability results are shown in Figures 3.59 and 3.60. In addition, Table 3.15 shows the root mean square error (RMSE) for various measurement batch spacing cases. The position and velocity RMSEs increase rapidly when the spacing between three measurement batches is near 12 hours. The position and velocity RMSEs corresponding to the best time between measurement batches indicated by the observability results are 79.793 m and 0.00556 m/s, respectively. The position and velocity RMSEs corresponding to the worst time between measurement batches indicated by the observability results are 8718.500 m and 0.634 m/s, respectively. For this system, selection of the best or

worst measurement batch spacing could result in a two order of magnitude difference in the position and velocity RMSEs.

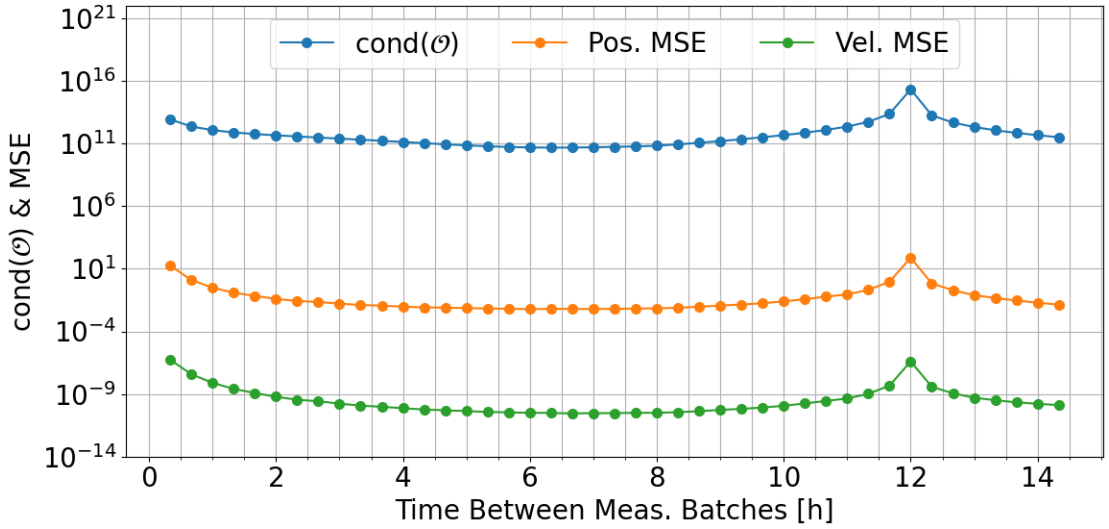

Figure 3.59. Comparison of the nonlinear batch LS MC mean square error to the condition number of the stochastic observability matrix.

Table 3.15. Position and velocity RMSE for several measurement batch spacing cases.

Time [h]	Position RMSE [m]	Velocity RMSE [m/s]
6.333 ($\min(\frac{s_6}{tol}(\mathcal{O}))$)	79.793	0.00556
12.0 ($\max(\frac{s_6}{tol}(\mathcal{O}))$)	8718.500	0.634

Table 3.16 shows measurement batch spacings which meet two conditions for the position RMSE. If a maximum position RMSE of 0.1 km is required, measurement batch spacings within 3.900 and 8.776 hours could be selected. Moreover, if a maximum position RMSE of 1.0 km is required, measurement batch spacings which are between 0.699 and 11.669 hours could be selected. Measurement batch spacings greater than 12.325 hours could also be selected, but an upper bound has not been

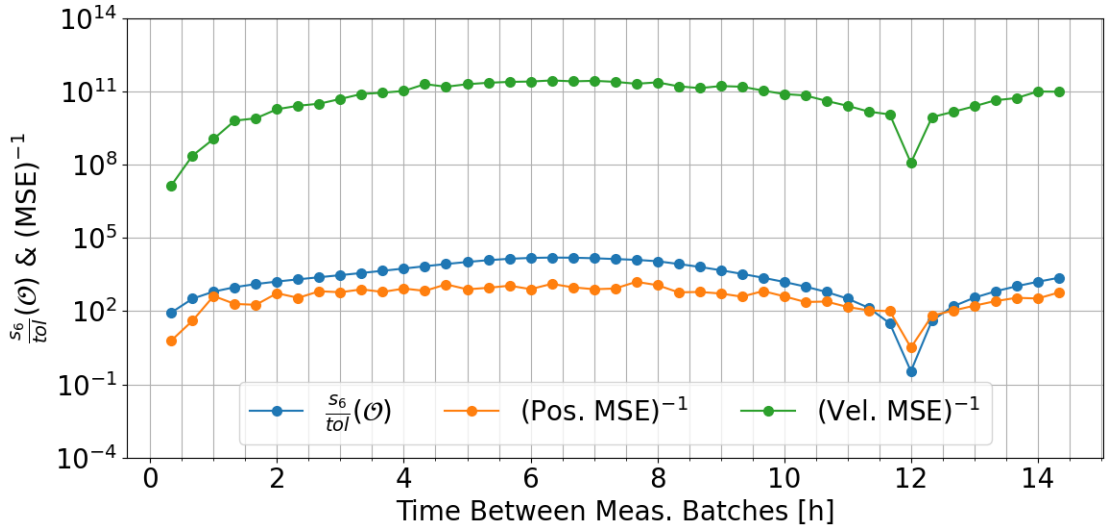

Figure 3.60. Comparison of the nonlinear batch LS MC mean square error to the ratio of the smallest singular value in the observability matrix to the tolerance line.

determined due to the limited analysis time in this simulation. For this system, there is a small region of measurement batch spacings which will result in large position RMSE errors greater than 1.0 km, but position RMSEs less than 1.0 km can be achieved with a range of measurement batch spacing cases which span approximately 11 hours. However, the observability and MSE results indicate that the later batch spacing cases have the caveat that extending the time between measurements further may result in a large increase in the estimation errors.

Table 3.16. Time between measurement batches for two position RMSE conditions.

Position RMSE = 0.1 km	Position RMSE = 1.0 km
3.900 h	0.699 h
8.776 h	11.669 h
–	12.325 h

The ratio of the observability matrix smallest singular value to the tolerance is significant for comparing the expected estimation errors of different measurement batch spacing cases. Therefore, observability analysis can be implemented for defining the weight parameter in the sensor tasking problem formulation from Frueh, Fiedler, & Herzog [13]. The observability of multiple RSOs could be analyzed to generate these curves of the observability matrix smallest singular value to the tolerance. For example, the observability results for the five GEO objects and the five LEO objects defined in Tables 3.2 and 3.1 are shown in Figures 3.61 and 3.62. The singular value-tolerance ratio is implemented for this analysis instead of the condition number of the observability matrix because the singular value-tolerance ratio includes a tolerance for determining whether the system is observable, in addition to the relative heights of the singular values for each measurement batch spacing case.

Each curve in Figures 3.61 and 3.62 represents a different object. Similarities in the different GEO and LEO objects are apparent with this observability representation. For example, GEO 2 and GEO 4 both have small inclinations and the observability matrix singular value-tolerance ratio curves are similar. Note that in Figure 3.62 the tolerance line at a value of one is not visible because all of the curves are above the tolerance.

An optimizer could use the curves in Figures 3.61 and 3.62 to select the measurement spacing cases for each object to maximize the overall singular value-tolerance ratio height. Note that this analysis has been limited to a single sensor which generates three measurement batches that are equally spaced. Both of these restrictions could be removed, but the results may no longer be as intuitive for a nearly-geostationary object, such as the GEO 4 object. Observability with multiple sensors is analyzed in Section 3.9.

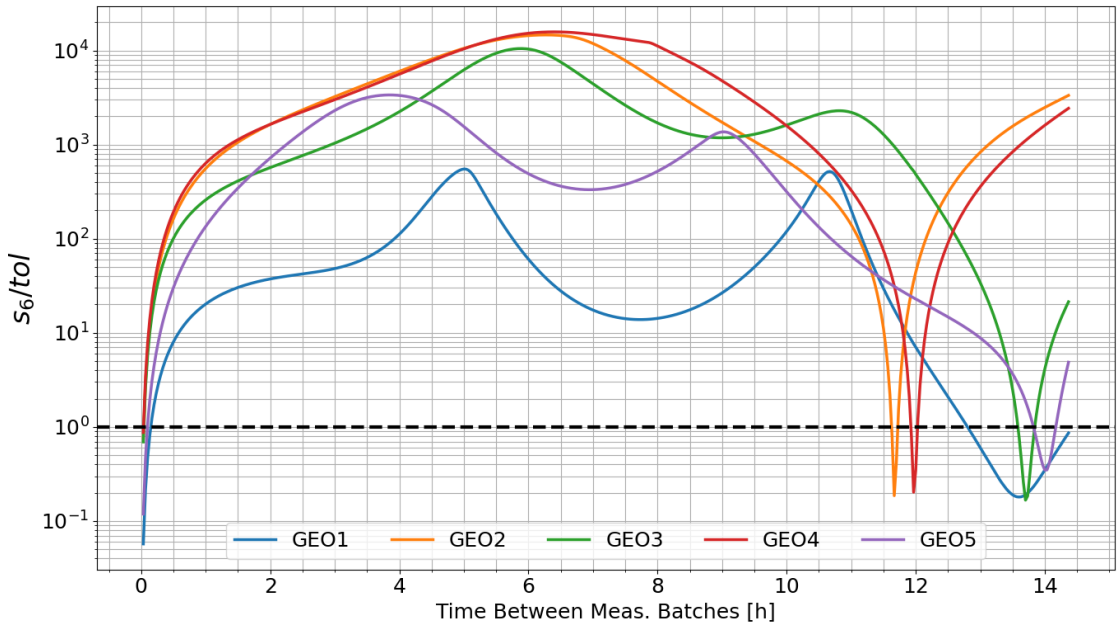

Figure 3.61. Observability matrix smallest singular-tolerance ratio versus time between measurement batches for the five GEO objects in Table 3.2.

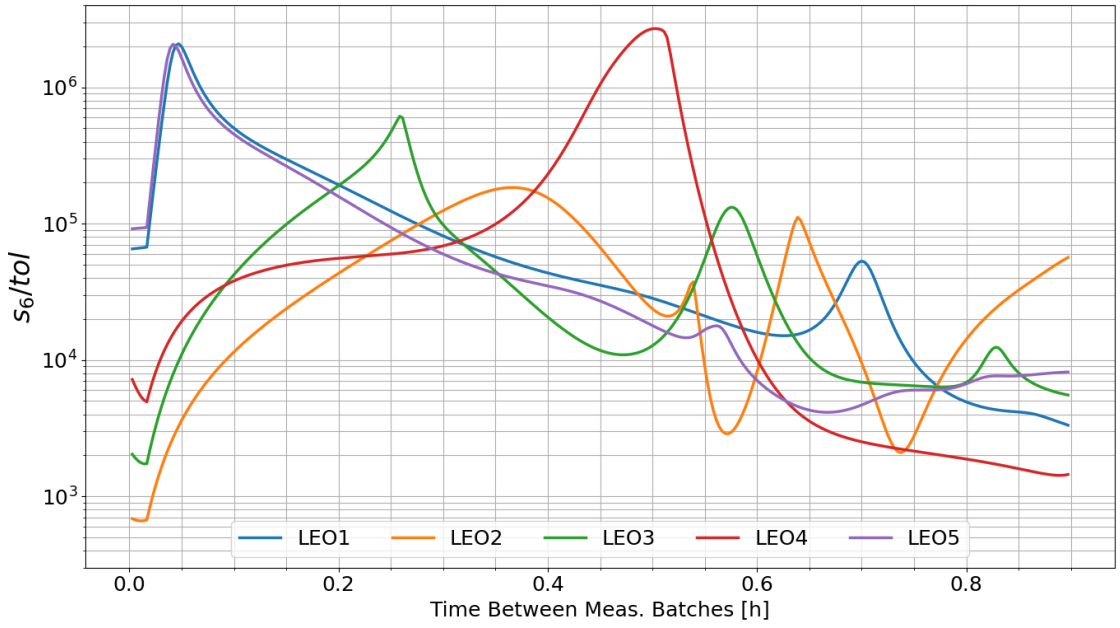

Figure 3.62. Observability matrix smallest singular-tolerance ratio versus time between measurement batches for the five LEO objects in Table 3.1.

3.8.3 Summary

For the GEO 4 object, the singular value-tolerance ratio has a region near the maximum value, at approximtely 6.333 hours, which does not rapidly reduce. Therefore, measurement batch spacing cases in the neighborhood of the maximum would be expected to have similar state estimation errors. In addition, regions of potentially large state estimation errors can be identified with the observability analysis. When measurement batches are spaced by 12 hours, there is a sharp decline in the singular value-tolerance ratio which indicates that the state estimation errors for an estimator with this measurement sequence may result in an inaccurate state estimate.

This analysis has shown that observability analysis results can be related to the mean square errors in a nonlinear batch least squares Monte Carlo analysis. When the observability matrix singular value-tolerance ratio or the condition number of the observability matrix is computed for a range of measurement batch spacing cases, the relative heights of these measures are indicative of the state estimation error trends in the nonlinear batch least squares solution. Therefore, these measures could be implemented in a sensor tasking optimizer to aid in determining when each object should be observed.

3.9 An Observability Use Case: Multiple Sensor and Observation Evaluation

As government and commercial entities develop and expand their sensor networks for Space Situational Awareness (SSA), large amounts of data will become available. Furthermore, the United States Air Force Research Laboratory, Air Force Space Command, Space and Missile Systems Center have developed the Unified Data Library (UDL) in an attempt to create a single source for storing and purchasing relevant SSA related data [159]. Within the UDL, SSA sensor network operators can upload their observations, processed data, and sensor services for purchase. In addition, details on the sensors which obtained the data can be provided through the UDL.

Although a catalog of the growing RSO population will continue to be a challenge, the UDL can be used to obtain observations from multiple data sources for SSA. With vast amounts of data, from many sources, comes the challenge of determining which data sources should be selected. A sensor network from one data provider may have more accurate sensors than another sensor network, but a second sensor network may have observations from a larger number of sensors. If observations are to be purchased given a limited budget, a purchaser will want to determine which data sources are most advantageous for a particular application. The following simulation analyzes a system with multiple observers compared to a system with a single observer to determine the impact on observability. In addition, the accuracy of multiple observers is varied to determine if a single, more accurate sensor or multiple, less accurate sensors are more beneficial.

In the following simulations the observability of an Atlas V upper stage, identified by NORAD satellite number 40295 and international designator 2014-068B, is analyzed. The position and velocity of the Atlas V object at an epoch of 58932.0974 MJD are defined in Table 3.17. In addition, two observers, otherwise known as ground stations, are implemented in these simulations of observability. The latitude and longitude of two fictitious ground stations are defined in Table 3.18.

Table 3.17. Atlas V upper stage position and velocity at epoch.

x [km]	y [km]	z [km]	v_x [km/s]	v_y [km/s]	v_z [km/s]
-20189.516	7946.505	16631.776	0.487	-3.108	2.167

The simulations in this analysis compare the observability of two systems: two, less accurate ground stations and a single, more accurate ground station. The first ground station location, designated by GS_1, is used in both systems. For the system with one ground station only, the measurement noise is defined by a standard deviation of 0.1 arcseconds in the right ascension measurements and a standard deviation

Table 3.18. Ground station coordinates.

Ground Station	Latitude [°]	Longitude [°]
GS_1	37.5	-115.0
GS_2	25.0	-105.0

of 0.05 arcseconds in the declination measurements. When two ground stations are used in the observability analysis, a range of measurement uncertainties are implemented to compare advantages of multiple observers for observability in the presence of measurement uncertainties. Recall from Section 3.4 that the ratio of the measurement uncertainty between the right ascension and declination measurements has an impact on the time to become observable. When the measurement noise is equal between the two measurement variables, the binary criteria of observability will not be theoretically impacted. Figure 3.63 shows the impact of the variance ratio on the time to become observable for the Atlas V object and ground station one only. For the Atlas V object, the impact on the time to become observable due to the measurement noise variance ratio is similar to the inclined orbits in Figures 3.1 and 3.2. Moreover, when the measurement uncertainty in declination is larger than the measurement uncertainty in right ascension, the time to become observable increases more than the opposite case.

Because the system observability is impacted by the measurement noise variance ratio, this quantity is varied to define sensors with more or less accuracy. Table 3.19 shows the standard deviation in the right ascension and declination measurements for each case in this analysis. When two observers are implemented, both observers have the same measurement noise given by the values in Table 3.19.

Three simulations, differing in measurement sequence and length, are shown in the following. First, the observability of the Atlas V object with one observer and with two observers is compared for an analysis time of 100 seconds. The goal of this

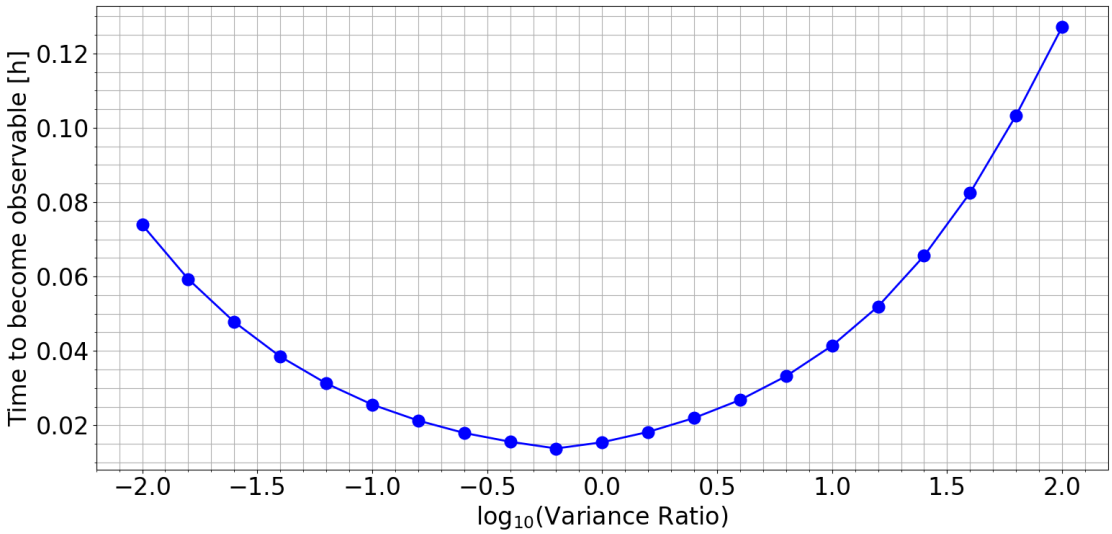

Figure 3.63. Time to become observable versus measurement noise variance ratio, $\sigma_\delta^2/\sigma_\alpha^2$, for the Atlas V object.

Table 3.19. Different right ascension and declination measurement noise standard deviation cases.

Ground Station	σ_α [arcsec]	σ_δ [arcsec]	$\sigma_\delta/\sigma_\alpha$
GS_1	0.1	0.05	0.5
GS_1 & GS_2	0.1	0.05	0.5
GS_1 & GS_2	0.1	1.0	10.0
GS_1 & GS_2	0.1	100.0	1000.0
GS_1 & GS_2	0.1	1.0×10^5	1.0×10^5
GS_1 & GS_2	0.1	1.0×10^6	1.0×10^7

simulation is to determine the impact of adding a second observer on the time to become observable. In addition, the influence of the measurement noise ratio with two observers on the time to become observable is analyzed.

Figure 3.64 shows the smallest singular value of the observability matrix and the tolerance line for several systems. The blue line represents the single observer with a more accurate sensor. The remaining curves represent systems with two observers but less accurate sensors compared to the single observer case. A tolerance line is also defined for each system, in the corresponding color, as defined by Equation 2.15. The single observer case becomes observable in approximately 50 seconds. The systems defined by two observers with a measurement noise standard deviation ratios of 1000.0 and 1.0×10^5 become observable within the first few measurements. The final, two observer system in brown does not become observable in this analysis time.

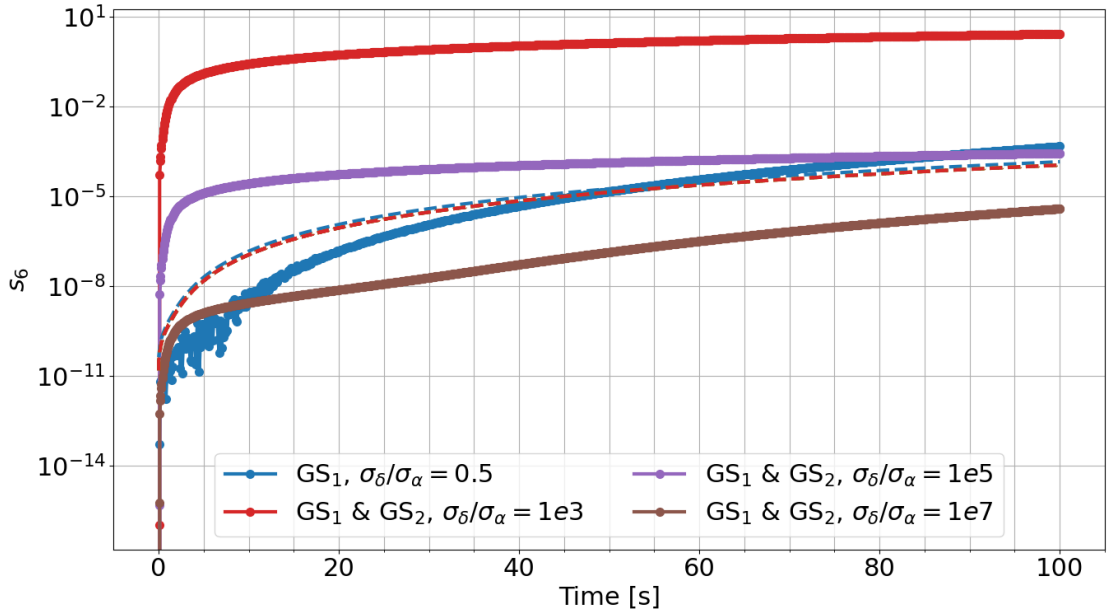

Figure 3.64. Comparison of the observability matrix smallest singular values for a case with one observer and several cases with two observers.

The observability results are presented in a different way in Figure 3.65. The previous section investigated the importance of the height of the observability matrix singular values above the tolerance line. Therefore, instead of showing both the smallest singular value and the tolerance line, the observability matrix smallest singular value-tolerance ratio is shown in Figure 3.65. With this ratio, a system is considered

observable when the ratio is larger than one. For the remaining simulations, this representation of the observability results is implemented.

For the cases with two observers, there is a large initial spike in the singular value-tolerance ratio, and then this value slowly reduces for the remainder of the simulation. This decrease in the singular value-tolerance ratio is not due to a decrease in the singular values of the observability matrix. When comparing to the singular values in Figure 3.64, the singular values continue to increase in the analysis but the rate at which they increase reduces.

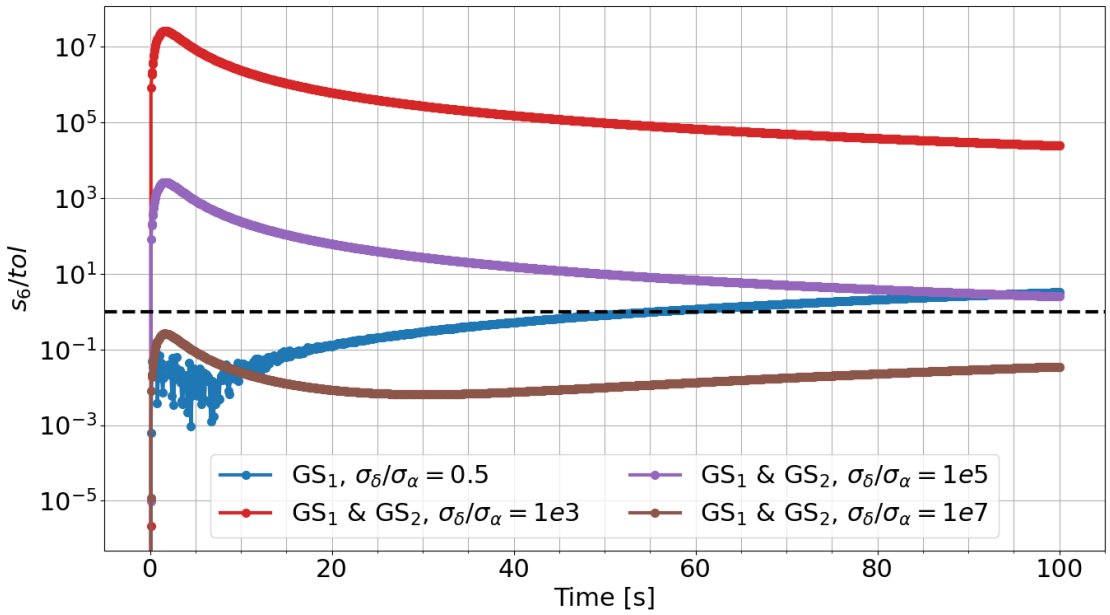

Figure 3.65. Singular value-tolerance ratio for short time span.

The percent increase in the smallest singular value resulting from the GS$_2$ measurement is shown in Figure 3.66 to explain this behavior in more detail. For the cases with two observers, measurements are processed from both observers at the same time. Initially, the percent increase from a second observer is large, but as time progress the percent increase reduces. This behavior occurs because an observer at a different location creates a larger geometric difference in the measurements of the Atlas V object. Therefore, the system becomes observable much quicker. However,

as more measurements are acquired and the orbit of the Atlas V object is more resolved by the measurements, the percent increase in the singular values attributed to the second observer is not as significant. Note that the larger measurement noise ratio case has a larger percent increase in the smallest singular value compared to the other measurement noise cases because the less accurate sensors require more measurements to improve the knowledge of the orbit.

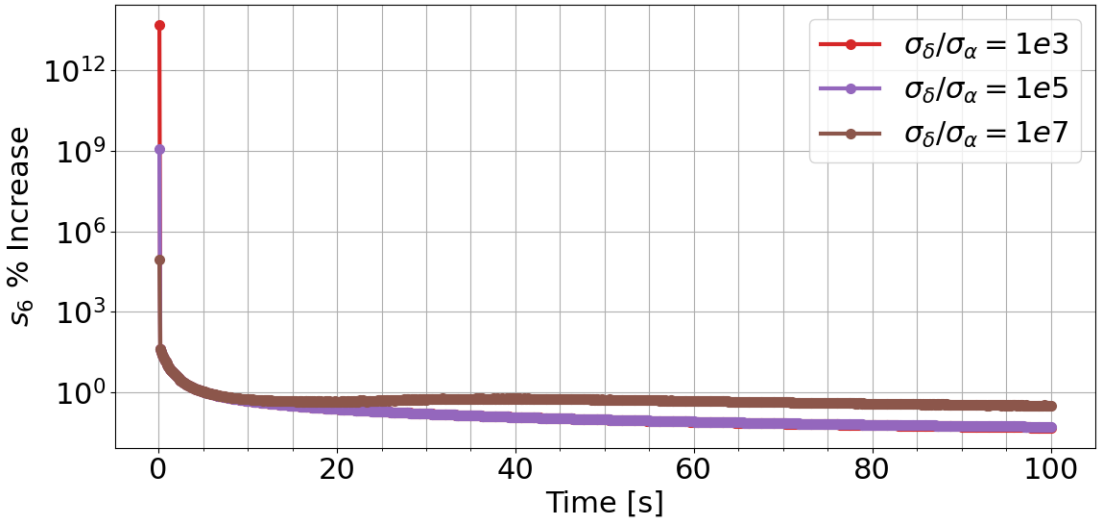

Figure 3.66. Percent increase in the smallest singular value due to the second observer.

Over a short analysis time, two observers with less accurate sensors compared to a single, more accurate sensor, are advantageous for achieving observability. The second sensor provides a large geometrical advantage for gaining knowledge of an orbit from right ascension and declination angles. A comparison of the single observer to two observer systems continues with a longer analysis time. Figure 3.67 shows the smallest singular value-tolerance ratio for the single observer system and several two observer systems with differing measurement noise variance ratios. All of the measurement noise cases in Table 3.19 are shown in Figure 3.67.

The blue curve represents the single observer case, and the yellow curve represents the system with two observers where both sensors are as accurate as the single observer

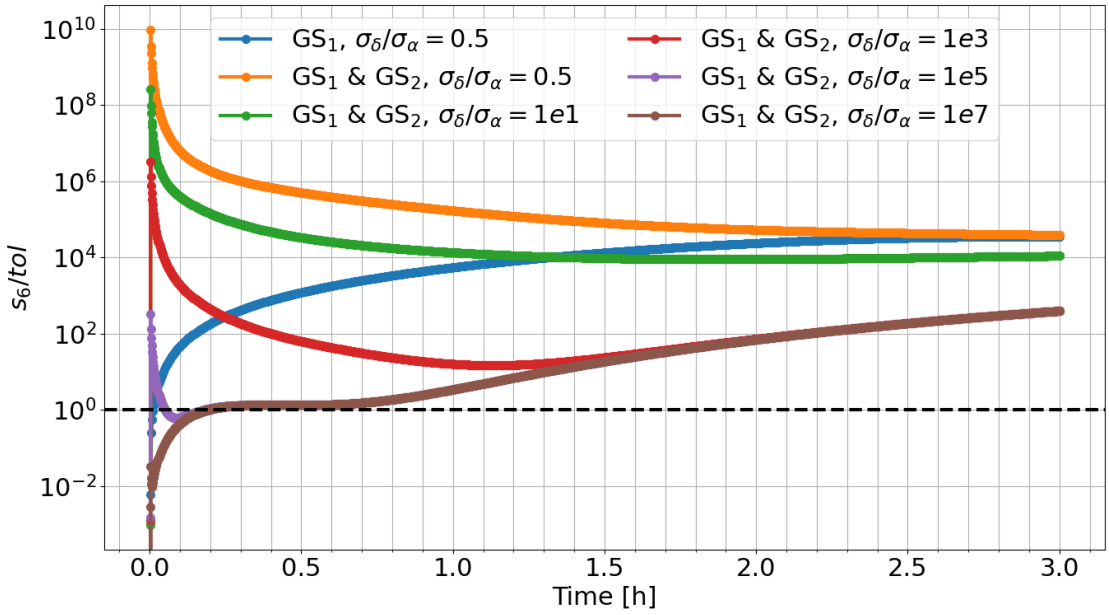

Figure 3.67. Singular value-tolerance ratio over longer time scales.

case. Similar to the previous observability results, the two observer case has a large increase in the singular value-tolerance ratio initially, but the ratio decreases with time. In contrast, the single observer case has a singular value-tolerance ratio which continues to increase throughout the analysis. After three hours of analysis, the single observer case and the two observer case with the same measurement noise ratio have the same singular value-tolerance ratios. This indicates that the second observer initially provides a large amount of knowledge about the orbit due to the geometric difference of the second ground station, but after three hours, the advantages resulting from the second observer are no longer significant when the single observer case has the same ratio value.

When the noise is increased in the declination measurement for the two observers, the system still becomes observable faster than the single observer system, except for the largest measurement noise case. However, when two sensors are less accurate than a single sensor, the singular value-tolerance ratio will be smaller after some time due to the influence of the measurement noise on the system. In the three most

extreme measurement noise variance ratio cases for the two observers, the singular value-tolerance ratios at the end of the analysis time are all the same.

Next, the percent increase in the smallest singular value of the observability matrix due to the second observer is shown in Figure 3.68. The percent increase in the first few measurements is large compared to the percent increase later in the analysis. As previously discussed, this large change in the percent increase is due to the initial geometric diversity provided by the second observer, and when the orbit knowledge is resolved with the measurements, the impact of the second observer reduces.

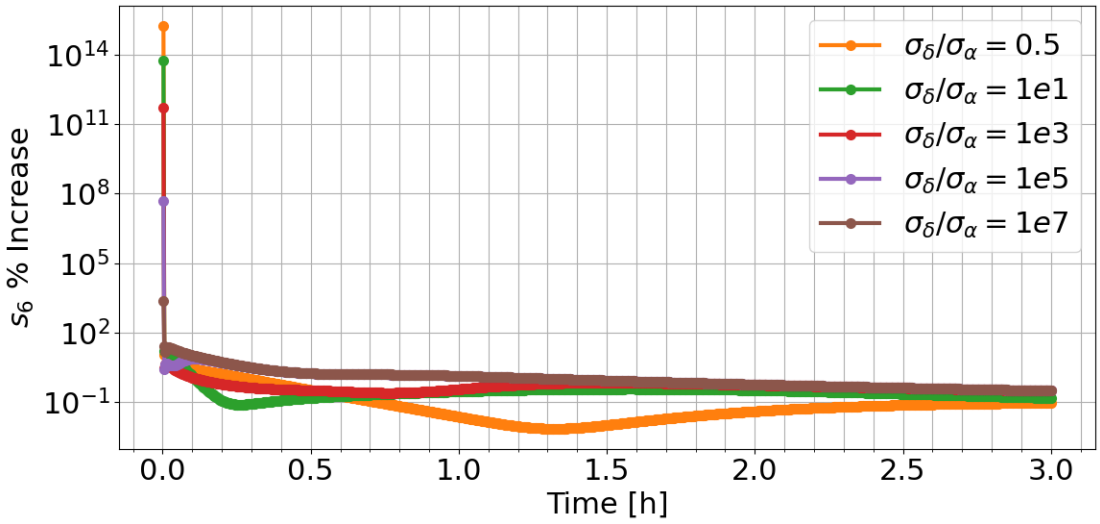

Figure 3.68. Percent increase in the smallest singular value over longer time span.

Figure 3.69 shows the percent increase after the first few measurements in more detail. Similar to the shorter simulation, the percent increase in the smallest singular value of the observability matrix is lower at the end of the analysis when the measurement noise variance ratio is lower because of the influence of the measurement noise on the observability.

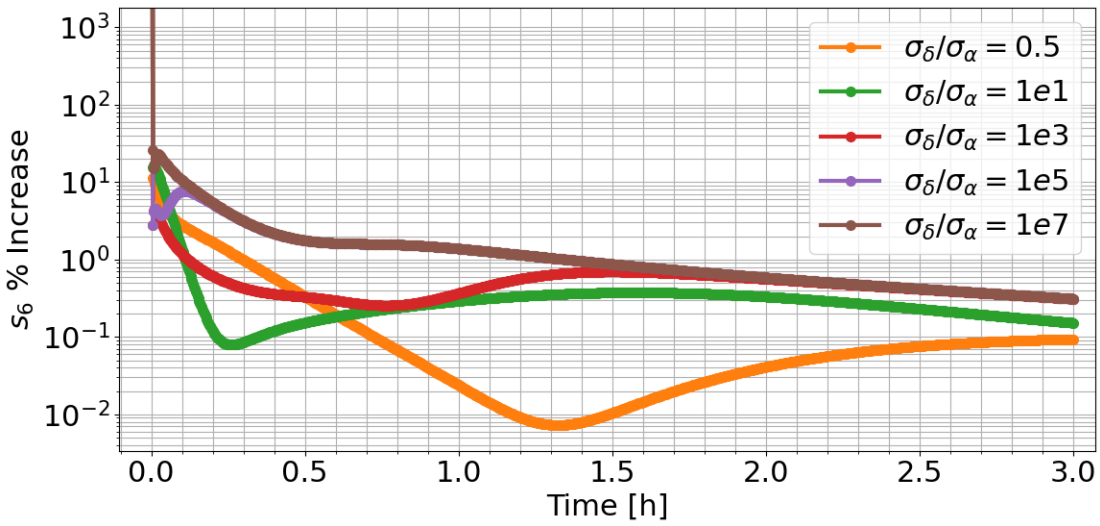

Figure 3.69. Percent increase in the smallest singular value over longer time span, zoomed in to show detail.

The final simulation is the same length as the previous simulation, but measurements are more sparse. For the single observer and the two observer cases, measurements are spaced every half hour. Figure 3.70 shows the singular value-tolerance ratio for the systems given in Table 3.19. When this system contains two observers, observability is still achieved faster than the single observe case, except for the two most extreme measurement noise variance ratio cases. However, after a few time steps, the single observer has a higher singular value-tolerance ratio than each of the two observer cases except for the sensors with accuracy equal to the single observer.

Finally, Figure 3.71 shows the percent increase in the smallest singular value due to the second observer. For the two most extreme measurement noise cases in Figure 3.71 the percent increase grows after the first time step because these cases are still unobservable during the first time step. However, after the first time step, the percent increase begins to reduce similarly to the other measurement noise cases. When the measurements in this system are more sparse, the advantages of a second observer for observability are not as evident.

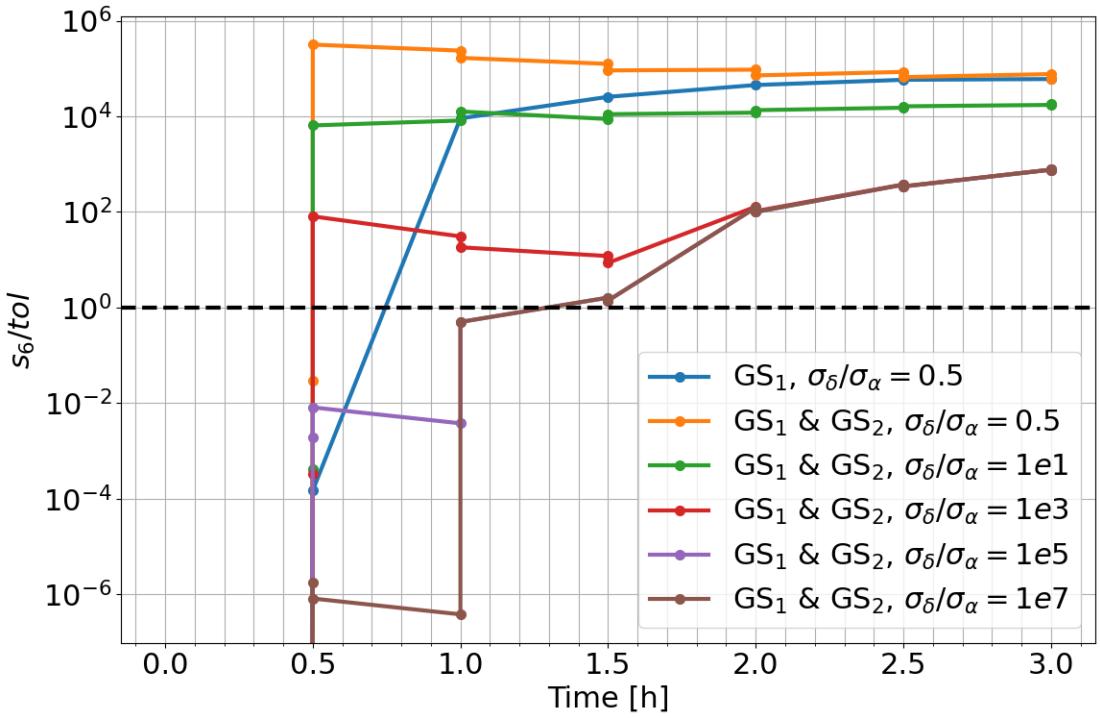

Figure 3.70. Singular value-tolerance ratio over longer time scales with sparse measurements.

This analysis compared the observability of a system consisting of a single, more accurate sensor and a system consisting of two, less accurate sensors. The observability results have shown that a second sensor provides a large geometric advantage for obtaining sufficient knowledge of an orbit. This advantage is large initially, and even large measurement noise variance ratios still result in a faster time to become observable, except for extreme measurement noise cases. However, for the Atlas V object after approximately three hours, the advantages of two sensors are no longer apparent in the singular values of the observability matrix when compared to the single sensor case. When the single sensor and two sensor cases both have the same measurement noise variance ratios, the singular value-tolerance ratios are the same after three hours. This indicates that the single observer measurements are able to obtain the same knowledge of the orbit through right ascension and declination mea-

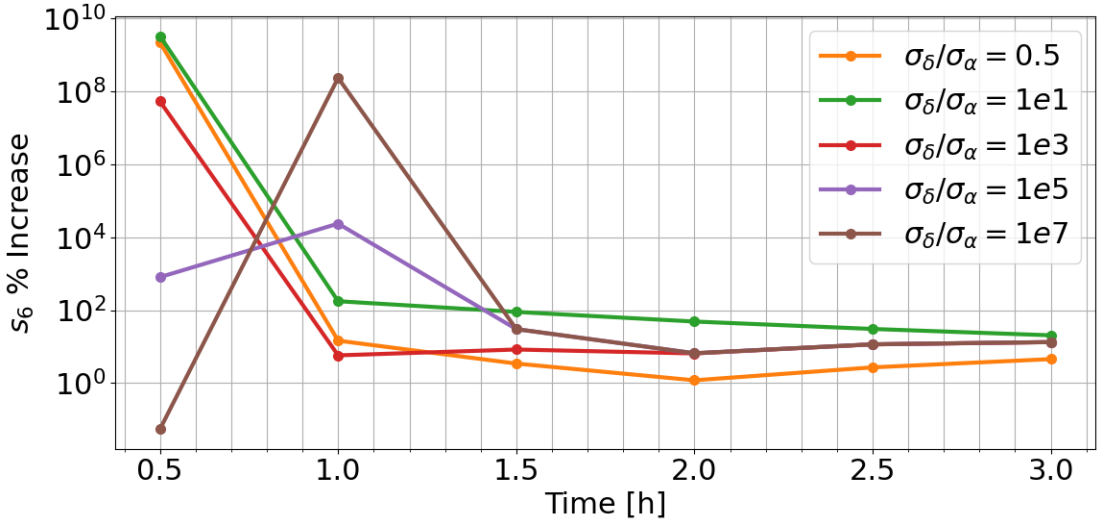

Figure 3.71. Percent increase in the smallest singular value over longer time span with sparse measurements.

surements. However, when the two sensors are less accurate than the single sensor, the singular value-tolerance ratio is smaller at the end of the analysis.

These findings could be applied to data purchasing decisions. For example, the UDL provides information on what data products are available from various sensors at different locations around the Earth. Assuming that the measurement noise covariance for each sensor is also provided, stochastic observability analysis could be performed with different combinations of sensors. A trade-off analysis between cost and desired observability results could be performed to determine if fewer, more accurate sensors are advantageous over many, less accurate sensors. Similarly, this observability analysis could aid in sensor network development decisions. More sensors will be able to provide greater geometrical diversity for observability, but if these sensors are less accurate than only a few, more accurate sensors, the initial geometrical advantages may not be as significant. Overall, these observability analysis methods can be implemented to inform cost-performance based decisions for SSA.

4. OBSERVABILITY-ESTIMABILITY INFORMED CONSIDER FILTER

The previous chapter on observability of the orbit problem demonstrated the power of observability analysis for prediction of estimation accuracy. Observability utilizes the state and measurement dynamical models for a system to determine whether measurements are sufficient for obtaining knowledge of the states. Therefore, observability is primarily thought of as an analysis tool prior to performing estimation. Where observability is a predictive tool for estimation, estimability is a post-evaluation tool for estimation. Estimability is applied to the orbit problem with extended states to evaluate what knowledge can be gained from the method.

In addition, observability and estimability are applied in a Consider Filter approach to the orbit problem with an extended state. Observability is implemented as a measure for indicating when consider parameters should be estimated, and estimability is implemented to evaluate the order in which consider parameters should be estimated. Accuracy of state estimates are compared for the Extended Kalman Filter (EKF) and observability-estimability informed Consider Filter.

4.1 Estimability

Many methods exist for evaluating deterministic observability, stochastic observability, and estimability for dynamical control systems. As introduced in Section 2.6, the terminology for stochastic observability versus estimability is not always consistent. Some works analyzing the *a priori* and *a posteriori* state estimation error covariance label this analysis as stochastic observability, but in the scope of this work, stochastic observability is limited to analysis of the state and measurement models with initial state and measurement uncertainties. Therefore, methods analyzing *a*

priori and *a posteriori* state estimation error covariance for evaluating estimation performance are considered as estimability analysis.

In this work, the distinction between observability and estimability is defined by what aspects of a system is analyzing. Observability analyzes the system models to determine whether measurement information is sufficient for acquiring the states of a system. Even though observability has been shown to be an integral part of estimation in Chapter 3, the fundamental concept of observability is a method for exploring the measurement to state relationship through dynamical models. Moreover, Silva notes that the term observability should be restricted to investigation of a system with the system model matrices as in the observability matrix rank test [48].

Estimability, as applied in this work, focuses on evaluation of estimation performance, and common methods for this evaluation focus on the state estimation error covariance matrix over time [28, 39, 45, 47, 48, 52–54, 57, 59, 86]. Many of these works implement measures which consider a large decrease in state estimation error covariance as an indicator for an observable system. However, Hong et. al. [28] has shown that such a measure can be misleading due to the sensitivity to the initial error covariance of the state. In this work, the test for estimability is restricted to the methods developed by Ham [25, 43]. More specifically, the methods from Ham determine the relative estimation performance among the state variables with the eigenvalues and eigenvectors of a normalized error covariance matrix. Therefore, estimability is restricted to defining a relative result among the state variables and not an absolute result for the system as a whole.

4.2 Observability-Estimability Informed Consider Filter

Section 2.5.3 introduces the Schmidt-Kalman Filter (SKF), otherwise known as the Consider Filter (CF), as a method for improving the estimation of a system with parameters which are challenging to estimate. The stochastic observability matrix rank is implemented in this work as a measure for determining when consider pa-

rameters should change from considered to estimated. The system of interest for application of the CF is the state vector extended beyond position and velocity with SRP parameters, AMR and C. Previous analysis of this system has shown how the SRP perturbation has a small impact on the position and velocity of the orbit. Therefore, the SRP variables are more challenging to estimate compared to the position and velocity states, in general. While the rank of the stochastic observability matrix is less than or equal to six, the number of Cartesian position and velocity states in this system, the SRP extended state variables are defined as consider parameters. When the rank increases to seven, one of the SRP variables is changed from a consider parameter to an estimated state. If the rank of the observability matrix reaches eight, both SRP variables become estimated states.

However, a challenge exists for determining which consider parameters are estimated first. The CF approach thus far is informed by observability measures alone. Estimability is implemented for determining which SRP parameter should be changed from considered to estimated first when the rank of the stochastic observability matrix is increased from six to seven. Section 4.3 investigates estimability applied to the extended state orbit problem for determining the order in which the SRP parameters should be estimated in the CF approach.

4.3 Estimability of the Orbit Problem Results

Prior to applying observability and estimability for informing a CF, estimability analysis is investigated for the extended state system of Section 3.6.3. The estimability methods from Ham are applied to this system with the EKF, and the relative estimability of the state variables is evaluated. In addition, a fictitious problem is defined for exploring the relationship between uncorrelated states and estimability results.

An important feature of the estimability analysis is the covariance of the initial state because the normalization procedure of Equation 2.83 divides the *a posteriori*

state estimation error covariance matrix by the components of the initial state estimation error covariance matrix. In the estimability method from Ham, the initial state estimation error covariance matrix is assumed to diagonal, thus have uncorrelated state variables. As the initial state estimation error covariance is an important feature of the estimability analysis method, the initial state uncertainties should be defined with realistic values for an orbit and object. For the orbit problem, the *a posteriori* state estimation error covariance is typically non-diagonal, with correlated components among the state variables. Therefore, uncorrelated components of a realistic state estimation error covariance must be determined for use as the initial state estimation error in the estimability analysis. A method developed by List is implemented for splitting a covariance matrix into correlated and uncorrelated parts [160].

The GEO 4 object, defined in Table 3.2, with a state extended beyond position and velocity with time-varying AMR and C was estimated over five orbits with the EKF to define the initial state estimation error for estimability analysis. The uncorrelated part of the *a posteriori* state estimation error covariance matrix from that EKF simulation was computed with the method from List. Next, the uncertainties from the uncorrelated part of the covariance were scaled up by 1.0×10^5 to define the initial state estimation error for this investigation of estimability of the orbit problem. Table 3.4 gives the initial state uncertainties implemented throughout this analysis of estimability. In addition, the same measurement uncertainties, observer, and extended state cases from Section 3.6.3 are used in the following simulations.

4.3.1 Estimability with an Uncorrelated State

An eigenvector for the $\mathbf{P}(t_k)^{N^+}$ matrix shows a vector direction in the eigenspace, and the vector direction can depend on a single state component or multiple state components. The former case would clearly define the relative estimability of a state variable depending on the eigenvalue associated with the eigenvector. However, the latter case represents a linear combination of states which is more or less estimable,

rather than representing the estimability of a single state variable. Therefore, the correlated nature of the state estimation error covariance matrix in the orbit problem can result in challenging interpretation of the system estimability. Prior to applying estimability methods with a state vector extended by the AMR and C variables, which are correlated within the SRP perturbation, a system is defined as an example for demonstrating how uncorrelated states result in more clear estimability eigenvector directions.

In the following analysis, the variable β is completely uncorrelated from the state dynamics and measurements. A thorough discussion of the eigenvalue and eigenvector curves for estimability is left for the extended state results with AMR and C in Sections 4.3.2 and 4.3.3. For this example problem, only a few of the eigenvectors of the normalized state estimation error covariance matrix are presented to demonstrate the affect of uncorrelated states on estimability. Figure 4.1 shows two of the eigenvectors of the normalized state estimation error covariance matrix after EKF estimation of this system with a state extended beyond position and velocity with β. The different curves in Figure 4.1 represent the values of the eigenvector components associated with each state variable over time.

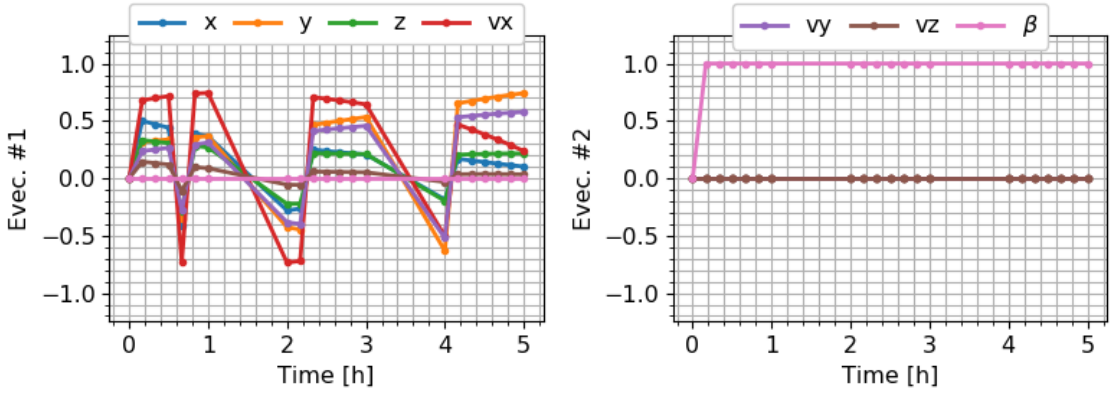

Figure 4.1. Two eigenvectors of the normalized state estimation error covariance matrix for the example problem with an uncorrelated state, β.

In this system, the β variable is completely uncorrelated from the other states in the dynamics. Therefore, one of the eigenvectors in the estimability analysis is expected to be directed towards the β state. The second eigenvector, on the right of Figure 4.1, confirms this expected behavior. This eigenvector direction indicates the relative estimability of the β state variable rather than the estimability of a linear combination of states. For a system which is highly correlated, the estimability eigenvector directions are not as clearly interpreted. For example, the first eigenvector, on the left of Figure 4.1 has components associated with each of the position and velocity states. Therefore, these eigenvector directions indicate the relative estimability of the linear combination of the state variables.

For a system with an uncorrelated state or multiple uncorrelated states, the estimability methods from Ham clearly show the relative estimability of the uncorrelated state or states. However, for a system with highly correlated states, as is the case of the Cartesian position and velocity states of the orbit problem, the interpretation of the estimability results is more challenging, but improved understanding of a system can still be achieved with estimability analysis. Next, estimability analysis is applied to the state cases of Section 3.6.3 to determine the relative estimability of the states in a system extended with SRP parameters. In addition, this analysis focuses on utilizing estimability for informing CF decisions.

4.3.2 Constant AMR and C

The following estimability analysis is performed in conjunction with the EKF estimation analysis of Section 3.6.3. The initial state uncertainty from Table 3.4 and the *a posteriori* state estimation error covariance in each of the extended state cases is used to compute the normalized state estimation error covariance of Equation 2.82. The eigenspace is determined for the normalized state estimation error covariance matrix at the time of each measurement within the estimation.

The interpretation of the normalized state estimation error eigenspace defines the relative estimability of the state variables. Figure 4.2 presents the eigenvalues of the normalized state estimation error covariance matrix. The eigenvalues are bounded between zero and eight, the number of state variables. Large eigenvalues correspond to eigenvector directions with weak relative estimability, and small eigenvalues correspond to eigenvector directions with strong relative estimability. The estimability results are relative among the state variables.

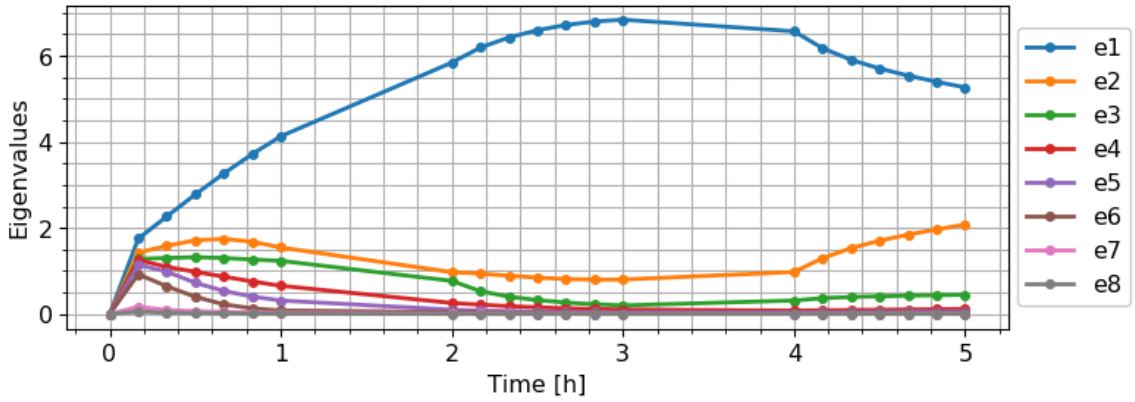

Figure 4.2. Eigenvalues of the normalized covariance matrix of the state estimation error for constant AMR and C.

The eight eigenvectors associated with the eigenvalues of Figure 4.2 are shown in Figure 4.3. The numbers assigned to each eigenvalue curve are associated with the same eigenvector number in Figure 4.3. For example, the largest eigenvalue curve, e_1, of Figure 4.2 corresponds to eigenvector one of Figure 4.3. Therefore, the direction with the strongest relative estimability is depicted with eigenvector one, and the direction with the strongest relative estimability is depicted with eigenvector eight.

There are eight curves corresponding to each of the state directions for each of the eigenvectors. Over time, the eigenvector curves for each state variable depict how much the state contributes to the weak or strong relative estimability. Therefore, at each time step, the relative estimability can be compared for the linear combinations of states defining the eigenvector direction at each time step. When the states of

a system are strongly correlated, the interpretation of the eigenvector directions is challenging. If a state is uncorrelated from the dynamics of the system, the relative estimability of that state alone is easier to interpret as shown in Section 4.3.1.

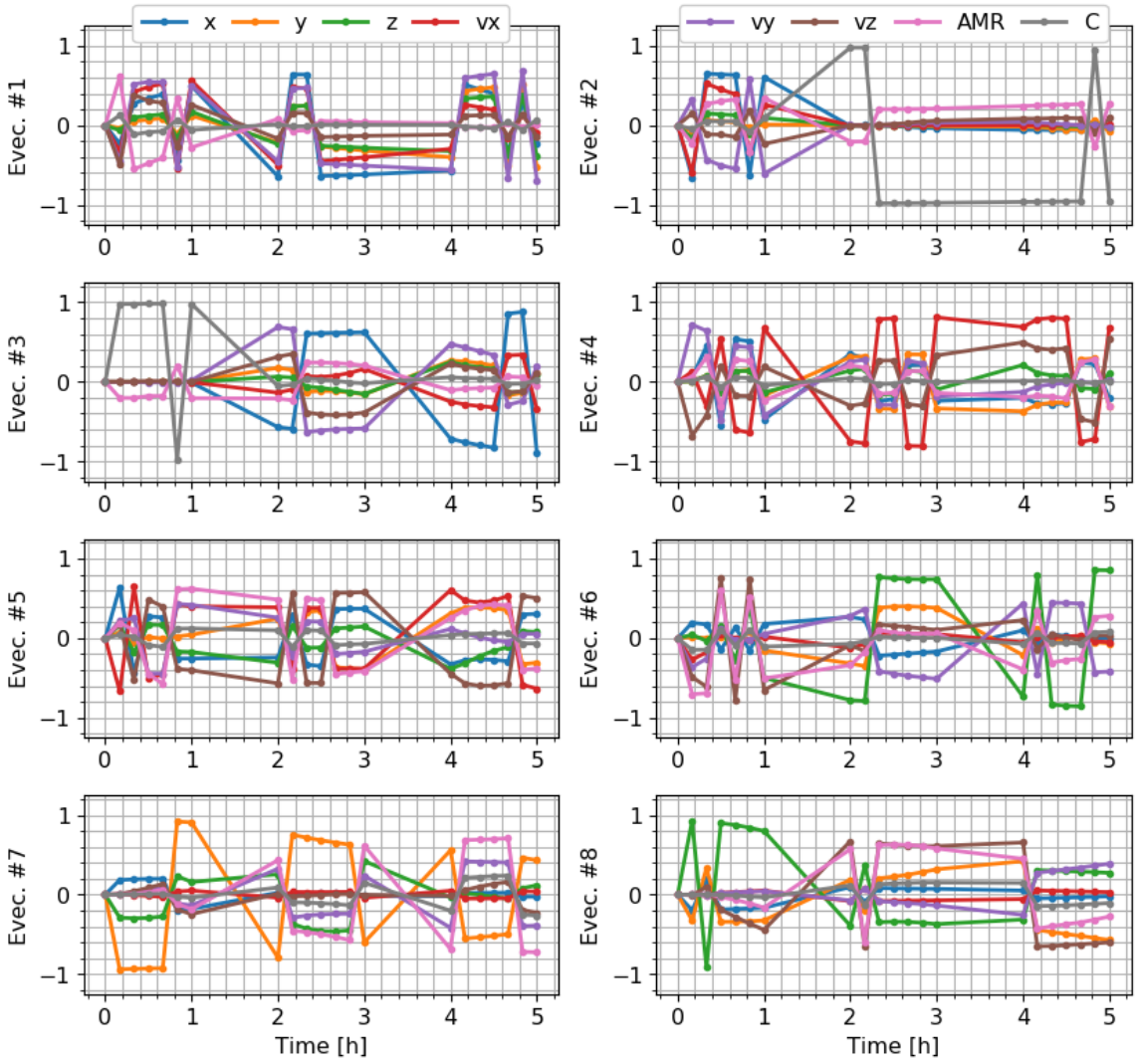

Figure 4.3. Eigenvectors of the normalized covariance matrix of the state estimation errors for constant AMR and C.

Within the first batch of measurements, up until one hour from epoch, two of the eigenvalues in Figure 4.2 are smaller compared to the other six eigenvalues. These two eigenvalues correspond to eigenvector directions which have stronger relative estima-

bility. In Figure 4.3, the corresponding eigenvectors to the two smallest eigenvalues within the first batch of measurements are dominated by position vector components. The dominant position component of eigenvector seven is the y position component, and the dominant component of eigenvector eight is the z position component. For the estimation of an orbit given angles-only measurements, estimation of the position is expected to be initially better than the estimation of the velocity. This is confirmed through estimability analysis. A linear combination of the position state variables has a stronger relative estimability than linear combinations of the other states in the system.

The directions of weakest relative estimability are given by eigenvectors one through three as the corresponding eigenvalues are larger than the other eigenvalues in Figure 4.2. The first eigenvalue is much larger than the other seven eigenvectors, but the second and third eigenvalues are also larger than the remaining five eigenvalues. The direction of weakest relative estimability, as shown by the first eigenvector of Figure 4.3, is a linear combination of all of the state variables over the first batch of measurements. However, the velocity components of the state, the x position state, and the AMR state dominate the first and second eigenvector directions. By comparing the first and second eigenvectors to the seventh and eighth eigenvectors, the weaker relative estimability of the velocity compared to position is evident.

The third eigenvector direction is initially dominated by AMR and C, and after several batches of measurements, the second eigenvector direction is dominated by the extended state SRP variables. Note that the C variable contributes more to the linear combinations of AMR and C in these two weaker relative estimability directions. This behavior follows the findings from Section 3.6 where the observability of a state extended with C took longer to become observable than a state extended with AMR.

In this system with constant AMR and C, these extended state SRP variables are expected to have weaker relative estimability because the SRP perturbation has a small impact on the position and velocity. However, the estimability analysis of Figures 4.2 and 4.3 do not show the AMR and C state variables as possessing the weakest

relative estimability compared to the position and velocity states. Initially, the measurement are not sufficient for computing the position and velocity state variables of the system, so a linear combination of all of the states as the direction of weakest relative estimability is in agreement with the initial estimation challenges. Over a longer analysis time, the AMR and C variables are expected to be the directions of weakest relative estimability.

Figures 4.4 and 4.5 show the estimability results for the constant AMR and C case for a longer analysis time. Two of the eigenvalues in Figure 4.4 are significantly larger than the other eigenvalues. The corresponding eigenvector directions in Figure 4.5 show the directions of weakest relative estimability. Note that the absolute value of the eigenvector components is presented in Figure 4.5 to make the dominant components more clear.

As expected, a linear combination of the AMR and C variables have the weakest relative estimability after approximately 14 hours in the first eigenvector. Moreover, the AMR and C variables are the only components defining the weakest relative estimability direction in the first eigenvector after approximately 14 hours. In the second eigenvector, a linear combination of the AMR and C states is the dominant direction from approximately 2 hours to 14 hours. Earlier in the analysis, a linear combination of all of the states, with x position and velocity components being dominant, has the weakest relative estimability, but over time, the estimability of the position and velocity states improves and the estimability of the SRP variables weakens. As this analysis primarily focuses on the relative estimability of the SRP variables, the remaining eigenvectors are shown in Appendix B.1.1.

4.3.3 Time-Varying AMR and C

Next, the estimability is analyzed for the state extended beyond position and velocity with time-varying AMR and C. The eigenvalues and eigenvectors for the time-varying AMR and C case are nearly identical over three batches of measurements

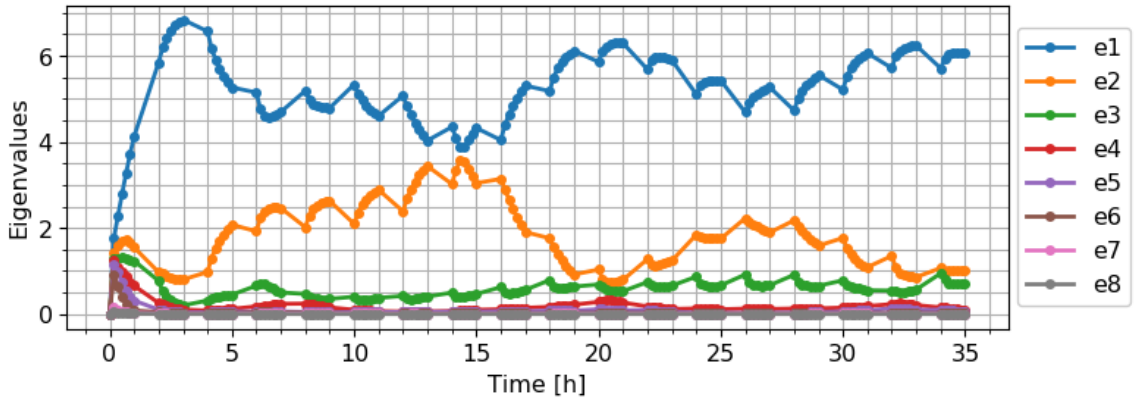

Figure 4.4. Eigenvalues of the normalized covariance matrix for the constant AMR and C case with a longer analysis time.

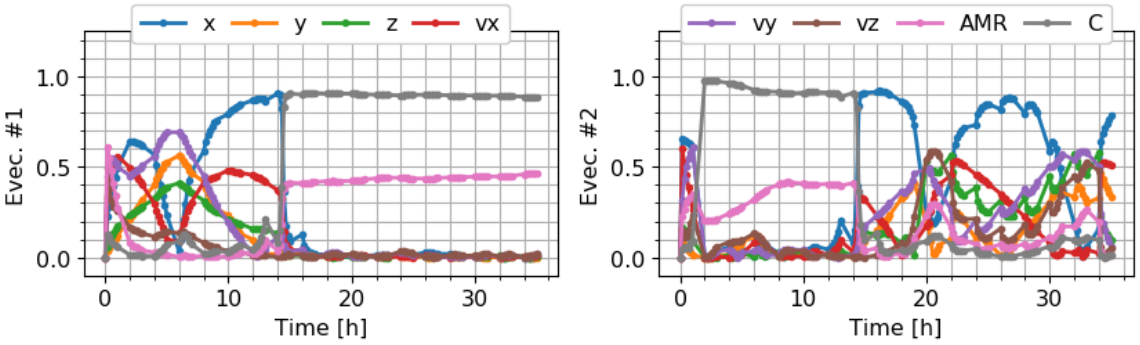

Figure 4.5. 1st and 2nd eigenvectors of the normalized covariance matrix for the constant AMR and C case with a longer analysis time.

to the eigenvalues and eigenvectors of the constant AMR and C case. Due to the similarity of the estimability results for the constant AMR and C case compared to the time-varying AMR and C case, focus is placed on differences in the estimability results. The full estimability results for the constant AMR and C case are shown in Appendix B.1.2.

Figure 4.6 shows the eight eigenvalues of the normalized state estimation error covariance matrix for the time-varying AMR and C case. Similar to Figure 4.4, three of the eigenvalues are larger compared to the other five. Figure 4.7 shows the first two eigenvectors of the normalized state estimation error covariance matrix over

time, which correspond to the two largest eigenvalues in Figure 4.6 and indicate the directions of weakest relative estimability.

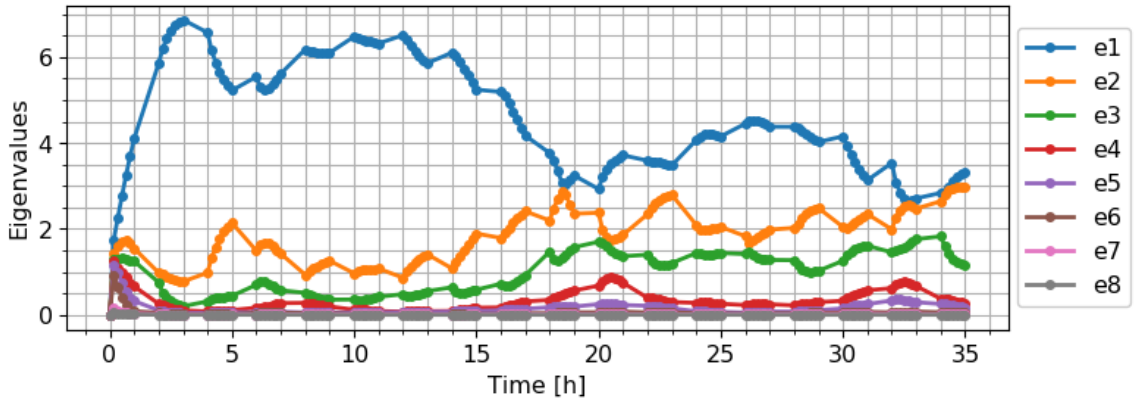

Figure 4.6. Eigenvalues of the normalized covariance matrix for the time-varying AMR and C case.

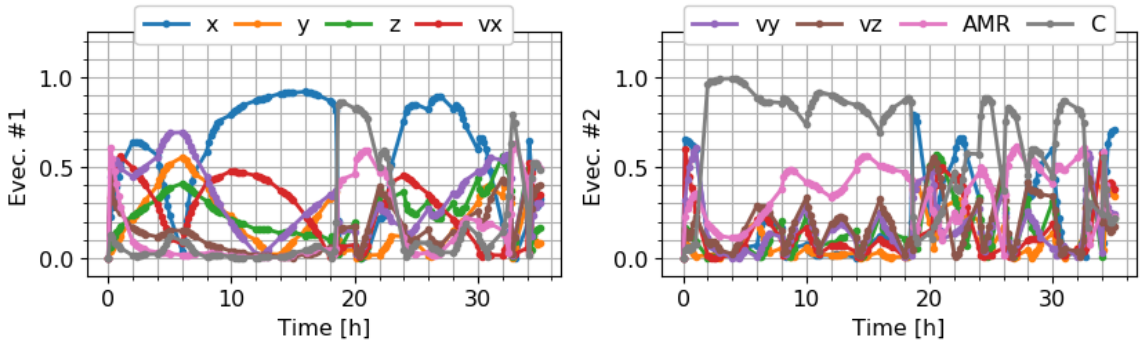

Figure 4.7. 1st and 2nd eigenvectors of the normalized covariance matrix for the time-varying AMR and C case.

When comparing the weakest relative estimability directions of Figures 4.5 and 4.7, the trends in the linear combinations of the states initially appear the same. The first eigenvectors are a linear combinations of all the state components, and after approximately eight hours, the x component of position and velocity dominates the linear combination of the states. Significant differences arise between the first eigenvector for the extended state cases after approximately 14 hours. The SRP variables begin to dominate the linear combination of states for constant AMR and C case and

continue to be the largest components of the weakest relative estimability direction. However, in the time-varying AMR and C case, the SRP variables are only dominant components of the first eigenvector for a few hours. In Figure 4.7, a linear combination of all of the states dominates the direction of weakest relative estimability, except for hours 18 through 22, where the AMR and C states dominate the weakest eigenvector direction. In the second eigenvector, the AMR and C components are more dominant when compared to the constant AMR and C estimability results.

This change in the dominant components of the direction of weakest relative estimability for the time-varying AMR and C extended state case compared to the constant AMR and C extended state case agrees with the findings of Section 3.6.3. The SRP perturbation is affected by the SRP variables differently because the AMR and C variables vary with time. Therefore, the contribution of AMR and C can be identified within the measurements. Also, C still has a larger eigenvector component in the first and second eigenvectors compared to the AMR contribution, which aligns with the comparison of the times to become observable for the state extended by AMR and the state extended by C in Section 3.6.1.

The extended state cases with one time-varying SRP parameter and one constant SRP parameter are shown in Appendix B.1.3 and Appendix B.1.4. Similar to the analysis in Section 3.6.3, these cases with one time-varying SRP parameter and one constant SRP parameter have similar results to the constant and time-varying AMR and C cases. The estimability results for the time-varying AMR and constant C extended state case are nearly identical to the estimability results of the time-varying AMR and C extended state case. The estimability results for the constant AMR and time-varying C extended state case are nearly identical to the estimability results of the constant AMR and C extended state case.

4.3.4 Summary

Estimability analysis methods from Ham shows how well the states of a system are estimated relative to one another. The *a posteriori* state estimation error covariance matrix is normalized with the initial state uncertainty, which must be uncorrelated. The normalization makes the estimability analysis sensitive to the initial state uncertainty. Unlike observability analysis, an overall binary result does not exist with estimability analysis where a system could be said to be estimable or not. However, the estimability analysis does show how well the states of a system are estimated compared to one another. This knowledge of state performance relative to other states is not defined for observability analysis in general.

A major challenge facing estimability for the orbit problem is the correlated nature of the Cartesian position and velocity state variables. When a state is uncorrelated, the estimability analysis clearly indicates where the estimability of that uncorrelated state resides compared to the other states. However, when many of the state variables are correlated, the directions of relative estimability shown with the eigenvectors are linear combinations of the state variables. Even with this challenge of correlated state variables, general trends appear in the estimability results which align with knowledge of the orbit problem. For example, linear combinations of the position state variables have stronger estimability than linear combinations of the velocity state variables, in general. Also, the difficulty in estimating the SRP parameters in this system is evident with the estimability analysis. Moreover, the C eigenvector component is often more dominant than the AMR eigenvector component, which agrees with the time to become observable for a system extended with C compared to a system extended with AMR. This knowledge of the estimability of the AMR and C state variables is utilized in a CF approach in an attempt to improve state estimation errors.

4.4 Observability-Estimability Informed Consider Filter Results

Estimability analysis has shown that the SRP extended state variables are challenging to estimate for the system extended beyond position and velocity with AMR and C. Observability analysis in Section 3.6 has shown that the time to become observable increases when a state consisting of Cartesian position and velocity is extended by AMR, C, or a combination of the two SRP parameters. In addition, when both parameters are included in the state vector as separate, solve-for variables, the time for the seventh singular value of the observability matrix to cross the tolerance line increases compared to the combined AMR$\cdot C$ case. This indicates that a system with more state variables which are more difficult to observe is detrimental to the time to become observability.

The knowledge gained from estimability and observability is applied to the CF approach in an effort to improve the state estimation errors resulting from the EKF. Stochastic observability with measurement uncertainty is implemented as a measure for determining when consider parameters should be estimated. The state vector for the consider approach is given by Equation 2.80, where the state components are defined as

$$\mathbf{s} = \begin{bmatrix} x & y & z & \dot{x} & \dot{y} & \dot{z} \end{bmatrix}^T, \qquad \mathbf{p} = \begin{bmatrix} \text{AMR} & C \end{bmatrix}^T, \tag{4.1}$$

The states to be estimated, $\mathbf{s}$, are the Cartesian position and velocity, and the consider parameters, $\mathbf{p}$, are the SRP variables, AMR and C. The AMR and C cases in Table 3.3 are implemented in the CF. The stochastic observability measure is implemented such that one of the consider parameters is added to the estimated states each time the rank of the stochastic observability matrix increases beyond six. For example, when the rank of the stochastic observability matrix is seven, either AMR or C is added to the estimated states, and when the rank of the observability matrix is eight, both SRP parameters are added to the estimated states. In addition, if the rank of the observability matrix decreases, the consider parameter which was most recently turned into an estimated state is changed to a consider parameter once again.

With this consider approach, a decision must be made as to which consider parameter should be added to the state first when the rank of the observability matrix increases to seven. The observability rank measure for determining when to move a consider parameter to the estimated states is not sufficient for determining which consider parameter should be added first when multiple consider parameters exist. Estimability analysis has shown that the C state is more difficult to estimate relative to the AMR state. The impact of estimating the C variable first in the consider approach compared to estimating the AMR variable first is explored for each of the AMR and C cases of Table 3.3. In addition, the state estimation errors without the CF approach are shown to determine if the consider approach improves the estimation of this system.

4.4.1 Constant AMR and C

First, recall the rank of the stochastic observability matrix with measurement uncertainties in Figure 3.14. When AMR and C are both constants, the rank of stochastic observability matrix changes from six to seven after approximately two hours of analysis, and the rank of the observability remains at seven until the end of the analysis. Therefore, with the observability matrix rank as a measure for the CF, one of the SRP state variables will be added to the estimated states after approximately two hours, and the second SRP parameter will remain as a consider parameter for the duration of the analysis.

Figure 4.8 shows the absolute value of the state estimation errors for the three estimations. The state estimation errors resulting from the EKF with all of the states estimated is given in red, the state estimation errors from the CF with AMR added first to the estimated states is given in blue, and the state estimation errors from the CF with C added first to the estimated states is given in green.

For the position and velocity state variables, the state estimation errors for each approach are all similar. The largest differences among the position and velocity

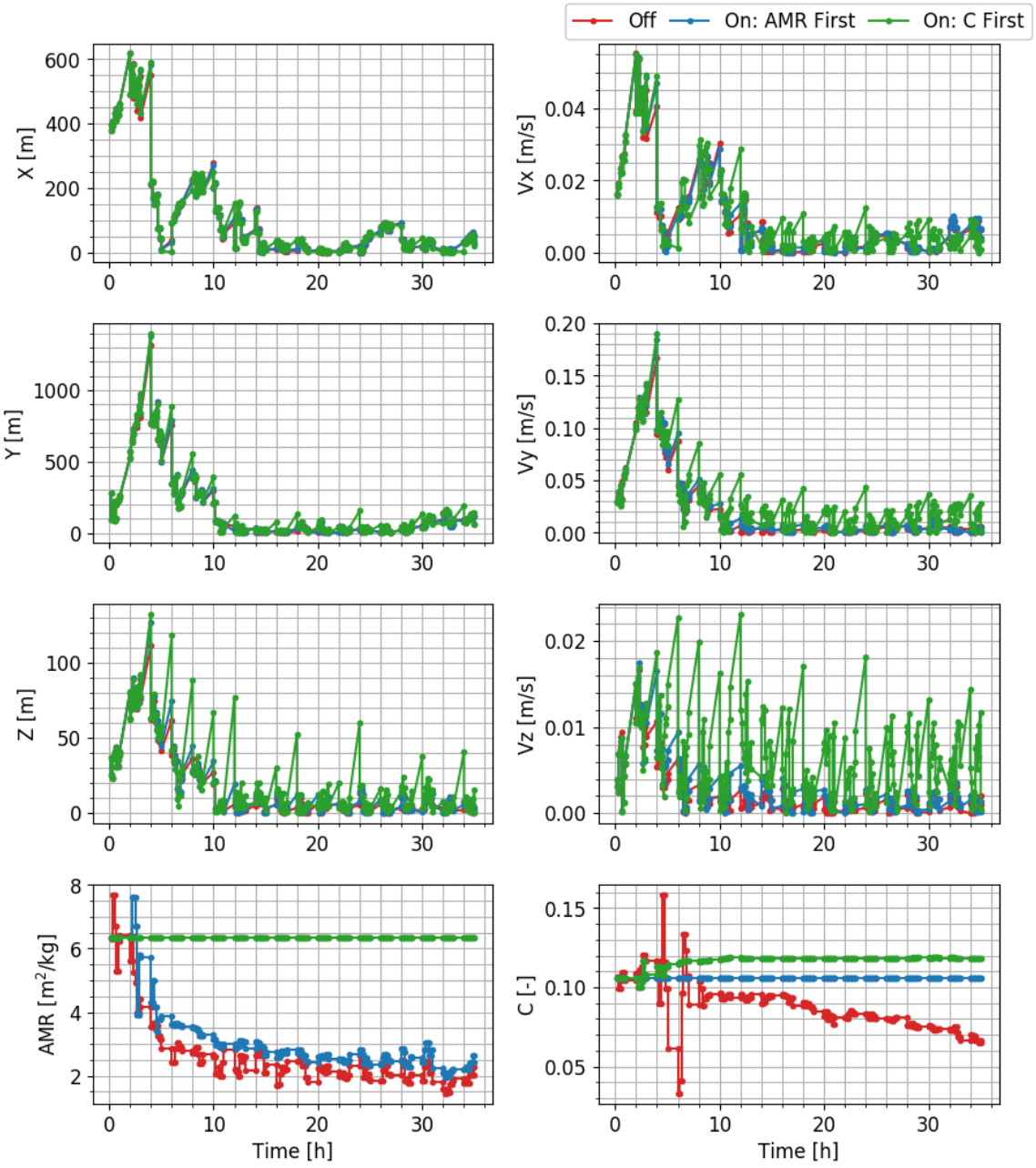

Figure 4.8. Consider filter state estimation errors for the constant AMR and C case.

state estimation errors exist with the z component of velocity. The CF approach where C is added first to the estimated states, has larger state estimation errors than the other approaches. The most significant state estimation error differences

appear in the AMR and C plots of Figure 4.8. For both variables, the approach with C added first has the largest state estimation errors. In addition, the EKF estimation without a consider approach has lower state estimation errors compared to both consider approaches. Also, the state estimation errors in the AMR variable are constant for the approach where C is added to the estimated state first in the CF. Likewise, the state estimation errors are constant in the C variable for the approach where AMR is added to the estimated state first in the CF. These constant state estimation errors show how these variables remain as consider parameters because the rank never reaches eight for the constant AMR and C system.

The consider approach for the system with a state extended by constant AMR and C is detrimental to the state estimation because the stochastic observability matrix never reaches full rank. As a result, one of the SRP variables is not estimated. Since the AMR and C variables are multiplied together in the SRP perturbation, a bias will exist in the estimation of the other SRP variable which is added to the estimated states in the consider approach. Therefore, this system is highly sensitive to the initial estimate of the SRP parameters when the consider approach is implemented.

4.4.2 Time-Varying AMR and C

Next, state estimation errors for the time-varying AMR and C extended state case are given in Figure 4.9. Recall the stochastic observability results of Figure 3.16. The rank of the stochastic observability matrix with measurement uncertainties changes from six to seven after approximately two hours of analysis. Shortly thereafter the rank increases from seven to eight. Even though the deterministic observability matrix rank decreases to seven after 23 hours, the stochastic observability matrix remains at eight for the rest of the analysis. This change in the observability matrix rank is applied to the CF for adding SRP parameters to the vector of estimated states.

This system is stochastically observable as demonstrated by the full rank stochastic observability matrix. Therefore, the state estimation errors for the AMR and C

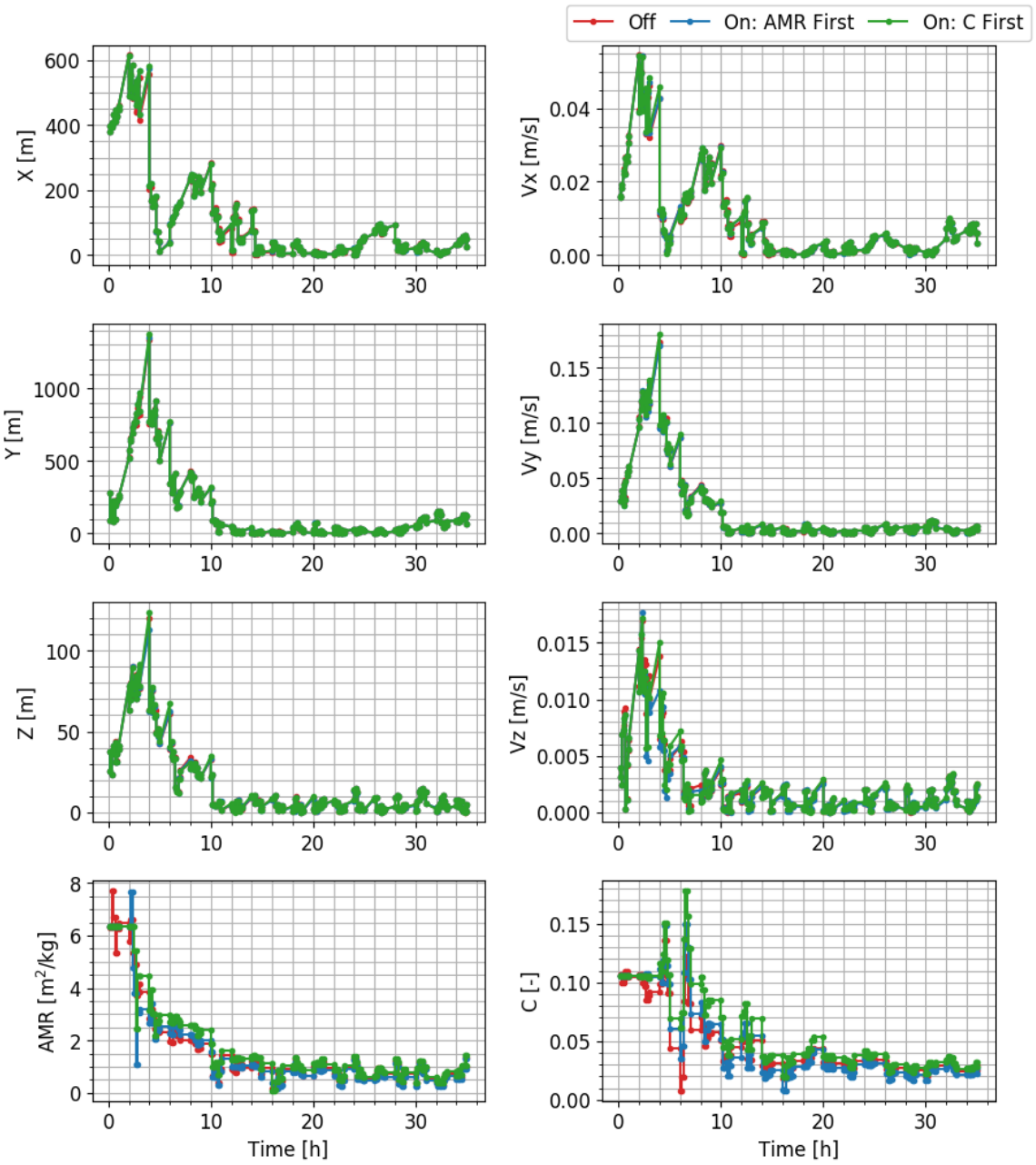

Figure 4.9. Consider filter state estimation errors for the time-varying AMR and C case.

variables should be improved when compared to the constant AMR and C system, as shown in Figure 4.9. The state estimation errors for the position and velocity states are nearly identical for the three estimation approaches. For the AMR and C

variables, the CF with the AMR added first to the analysis has lower state estimation errors than the approach estimating all of the state variables, given by the red curve, for the majority of the analysis. Although the state estimation error difference is minor between the two estimation approaches, keeping the SRP parameters as consider parameters until the rank of the observability matrix increased beyond seven, improved the estimation of the SRP parameters when they were changed from consider parameters to estimated states.

4.4.3 Time-Varying AMR, Constant C

Similar to the corresponding observability analysis and estimability analysis, the following comparison of the state estimation errors for the three estimation approaches with a state extended by time-varying AMR and constant C is similar to the results of the time-varying AMR and C extended state case. Figure 4.10 shows the state estimation errors for the EKF estimation and the two CF approaches. The analysis of the observability of a system with a state extend by C has shown that the partial derivatives of the dynamics with respect to C for the STM computation are considerably smaller than the other partial derivatives due to the units of AMR. When the C variable is time-varying or constant, this partial derivative will not change significantly due to the large order of magnitude differences among the partial derivatives of the dynamics for the STM computation. Hence, the state estimation errors for this case are expected to be similar to the time-varying AMR and C extended state case.

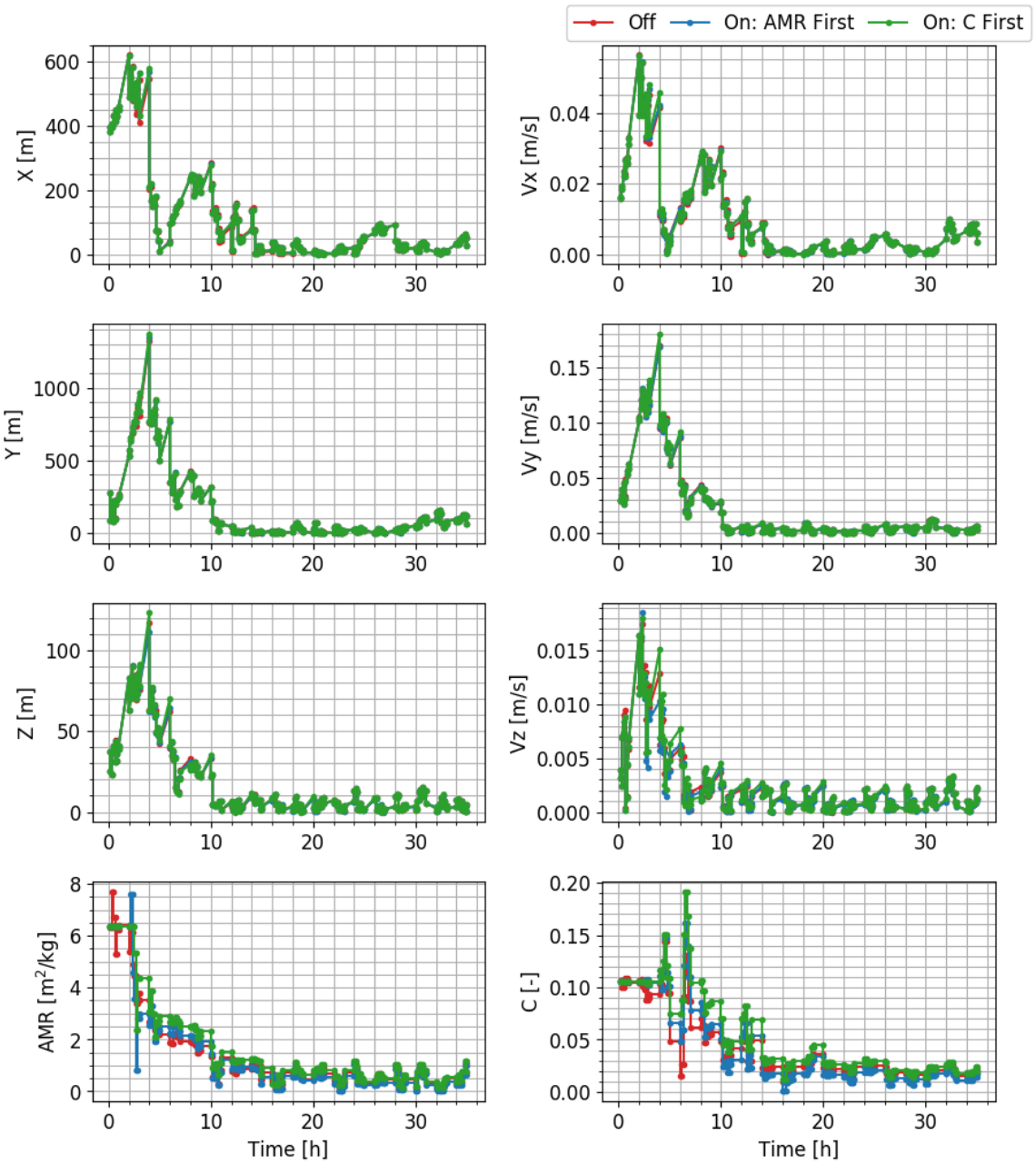

Figure 4.10. Consider filter state estimation errors for the time-varying AMR and constant C case.

4.4.4 Time-Varying C, Constant AMR

The final extended state case, with time-varying C and constant AMR, does differ from previous CF results. The rank of the stochastic observability matrix over time is shown in Figure 3.22. The rank increases from six to seven after approximately one hour, and the rank increases from seven to eight after approximately two hours. However, after approximately ten hours, the rank of the stochastic observability matrix decreases to seven. The CF approach follows this change for adding, and in this case removing, consider parameters to the estimated states.

Figure 4.11 shows the state estimation errors for each state variable and each estimation approach. As with the other AMR and C cases, the position and velocity state estimation errors are nearly identical for the three estimation approaches. Small differences do appear in the z velocity state estimation errors for the case where C is added to the state first when the rank of the observability matrix reaches seven.

The observability-estimability informed CF shows improved performance in the state estimation errors of the AMR and C variables when AMR is added to the estimated states first. The AMR state estimation errors with the consider approach are only slightly lower than the state estimation errors for the approach without consider parameters. However, the C state estimation errors remain constant for the CF approach with AMR estimated first because the observability matrix rank reduces from eight to seven after ten hours. The variable C is changed from an estimated state to a consider parameter at that time. Therefore, the consider approach reduced the detrimental effect of the C variable when the measurements no longer provided sufficient information to determine the observability of the system.

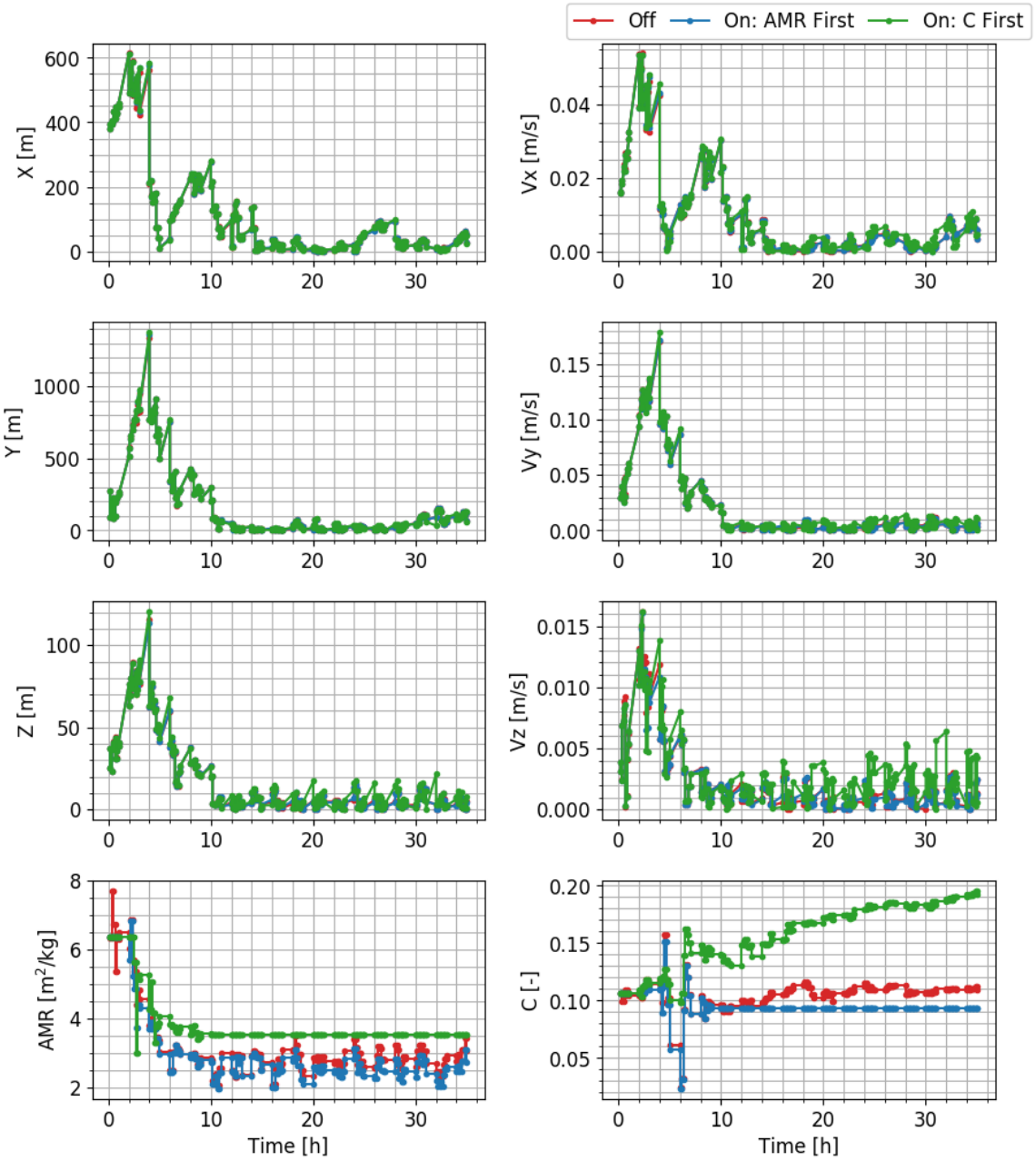

Figure 4.11. Consider filter state estimation errors for the time-varying C and constant AMR case.

4.4.5 Summary

The observability-estimability informed CF implemented the rank of the stochastic observability matrix as a measure for determining when consider parameters should be estimated. In the case of multiple consider parameters, this observability measure does not indicate which consider parameter should be estimated first because a one-to-one mapping of the singular values of the observability matrix to the state variables of the system typically does not exist. Therefore, estimability analysis was explored for informing the CF of the order in which the consider parameters should be estimated. Due to the challenge of correlated state variables, the estimability results are not always clear for the orbit problem. However, for the constant AMR and C extended state case, a linear combination of the AMR and C state variables has the weakest relative estimability compared to the other state variables or linear combinations of state variables in the system after some time. Also, the C component in the linear combination of AMR and C is dominant in defining the eigenvector direction of weakest relative estimability. Therefore, the estimability analysis could be interpreted as indicating that C is more difficult to estimate than AMR. From an observability perspective, this has been shown with the time to become observable for the C extended state versus the AMR extended state.

Two CFs have been implemented for the different constant and time-varying cases of AMR and C. The CFs differ by which extended state variable is changed from a consider parameter to an estimated state first. In most cases, the state estimation errors from the EKF without the consider approach are less than or equal to the state estimation errors when the consider approach is implemented. When the system is observable, as in the case of time-varying AMR and C, there is a small improvement in the state estimation errors for the AMR and C variables compared to the EKF without the consider approach. The most significant state estimation error differences occurs with the C variable for the time-varying C and constant AMR extended state case. The stochastic observability matrix rank increases to eight, but then reduces to

seven after ten hours of analysis. As a result, detrimental effects of poorly estimated extended states are reduced for the case where AMR is added to the state first because the C state is changed back from an estimated state variable to considered parameter. For some systems with low observability, the observability-estimability informed CF may aid in reducing the state estimation errors. For the orbit problem, only minor improvements in the state estimation errors exist for some extended state systems, and some extended state cases do not benefit from the consider approach.

5. OBSERVABILITY OF LIGHT CURVE INVERSION

The general principle of observability is exploration of the relationship between the measurements and the states of a system, as introduced in Section 2.1. Rather than using observability as a concept specifically for control systems, observability is analyzed for light curve inversion in this chapter. Moreover, observability is applied in a general sense to the challenge of obtaining light curve measurements which sufficiently sample the observer-object-Sun geometry and object attitude profile.

If the light curve measurements do not sufficiently cover the observer-object-Sun geometry and the object attitude profile, light curve inversion may not produce accurate object representations. The method for overcoming this challenge and ensuring sufficient sampling of the system has historically been to collect large amounts of data [136, 161, 162]. However, due to darkness constraints for many optical telescopes and high demand for optical telescope resources, collecting large sets of data for light curve inversion is not sustainable for the growing resident space object (RSO) population. Moreover, the times at which light curves may be collected are often influenced by telescope operational constraints and resource demands, leading to a more or less random selection of times for generating shorter light curves.

The challenge of sufficiently sampling the light curve system geometry for light curve inversion and the high demand for telescope resources led to the investigation of observability as a method for improving the efficiency of collecting measurements for light curve inversion. The analysis of observability seeks to determine the number of measurements required and when measurements should be acquired for light curve inversion. As discussed in Section 2.7, the Extended Gaussian Image (EGI) minimization step is the only component of the light curve inversion process which directly utilizes the light curve measurements. Therefore, this work focuses on the observability of the EGI minimization.

5.1 EGI Minimization Observability Derivation

The EGI minimization step of the light curve inversion process estimates the albedo-area vector associated with the surface normal directions of the EGI faceted sphere. Recall the form of the optimization problem for determining the albedo-area vector, which was presented in Section 2.7,

$$\begin{aligned} min \quad & J = ||\mathbf{L} - \mathbf{G}\ \mathbf{a}||^2, \\ subject\ to \quad & \mathrm{a}_s \geq 0\ \forall \mathrm{a}_s \text{ in } \mathbf{a} = [\mathrm{a}_1, \ldots, \mathrm{a}_m]^T, \end{aligned} \tag{5.1}$$

where $\mathbf{L}$ is a vector of light curve measurements, $\mathbf{G}$ is the reflection matrix, and $\mathbf{a}$ is the albedo-area vector.

The reflection model implemented in the observability of light curve inversion is a classical Lambertian model. The reflection matrix models the contribution from each surface normal vector with associated albedo-area under specific light and observer-object-Sun conditions to the light curve measurement. The reflection matrix is defined by

$$\begin{aligned} \mathbf{G}(t_k) = I_\odot\ \frac{1}{\pi||\mathbf{o}(t_k)||^2}\ \Big[& \hat{\mathbf{o}}(t_k) \cdot \hat{\mathbf{n}}_s \\ & + \lambda\ \delta\Big(\hat{\mathbf{o}}(t_k) \cdot \hat{\mathbf{n}}_s - \hat{\mathbf{n}}_s \cdot \hat{\mathbf{s}}(t_k)\Big)\ \delta\Big(\hat{\mathbf{s}}(t_k) \times \hat{\mathbf{n}}_s - \hat{\mathbf{n}}_s \times \hat{\mathbf{s}}(t_k)\Big)\Big], \end{aligned} \tag{5.2}$$

where $I_\odot$ is the mean solar irradiance, otherwise known as the solar constant, $\mathbf{o}(t_k)$ is the object-observer vector, $\mathbf{n}_s$ is the EGI surface normal vector for each s facet, $\mathbf{s}(t_k)$ is the object-Sun vector, and λ is a constant defining the relationship between the diffuse and specular components of the reflection model [95,99]. The EGI normal vectors are not time-varying because the reflection model is computed in the body frame. The δ function is defined as

$$\delta(x) = \begin{cases} 1, & x = 0 \\ 0, & \text{otherwise.} \end{cases} \tag{5.3}$$

The rows of the reflection matrix correspond to the time of each light curve measurement in $\mathbf{L}$. In addition, the columns of the reflection matrix correspond to each of

the EGI surface normal vectors as a result of the following relationship between the diffuse and specular coefficients.

A linear relationship between the reflection matrix and the albedo-area vector exists because a fixed relationship is assumed for the specular coefficient, C_s, and diffuse coefficient, C_d, in the reflection model. The relationship between the specular and diffuse coefficients is defined by

$$C_s = \lambda \, C_d. \tag{5.4}$$

For the Lambertian reflection model, energy conservation states that the following relation holds

$$C_s + C_d + C_a = 1, \tag{5.5}$$

where C_a is the absorption coefficient. This work assumes an object which does not reflect specularly, i.e. $C_s = 0$. Therefore, with these assumptions, the reflection matrix simplifies to

$$\mathbf{G}(t_k) = I_{\odot} \, \frac{1}{\pi ||\mathbf{o}(t_k)||^2} \, \left[\hat{\mathbf{o}}(t_k) \cdot \hat{\mathbf{n}}_s \right], \tag{5.6}$$

and the albedo-area vector equals

$$\mathbf{a} = [C_d A_1, \ldots, C_d A_s, \ldots, C_d A_m]^T, \tag{5.7}$$

where A_s is the area associated with each surface normal vector on the EGI.

This EGI minimization problem assumes a known attitude profile. The original object shape is not required, but the reflection matrix is defined by the object-observer-Sun geometry and attitude motion. Therefore, given the input values under which light curve measurements are acquired and an assumed attitude profile, the albedo-area vector, $\mathbf{a}$, can be determined by solving Equation 5.1.

When solving the EGI minimization problem in a linear least squares approach, common forms of observability appear. The following derivation defines the albedo-area least squares solution and defines an observability Gramian for the light curve inversion problem. First, Equation 5.1 is expanded as

$$= \mathbf{L}^T \, \mathbf{L} - 2 \, \mathbf{a}^T \, \mathbf{G}^T \, \mathbf{L} + \mathbf{a}^T \, \mathbf{G}^T \, \mathbf{G} \, \mathbf{a}. \tag{5.8}$$

To find the least squares solution, $\hat{\mathbf{a}}$, the first derivative of the cost, J, with respect to the albedo-area vector, $\mathbf{a}$, is set equal to zero.

$$\frac{\partial J}{\partial \mathbf{a}} = \frac{\partial}{\partial \mathbf{a}} \left[\mathbf{L}^T \, \mathbf{L} - 2 \, \mathbf{a}^T \, \mathbf{G}^T \, \mathbf{L} + \mathbf{a}^T \, \mathbf{G}^T \, \mathbf{G} \, \mathbf{a} \right], \tag{5.9}$$

$$= -2 \, \mathbf{G}^T \, \mathbf{L} + \frac{\partial}{\partial \mathbf{a}} \left[\mathbf{a}^T \, \mathbf{G}^T \, \mathbf{G} \, \mathbf{a} \right], \tag{5.10}$$

$$= -2 \, \mathbf{G}^T \, \mathbf{L} + \frac{\partial}{\partial \mathbf{a}} \left[(\mathbf{G} \, \mathbf{a})^T \, (\mathbf{G} \, \mathbf{a}) \right], \tag{5.11}$$

$$= -2 \, \mathbf{G}^T \, \mathbf{L} + 2 \, \mathbf{G}^T \, \mathbf{G} \, \hat{\mathbf{a}} = 0. \tag{5.12}$$

Finally, solving for $\hat{\mathbf{a}}$.

$$\hat{\mathbf{a}} = \left(\mathbf{G}^T \, \mathbf{G} \right)^{-1} \, \mathbf{G}^T \, \mathbf{L}. \tag{5.13}$$

The estimated albedo-area of Equation 5.13 requires the inversion of $\mathbf{G}^T \, \mathbf{G}$. The assumption that this matrix is non-singular is a fundamental aspect of observability. The matrix $\mathbf{G}^T \, \mathbf{G}$ is considered an observability Gramian in this work. Therefore, if the observability Gramian can be inverted, this system is considered observable.

For EGI minimization, an observable system depends on the observer-object-Sun geometry, object attitude profile, and spacing of observations. However, the light curve inversion process implemented in this work requires a known attitude profile for executing the inversion process. Methods exist to extract attitude information from light curve measurements [163–166]. Therefore, the observability of the EGI minimization assumes a known attitude profile and focuses on the analysis of the reflection matrix, $\mathbf{G}$, for determining the number of observations and spacing required for sufficient sampling of the EGI to estimate the albedo-area vector.

The following simulations, presented in Sections 5.2, 5.3, and 5.4, demonstrate the applicability of observability for light curve observation planning to perform light curve inversion. Observability of the system is evaluated by computing the rank of the observability Gramian, $\mathbf{G}^T\mathbf{G}$, for various measurement spacing sequences. In addition to the evaluation of the observability Gramian matrix rank, the linearly independent columns of $\mathbf{G}$ are determined with each measurement to visualize the facets of the EGI which have been sufficiently sampled. This method of visualizing the observability will be discussed in more detail when simulation results are presented.

Two methods of applying observability to the light curve inversion problem are presented. First, observability is analyzed independent of the original object shape in Sections 5.2 and 5.3. This application of observability focuses on determining when the EGI is sufficiently sampled to estimate the albedo-area vector. The second method of observability, presented in Section 5.4, assumes the original object shape is known in order to determine when critical features of an object, such as solar panels, become observable. This observability analysis focuses on differences in time to become observable for specific features when there are slight differences in an object model, e.g. errors in the deployment of solar panels resulting in not fully deployed solar panels.

5.2 EGI Observability Independent of Original Object Shape

The first EGI minimization observability simulations presented in this work consider low Earth orbit (LEO), medium Earth orbit (MEO), and geosynchronous Earth orbit (GEO) objects. Table 5.1 defines the orbital elements and epoch for the three objects. Cartesian position and velocity are propagated with two-body motion. Two attitude profiles are applied to each object: one is a simple, single-axis rotation about the body z-axis and one is a three-axis rotation. The rotation rates for each of the two attitude profiles are given in Table 5.2. In addition, an example of the three-axis rotation motion is shown in Figure 5.1. The color gradients depict the motion of the body-fixed axes over time. The body z-axis is tilted 30° from the inertial z-axis, and the rotation rate about the body z-axis is defined in Table 5.2.

The analysis of the LEO, MEO, and GEO objects focuses on the impact of the time between measurements and the EGI tessellation number on the observability of the EGI minimization. Therefore, observability analysis is performed for each object with a range of times between measurements and EGI tessellation numbers, given in Table 5.3. Recall that the EGI tessellation number defines the number of facets per

Table 5.1. LEO, MEO, and GEO orbit definitions.

Object	a [km]	e [-]	i [°]	Ω [°]	ω [°]	ν [°]	Epoch [MJD]
LEO	8124.967	0.147	32.869	55.826	53.880	0.0	53159.1
GEO	42170.238	9.734e-4	35.745	359.304	124.110	0.0	53159.1
MEO	26378.137	0.0001	40.0	60.0	50.0	0.0	58270.0

Table 5.2. LEO, MEO, and GEO attitude profiles.

Attitude Profile	Rotation Rate [°/s]	Spin Axis Angle [°]
single-axis	12.072	0.0
three-axis	25.096	30.0

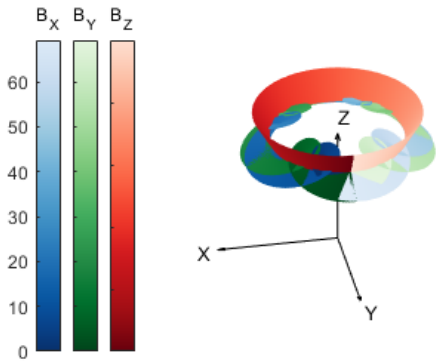

Figure 5.1. Body-fixed axes over time for the three-axis rotation case.

row and column on each side of the quad-cubed sphere, which is implemented for defining the discrete EGI representation.

Table 5.3. Measurement spacing and EGI tessellation numbers analyzed for the LEO, MEO, and GEO objects.

Object	Measurement Spacing [s]	EGI Tessellation Numbers
LEO	1, 2.5, 5, 10, 20	5, 7
GEO	1, 2.5, 5, 10, 20	5, 7
MEO	1, 2.5, 5, 10, 20	5, 7

5.2.1 LEO Object with Single-Axis Rotation

The analysis of the EGI minimization observability begins with a simulation of a LEO object with a simple, single-axis rotation. The rank of the observability Gramian in Equation 5.13 is calculated for a range of measurement spacing cases as defined in Table 5.3. For each case, measurements are spaced equally for a total analysis time of two hours. Figure 5.2 depicts the LEO simulation observability results with each line representing a different measurement spacing. This analysis is performed with a tessellation number of seven, which is equal to 294 surface normal directions on the EGI. The black dashed line in Figure 5.2 represents the number of EGI surface normal directions.

For this system to be observable, the rank of the observability Gramian must be equal to the number of EGI surface normal directions. Theoretically, the minimum number of observations required for the observability Gramian to be full rank is equal to the number of surface normal directions. However, the observer-object-Sun geometry and attitude profile over time may result in a system which requires a greater number of measurements than the number of surface normal directions. Moreover, the geometry and attitude profile may result in a system which never becomes full rank within the analysis time, which is the case for this LEO object with a single-axis rotation. All of the measurement spacing cases in Figure 5.2 do not reach full

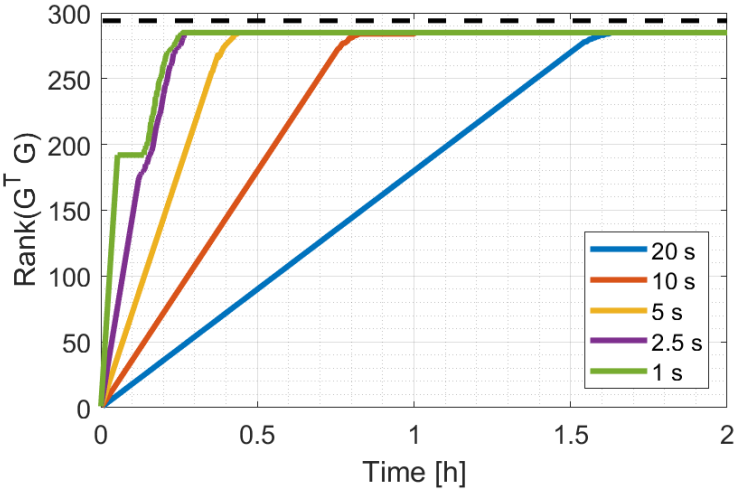

Figure 5.2. Rank of the observability Gramian versus time for the LEO object with single-axis rotation and 294 surface normal directions.

rank due to insufficient sampling of the EGI as the observer-object-Sun geometry and attitude change.

The complex relationship between the observer-object-Sun geometry, attitude profile, and the spacing of measurements is shown in more detail in Figure 5.3, which depicts the three smallest measurement spacing cases with a shorter analysis time. When the time between measurements is one second, there is a plateau in the observability Gramian rank curve from approximately 0.05 to 0.14 hours from the analysis epoch. During this plateau, more measurements are acquired, but the system geometry has not change sufficiently to increase the rank of the observability Gramian.

Another method of presenting the observability results for selection of efficient measurement spacing is a comparison of the observability Gramian rank to the number of measurements, as in Figure 5.4. As with the observability Gramian rank versus time, Figure 5.5 shows how redundant measurements exist for the 1 second and 2.5 second measurement spacing cases. The 1 second measurement spacing case has approximately 300 redundant measurements which do not increase the rank of the observability Gramian as shown by the plateau region in Figure 5.5. The 2.5 second

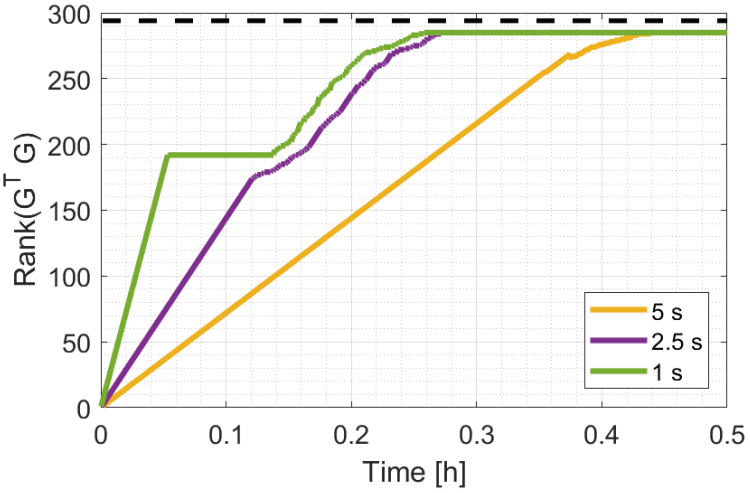

Figure 5.3. Rank of the observability Gramian versus time for the LEO object with shorter analysis time showing more detail of the smaller measurement spacing cases.

measurement spacing case does not have a single plateau for an extended period of time like the 1 second measurement spacing case, but the 2.5 second measurement spacing case does have measurements which do not increase the rank, and therefore, are redundant measurements.

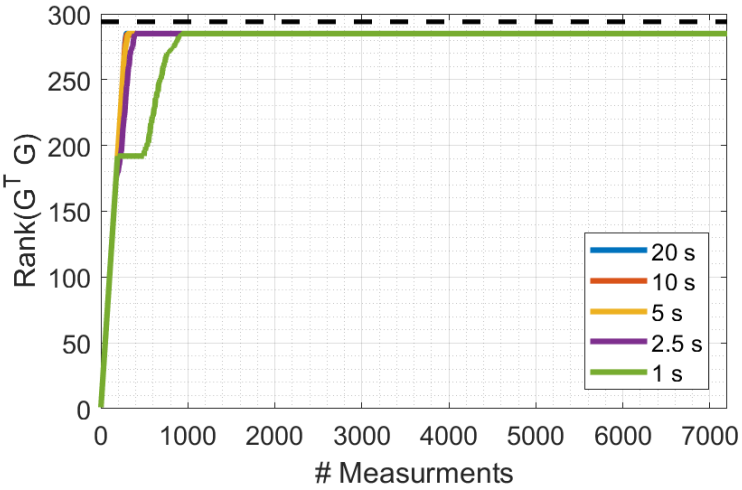

Figure 5.4. Rank of the observability Gramian versus number of measurements for the LEO object with single-axis rotation and 294 surface normal directions.

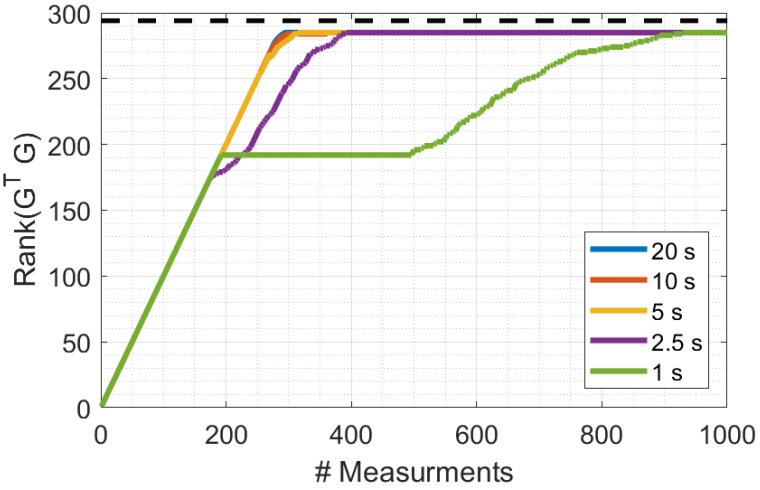

Figure 5.5. Rank of the observability Gramian versus number of measurements for the LEO object with single-axis rotation and 294 surface normal directions, zoomed in to show detail.

As expected, measurement spacing cases with longer times between each measurement result in fewer measurements to reach the maximum observability Gramian rank for this system. However, the conclusion that longer times between measurements will result in reaching a maximum matrix rank faster is not necessarily always true. Due to the connection of the observer-object-Sun geometry and the attitude profile, time between measurements could be selected which are detrimental to achieving a maximum matrix rank due to reoccurring surface normal directions being visible to the observer with each measurement.

The results presented thus far for the LEO object examined an EGI with 294 surface normal directions. Another method for analyzing the observability of the EGI minimization determines how the EGI tessellation number impacts rank of the observability Gramian. For the LEO object, EGI tessellation numbers of five and seven, which result in 150 and 294 surface normal directions, are analyzed. Because the number of surface normal directions is different, a direct rank comparison does not accurately show the impact of the EGI tessellation number on the observability.

Instead, it is more relevant to compare the different EGI tessellation number cases using the percentages of the matrix rank with respect to the total number of surface normal directions.

Figure 5.6 shows the percentage of the matrix rank over time with respect to the total number of surface normal directions. For each measurement spacing case, an

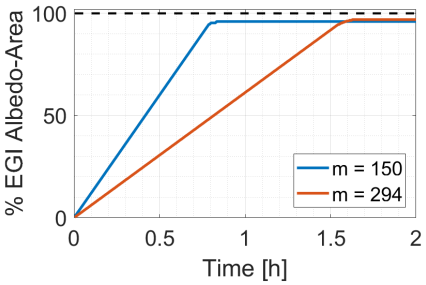

(a) 20 seconds.

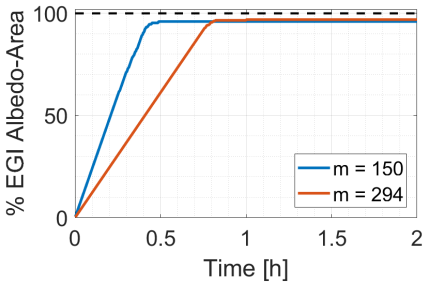

(b) 10 seconds.

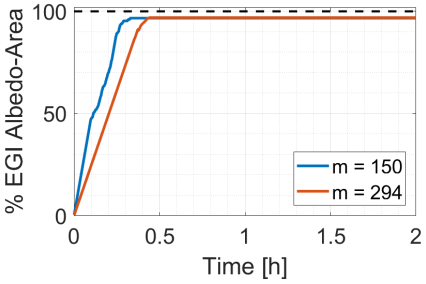

(c) 5 seconds.

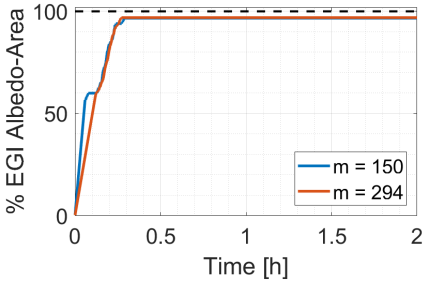

(d) 2.5 seconds.

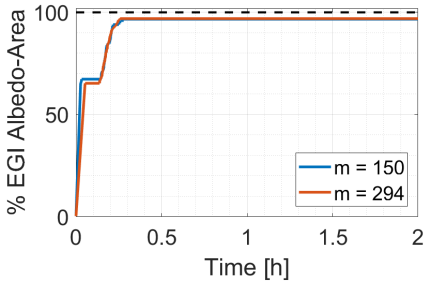

(e) 1 second.

Figure 5.6. Comparison of the percentage of the EGI albedo-area which is linearly independent for EGIs with 150 and 294 surface normal directions and the LEO object.

EGI defined by a tessellation number equal to seven takes longer to reach a maximum

rank compared to an EGI defined by a tessellation number equal to five, with the exception of the 1 and 2.5 second spacing cases because of the redundant measurements. This behavior is expected because the number of surface normal directions increases with the EGI tessellation number, requiring more measurements to reach the maximum rank. Given a system where the observer-object-Sun geometry and attitude profile were sufficiently sampled, the number of required measurements would be theoretically equal to the number of surface normal directions.

As introduced in Section 2.7, the EGI tessellation number relates to the resolution of the EGI. The EGI approximates the unit sphere more closely when the EGI tessellation number is larger because the EGI tessellation number defines the number of facets in each row and column of the quad-cubed sphere. As the time between measurements decreases in Figure 5.6, the two EGI tessellation cases progress similarly in terms of the percentage of EGI albedo-area. Therefore, for larger times between measurements, the EGI tessellation number has a larger impact on the increase of the matrix rank over time. Comparing the observability rank results for multiple EGI tessellation numbers for each measurement spacing case shows which factors in the system are limiting the progression of the rank to a maximum value. The larger measurement spacing cases are limited by the number of surface normal directions since the different tessellation numbers require significantly different times to reach a maximum rank. However, smaller measurement spacing cases are limited by the rotation rate of the object as the two tessellation number cases have similar curves, both exhibiting a plateau for the one second spacing case. In general, an EGI will better approximate an object with more surface normal directions. Therefore, finding a balance between being limited by the EGI tessellation number and limited by the measurement sampling rate will improve the efficiency of collecting measurements for light curve inversion.

5.2.2 GEO Object with Single-Axis Rotation

The preceding analysis of the LEO object is repeated for the GEO object with single-axis rotation. Figure 5.7 shows the rank of the observability Gramian over time for the GEO object with 294 EGI surface normal directions. Each measurement spacing reaches a maximum rank of 285 within 2.5 hours, resulting in a system which is not sufficiently sampled for EGI minimization.

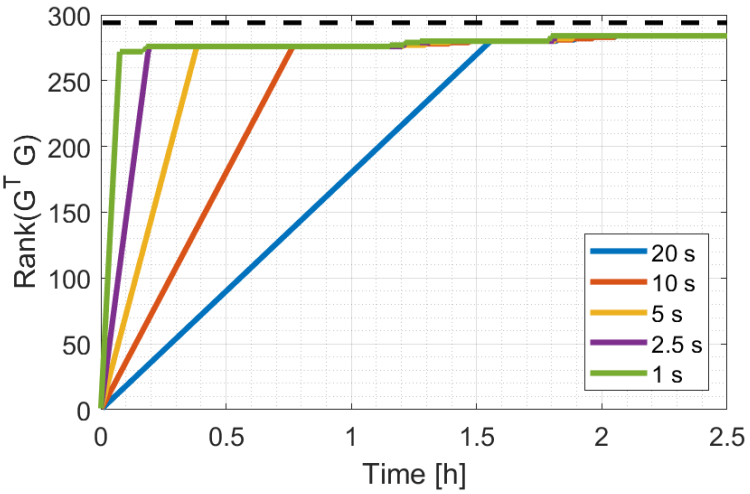

Figure 5.7. Rank of the observability Gramian versus time for the GEO object with single-axis rotation and 294 surface normal directions.

Unlike the LEO object observability results, the rank curves for each measurement case have a similar trend for the GEO object. The rank increases with an apparent constant slope for each measurement spacing before reaching a plateau. The differences in the behavior of the rank between the LEO object and GEO object are due to the differences in observer-object-Sun geometry for the two objects. The GEO object has small geometry changes over a 2.5 hour period, whereas the LEO object geometry will change significantly during the two hour analysis. In general, more geometric diversity can be considered as advantageous for observability. However, in the case of the LEO object compared to the GEO object, the rapidly changing geometry of

the LEO object system is detrimental for increasing the rank due to the relationship between the observer-object-Sun geometry and attitude.

Next, the rank of the observability Gramian is plotted against the number of measurements for the GEO object in Figure 5.8. As the time between measurements decreases, the number of required measurements to reach a maximum rank increases. This is expected because larger measurement spacing cases require more time than smaller measurement spacing cases for an equal number of measurements. The rank of the observability Gramian versus time and number of measurements could be used to select a measurement spacing which efficiently achieves a maximum rank depending on operator requirements for efficient observation planning. However, the GEO object system also does not reach full rank, so no matter which measurement spacing is selected for the given system and analysis time, the accuracy of the albedo-area estimates cannot be guaranteed.

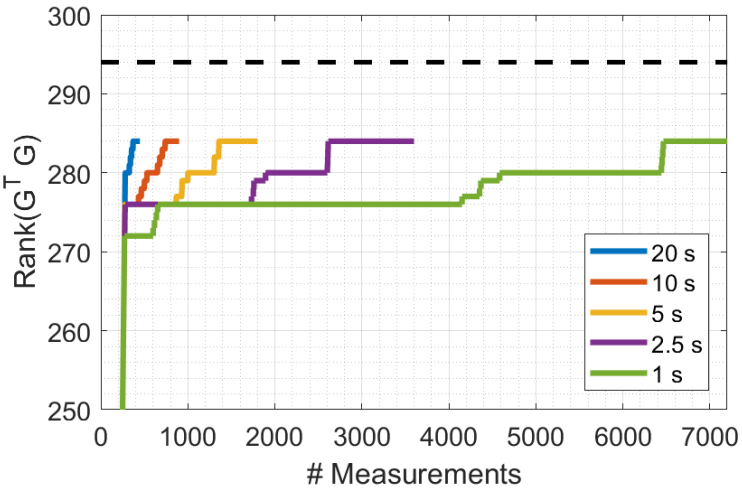

Figure 5.8. Rank of the observability Gramian versus number of measurements for the GEO object with single-axis rotation and 294 surface normal directions.

The impact of the EGI tessellation number on the rank of the GEO object system is shown in Figure 5.9. The trends for the impact of the EGI tessellation number for the GEO object are similar to the trends for the LEO object. As the time be-

tween measurements decreases, the EGI tessellation number impacts the observability results less.

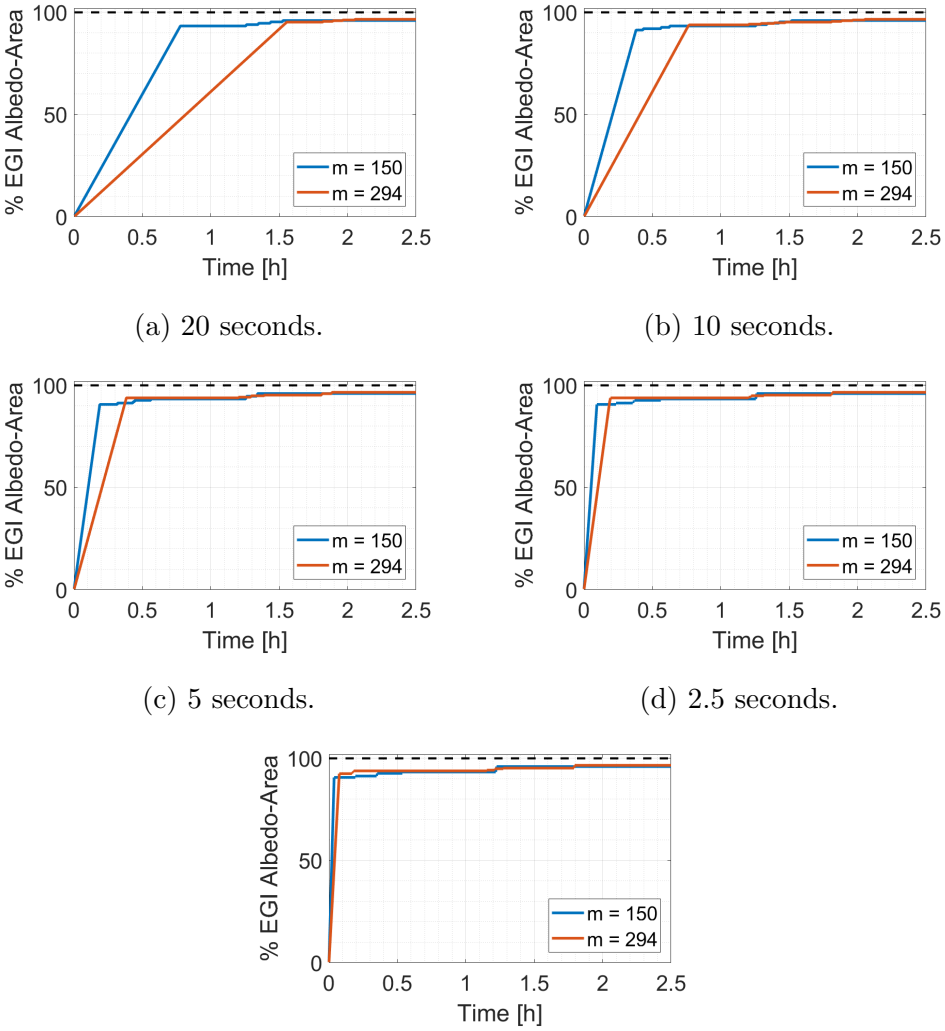

(a) 20 seconds.

(b) 10 seconds.

(c) 5 seconds.

(d) 2.5 seconds.

(e) 1 second.

Figure 5.9. Comparison of the percentage of the EGI albedo-area which is linearly independent for EGIs with 150 and 294 surface normal directions and the GEO object.

Analysis of the observability Gramian was also conducted for the MEO object with single-axis rotation. The observability results for the MEO object with single-axis rotation are nearly identical to the GEO object results. This is because both

orbit cases have significantly longer orbital periods than the LEO object. Therefore, the MEO results are shown in Appendix C.1.

5.2.3 Rank Deficiency of the Single-Axis Rotation Systems

For each of the LEO, MEO and GEO objects with single-axis rotations, the maximum values of the observability Gramian matrix rank do not equal the number of surface normal directions of the EGI for the given analysis time. Even though the rank of the observability Gramian is close to full rank for the LEO object, full rank is not achieved and the observability Gramian is non-singular. Therefore, accurate estimation of the albedo-area vector cannot be reliably guaranteed, potentially resulting in a poor object reconstruction through light curve inversion. In order to understand what aspects of this system result in the inability to achieve full rank of the observability Gramian, the reflection matrix is explored in more detail.

A limiting aspect of analyzing the matrix rank of the observability Gramian over time is that the matrix rank only quantifies the matrix as a whole. Therefore, the information about how each measurement is mapped to the surface normal directions is lost. However, as shown in Section 2.1.3, there are many mathematically equivalent methods for presenting the observability of a system. The singular values of the observability Gramian over time present greater insight into how the matrix rank varies with time. However, the singular value methods for depicting observability are not clear for the observability analysis of the light curve inversion as a result of the high dimension due to the number of EGI surface normal directions.

Another equivalent method for determining invertibility of a matrix is the linear independence of the columns of a matrix. As the EGI minimization has been defined as a linear problem, the linear independence of the columns of the reflection matrix, $\mathbf{G}$, directly correspond to each albedo-area value associated with each surface normal direction. The linear independence of the columns of the reflection matrix can be

visualized in a three-dimensional method for inspecting which aspects of the EGI do not have sufficient sampling.

QR factorization is implemented to determine which columns of the reflection matrix are linearly independent for each measurement [91]. Figure 5.10 shows a 3D representation of the linear independence of the reflection matrix columns over time for the LEO object with one second between measurements. The colorbar represents the measurement indices in the analysis, and in this case, also the analysis time. The EGI is defined by a tessellation number of seven, resulting in 294 surface normal directions. As measurements are accumulated and the columns of reflection matrix become linearly independent, the associated surface normal directions are assigned a color corresponding to the measurement index. Note that the EGI is viewed in the body frame viewed down the observer vector towards the object.

From the 3D visualization, the period of redundant measurements for increasing the rank, which is equivalent to the plateau in Figure 5.3, is clearly shown. The bottom row of Figure 5.10 contains a gap of color between blue and yellow which is another way the measurement redundancy is shown with the one second measurement spacing case. This visualization appears to show how the object becomes visible to the observer, but this is not the case. The color change of the facets over time is an indication of the linear independence of the reflection matrix columns.

Unlike the matrix rank of the observability Gramian, the specific regions of insufficient sampling of the system geometry are apparent in the 3D visualization. A gray region at the bottom of the EGI remains after all of the measurements have been accumulated, indicating that the columns of the reflection matrix associated with those specific surface normal directions have not been sampled sufficiently. This LEO object has an attitude profile defined by a simple rotation about the body z-axis. Therefore, the bottom of the EGI does not become illuminated and visible to the observer during the analysis time.

The linear independence of the reflection matrix is also analyzed for the GEO object with single-axis rotation to improve the understanding of why this system

is not sufficiently sampled. Figure 5.11 shows the 3D visualization of the linearly independent columns in the reflection matrix at several points along the analysis. The 10 second measurement spacing case is shown with 294 surface normal directions on the EGI. Similar to the LEO 3D visualization, the bottom of the GEO object remains gray for the analysis, indicating that the bottom of the EGI is not visible and illuminated for the observer throughout the analysis. Although there does not appear to be any changes in the 3D visualization after the 4th EGI depicted, the last image has a yellow colored facet on the top of the EGI. This region corresponds to the small increase in the matrix rank after approximately 1.25 hours in Figure 5.7. A similar visualization is presented for the MEO object in Appendix C.1.

Although full rank of the observability Gramian was not achieved with LEO, MEO, and GEO objects with single-axis rotation, the various presentations of the observability Gramian matrix rank demonstrate how observability analysis can be implemented for observation planning for light curve inversion. Efficient measurement selection can be thought of in several different ways with analysis of light curve inversion observability. One goal for efficient observation planning could be to reduce the time required to achieve full rank of the observability Gramian. Based on this goal, Figure 5.3 indicates that time between measurements of 1 second or 2.5 seconds will reach a maximum rank in approximately 0.26 hours. However, the plateau region of the one second spacing case has redundant measurements which do not increase the rank, so it may be advantageous for a telescope operator to not image this object during the period of the plateau in the matrix rank. To avoid the plateau of the one second measurement spacing case, a different measurement spacing could be selected or another object could be observed during the plateau region. If another measurement spacing case is selected, the 2.5 second or 5 second cases are efficient choices because each case has limited redundant measurements for increasing the matrix rank, and the time required to reach a maximum rank is close to the one second spacing case. The second option of observing another object during the plateau of the one second spacing case enables a telescope operator to collect light curves of this

LEO object quickly, but not use valuable resources on this object when the rank of the observability Gramian will not be improved.

Another goal for efficient light curve collection for light curve inversion might be to limit the number of measurements required. In this LEO case, Figure 5.5 indicates that the five second and larger measurement spacing cases reach the maximum rank with approximately the same number of measurements. However, the five second measurement spacing case reaches a maximum rank in less than half the time than the ten second measurement spacing case. For the GEO object with single-axis rotation, the 20 second measurement spacing case required the fewest measurements for achieving the maximum rank as a result of the small increases in rank in Figure 5.7 at approximately 1.25 and 1.75 hours. The shorter measurement spacing cases could be advantageous for reaching a large rank quickly, but the GEO object with a single-axis rotation requires the system geometry to change for several hours to reach a maximum rank. Next, the LEO, MEO, and GEO objects are analyzed with a more complex attitude profile.

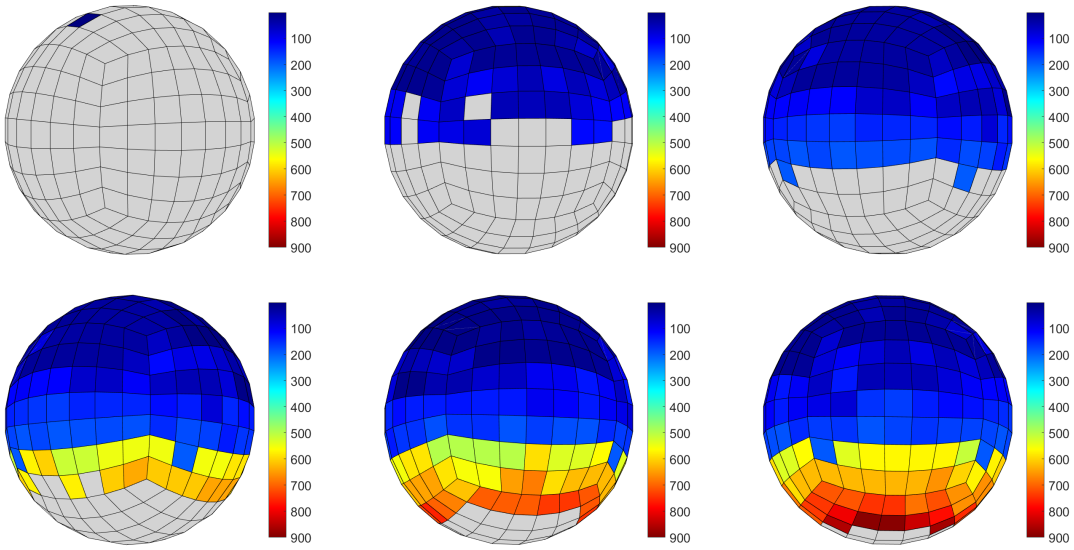

Figure 5.10. 3D visualization of the linearly independent columns in the reflection matrix for the LEO object with single-axis rotation, 294 surface normal directions, and one second between measurements, where the colorbar represents measurement indices.

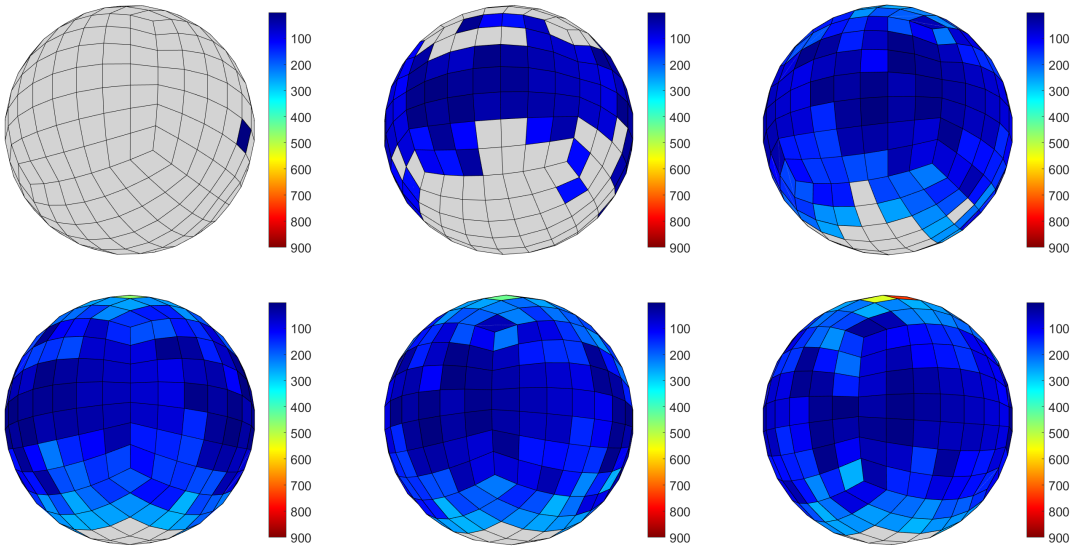

Figure 5.11. 3D visualization of the linearly independent columns in the reflection matrix for the GEO object with single-axis rotation, 294 surface normal directions, and 10 seconds between measurements, where the colorbar represents measurement indices.

5.2.4 LEO Object with Three-Axis Rotation

The single-axis rotation results indicated that a region of the EGI was not sufficiently sampled due to the interaction of the object attitude and the observer-object-Sun geometry. Therefore, the observability of the EGI minimization is performed for the same LEO, MEO, and GEO objects with a more complex attitude profile to determine whether a sufficient measurement sequence for reaching full rank of the observability Gramian is possible. When the LEO object has an attitude profile defined by three-axis rotation, it is possible to sufficiently sample the system geometry for EGI minimization, as shown in Figure 5.12.

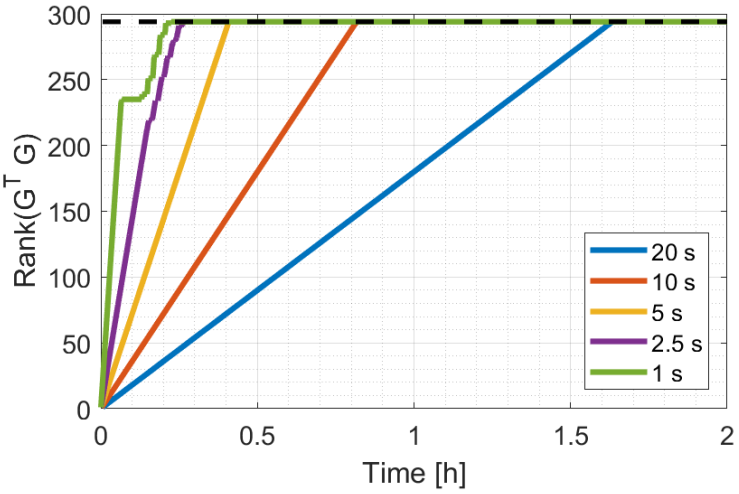

Figure 5.12. Rank of the observability Gramian versus time for the LEO object with three-axis rotation and 294 surface normal directions.

Similar to the single-axis rotation results, the 1 second and 2.5 second cases have measurements which are redundant in terms of increasing the observability Gramian matrix rank. Figure 5.13 shows the plateau region of the 1 second measurement spacing case in more detail. The redundancy in the 1 second and 2.5 second measurement spacing cases is more apparent in Figure 5.13 because the regions where the rank does not increase can be seen in greater detail.

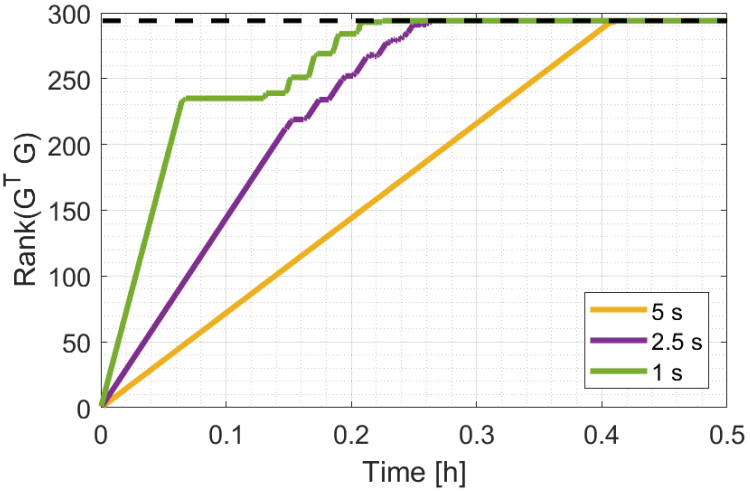

Figure 5.13. Rank of the observability Gramian versus time for the LEO object with three-axis rotation and 294 surface normal directions, zoomed in to show detail.

Figure 5.14 shows the rank of the observability Gramian versus the number of measurements. The 5, 10, and 20 second measurement spacing cases are all on top of one another in Figure 5.14 and contain no redundant measurements. This indicates that the 5, 10, and 20 second measurement spacing cases require the theoretical minimum number of measurements for achieving full rank. Analysis of the impact of the EGI tessellation number for the LEO object with three-axis rotation is shown in Appendix C.2 because the trends are comparable to the single-axis rotation results.

5.2.5 GEO Object with Three-Axis Rotation

Figures 5.15 and 5.16 show the observability matrix rank results for the GEO object with three-axis rotation. All of the measurement spacing cases reach full rank within two hours of analysis. In addition, the theoretical minimum number of measurements is sufficient for sampling the system geometry, as the number of measurements required for each measurement spacing case equals the number of EGI surface normal directions, 294. The impact of the EGI tessellation number on this

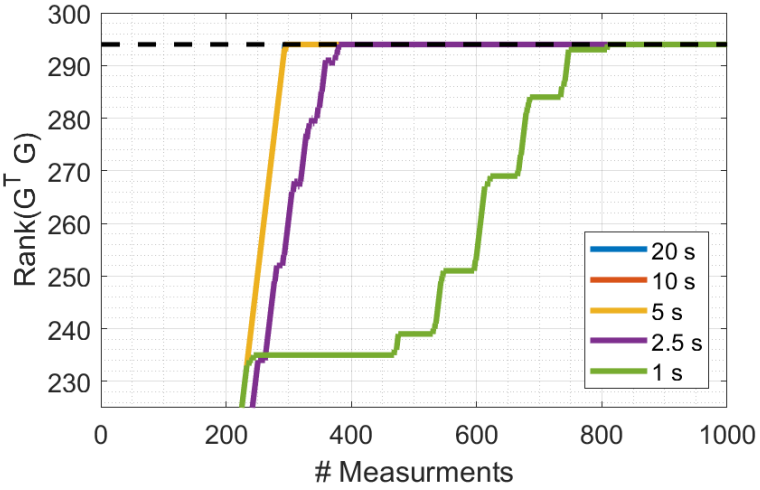

Figure 5.14. Rank of the observability Gramian versus number of measurements for the LEO object with three-axis rotation and 294 surface normal directions.

case and the three-axis rotation results for the MEO object are presented in Appendix C.3 and Appendix C.4, respectively.

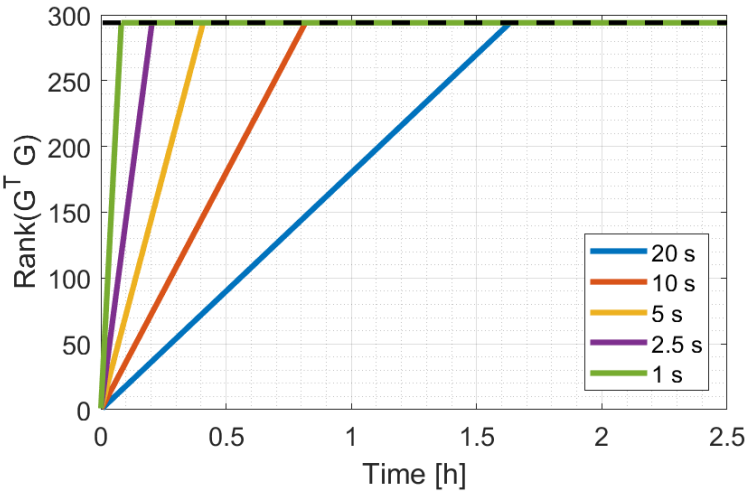

Figure 5.15. Rank of the observability Gramian versus time for the GEO object with three-axis rotation.

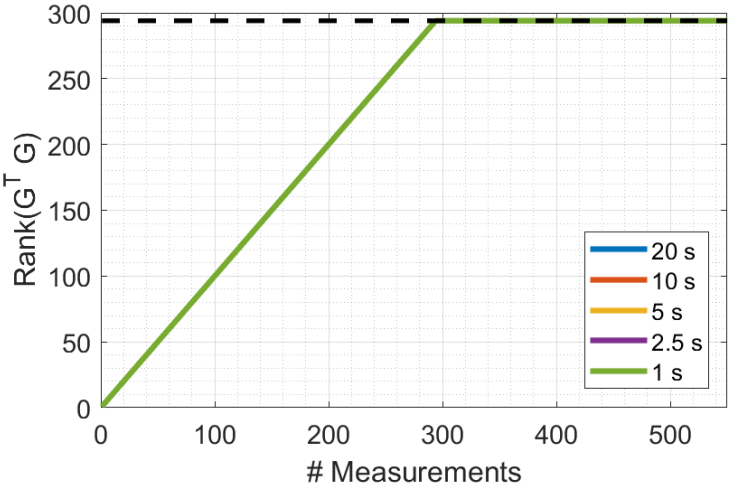

Figure 5.16. Rank of the observability Gramian versus number of measurements for the GEO object with three-axis rotation.

5.2.6 Three-Axis Rotation Summary

While the orbits for the LEO, MEO, and GEO objects remain the same compared to the single-axis rotation cases, the change in the attitude profiles from simple, single-axis rotation to more complex three-axis rotation results in systems which are sufficiently sampled for EGI minimization. The sampling of the object geometries is further explained by the 3D visualizations of the linear independence of the reflection matrix columns in Figures 5.17 and 5.18.

The 3D visualizations of the LEO object with three-axis rotation are similar to the single-axis rotation results in Figure 5.10. However, the single-axis rotation visualizations contained a gray region at the bottom of the EGI at the end of the analysis, representing the linear dependence of some columns in the reflection matrix, and the three-axis rotation results do not. The similarity of the 3D visualizations is a result of the 32.8° inclination of the LEO object used in this analysis. The 30° axis of rotation for the three-axis attitude profile appears as a nearly flat spin in Figure 5.17 because of the inclination, but the slight difference between the axis of rotation and

the inclination results in the bottom of the EGI becoming visible and illuminated to the observer.

The 3D visualization of the linearly independent columns of the reflection matrix over time for the GEO object with three-axis rotation is significantly different than the single-axis rotation case. With a simple, single axis rotation about the body z-axis, the 3D visualization of the linearly independent columns of the reflection matrix for the GEO object contained a region at the bottom of the EGI which was not visible nor illuminated for the observer throughout the analysis time. The more complex attitude profile results in sufficient sampling of all surface normal directions of the EGI, as shown in Figure 5.18.

Simulations of the LEO, MEO, and GEO objects have demonstrated how analysis of the rank of the observability Gramian can improve the understanding of how measurement spacing impacts the observability of a complex system. Also, a novel method for visualizing the linearly independent columns of the reflection matrix revealed which region of the EGI was insufficiently sampled for the simple, single-axis rotation cases. When the observability Gramian of the EGI minimization step of the light curve inversion process is full rank, the light curve measurements are sufficient for estimating the EGI albedo-area vector. In addition, comparison of the observability Gramian rank from different measurement spacing sequences can be used for efficient observation planning. For the LEO object with three-axis rotation, Figure 5.12 depicts how the five second measurement spacing case is efficient for reducing the number of redundant measurements, while still achieving full rank of the observability Gramian. Moreover, as all of the measurement spacing cases for the GEO object with three-axis rotation reached full rank with 294 measurements, i.e. the theoretical minimum number of required measurements for an EGI with 294 surface normal directions, any case could be considered efficient depending on telescope operation requirements.

Through analysis of the reflection matrix and the observability Gramian, the insufficient sampling of LEO, MEO, and GEO objects with single-axis rotation was

shown. Furthermore, the relationship between the attitude profile and the observability was shown when changing the attitude profile from a single-axis rotation to three-axis rotation resulted in full rank observability Gramians for all three objects. These methods for analyzing the observability of the EGI minimization step of the light curve inversion process confirm the understanding of the relationship between the orbital dynamics, reflection model, and attitude profile. Next, observability is analyzed for a more realistic system, with visibility and lighting constraints.

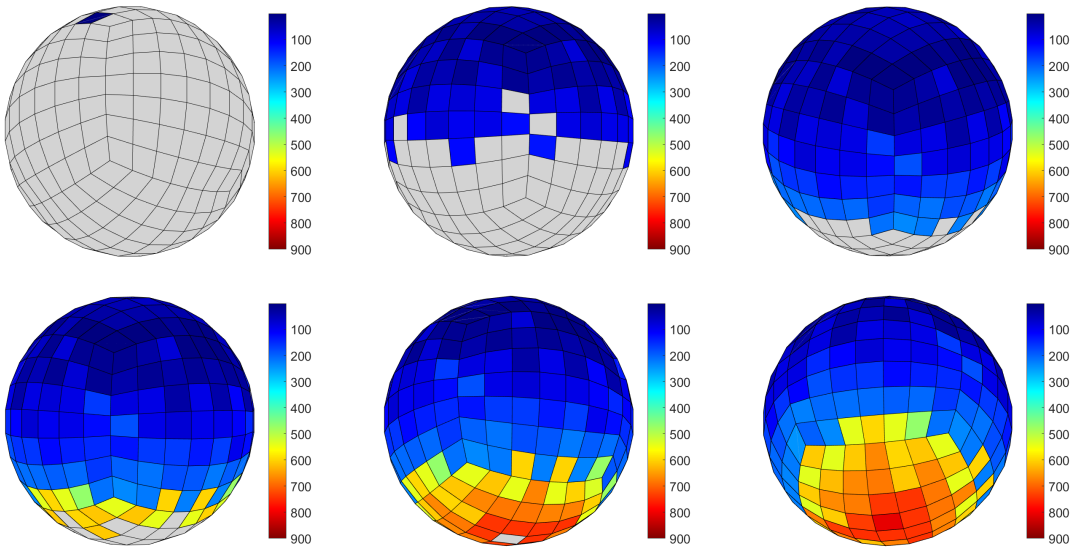

Figure 5.17. 3D visualization of the linearly independent columns in the reflection matrix for the LEO object with three-axis rotation, 294 surface normal directions, and 1 second between measurements, where the colorbar represents measurement indices.

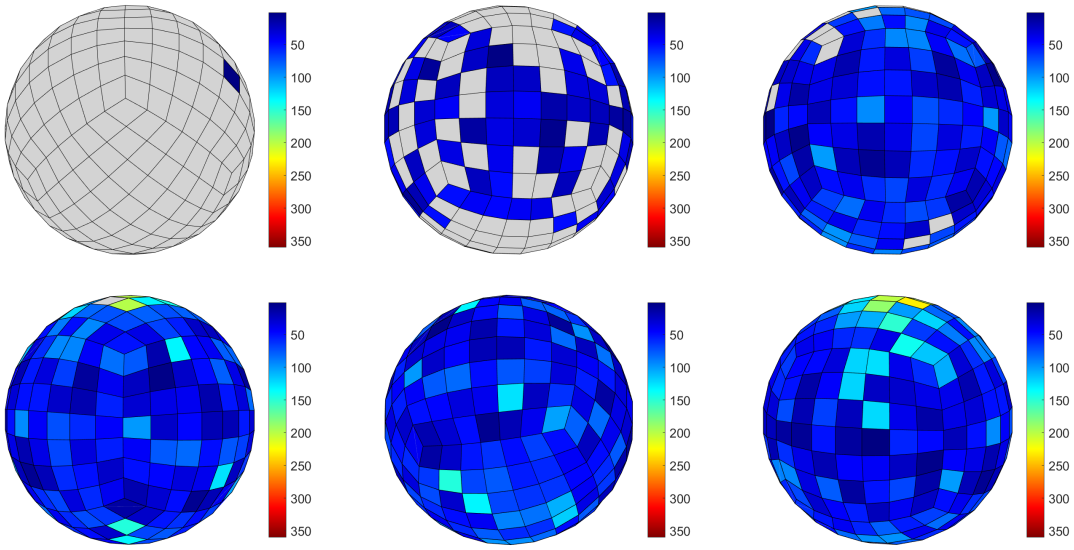

Figure 5.18. 3D visualization of the linearly independent columns in the reflection matrix for the GEO object with three-axis rotation, 294 surface normal directions, and 10 seconds between measurements, where the colorbar represents measurement indices.

5.3 Observability for LCI Sensor Tasking: Atlas V

Observability analysis of the EGI minimization step of the light curve inversion process is extended to include realistic constraints on measurements and perturbed orbit propagation. Collaborators at the Astronomical Institute of the University of Bern (AIUB) provided light curve measurements of an Atlas V upper stage, identified by NORAD satellite number 40295 and international designator 2014-068B. The goal of the observability analysis of the Atlas V upper stage is to determine if the provided light curve measurements are sufficient for light curve inversion of a real object. The orbit of the Atlas V upper stage for these simulations is defined by a two-line element (TLE) from 09 May 2015 and the epoch of the simulations is 10 May 2015 22:51:00 UTC. Throughout this observability analysis of the Atlas V, measurements are simulated in 20 minute batches, and within each measurement batch, measurements are

spaced every two seconds, resulting in 600 measurements per batch. Measurement batches are defined to be 20 minutes long to approximate the provided light curve measurements from AIUB. In addition, two seconds between measurements is consistent with the Charged Coupled Device (CCD) camera subframe technique used at the AIUB ZIMLAT telescope. Prior to performing observability analysis with constraints, similar analysis to Section 5.2 is performed to explore the impact of measurement batches and different measurement batch spacing cases on the observability of the Atlas V. Table 5.4 shows the various observability simulations of the Atlas V upper stage without constraints on when the measurements can be acquired. Each measurement spacing corresponds to the time between measurement batches defined by 20 minutes of measurements.

Table 5.4. Atlas V upper stage measurement spacing cases.

EGI Tessellation Numbers	Measurement Spacing [h]
5	0, 2, 4, 6, 8
7	0, 2, 4, 6, 8
13	2, 4, 6, 8, 10

Two-body propagation is implemented for orbit propagation for these initial cases of EGI minimization observability. For the EGI tessellation number equal to 13, or 1014 EGI facets, additional simulations, beyond the simulations defined in Table 5.4, are performed. First, an unconstrained case is simulated in attempt to select a measurement spacing which achieves full rank of the EGI gramian in the least amount of time and fewest measurement batches as possible. Next, two different arrangements of measurement batches were implemented based on visibility constraints at the AIUB ZIMLAT observatory. Table 5.5 shows the arrangements of the measurement batches in the presence of visibility constraints. The first constrained case is defined with two batches in each visibility window, and the second constrained case

is defined with only one measurement batch per visibility window. The Atlas V orbit for the additional analysis cases, given by Table 5.5, is propagated with the Simplified General Perturbations 4 (SGP4), which was introduced in Section 2.2.2. Two potential attitude profiles were determined for this Atlas V upper stage. The measurement cases presented in Table 5.5 are simulated for both attitude profiles. The methods implemented for determining the attitude profiles are described in the next section.

Table 5.5. Atlas V upper stage unconstrained and constrained batch start times, given in hours.

Batch #	Unconstrained	Constrained 1	Constrained 2
1	0.0	0.0	0.0
2	6.333	1.8333	24.0
3	70.667	73.1667	48.0
4	–	75.0	74.0
5	–	–	99.0
6	–	–	124.05
7	–	–	213.5

5.3.1 Attitude Profiles

The light curve inversion process studied in this work requires a known attitude profile. Techniques for determining the attitude of the Atlas V upper stage were implemented by collaborators at AIUB and colleagues at Purdue University. Two different methods for determining the attitude profile of an object using light curves were applied to the Atlas V object. The first method for determining the attitude profile assumes that an object model and a rotation period are known, but only requires one light curve. The assumed object model for the first method is given in Figure 5.19, where the different colors correspond to different surface materials, based

on known object properties. The second attitude determination method requires three light curves to determine the attitude from the intersection of three loci.

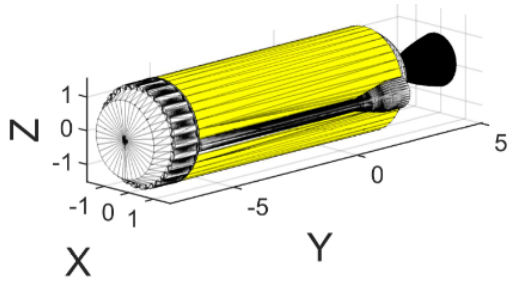

Figure 5.19. Three material Atlas V upper stage model.

Past observations have suggested that for a cylindrical body with length at least three times larger than diameter, stable motion is likely spinning about the maximum moment of inertia axis [167]. The maximum moment of inertia axis is defined inertially using right ascension and declination with respect to the J2000 vernal equinox. Since the object is likely spinning about its maximum moment of inertia axis, the ratio of maximum brightness and minimum brightness is a function of the orientation of the spin axis and the phase angle. Phase angle, i.e. the angle between the object-Sun vector and the object-observer vector, is often assumed information from either the observation or the orbit propagation. Therefore, it is possible to generate a locus of potential right ascension and declination angles of the spin axis from a single set of observation. If another observation is made at a different observation location, and thus a different phase angle, another locus can be traced out. The attitude can be concluded from the intersection of two loci because the spin axis of the same object at the same time must agree. If, however, the different observations are made at different times, the object attitude motion is assumed to be the same throughout. In actual application, error is allowed in the observation, and an intersection of regions is determined instead of an intersection of curves [165].

The attitude determination method using the object shape is a brute-force search method for determining the spin axis. The potential spin axis orientations, in right

ascension and declination, were sampled at a resolution of 1° using the assumption that the upper stage is exhibiting stable main-axis rotation. The rotation period of 64.7 seconds, determined with the previously described attitude determination method, was required for the brute-force attitude determination. For each sampled spin axis, using the assumed object model and rotation period, a light curve was simulated and compared to an actual light curve of the Atlas V upper stage from the ZIMLAT telescope operated by AIUB. The attitude profile which simulated a light curve which most resembled the actual light curve is defined by right ascension and declination of 318° and 9°, respectively. This spin axis orientation is labeled attitude A in this work.

The second attitude profile was determined in the work by Koller, where the attitude profile of the Atlas V upper stage is derived with methods from Williams and three light curve observations [165]. In the work by Koller, no shape information is necessary, but multiple light curves are required. The orientation of the spin axis determined by Koller is defined by right ascension of 298° and declination of 9° using observations from multiple nights from one location. This spin axis orientation is labeled attitude B in this work. The solution by Koller was also determined to be a viable solution using the brute-force search method. However, attitude A, defined by right ascension and declination of 318° and 9°, respectively, reproduced the actual light curve more closely. Table 5.6 shows the spin axis orientations for each of the attitude profiles.

Table 5.6. Atlas V attitude profiles.

Profile	Right Ascension [°]	Declination [°]
Attitude A (Brute-Force)	318	9
Attitude B (Koller)	298	9

The observability analysis of the Atlas V upper stage system begins with simulations of several measurement spacing cases and EGI tessellation numbers without constraints on when the measurements occur. The unconstrained observability analysis is simulated using attitude profile A. Next, constraints are applied to determine the observability of the EGI minimization in a more realistic observation scenario. The minimum elevation which the Atlas V upper stage could be observed is set at 15°. Observations are also restricted to astronomical dark which requires a solar depression angle of at least 18°. These constraints are applied to determine observation windows for the Atlas V upper stage and observation sequences are defined based on the visibility windows. The different measurement cases for the constrained analysis are given in Table 5.5.

5.3.2 Unconstrained Analysis

The tessellation numbers used in this analysis, 5, 7 and 13, equate to 150, 294, and 1014 surface normal directions, respectively. The measurement spacing cases analyzed for the unconstrained observability are given in Table 5.4. The time between batches is increased for the 1014 surface normal direction case to counter the increased computational time required for the greater number of surface normal directions on the EGI. Figure 5.20 through Figure 5.27 compare the spacing between batch cases without constraints on the measurement times.

For the unconstrained analysis of the Atlas V upper stage EGI minimization observability, approximately five hours is required for the system geometry to progress enough to achieve a full rank observability Gramian. Figure 5.20 presents the observability Gramian rank in the same manner as Section 5.2, where the rank over time is shown for each measurement batch spacing case and the number of EGI surface normal directions is defined by the black dashed line. These observability results are generated with an EGI defined by a tessellation number equal to five, or 150 surface normal directions.

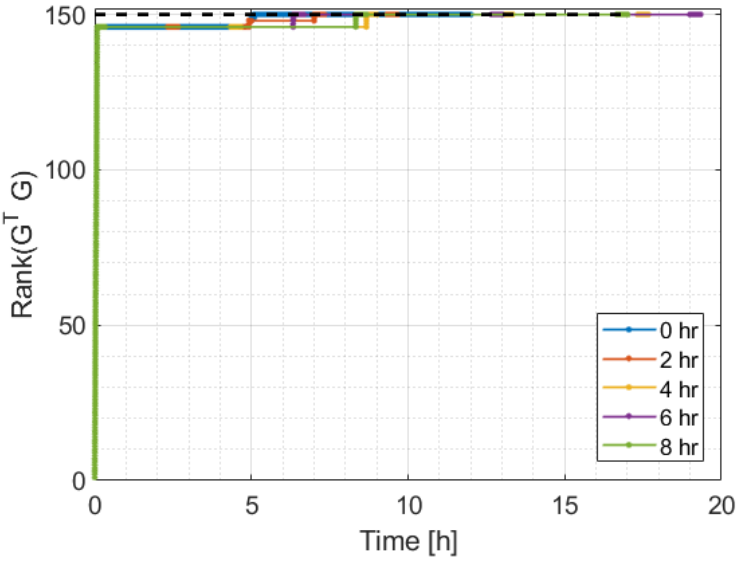

Figure 5.20. Rank of the observability Gramian versus time for several measurement batch spacing cases with an EGI tessellation number equal to five or 150 facets.

After one 20 minute batch of measurements, 600 measurements in total, the observability Gramian rank is 146, which can be seen more clearly in Figure 5.21. Figure 5.22 shows the rank of the observability Gramian compared to the number of measurements, which more clearly depicts the rank of the observability Gramian after the first batch of measurements. Even with continuous measurements, given by the zero hour measurement spacing case, the observability Gramian does not reach full rank until approximately five hours from epoch. The large difference between the first batch of measurements resulting in a matrix rank which is near full and the long time until full rank is actually achieved indicates that the geometry of the system must progress for all of the EGI surface normal directions to be sufficiently sampled.

Therefore, for this EGI tessellation number and epoch, measurements after the first batch and before approximately five hours are redundant for light curve inversion. This knowledge of the system observability can be analyzed for developing an efficient light curve observation collection strategy of future measurements for light curve inversion. As the six and eight hour batch spacing cases do not have measurements

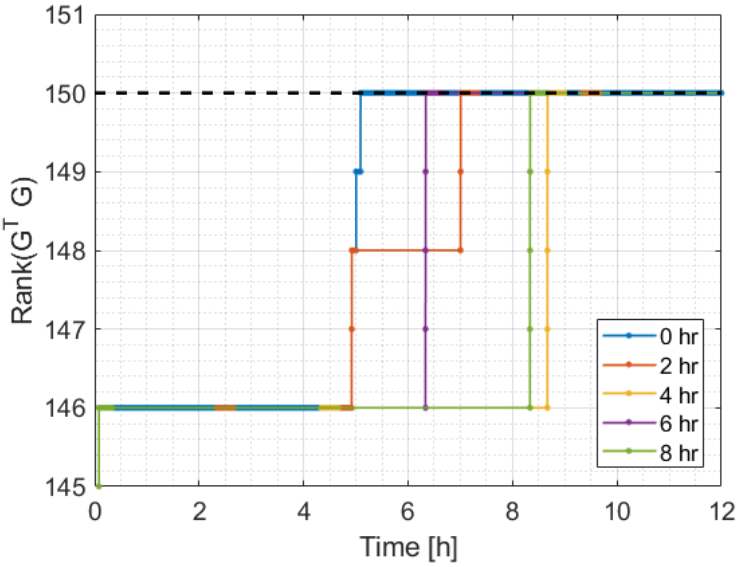

Figure 5.21. Rank of the observability Gramian versus time for several measurement batch spacing cases with an EGI tessellation number equal to five or 150 facets, zoomed in to show detail.

within the five hour window where the rank is not increased for this system, only two batches of measurements are required to achieve full rank, as shown in Figure 5.23. Therefore, a telescope operator may find that observing this system with two batches spaced greater than five hours reduces the number of required measurements for light curve inversion.

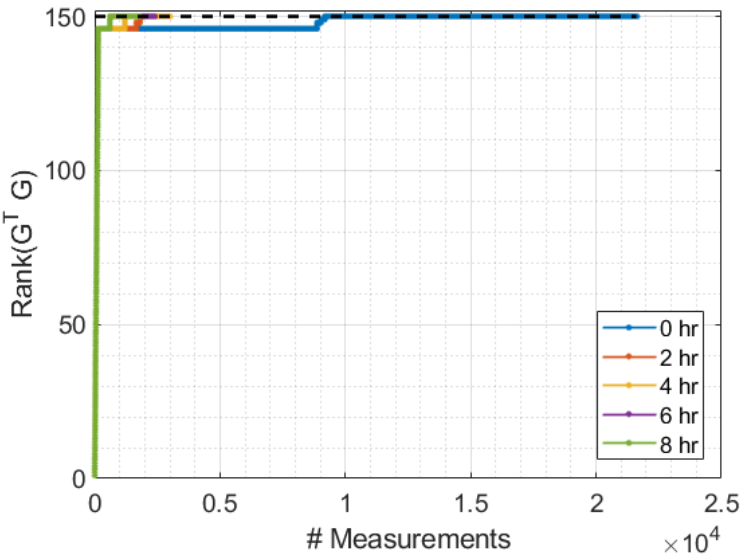

Figure 5.22. Rank of the observability Gramian versus number of measurements for several measurement batch spacing cases with an EGI tessellation number equal to five or 150 facets.

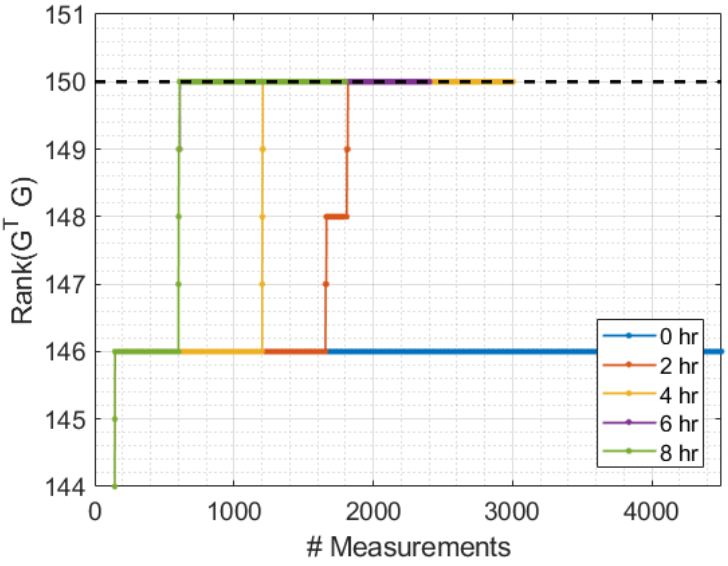

Figure 5.23. Rank of the observability Gramian versus number of measurements for several measurement batch spacing cases with an EGI tessellation number equal to five or 150 facets, zoomed in to show detail.

Next, observability Gramian rank curves are presented for various measurement batch spacing cases with an EGI tessellation number equal to seven in Figure 5.24 through Figure 5.26. Initially, the rank curves of the observability Gramian with 294 surface normal directions appear to be similar to the rank curves of the observability Gramian with 150 surface normal directions. Figure 5.25 shows how the first batch of measurements increases the rank to 288, indicating that the geometry is well sampled in the first batch with the exception of a few surface normal directions. However, after the second batch of measurements, the six and eight hour measurement batch spacing cases do not reach full rank, but have a rank deficiency of one. During the third batch of measurements, the six and eight hour batch spacing cases reach full rank of the observability Gramian. Figure 5.26 shows the rank of the observability Gramian versus the number of measurements for the different measurement batch spacing cases and an EGI defined with 294 surface normal directions.

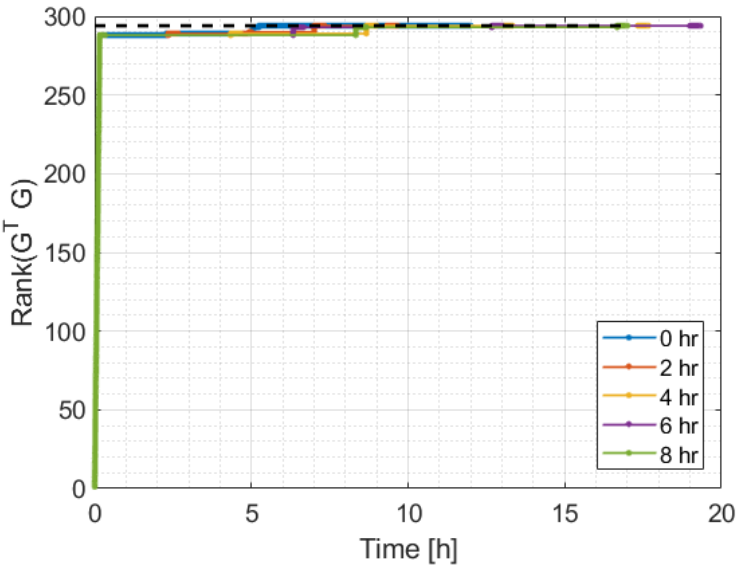

Figure 5.24. Rank of the observability Gramian versus time for several measurement batch spacing cases with an EGI tessellation number equal to seven or 294 facets.

For the case with an EGI defined by 294 facets, the six and eight hour measurement spacing cases take significantly longer than the other spacing cases due to the required

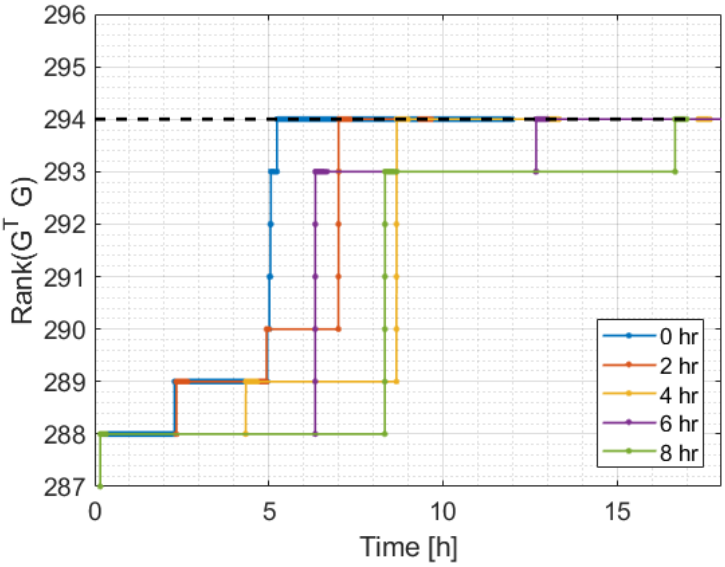

Figure 5.25. Rank of the observability Gramian versus time for several measurement batch spacing cases with an EGI tessellation number equal to seven or 294 facets, zoomed in to show detail.

third batch to reach full rank, as shown in Figure 5.25. Therefore, for this system, the four hour batch spacing case may be advantageous for collecting light curves for inversion since the time to reach full rank for the observability Gramian is shorter than the six and eight hour spacing cases, and the number of measurements required for the four hour spacing case is less than the zero or two hour spacing cases.

For an EGI with 150 surface normal directions, only two batches are required for the six and eight hour spacing cases to reach full rank, but for an EGI with 294 surface normal directions, three batches are required. This comparison of the rank for two different EGIs, indicates how sensitive the EGI minimization step of the light curve inversion can be to the EGI tessellation number. Moreover, a higher EGI tessellation number is advantageous for capturing all features of an object through light curve inversion.

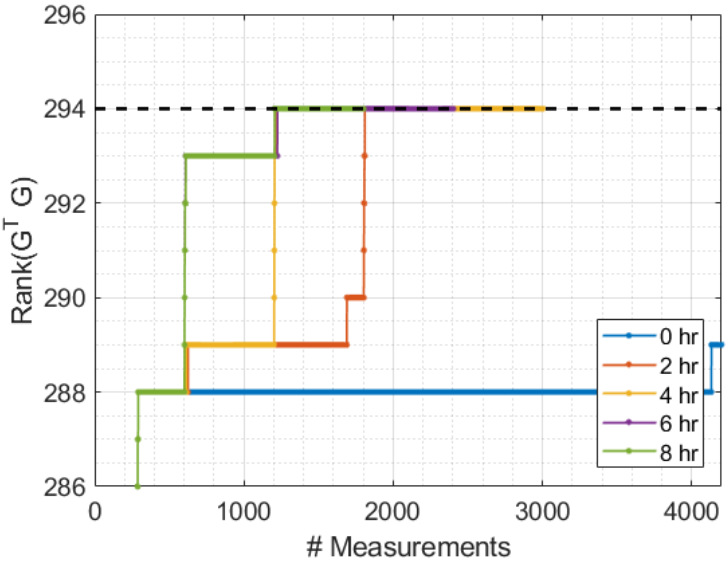

Figure 5.26. Rank of the observability Gramian versus number of measurements for several measurement batch spacing cases with an EGI tessellation number equal to seven or 294 facets, zoomed in to show detail.

Finally, the unconstrained case is presented for a larger EGI tessellation number. Figure 5.27 through Figure 5.30 show rank of the observability Gramian versus time and number of measurements, for an EGI with 1014 surface normal directions. With one batch of measurements for each measurement spacing case, the rank of the observability Gramian reaches a rank of 600, as shown in Figure 5.27. As there are 600 measurements per batch, this is the theoretical maximum rank that can be achieved within one batch, which indicates sufficient sampling of the EGI over the first batch of measurements.

The rank of the observability Gramian reaches 1013, a rank deficiency of one, within three batches of measurements for each spacing case, which can be seen in Figures 5.28 and 5.30. The six hour spacing case requires only two batches of measurements to reach a rank of 1013, but the other batch spacing cases require three batches to reach a rank of 1013. Since each batch of measurements consists of 600 measurements, a minimum of two batches is required to sufficiently sample the 1014

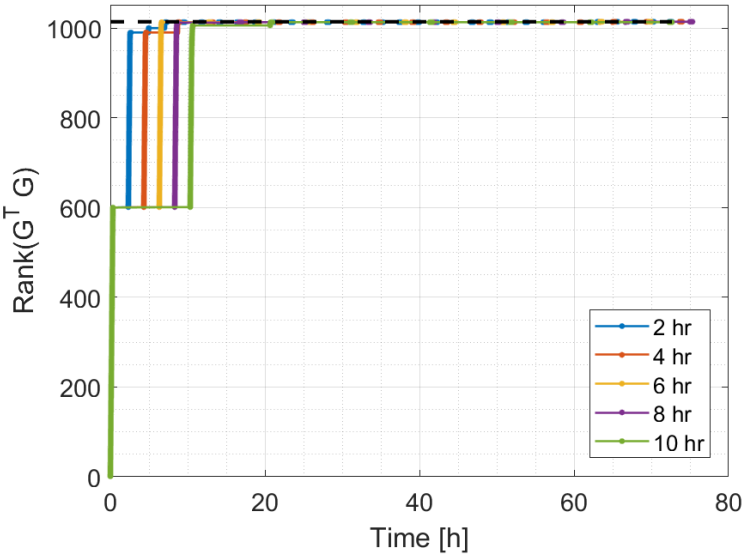

Figure 5.27. Rank of the observability Gramian versus time for several measurement batch spacing cases with an EGI tessellation number equal to 13 or 1014 facets.

EGI surface normal directions. Although all of the spacing cases reach a rank of 1013 after only three batches, full rank is not achieved until approximately 62 hours from the analysis epoch, and full rank is not achieved within the analysis time for the 10 hour spacing case.

For larger EGI tessellation numbers, as shown with the 294 and 1014 surface normal direction observability results, one surface normal direction is not sufficiently sampled early in the analysis given measurement batches that are equally sampled. The system geometry requires a significant amount of time to progress so that full rank of the observability Gramian can be achieved by sufficient sampling of the EGI surface normal directions. Therefore, if measurement batches were spaced equally until the observability Gramian reaches full rank, many of the measurements would be redundant as the geometry has not progressed enough during the plateaus of Figures 5.24 and 5.27. Instead of equally spaced measurement batches, which result in many redundant measurements for this system, three different spacing cases with uneven

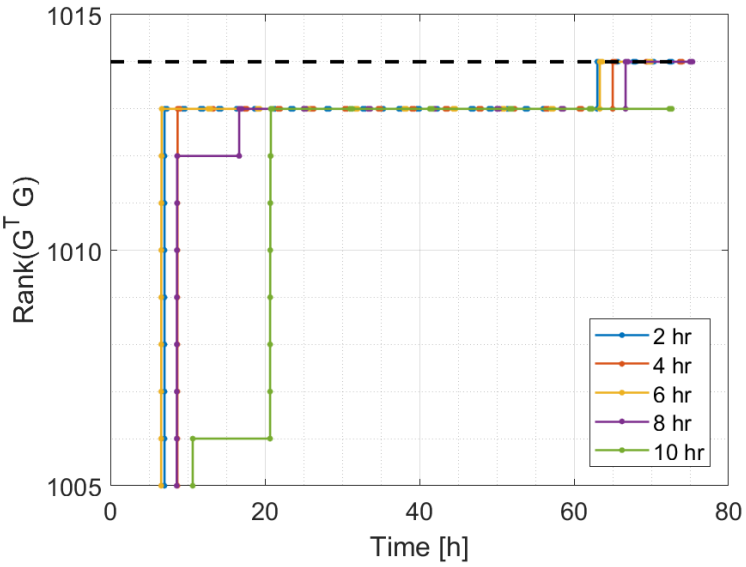

Figure 5.28. Rank of the observability Gramian versus time for several measurement batch spacing cases with an EGI tessellation number equal to 13 or 1014 facets, zoomed in to show detail.

spacing are proposed and analyzed. Furthermore, two of the new measurement batch spacing cases are constrained to windows of object visibility from the ground station.

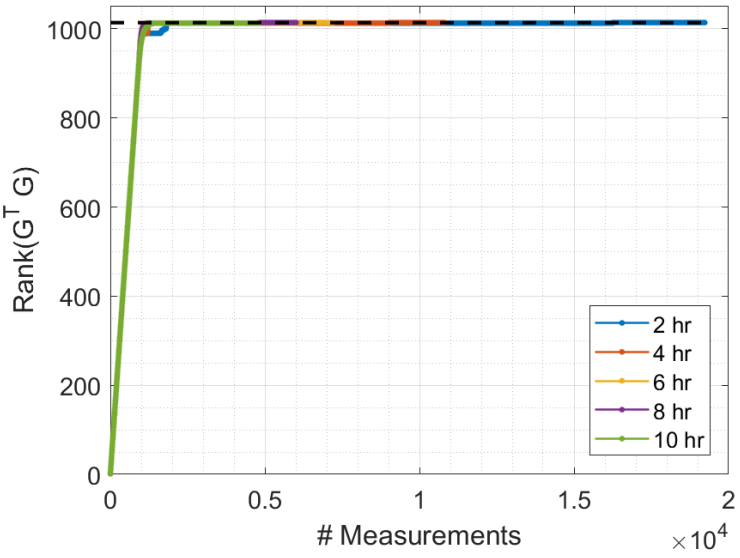

Figure 5.29. Rank of the observability Gramian versus number of measurements for several measurement batch spacing cases with an EGI tessellation number equal to 13 or 1014 facets.

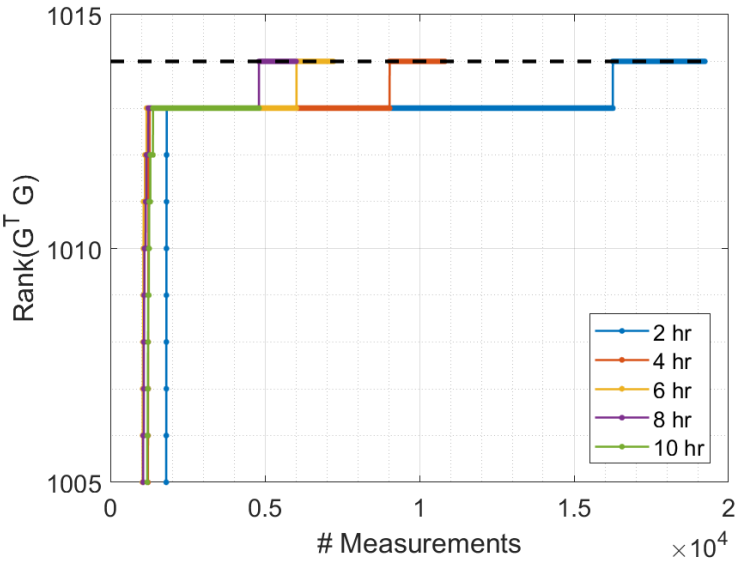

Figure 5.30. Rank of the observability Gramian versus number of measurements for several measurement batch spacing cases with an EGI tessellation number equal to 13 or 1014 facets, zoomed in to show detail.

5.3.3 Constrained Analysis: Attitude Profile A

Rather than limit the measurement batch spacing to equal time between batches, knowledge gained from the unconstrained analysis in the previous section is employed to determine an efficient light curve observation strategy for light curve inversion. This section uses the same attitude profile, as the unconstrained analysis, attitude A defined by right ascension and declination of 318° and 9°, respectively. The observability of three batch spacing cases with unequal measurement spacing, defined in Table 5.5, is determined for an EGI with 1014 surface normal directions. Two of the cases analyzed are constrained by the solar depression angle and the object visibility given elevation constraints at the AIUB ground station. These constraints assume that if the object is illuminated and above the elevation constraints of the ground station, then it will be visible to the observer. The solar depression angle is given by 18° or astronomical dark, and the minimum elevation for the object to be visible to the observer is 15°. In addition, as more realistic measurement sequences and constraints are applied for this analysis, the fidelity of the orbit propagation is also increased through the implementation of SGP4 rather than two-body propagation. The impact of propagation method on these observability results is discussed in Section 5.3.6 with results shown in Appendix C.6.

The unconstrained batch spacing is defined from the knowledge gained in the previous analysis of an EGI with 1014 surface normal directions and the same attitude profile. Two batches are spaced by 6 hours and then a third batch is 64 hours after the end of the second batch. This gap between the second and third measurement batch accounts for the plateau in Figure 5.30 where the rank does not increase. The first constrained measurement spacing case places two batches within two different visibility windows, resulting in four total batches of measurements. The two batches within each window are separated by approximately 1.5 hours, starting at the beginning of the visibility window. The second set of measurement batches for the first constrained spacing case occurs in the next available window after the period where

the rank of the observability Gramian does not increase in Figure 5.30. The second constrained measurement spacing case places one batch of measurements in each visibility window, spaced by approximately 24 hours. Note that there is a large gap between the sixth and seventh batches due to visibility windows which are not long enough to contain the 20 minute batch of measurements, or do not exist for a given night.

Figure 5.31 shows the rank of the observability Gramian for the three unequal measurement spacing cases. Night hours and object visibility times are defined by the gray and green bars, respectively. The two constrained measurement spacing cases have measurements only within the green regions. The unconstrained case with unequal spacing is not restricted to the green or gray regions.

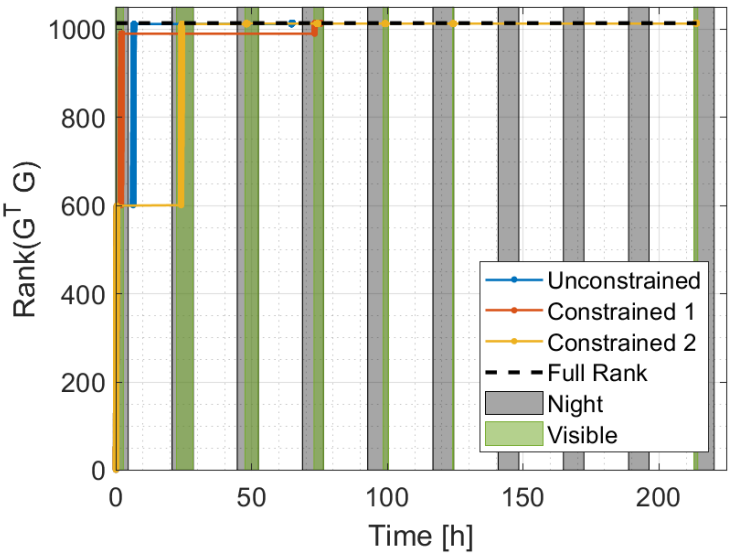

Figure 5.31. Rank of the observability Gramian versus time with visibility constraints and attitude A.

The unconstrained case reaches a rank of 1012 after two batches of measurements in Figure 5.32, which is nearly identical to the six hour spacing case in Figure 5.27, and full rank of the observability Gramian is achieved with a third batch of measurements. The first constrained case does not achieve as high of rank after two measurement

batches when compared to the unconstrained case. As the second batch of the first constrained case is approximately 1.5 hours from the first batch, the geometry and attitude does not change as much as the time between the first and second batches of the unconstrained spacing case. The first constrained case reaches full rank within the fourth batch measurements, after approximately 75 hours. The second constrained case reaches a rank of 1013 after three batches of measurements, but full rank is not achieved until the seventh measurement batch after approximately 215 hours from epoch. The number of batches required for the second constrained case was selected so that full rank was achieved in the last batch of measurements. Note that more optimal placements of each measurement batch in the visibility windows may exist for the second constrained case where only one measurement batch occurred in each window. Differences in the required number of observations between the measurement spacing cases is more clearly shown in Figure 5.33.

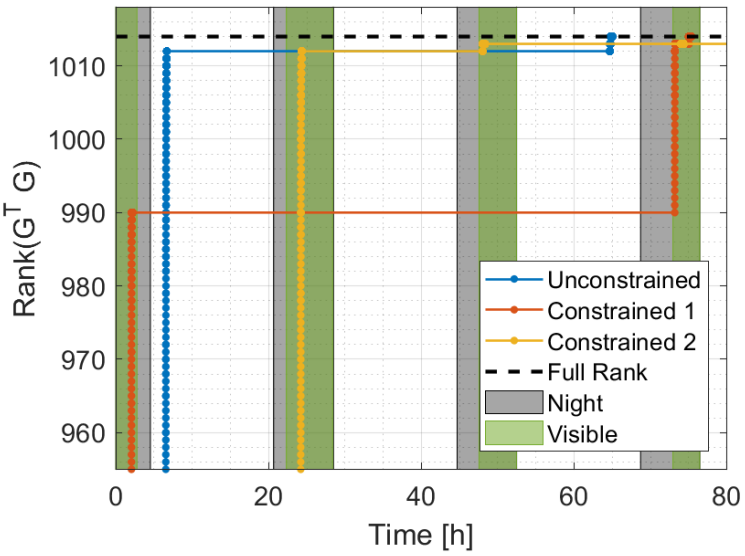

Figure 5.32. Rank of the observability Gramian versus time with visibility constraints and attitude A, zoomed in to show detail.

For this system with an EGI defined by 1014 facets, multiple batches of measurements within each visibility window resulted in a more efficient observation plan for

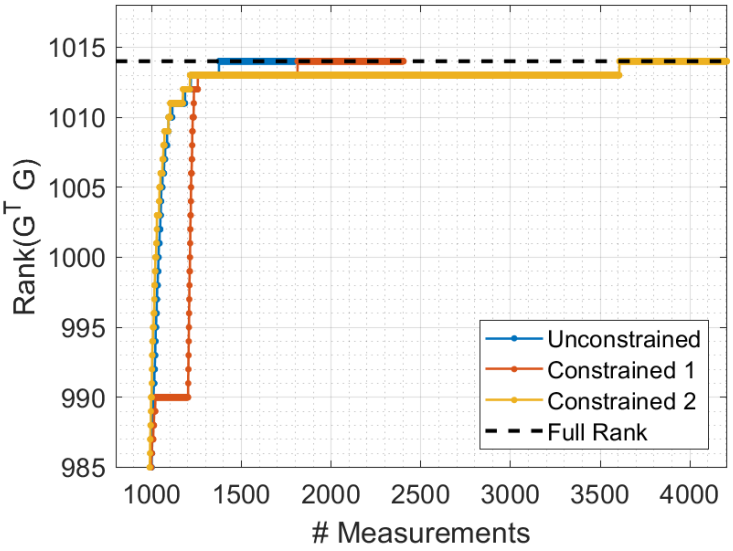

Figure 5.33. Rank of the observability Gramian versus number of measurements with visibility constraints and attitude A.

light curve inversion compared to one batch of measurements per visibility window. Multiple measurement batches per visibility window improve the chances of greater geometric diversity among the measurements. When one batch of measurements occurs in each visibility window, there is a potential for selecting measurement times which do not add geometric diversity to the measurement space. This analysis of observability for EGI minimization with realistic constraints on windows of object visibility have shown that light curves do not have to be taken continuously or for many hours to achieve sufficient sampling of an object for light curve inversion.

5.3.4 Constrained Analysis: Attitude Profile B

The same unconstrained and constrained measurement batch cases from Table 5.4 are applied with the second attitude profile to determine the sensitivity of the observability results to changes in attitude. Figure 5.34 through 5.37 reproduce the observability analysis from the previous section with attitude B, defined by right

ascension and declination of 298° and 9°, respectively. With this different attitude profile, the rank of the observability Gramian fails to equal the number of EGI surface normal directions, 1014, for the three spacing cases. The second constrained case, with one batch of measurements per visibility window, reaches the highest rank, but is still short of full rank. Such a significant difference in the observability results from a change in the attitude profile prompted a more detailed investigation of the observability of this system with the second attitude profile.

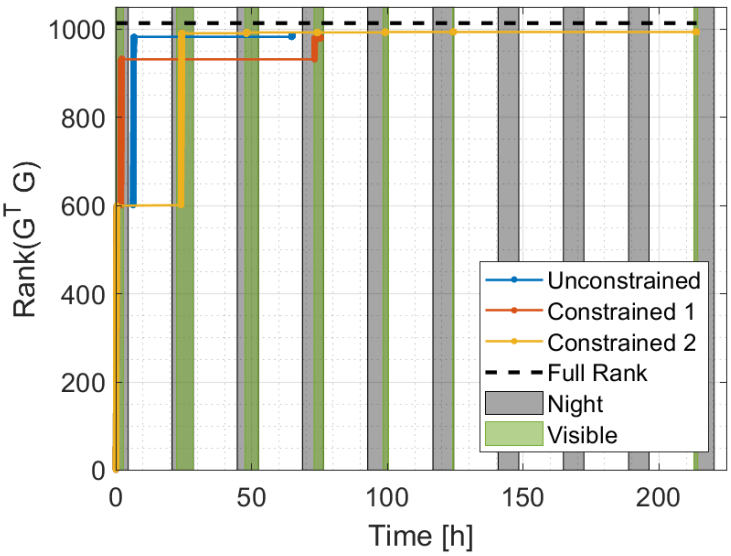

Figure 5.34. Rank of the observability Gramian versus time with visibility constraints and attitude B.

5.3.5 Rank Deficiency of Attitude Profile B

In order to understand the rank deficiency of this system with attitude B for EGI minimization, the linear independence of the columns of the reflection matrix is visualized for the first constrained spacing case in Figure 5.38. This method of visualizing the linear independence of the reflection matrix columns is analogous to the results in Appendix 5.2.3. Figure 5.38a shows the view from the observer to the

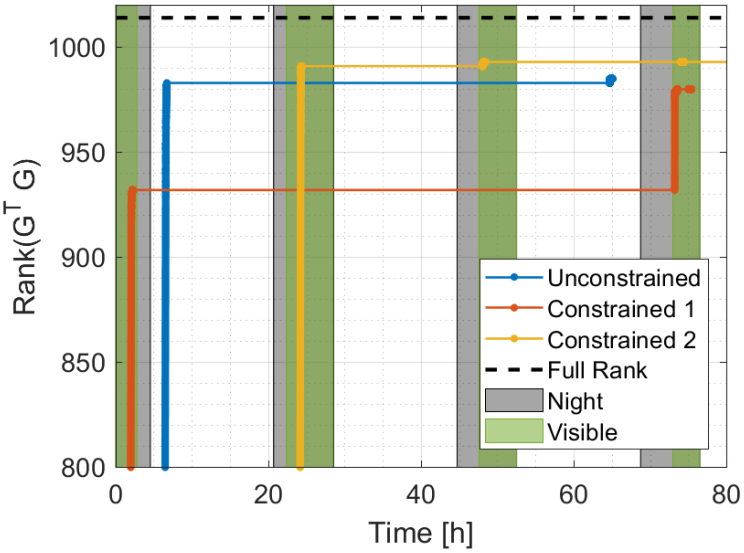

Figure 5.35. Rank of the observability Gramian versus time with visibility constraints and attitude B, zoomed in to show detail.

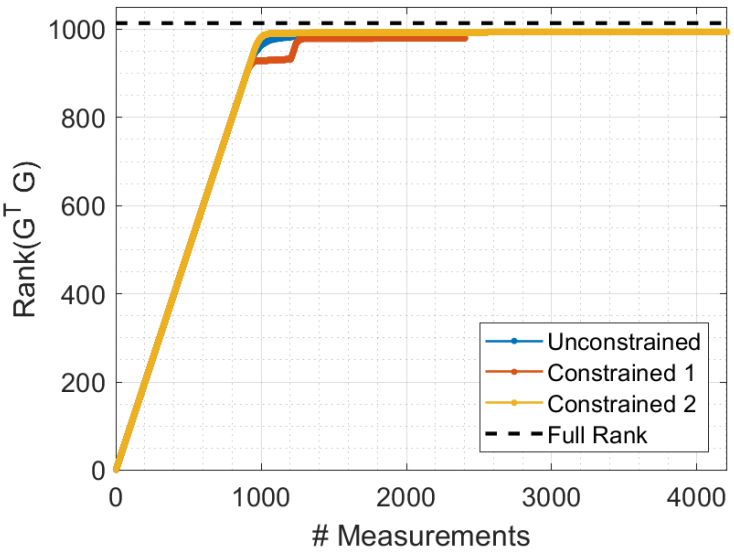

Figure 5.36. Rank of the observability Gramian versus number of measurements with visibility constraints and attitude B.

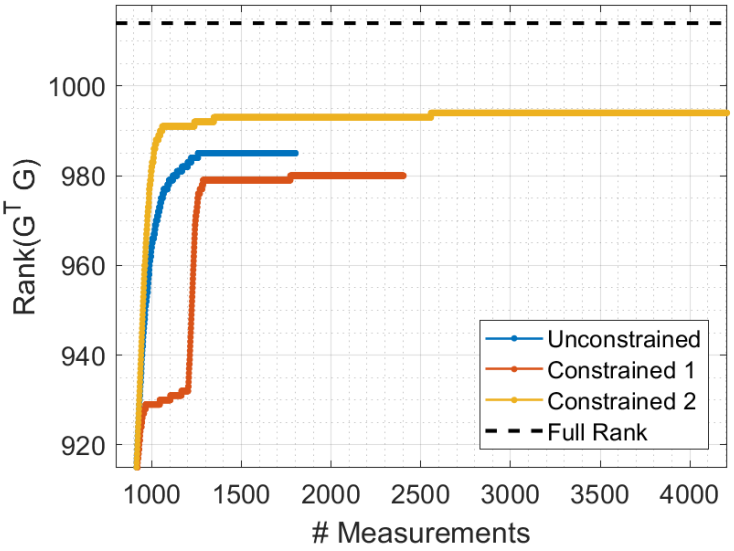

Figure 5.37. Rank of the observability Gramian versus number of measurements with visibility constraints and attitude B, zoomed in to show detail.

object at the end of the last measurement. A second view of the visualization at the same time of the last measurement is given in Figure 5.38b, showing a region where the second batch of measurements sufficiently sampled the surface normal directions of the EGI. At first it appears that all surface normal directions have all been sampled, but Figure 5.38c, a different orientation of the visualization at the same time, shows a region of surface normal directions which were insufficiently sampled. Therefore, this one region of the EGI was not illuminated and visible to the observer or did not have enough measurements to sufficiently sample the EGI surface normal directions for EGI minimization. The rank deficiency of attitude profile B is explored further in Appendix C.5 with unconstrained, equally spaced measurements. Even with constraints removed, this attitude profile remains rank deficient for the given observer-object-Sun geometry. For comparison, the visualization of the linearly independent columns of the reflection matrix for attitude A with the same measurement sequence, shown in Figure 5.39. All surface normal directions of the EGI are sufficiently sampled after four batches of measurements.

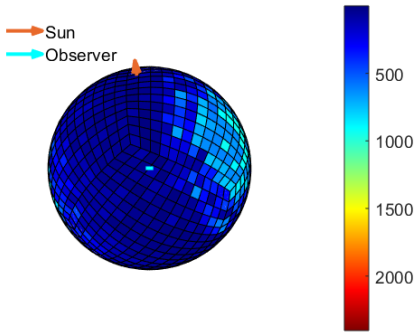

(a) Observer view to the observer after last measurement.

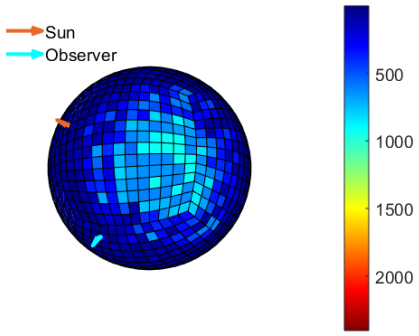

(b) Orientation depicting region sampled during second batch of measurements.

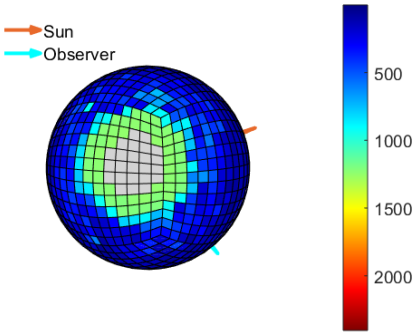

(c) Insufficiently sampled region after last measurement.

Figure 5.38. 3D visualization of the observability Gramian rank for the Atlas V upper stage with attitude B and the first constrained measurement case.

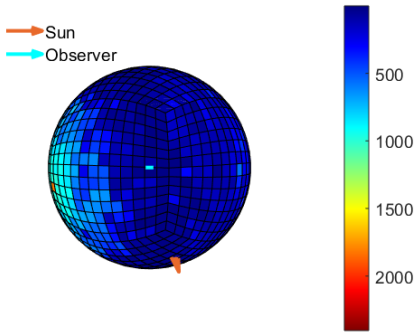

(a) Observer view to the observer after last measurement.

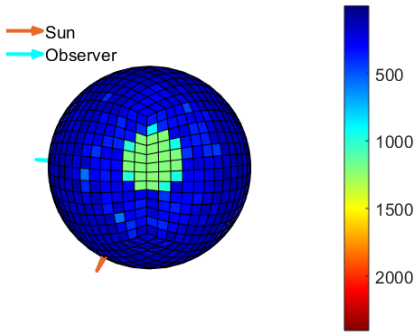

(b) Orientation depicting region sampled during second batch of measurements.

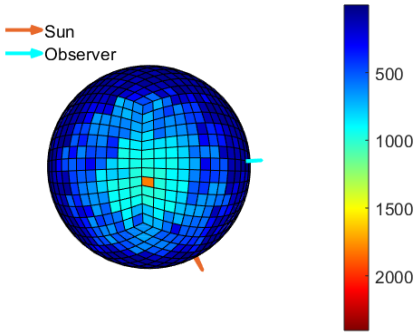

(c) Orientation depicting region sampled during last batch of measurements.

Figure 5.39. 3D visualization of the observability Gramian rank for the Atlas V upper stage with attitude A and the first constrained measurement case.

5.3.6 Atlas V Constrained Analysis Summary

The observability of the EGI minimization was analyzed for the Atlas V rocket body with realistic constraints and measurement spacing. A requirement of this observability analysis of the EGI is a known attitude profile. Two different methods were implemented for determining potential attitude profiles for the Atlas V given light curve measurements from collaborators at AIUB. Attitude profiles A and B in Table 5.6 were both determined as viable profiles using the brute-force sampling method. Through observability analysis with realistic constraints and attitude A, an efficient measurement sequence was determined for sufficient sampling of the Atlas V system geometry to perform light curve inversion. In addition, the sensitivity of the observability results to different attitude profiles was explored by also analyzing a system defined by attitude B, and this system was found to be sensitive to different spin axes because the same measurement sequence for the attitude A profile resulted in insufficient sampling for attitude B.

Further analysis was conducted on the sensitivity of the observability results to the orbit propagator used for the object position. Observability results with two-body propagation and SGP4 propagation are presented in Appendix C.6. Over shorter analysis periods, the impact of the orbital propagator, two-body propagation or SGP4, is minimal as the orbit geometry difference with the two propagators is small. However, as the propagation time is increased to 180 days between two sets of measurement batches, the two-body propagated orbit and SGP4 propagated orbits result in significant differences in the observability results. For the system analyzed in this work, the SGP4 propagated orbit was detrimental to the rank of the observability Gramian. Greater geometric diversity from a perturbed orbit reduced the observability of the EGI surface normal vectors. As a result, two-body propagation may be sufficient for observability of the EGI minimization over short analysis times, but when longer propagation is desired, more realistic orbit propagation is important for analysis of the EGI minimization observability.

This analysis has shown that observability can be applied to light curve inversion for determining when an EGI is sufficiently sampled for estimating albedo-areas. Under realistic observation constraints and with attitude profile A, four 20 minute batches of measurements are sufficient for sampling the EGI surface normal directions. Although the observability of this system was found to be sensitive to changes in the geometry over time, the application of observability successfully demonstrated that hours of continuous light curve measurements are not required for light curve inversion. In addition, these observability methods can be applied to planned observation campaigns to determine efficient measurement sequences for light curve inversion.

5.4 Observability for Investigating Satellite Deployment, Given Original Object Shape

Previous analysis of observability in Sections 5.2 and 5.3 were conducted without knowledge of the original object shape. Note that the analysis of the Atlas V upper stage did include assumptions of the object shape to determine the attitude profile. The observability analysis of the EGI minimization independent of object shape focuses on ensuring the sampling of the EGI is sufficient for light curve inversion.

When an object is represented by an EGI, many of the surface normal directions on the EGI may not have associated albedo-areas as the original object may not have corresponding surface normal directions. This relationship between the original object and EGI is exploited in this section. The mapping matrix developed during the generation of the EGI is used to determine when specific surface normal directions of the original object become observable. The term observable is used loosely here as the observability Gramian matrix may not be full rank in this analysis, but conclusions are drawn on the observability of specific object features. This notion of deeming specific features observable is possible because the EGI minimization is linear with respect to the albedo-area vector. Therefore, specific features are deemed observable

when the linearly independent columns associated with surface normal directions are mapped back to specific features on the original object.

The time for specific features of a box-wing satellite to become observable is explored in this work. The mapping of a box-wing satellite to an EGI is shown in the bottom row of Figure 2.4 in Chapter 2. This box-wing satellite is modeled after the Astra 1D satellite which is composed of a main satellite bus with two antennae and two solar panels. The attitude profile for a typical box-wing satellite, e.g. a GPS or a communication satellite, is to align the solar panel normal vector with the Sun vector for maximum power generation, and the antenna are directed towards the Earth [168]. Therefore, both the solar panels and antenna articulate over time. The box-wing model is simplified for this observability analysis, and a faceted, simplified Astra 1D model is shown in Figure 5.40. The antenna are removed from the model and the solar panels are kept fixed with the orientation of the satellite bus, resulting in an attitude profile which maintains alignment with the Sun vector over time.

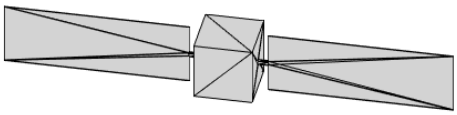

Figure 5.40. Simplified Astra 1D model with antennae removed.

In order to determine when specific features of the original model become observable, the mapping matrix from the original model to the EGI is used in reverse. First, observability analysis of the reflection matrix is performed to determine which EGI surface normal directions are sufficiently sampled. Next, the linearly independent columns of the reflection matrix, which are associated with the surface normal directions of the EGI, are mapped back to the original object. Note that the mapping from the original object to the EGI is not one-to-one, i.e. many of the EGI surface normal directions do not have associated albedo-areas with respect to the original object. The EGI representation examples of Figure 2.4 shows how many of the EGI surface normal directions may have associated albedo-areas equal to zero.

For the cuboid shape, only six of the EGI surface normal directions have non-zero albedo-areas. In addition, multiple facets of the original object may have the same surface normal direction, so they are mapped to a single surface normal direction on the EGI. For example, in Figure 2.4, the box-wing model has one face of the satellite bus with a normal vector which is the same as the solar panel surface normal vectors, and therefore, the facets defined by this surface normal vector are associated with one surface normal vector on the EGI.

When observability analysis is applied for identifying key features mapped from the EGI to the original model, focus is placed on the solar panels. Two box-wing satellite models are generated, one with fully deployed solar panels and one with an error in the solar panel deployment, to analyze the impact of solar panel misalignment on the time to become observable. Deployed solar panels are defined by an angle of 90° between the satellite bus and the solar panel. However, if an error were to occur in the deployment of the solar panels, this alignment angle could be different from 90°. The box-wing model with fully deployed solar panels is shown in Figure 5.41a, and the box-wing model with an error of 5° in the alignment angle of the solar panels is shown in Figure 5.41b. As the solar panels do not have the same normal vector when there is an error in the deployment angle, the attitude profile in this work aligns one of the solar panel normal vectors with the Sun vector. Therefore, the second solar panel exhibits a 10° yaw error in the pointing of the solar panel which is not aligned with the Sun vector, due to the deployment error of 5°.

(a) Panels deployed 90° from bus. (b) Panels deployed 85° from bus.

Figure 5.41. Two solar panel orientation cases, fully deployed and deployed with an error of 5°.

The impact of measurement spacing and EGI tessellation number is investigated for the box-wing model in Figures 5.42, 5.43, and 5.44. The measurement spacing and EGI tessellation numbers analyzed for this object are given in Table 5.7. The linearly independent columns of the reflection matrix and the original model to EGI mapping matrix are used to compute the percent of the box-wing albedo-area which is sufficiently sampled over time.

Table 5.7. Astra 1D cases analyzed.

Measurement Spacing [s]	EGI Tessellation Numbers
3, 5, 10, 20	5, 7, 9, 11

Figure 5.42 shows the percent of the Astra 1D model albedo-area which is associated with the surface normal directions of the EGI which have been sufficiently sampled. For this system and Astra 1D model with fully deployed solar panels, time between measurements ranging from 3 seconds to 20 seconds does not have an impact on the observability of the box-wing model. The diamond marker in the plot represents the time when the solar panels are sufficiently sampled. For approximately 6 hours, none of the EGI surface normal directions which were sufficiently sampled are associated with surface normal directions on the Astra 1D model. The solar panels are sufficiently sampled after approximately 9.5 hours from epoch. When the solar panels are sufficient sampled, there is slight variation in the different measurement spacing cases, as shown in Figure 5.43.

Next, different EGI tessellation numbers, from 5 to 11, are analyzed for the Astra 1D model. The number of surface normal directions for these EGIs range from 150 to 726. As the EGI resolution increases, surface normal directions on the original model which are close in direction are more likely to be mapped to different directions on the EGI. When the original model can be mapped to the EGI with higher resolution, the light curve inversion result is likely to be better. Therefore, a range of EGI tessellation

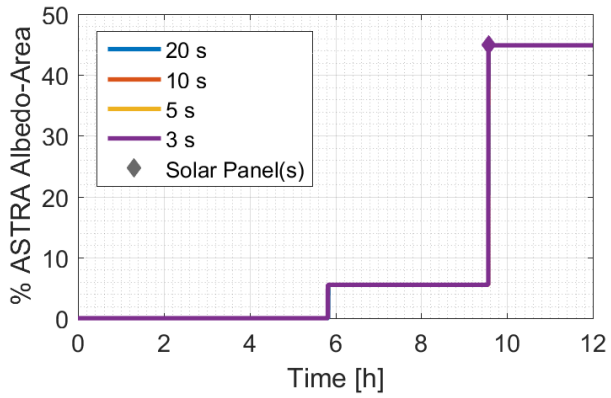

Figure 5.42. Astra 1D albedo-area associated with the EGI rank for various measurement spacing cases.

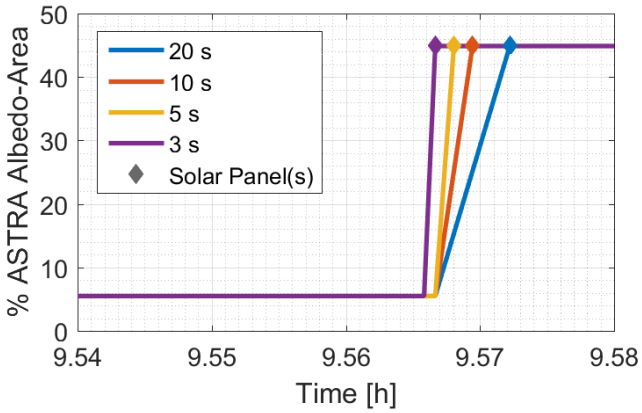

Figure 5.43. Astra 1D albedo-area associated with the EGI rank for various measurement spacing cases, zoomed in to show details.

numbers are analyzed for the Astra 1D model with an error in the alignment of the solar panels to determine when major components are visible separately in the observability analysis. For the fully deployed model, the solar panels and a side of the satellite bus have the same surface normal vector so they are mapped to the same EGI surface normal direction, thus prompting the use of the other Astra 1D model. Figure 5.44 shows the percentages of the Astra 1D albedo-area which have become observable with time.

The angle between surface normal directions on the EGI can be approximated by the EGI tessellation number. This angle gives an indication of how different features of a model will be grouped and mapped to the EGI. For an EGI tessellation number of 5, the angle between adjacent surface normal directions is 10°; whereas, for an EGI tessellation number of 11, the angle is approximately 5°. For the Astra 1D model with a 5° error in the solar panel deployment angle, the angle between the two solar panels is 10° due to the error in each panel. Therefore, the observability results for an EGI tessellation number of five should show two solar panel percentage increases together, but the EGI tessellation number of 11 results should show the solar panel percentages increasing separately.

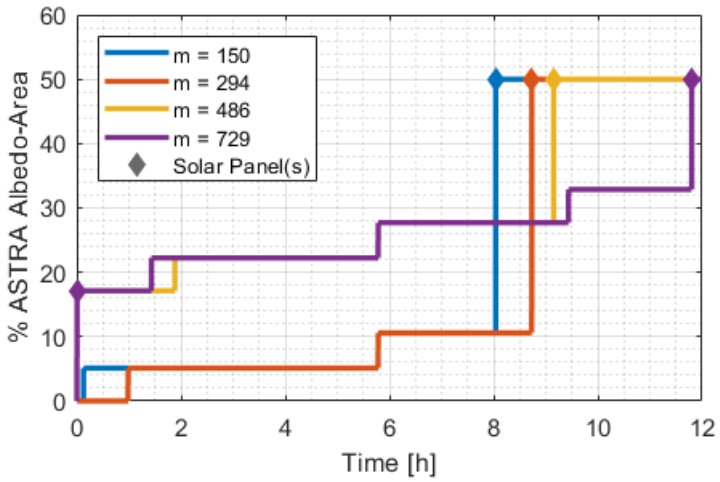

Figure 5.44. Astra 1D albedo-area associated with the EGI rank for several EGI tessellation numbers.

This behavior is confirmed in Figure 5.44. For the $m = 729$ results, the percentage of the Astra 1D albedo-area which has become observable increases by approximately 17.5% initially, which is the albedo-area percent of one solar panel. Next, three smaller increases of approximately 5% occur, which is representative of the faces of the satellite bus. Finally, the second solar panel becomes observable as represented by the last increase of approximately 17.5% for $m = 729$ results. The smallest EGI

tessellation, with $m = 150$, has a significantly different profile for how the percentage of the Astra 1D albedo-area increases with time. Two of the satellite bus facets become observable as given by the two increases of 5%. The next increase in percent is approximately 40% which contains both of the solar panels and one of the satellite bus faces. The structure of the increase percent albedo-area for each EGI tessellation number case can be explained by the angle between adjacent surface normal directions on the EGI. This analysis shows that the selection of the EGI tessellation number can have a large impact on identifying when specific features of the original model become observable.

Next, the observability of the two Astra 1D models is compared. Prior to comparing when specific features of the two box-wing models become observable, the observability of each EGI associated with the attitude profiles is evaluated. An EGI tessellation number of 11, or 726 surface normal directions, and the spacing between measurements of 10 seconds is used for this analysis unless specified otherwise. Figure 5.45 shows the percentage of the total EGI albedo-area for the two box-wing models. The percentage of the EGI albedo-area is used instead of matrix rank because this work focuses on identifying specific features in the observability analysis over time.

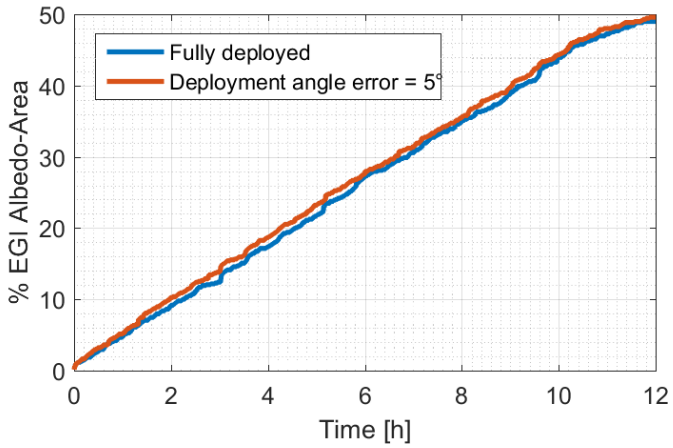

Figure 5.45. Percentage of the EGI albedo-area over time for the two different solar panel alignment angles.

The EGI representations of the two box-wing models have similar percentages over time, as shown in Figure 5.45. The different orientations of the solar panels results in two EGIs with different attitude profiles. The small difference in the solar panel alignment angle cause the differences in the percentage of the EGI albedo-area over time. In addition, as the attitude profile aligns the box-wing models and EGIs with the Sun vector, only half the model is ever illuminated, and therefore, only half of the model becomes observable.

Although the EGI albedo-area percentages are similar for the two Astra 1D models, the differences in the attitude profiles and differences in the model geometries may result in significantly different times to become observable for specific features on the original models. Figure 5.46 shows the percentage of the albedo-area which is sufficiently sampled for the fully deployed box-wing model and the model with a 5° error in the deployment angle.

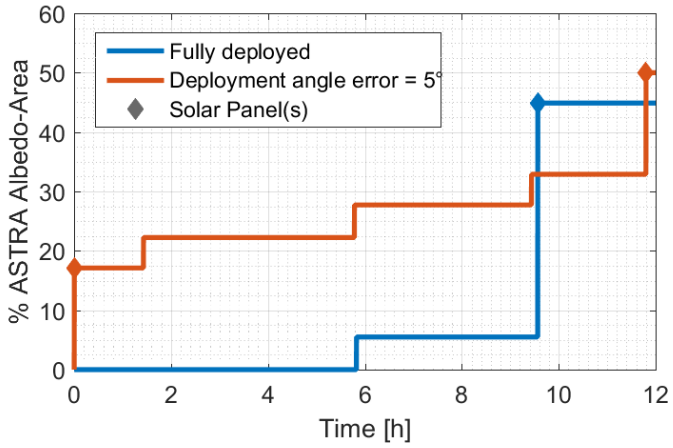

Figure 5.46. Solar panel alignment angle comparison.

The model with fully deployed solar panels only has two occasions where the percentage of the albedo-area increases for this analysis time. This occurs because the solar panels and one of the bus faces have the same surface normal direction, and when the surface normal direction on the EGI corresponding to that surface normal direction is sufficiently sampled, the percentage of the albedo-area increases

with a value representative of those three components. The model with a solar panel deployment error has five occasions where the albedo-area percent increases, as a result of the greater geometric diversity of the surface normal directions on this model. Also, a comparison of the percentages after 12 hours shows a different total for the two models. The model with an error in the solar panel deployment has a greater percentage at the end of the analysis due to a more diverse model geometry and a different attitude profile.

The times for features of the Astra 1D models to become observable can also be shown with the 3D visualization methods of Sections 5.2 and 5.3. Figure 5.47 shows the 3D representation of the reflection matrix linearly independent columns on the EGI. The surface normal directions which are associated with the linearly independent columns of the reflection matrix are mapped back to the original model using the mapping matrix from the original model to the EGI. The 3D visualizations for the Astra 1D model with an error in the deployment angle of the solar panels are shown in Figure 5.48.

The side-by-side comparison of the EGIs and the original Astra models demonstrates how many of the EGI surface normal directions may be sampled without corresponding surface normal directions on the original models. Each 3D visualizations of the EGIs and Astra models represent the same time in the analysis when comparing the two sets of images. Note that the last row of each figure is not the end of the analysis because at the end of the analysis the Astra model solar panels are oriented approximately 90° from the observer so the facet colors are difficult to see. For the model with the fully deployed solar panels, the solar panels and the satellite bus face with the same normal vector all have the same color in the last row of Figure 5.47. However, the model with an error in the solar panel deployment angle has a different color for the solar panel and satellite bus facet with a surface normal vector close in angle. The second solar panel does not have a color because this solar panel becomes observable for this model near the end of the analysis, after the time of this visualization.

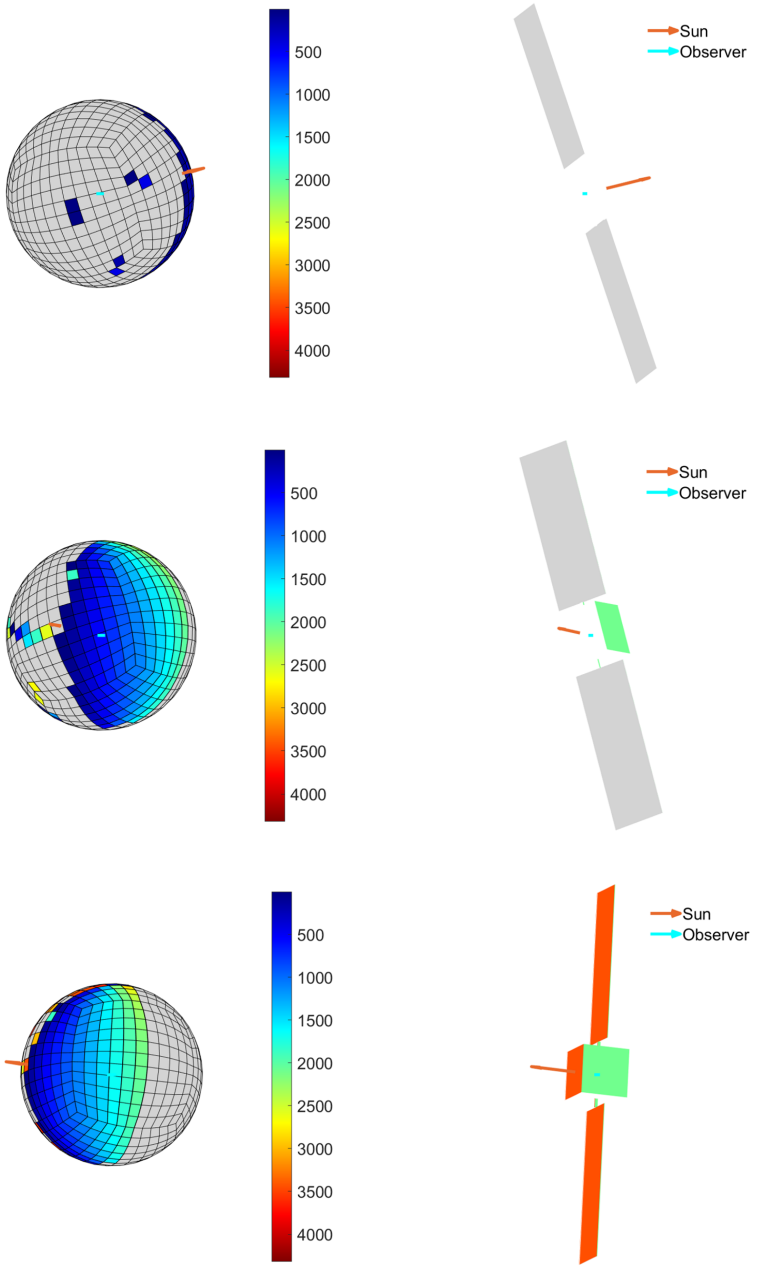

Figure 5.47. Progression of the rank of the Gramian as more measurements are added for the box-wing model with fully deployed solar panels.

When the original object shape is implemented with observability analysis of the EGI minimization for light curve inversion, the time for major features of a model to become observable can be determined. This analysis has shown how many surface

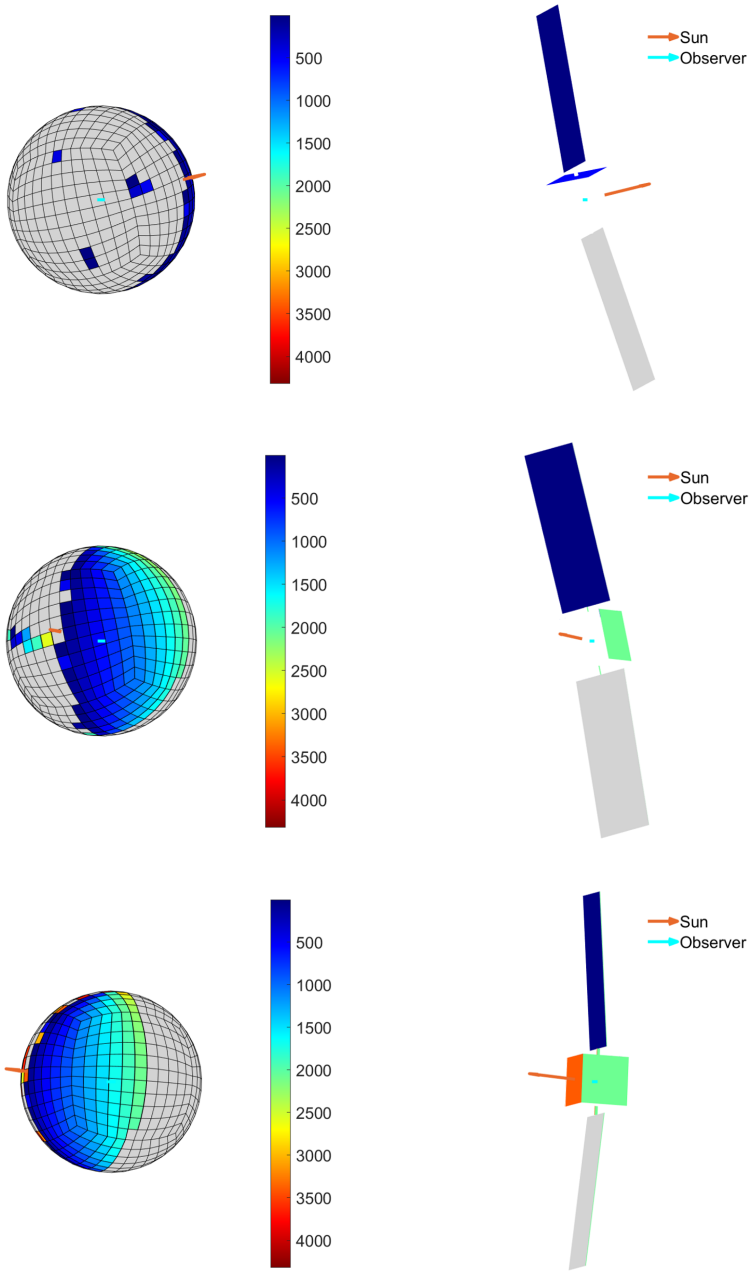

Figure 5.48. Progression of the rank of the Gramian as more measurements are added for the box-wing model with a 5° error in the solar panel alignment angle.

normal directions of the EGI may have an associated albedo-area equal to zero because of the mapping from an object to the EGI representation. Furthermore, small errors

in an object model may have a significant impact on the time for major features of a model to become observable.

5.5 Summary

This work has demonstrated how observability can be applied to light curve inversion, specifically EGI minimization, for albedo-area estimation and for operational support regarding satellite deployment. Analysis of observability was conducted independent of the original object shape to determine when light curve measurements sufficiently sample the system geometry. When the system geometry is sufficiently sampled, the albedo-area vector can be estimated and then the rest of the light curve inversion process can be completed. A challenge of sampling the system geometry is the complex relationship between the measurement sequence, observer-object-Sun geometry, and the attitude profile of the object. However, through analysis of observability, efficient measurement sequences can be established which capture all aspects of the EGI surface normal vectors.

Throughout this analysis, a novel 3D visualization method of the linearly independent columns of the reflection matrix was shown to investigate how the observability of the system progresses over time. The 3D visualization provides more information than the rank of the observability Gramian as the specific regions of the EGI which are sufficiently sampled or not can be identified. Knowledge of the system geometry from the observability Gramian matrix rank and the 3D visualization of the reflection matrix linearly independent columns can be combined to determine efficient measurement sampling which does not include redundant measurements, but still achieves sufficient sampling of the system geometry.

In addition, constraints on the measurement geometry were applied to evaluate the observability for a realistic scenario. Even with measurement constraints, sufficient sampling of the EGI for albedo-area estimation in the light curve inversion process was achieved in three 20 minute batches of measurements. Therefore, continuous

measurements for many hours are not required for performing light curve inversion. Furthermore, the observability analysis with constraints determined that multiple measurement batches within a single visibility window is advantageous for sufficiently sampling the system geometry compared to only one measurement batch per visibility window.

The observability of the EGI minimization was found to be sensitive to the attitude profile of an Atlas V rocket body. For a system with the same measurement sequence but two different assumed attitude profiles, one attitude profile resulted in a full rank observability Gramian and the other attitude profile resulted in a rank deficient observability Gramian. The 3D visualization of the observability over time showed that a small region of the EGI was not illuminated and visible to the observer for the rank deficient attitude profile case.

Observability was also applied including knowledge of the original object shape to identify when major features of the original object become observable. As the EGI may contain many surface normal directions with associated albedo-areas equal to zero, major features of an original object may be sufficiently sampled even if an EGI is not sufficiently sampled. Therefore, the mapping from the original object to the EGI was exploited for mapping the linearly independent columns of the reflection matrix back to the original object. Two box-wing satellites were analyzed in this analysis, one with fully deployed solar panels and a second with an error in the angle of the solar panel deployment. As the attitude profile of the box-wing satellite was defined to align the solar panels with the Sun vector, differences in the observability of the two models were apparent due to the error in the solar panel deployment of the one model. Although the error in the solar panel deployment may result in a reduction in the energy received by the solar panels, the difference in the solar panel angle is advantageous from an observability perspective as there is greater geometric diversity in the model and system geometry.

6. CONCLUSIONS

As the resident space object population continues to grow, the risk of collision among the objects increases, thus threatening the sustainable use of near-Earth space. The observability methods and measures developed in this work are suitable for the problem of Space Situational Awareness to ensure that measurements are acquired most efficiently and that the knowledge contained within the measurements can be utilized for maximum knowledge about resident space objects. With an improved understanding of the relationship between the measurements and the states in these systems through observability analysis, decisions on how and when to acquire measurements are informed, instead of random decision making or decisions dictated by heuristics or local constraints only. Observability methods have been developed to exactly quantify measurement and sensor trade-offs, and as a result, observability has become a beneficial tool for improving knowledge of object characteristics for precise orbit propagation and for improving the efficiency of measurement acquisition for Space Situational Awareness applications. Observability of the orbit problem and observability of light curve inversion are two primary areas of focus in this work.

Although two-body motion is commonly used as a method for propagating an orbit, perturbations are known to significantly change an orbit over time. Non-conservative perturbing forces are often directly dependent on object characteristics, such as area-to-mass ratio, material reflectivity properties, and shape. Therefore, accurate knowledge of object characteristics is vital for precise orbit propagation. In this work, observability of a system with a state extended beyond position and velocity with area-to-mass ratio, AMR, and the reflectivity coefficient, C, has been analyzed to improve the knowledge of how object characteristics can be determined with optical angle measurements. The state extension significantly increases the time to become observable compared the time to become observable for a state with po-

sition and velocity only. When AMR and C are both defined as constants, a state vector extended with these variables as separate parameters is not observable using optical angle measurements alone. This observability result agrees with current understanding of the ability to determine these two parameters separately when optical angle measurements are used in the orbit problem. However, through observability analysis, this work has found conditions where AMR and C can be determined as two independent and separate parameters. If AMR and C are time-varying parameters, a state extended beyond position and velocity with these parameters has been shown to be observable with optical angle measurements. Therefore, observability can be implemented to determine the conditions under which knowledge of object characteristics is contained within measurements.

As computational capabilities have grown, the Kalman Filter and other estimators have become more widely used in many engineering applications, including Space Situational Awareness. Observability was initially developed by Kalman to determine when a solution is guaranteed for the optimal regulator problem. However, observability is not always considered when estimation is performed, and unless the estimator fails to converge, an estimation solution is produced. This solution may appear to be reasonable, but it may not be an accurate representation of the truth. In this work, the connection between observability and estimation of the orbit problem has been explored through a Monte Carlo approach to demonstrate how estimation accuracy is not always guaranteed for a system which is not observable. For a state consisting of position and velocity only, the observability matrix with measurement uncertainties, otherwise known as the stochastic observability matrix, indicated an observable system. Also, the distribution of the state estimation errors from the Monte Carlo analysis followed the statistically significant standard deviation percentages defined by the 68-95-99.7 rule. However, the stochastic observability matrix did not indicate an observable system for an extended state with constant AMR and C, and the distribution of the estimation errors did not adhere to the 68-95-99.7 rule. Some of the estimation errors remained within the estimation error standard deviation bounds,

but the distribution of the errors did not maintain statistical significance. Therefore, this work has shown that when the orbit problem with an extended state is not observable, estimation accuracy is not guaranteed. In the absence of the ground truth, those inaccurate estimation results may appear reasonable, which could lead to detrimental results and potentially false decision-making.

Measurements should be acquired efficiently for Space Situational Awareness applications because the resident space object population is large compared to the limited number of sensors dedicated for Space Situational Awareness. In addition, planned, large constellations of satellites will drastically increase the number of non-debris objects in the resident space object population. For determining an orbit, six measurement quantities are required, relating to the three position and three velocity state components. However, classical orbit determination methods do not strictly define how measurements should be spaced relative to one another. This work has evaluated whether observability could indicate relative accuracy of orbit determination for different measurement spacing cases. Observability analysis and Monte Carlo analysis with nonlinear batch least squares estimation have both been performed for multiple measurement spacing cases, where the time between three equally spaced measurement is different for each case. The trends in the observability results reflect the trends in the mean square error for the Monte Carlo results with the same measurement spacing cases. Therefore, the relative heights in the observability matrix singular values for different measurement spacing cases are indicative of potential orbit determination accuracy. Moreover, these observability analysis results could be used to inform a sensor tasking optimizer of the importance of observing objects at specific times based on their likelihood of resulting in accurately determined orbits. An explicit connection to such a sensor tasking optimizer has been outlined in this work.

As more sensor networks are developed for Space Situational Awareness, purchasing an abundance of data will become easier through systems like the Unified Data Library. The different sensors in such a data library have vastly different capabilities,

advantages, and disadvantages, which are not straight forward to evaluate against each other. Simple heuristics are bound to fail. This work has implemented observability analysis for determining how two sensors at different locations affected the observability of position and velocity compared to observability with a single sensor. Even in the presence of large measurement noise, the position and velocity of an object becomes observable faster with two sensors at different locations compared to one sensor due to the geometrical differences provided by measurements from the two sensors. When the measurement noise for two sensors is the same as a single sensor, the singular values of the observability matrix eventually converge to the same value for the system analyzed in this work. This indicates that a single sensor would be able to provide the same knowledge of the position and velocity as two sensors, but a single sensor would require more time. The observability analysis is readily scalable to a large number of sensors, allowing quantification of the full trade-space. Therefore, observability analysis can aid in a cost-benefit analysis for evaluating whether many, less accurate sensors are more beneficial than fewer, more accurate sensors.

Although observations of resident space objects from ground-based observers are often non-resolved because of the large distances between the objects and the observers, the brightness of an object over time, i.e. a light curve, can be utilized for recovering object shape and reflectivity characteristics. The light curve inversion process requires sufficient sampling of the observer-object-Sun geometry and the attitude profile of an object with light curve measurements. If light curve measurements do not sufficiently capture the system geometry, the resulting shape and characteristic estimates are not guaranteed to be accurate. Previous methods for increasing the likelihood of sufficient sampling involve acquisition of unfeasibly large amounts of light curve data, which binds valuable sensor resources to focus on one object for long periods of time. In this work, observability of the light curve inversion process has been analyzed to determine when light curve measurements sufficiently sample the system geometry and to develop efficient measurement strategies. Because the Extended Gaussian Image minimization step of the light curve inversion process is the only one

which utilizes light curve measurements, the Extended Gaussian Image minimization has been the focus of the observability analysis in this work. Simulations of orbits in three orbital regimes, low Earth orbit, medium Earth orbit, and geosynchronous Earth orbit, have been preformed with single-axis rotation and three-axis rotation to determine when these systems have been sufficiently sampled for light curve inversion. Regions where the knowledge of the system geometry does not increase have been identified with observability analysis. Therefore, efficient measurement sequences can be selected based on the observability analysis to avoid measurements which do not improve the knowledge of the system geometry. A more realistic orbit and attitude motion have been implemented to determine whether supplied light curve measurements of an Atlas V upper stage from collaborators at the Astronomical Institute at the University of Bern are sufficient for light curve inversion. Simulations of the observability have been performed with measurement batches modeled after the supplied light curve measurements. In addition, realistic constraints, based on astronomical dark and telescope elevation constrains, have been placed on measurement batches acquisition times. For an attitude profile determined with light curve measurements by a colleague at Purdue, an efficient and realistic measurement sequence consisting of four measurement batches spread over two nights has been found which sufficiently sampled the Extended Gaussian Image for estimation of the albedo-area. However, this system has been determined to be sensitive to the attitude motion of the object. A second, valid attitude profile, determined through a different method, has been analyzed, but a measurement sequence which sufficiently sampled the system has not been found.

This work developed a novel method for visualizing the insufficient sampling of the Extended Gaussian Image to demonstrate which albedo-area vector components have been insufficiently sampled. Overall, the observability of the Extended Gaussian Image minimization provided extensive insight into the acquisition of light curve measurements for light curve inversion. In the use case of the Atlas V upper stage under realistic constraints, a drastic reduction of the required number of measurements

and the measurement time has been obtained. This opens the horizon for efficient and effective object characterization on a routine basis within a sensor network, thus making dedicated, several night-long observations of one object for characterization obsolete. This observability method can be implemented for generation of efficient light curve measurement sequences rather than collection of large sets of data for light curve inversion.

6.1 Recommendations

This section defines recommendations for how the findings in this work should be implemented, and also suggests areas of research to expand upon in the future. If the solar radiation pressure parameters, AMR and C, are constants and are sought to be determined with angles-only measurements, a state consisting of position and velocity should only be extended by a single variable, i.e. AMR, C, or the combined parameter AMR$\cdot C$, to ensure an observable system. Of these three state extensions, observability will be achieved fastest with AMR as an extended state variable. If AMR and C must be determined as separate solve-for parameters, an observable system can only be achieved if one or both of these variables are time-varying in the actual system, e.g. an object is tumbling with a non-stable attitude.

Because real systems are stochastic in nature, observability should also include uncertainties. If a system is unobservable, an accurate estimation result is not guaranteed and should not be utilized because in the absence of the ground truth, the estimation result may still appear reasonable. Moreover, observability can be used to inform a Schmidt-Kalman Filter, but for a state extended beyond position and velocity with AMR and C, improvements to the state estimation errors compared to not using a Schmidt-Kalman Filter approach may be minimal. In the sensor tasking problem defined by Frueh, Fiedler, & Herzog and other weighted sensor tasking schemes, the weighting parameter for each object could be computed from the observability analysis trends for different resident space objects. Moreover, observability analysis

can be part of a cost-benefit analysis for developing a sensor network or selecting measurement data from existing sensor networks.

When object characterization through light curve measurements is sought, heuristic assumptions lead to prohibitively long measurement times. Observability analysis is integral to finding the best times to collect characterization information. This greatly reduces required overall observation times. It should be noted that characterization measurements are sensitive to specific time intervals, as mapped out by the observability and dictated by a specific attitude profile. Sensor tasking for orbital and extended state parameters is more robust, which is inherent to the orbit versus the characterization problem.

Future work could determine when the accuracy of results presented here break down due to linearization errors. Additional perturbing forces could be implemented in these methods to evaluate the sensitivity of the observability results to additional perturbations. The steps required for implementing observability results for each object in a sensor tasking optimizer must be determined. In order to complement the existing observability characterization results, observability of reflectivity parameters could be investigated.

REFERENCES

[1] J. A. Kennewell and B. Vo. An Overview of Space Situational Awareness. In *Proceedings of the 16th International Conference on Information Fusion*, pages 1029–1036. IEEE, 2013.

[2] W. Rathgeber. Europe's Way to Space Situational Awareness (SSA). *ESPI Report*, 10, 2008.

[3] W. Flury and J. M. Contant. The Updated IAA Position Paper on Orbital Debris. In *Space Debris*, volume 473, pages 841–849, 2001.

[4] W. Flury. The Space Debris Environment - Past and Present. In *Symposium-International Astronomical Union*, volume 196, pages 181–184. Cambridge University Press, 2001.

[5] U.S. Strategic Command. U.S. Strategic Command Fact Sheet Combined Space Operations Center/614th Air Operations Center, 2018.

[6] C. Frueh. *Available Space Object Catalogs and Two Line Elements (TLE)*, chapter 3. Space Traffic Management (AAE 590), Purdue University, 2019.

[7] J. N. Pelton. Tracking of Orbital Debris and Avoidance of Satellite Collisions. In *Handbook of Satellite Applications*, pages 1–13. Springer New York, 2016.

[8] D. W. Miller. NASA Technology Roadmaps: Introduction, Crosscutting Technologies, and Index. *NASA Report*, 2015.

[9] K. Fletcher. *Space Operations. Space Debris: The ESA Approach.* An ESA Production, 2017.

[10] E. L. Christiansen. Meteoroid/Debris Shielding. Technical report, NASA, 09 2003.

[11] J. L. Hyde, E. L. Christiansen, D. M. Lear, K. Nagy, and E. L. Berger. Surveys of Returned ISS Hardware for MMMOD Impacts. In *7th European Conference on Space Debris*, 2007.

[12] J. Straub. Cubesats: A Low-Cost, Very High-Return Space Technology. In *Proceedings of the 2012 Reinventing Space Conference*, 2012.

[13] C. Frueh, H. Fielder, and J. Herzog. Heuristic and Optimized Sensor Tasking Observation Strategies with Exemplification for Geosynchronous Objects. *Journal of Guidance, Control, and Dynamics*, 41(5):1036–1048, 2018.

[14] D. A. Vallado. *Fundamentals of Astrodynamics and Applications.* Springer Science & Business Media, 2001.

[15] R. Kalman. On the General Theory of Control Systems. *IRE Transactions on Automatic Control*, 4(3):110–110, 1959.

[16] K. Ogata. *State Space Analysis of Control Systems*. Prentice-Hall, 1967.

[17] B. Friedland. *Control System Design: An Introduction to State-Space Methods*. McGraw-Hill Series in Electrical Engineering. Control Theory. McGraw-Hill, 1986.

[18] Z. Gajic and M. Lelic. *Modern Control Systems Engineering*. Prentice-Hall, Inc., 1997.

[19] J. S. Bay. *Fundamentals of Linear State Space Systems*. McGraw-Hill Science/Engineering/Math, 1 edition edition, 1998.

[20] R. Hermann and A. Krener. Nonlinear Controllability and Observability. *IEEE Transactions on Automatic Control*, 22(5):728–740, 1977.

[21] J. L. Casti. *Nonlinear System Theory*. Mathematics in Science and Engineering; v. 175. Academic Press, 1985.

[22] E. D. Sontag. *Mathematical Control Theory Deterministic Finite Dimensional Systems*. Texts in Applied Mathematics, 6. Springer Science & Business Media, second edition edition, 1998.

[23] R. G. Brown. Not Just Observable, but How Observable? (Observability and Controllability in Providing Heuristic Understanding of Control Problems, Noting Kalman Filter Theory). In *22nd National Electronics Conference, Chicago, IL*, pages 709–714, 1966.

[24] H. L. Ablin. *Criteria for Degree of Observability in a Control System*. PhD Thesis, Iowa State University, 1967.

[25] F. M. Ham. *Determination of the Degree of Observability in Linear Control Systems*. PhD Thesis, Iowa State University, 1980.

[26] D. Georges. The Use of Observability and Controllability Gramians or Functions for Optimal Sensor and Actuator Location in Finite-Dimensional Systems. In *Proceedings of the 34th IEEE Conference on Decision and Control*, volume 4, pages 3319–3324, 1995.

[27] I. Hwang, H. Balakrishnan, and C. Tomlin. Observability Criteria and Estimator Design for Stochastic Linear Hybrid Systems. In *2003 European Control Conference (ECC)*, pages 3317–3322, 2003.

[28] S. Hong, H. H. Chun, S. H. Kwon, and M. H. Lee. Observability Measures and Their Application to GPS/INS. *IEEE Transactions on Vehicular Technology*, 57(1):97–106, 2008.

[29] A. J. Krener and K. Ide. Measures of Unobservability. In *Proceedings of the 48th IEEE Conference on Decision and Control, 2009 Held Jointly with the 2009 28th Chinese Control Conference. CDC/CCC 2009*, pages 6401–6406, 2009.

[30] Y. Subaşi and M. Demirekler. Quantitative Measure of Observability for Stochastic Systems. *IFAC Proceedings Volumes*, 44(1):4244–4249, 2011.

[31] J. Ma, Q. Ge, and T. Shao. Impact Analysis between Observable Degrees and Estimation Accuracy of Kalman Filtering. In *2015 International Conference on Estimation, Detection and Information Fusion (ICEDIF)*, pages 124–128, 2015.

[32] Q. Ge, J. Ma, S. Chen, Y. Wang, and L. Bai. Observable Degree Analysis to Match Estimation Performance for Wireless Tracking Networks. *Asian Journal of Control*, 19(4):1259–1270, 2016.

[33] K. Shen, A. V. Proletarsky, and K. A. Neusypin. Quantitative Analysis of Observability in Linear Time-Varying Systems. In *2016 35th Chinese Control Conference (CCC)*, pages 44–49, 2016.

[34] V. L. Bageshwar, D. Gebre-Egziabher, W. L. Garrard, and T. T. Georgiou. Stochastic Observability Test for Discrete-Time Kalman Filters. *Journal of Guidance, Control, and Dynamics*, 32(4):1356–1370, 2009.

[35] J. A. Wilson and S. Y. Guhe. Observability Matrix Condition Number in Design of Measurement Strategies. In *Computer Aided Chemical Engineering*, volume 20 of *European Symposium on Computer-Aided Process Engineering-15, 38th European Symposium of the Working Party on Computer Aided Process Engineering*, pages 397–402. Elsevier, 2005.

[36] J. Geeraert, J. W. McMahon, and B. A. Jones. Orbit Determination Observability of the Dual-Satellite Geolocation System with TDOA and FDOA. In *AIAA/AAS Astrodynamics Specialist Conference*, page 5367, 2016.

[37] L. Jiazhen, X. Lili, Z. Chunxi, and W. Yan. An Improved Determinant Method of Observability and Its Degree Analysis. In *Proceedings 2013 International Conference on Mechatronic Sciences, Electric Engineering and Computer (MEC)*, pages 147–153, 2013.

[38] J. L. Dong and B. Mo. The Method of System Observability Analysis Using Pseudo-Inverse of System Observability Matrix. In *Proceedings of the 32nd Chinese Control Conference*, pages 55–59, 2013.

[39] M. Aoki. On Observability of Stochastic Discrete-Time Dynamic Systems. *Journal of the Franklin Institute*, 286(1):36–58, 1968.

[40] A. H. Jazwinski. *Stochastic Processes and Filtering Theory*. Academic Press, 1970.

[41] H. Chen. On Stochastic Observability and Controllability. *Automatica*, 16(2):179–190, 1980.

[42] A. D. Dianetti, R. Weisman, and J. L. Crassidis. Observability Analysis for Improved Space Object Characterization. *Journal of Guidance, Control, and Dynamics*, 41(1):137–148, 2018.

[43] F. M. Ham and R. G. Brown. Observability, Eigenvalues, and Kalman Filtering. *IEEE Transactions on Aerospace and Electronic Systems*, AES-19(2):269–273, 1983.

[44] Y. Baram and T. Kailath. Estimability and Regulability of Linear Systems. *IEEE Transactions on Automatic Control*, 33(12):1116–1121, 1988.

[45] D. Goshen-Meskin and I. Y. Bar-Itzhack. On the Connection between Estimability and Observability. *IEEE Transactions on Automatic Control*, 37(8):1225–1226, 1992.

[46] J. H. Moon, S. Hong, H. Chun, and M. H. Lee. Estimability Measures and Their Application to GPS/INS. *Journal of Mechanical Science and Technology*, 22(5):905, 2008.

[47] J. J. Morales. Stochastic Observability and Uncertainty Characterization in Simultaneous Receiver and Transmitter Localization. *IEEE Transactions on Aerospace and Electronic Systems*, page 9, 2017.

[48] F. O. Silva, E. M. Hemerly, and W. C. Leite Filho. On the Error State Selection for Stationary SINS Alignment and Calibration Kalman Filters—Part II: Observability/Estimability Analysis. *Sensors (Basel, Switzerland)*, 17(3), 2017.

[49] B. D. Tapley, B. E. Schutz, and G. H. Born. *Statistical Orbit Determination*. Academic Press, 2004.

[50] O. Montenbruck and E. Gill. *Satellite Orbits: Models, Methods, and Applications*. Springer Science & Business Media, 2000.

[51] P. J. Huxel. *Navigation Algorithms and Observability Analysis for Formation Flying Missions*. PhD Thesis, The University of Texas at Austin, 2006.

[52] V. L. Bageshwar, D. Gebre-Egziabher, W. L. Garrard, and T. T. Georgiou. Stochastic Observability Test for Discrete-Time Kalman Filters. *Journal of Guidance, Control, and Dynamics*, 32(4):1356–1370, 2009.

[53] A. D. Dianetti, R. M. Weisman, and J. L. Crassidis. Application of Observability Analysis to Space Object Tracking. In *AIAA Guidance, Navigation, and Control Conference, AIAA SciTech Forum*. American Institute of Aeronautics and Astronautics, 2017.

[54] Y. Shao. *Observability and Performance Analysis of Integrated GPS/INS Navigation Systems*. PhD Thesis, University of Minnesota, 2006.

[55] Y. Wu, H. Zhang, M. Wu, X. Hu, and D. Hu. Observability of Strapdown INS Alignment: A Global Perspective. *IEEE Transactions on Aerospace and Electronic Systems*, 48(1):78–102, 2012.

[56] F. M. Mirzaei and S. I. Roumeliotis. A Kalman Filter-Based Algorithm for IMU-Camera Calibration: Observability Analysis and Performance Evaluation. *IEEE Transactions on Robotics*, 24(5):1143–1156, 2008.

[57] Y. Rothman, I. Klein, and S. Filin. Analytical Observability Analysis of INS with Vehicle Constraints. *Navigation*, 61(3):227–236, 2014.

[58] M. H. Lee, J. H. Lee, Y. H. Koh, H. G. Park, J. H. Moon, and S. P. Hong. Observability and Estimability Analysis of the GPS and INS in the Vehicle. *Journal of Mechanical Systems for Transportation and Logistics*, 3:537–551, 2010.

[59] M. H. Lee, W. C. Park, K. S. Lee, S. Hong, H. G. Park, H. H Chun, and F. Harashima. Observability Analysis Techniques on Inertial Navigation Systems. *Journal of System Design and Dynamics*, 6:28–44, 2012.

[60] Y. M. Yoo, J. G. Park, D. H. Lee, and C. G. Park. A Theoretical Approach to Observability Analysis of the SDINS/GPS in Maneuvering with Horizontal Constant Velocity. *International Journal of Control, Automation and Systems*, 10(2):298–307, 2012.

[61] D. C. Woffinden and D. K. Geller. Observability Criteria for Angles-Only Navigation. *IEEE Transactions on Aerospace and Electronic Systems*, 45(3):1194–1208, 2009.

[62] A. Carmi and Y. Oshman. Nonlinear Observability Analysis of Spacecraft Attitude and Angular Rate with Inertia Uncertainty. *The Journal of the Astronautical Sciences*, 57:129–148, 2013.

[63] J. Grzymisch and W. Fichter. Analytic Optimal Observability Maneuvers for In-Orbit Bearings-Only Rendezvous. *Journal of Guidance, Control, and Dynamics*, 37(5):1658–1664, 2014.

[64] D. Sun and J. L. Crassidis. Analysis of Six-Degree-of-Freedom Configuration Determination Using Vector Observations. *Journal of Guidance, Control, and Dynamics*, 25(6):1149–1157, 2002.

[65] R. Zanetti and C. N. D'Souza. Observability Analysis and Filter Design for the Orion Earth–Moon Attitude Filter. *Journal of Guidance, Control, and Dynamics*, 39(2):201–213, 2016.

[66] J. C. Hinks, R. Linares, and J. L. Crassidis. Attitude Observability from Light Curve Measurements. In *AIAA Guidance, Navigation, and Control (GNC) Conference*, page 5005, 2013.

[67] S. C. Nardone and V. J. Aidala. Observability Criteria for Bearings-Only Target Motion Analysis. *IEEE Transactions on Aerospace and Electronic Systems*, AES-17(2):162–166, 1981.

[68] S. E. Hammel and V. J. Aidala. Observability Requirements for Three-Dimensional Tracking via Angle Measurements. *IEEE Transactions on Aerospace and Electronic Systems*, AES-21(2):200–207, 1985.

[69] E. Fogel and M. Gavish. Nth-Order Dynamics Target Observability from Angle Measurements. *IEEE Transactions on Aerospace and Electronic Systems*, 24(3):305–308, 1988.

[70] Z. Yu, P. Cui, and S. Zhu. Observability-Based Beacon Configuration Optimization for Mars Entry Navigation. *Journal of Guidance, Control, and Dynamics*, 38(4):643–650, 2015.

[71] J. L. Crassidis, R. Alonso, and J. L. Junkins. Optimal Attitude and Position Determination From Line-of-Sight Measurements. *Journal of Astronautical Sciences*, 48(2):391–408, 2000.

[72] R. Linares and J. L. Crassidis. Dynamic Observability Analysis for Attitude, Angular Velocity, Shape, and Surface Parameters. In *26th AAS/AIAA Space Flight Mechanics Meeting*, 2016.

[73] A. M. Friedman and C. Frueh. Observability Analysis Applied to Artificial Near-Earth Objects with Noise. In *27th AAS/AIAA Space Flight Mechanics Meeting*, 2017.

[74] A. M. Friedman and C. Frueh. Determining Debris Characteristics from Observability Analysis of Artificial Near-Earth Objects. In *7th European Conference on Space Debris*, 2017.

[75] A. M. Friedman and C. Frueh. Determining Characteristics of Artificial Near-Earth Objects Using Observability Analysis. *Acta Astronautica*, 144:405–421, 2018.

[76] A. M. Friedman and C. Frueh. Observability and Estimability Analysis of the Orbit Problem. *Journal of Astronautical Sciences, submitted*, 2019.

[77] A. M. Friedman, S. Fan, and C. Frueh. Light Curve Inversion Observability Analysis. In *2019 AAS/AIAA Astrodynamics Specialist Conference*, 2019.

[78] A. M. Friedman and C. Frueh. Observability and Estimability Analysis of the Orbit Problem. In *2019 AAS/AIAA Astrodynamics Specialist Conference*, 2019.

[79] S. Fan, A. M. Friedman, and C. Frueh. Satellite Shape Recovery from Light Curves with Noise. In *Advanced Maui Optical and Space Surveillance Technologies Conference (AMOS)*, 2019.

[80] A. M. Friedman, S. Fan, C. Frueh, and T. Schildknecht. Observability of Light Curve Shape Inversion Based on Optical Data. In *First International Orbital Debris Conference*, 2019.

[81] R. L. Williams and D. A. Lawrence. *Linear State-Space Control Systems*. Wiley, 1 edition edition, 2007.

[82] R. H. Battin. *An Introduction to the Mathematics and Methods of Astrodynamics, Revised Edition*. American Institute of Aeronautics and Astronautics, 1999.

[83] R. A. DeCarlo. *Linear Systems: A State Variable Approach with Numerical Implementation*. Prentice-Hall, Inc., 1989.

[84] D. S. Bernstein. *Matrix Mathematics: Theory, Facts, and Formulas*. Princeton university press, 2009.

[85] R. Longman and S. Sirlin. The Fundamental Structure of Degree of Controllability and Degree of Observability. In *Astrodynamics Conference*, page 1434, 1982.

[86] Z. Chen. Local Observability and Its Application to Multiple Measurement Estimation. *IEEE Transactions on Industrial Electronics*, 38(6):491–496, 1991.

[87] J. L. Dong and B. Mo. The Method of System Observability Analysis Using Pseudo-Inverse of System Observability Matrix. In *Proceedings of the 32nd Chinese Control Conference*, pages 55–59, 2013.

[88] J. H. Wilkinson. *The Algebraic Eigenvalue Problem*. Oxford University Press, Inc., 1988.

[89] W. H. Press, S. A. Teukolsky, W. T. Vetterling, and B. P. Flannery. *Numerical Recipes 3rd Edition: The Art of Scientific Computing*. Cambridge University Press, 3 edition, 2007.

[90] N. J. Higham. *Accuracy and Stability of Numerical Algorithms*, volume 80. Siam, 2002.

[91] E. Kreyszig. *Advanced Engineering Mathematics, 7th Edition*. Wiley, 1993.

[92] J. Ashbrook. Tycho Brahes Nose. *Sky and Telescope*, 6:353–358, 1965.

[93] V. E. Thoren and J. R. Christianson. *The Lord of Uraniborg: A Biography of Tycho Brahe*. Cambridge University Press, 1990.

[94] G. Beutler. *Methods of Celestial Mechanics. Vol. II: Application to Planetary System Geodynamics and Satellite Geodesy*, volume 2. Springer-Verlag, 2005.

[95] C. Frueh. *Orbit Propagation and Perturbations in the Near Earth Space*, chapter 8. Space Traffic Management (AAE 590), Purdue University, 2019.

[96] F. R. Hoots, P. W. Schumacher Jr, and R. A. Glover. History of Analytical Orbit Modeling in the US Space Surveillance System. *Journal of Guidance, Control, and Dynamics*, 27(2):174–185, 2004.

[97] National Academies of Sciences, Engineering, and Medicine. *Finding Hazardous Asteroids Using Infrared and Visible Wavelength Telescopes*. The National Academies Press, Washington, DC, 2019.

[98] F. Sanson and C. Frueh. Noise Quantification in Optical Observations of Resident Space Objects for Probability of Detection and Likelihood. In *AIAA/AAS Astrodynamics Specialist Conference*. AAAI Press, 2016.

[99] C. Frueh. *Observations*, chapter 4. Space Traffic Management (AAE 590), Purdue University, 2019.

[100] F. Sanson and C. Frueh. Quantifying Uncertainties in Signal Position in Non-Resolved Object Images: Application to Space Object Observation. *Advances in Space Research*, 2019.

[101] D. Lang, D. W. Hogg, K. Mierle, M. Blanton, and S. Roweis. Astrometry.net: Blind Astrometric Calibration of Arbitrary Astronomical Images. *The Astronomical Journal*, 137:1782–2800, 2010.

[102] D. A. Vallado and S. Alfano. Updated Analytical Partials for Covariance Transformations and Optimization. In *AIAA/AAS Astrodynamics Specialists Conference*, pages 15–537, 2015.

[103] F. E. Nicodemus. Self-Study Manual on Optical Radiation Measurements: Part 1Concepts, chapters 1 to 3, 1977.

[104] F. E. Nicodemus, J. C. Richmond, J. J. Hsia, I. W. Ginsberg, and T. Limperis. Geometrical Considerations and Nomenclature for Reflectance. *NBS monograph*, 160:4, 1992.

[105] B. D. Little and C. Frueh. Space Situational Awareness Sensor Tasking: Comparison of Machine Learning with Classical Optimization Methods. *Journal of Guidance, Control, and Dynamics*, 43(2):262–273, 2020.

[106] B. D. Little. *Optical Sensor Tasking Optimization for Space Situational Awareness*. PhD Thesis, Purdue University Graduate School, 2019.

[107] A. D. Dianetti and J. L. Crassidis. Space Object Material Determination from Polarized Light Curves. In *AIAA Scitech 2019 Forum*, page 0377, 2019.

[108] C. Früh and T. Schildknecht. Variation of the Area-to-Mass Ratio of High Area-to-Mass Ratio Space Debris Objects. *Monthly Notices of the Royal Astronomical Society*, 419(4):3521–3528, 2012.

[109] H. Rodriguez, K. Abercromby, M. Mulrooney, and E. Barker. Optical Properties of Multi-Layered Insulation. In *Advanced Maui Optical and Space Surveillance Technologies Conference*, 2007.

[110] C. Frueh. *Orbit Improvement/Filtering: Minimum Mean Square Error Estimation*, chapter 9. Space Traffic Management (AAE 590), Purdue University, 2019.

[111] S. F. Schmidt. Application of State-space Methods to Navigation Problems. In *Advances in control systems*, volume 3, pages 293–340. Elsevier, 1966.

[112] D. Woodbury and J. Junkins. On the Consider Kalman Filter. In *AIAA Guidance, Navigation, and Control Conference*, 2010.

[113] R. Zanetti and C. D'Souza. Recursive Implementations of the Schmidt-Kalman Consider Filter. *The Journal of the Astronautical Sciences*, 60(3-4):672–685, 2013.

[114] R. A. Horn and C. R. Johnson. *Matrix Analysis*. Cambridge university press, 2012.

[115] H. N. Russell. On the Light Variations of Asteroids and Satellites. *The Astrophysical Journal*, 24:1–18, July 1906.

[116] H. N. Russell. On the Albedo of the Planets and Their Satellites. *The Astrophysical Journal*, 43:173–196, April 1916.

[117] I. Groeneveld and G. P. Kuiper. Photometric Studies of Asteroids. I. *The Astrophysical Journal*, 120:200, September 1954.

[118] T. Gehrels. Photometric Studies of Asteroids.VI. Photographic Magnitudes. *The Astrophysical Journal*, 125:550, March 1957.

[119] S. B. Weideenschilling, C. R. Chapman, D. R. Davis, R. Greenberg, D. G. Levy, and S. Vail. Photometric Geodesy of Main-belt Asteroids: I. Lightcurves of 26 Large, Rapid Rotators. *Icarus*, 70(2):191–245, 1987.

[120] J. D. Drummond, S. J. Weidenschilling, C. R. Chapman, and D. R. Davis. Photometric Geodesy of Main-belt Asteroids II. Analysis of Lightcurves for Poles, Periods, and Shapes. *Icarus*, 76(1):19–77, October 1988.

[121] M. Kaasalainen and J. Torppa. Optimization Methods for Asteroid Lightcurve Inversion. I. Shape Determination. *Icarus*, 153:24–36, September 2001.

[122] M. Kaasalainen, J. Torppa, and K. Muinonen. Optimization Methods for Asteroid Lightcurve Inversion. II. The Complete Inverse Problem. *Icarus*, 153:37–51, September 2001.

[123] M. Kaasalainen, J. Torppa, and J. Piironen. Models of Twenty Asteroids from Photometric Data. *Icarus*, 159:369–395, October 2002.

[124] D. Lynch, R. Russell, R. Rudy, D. Gutierrez, M. Turpin, K. Crawford, Y. Dotan, D. Kim, and M. Skinner. 3 - 13 μm Spectra of Geosynchronous Satellites. In *Advanced Maui Optical and Space Surveillance Technologies Conference*, 2006.

[125] P. Seitzer, K. Abercromby, E. Barker, and H. Rodriguez. Optical Studies of Space Debris at GEO - Survey and Follow-up with Two Telescopes. In *Advanced Maui Optical and Space Surveillance Technologies Conference*, 2007.

[126] T. Schildknecht, R. Musci, C. Fruh, and M. Ploner. Color Photometry and Light Curve Observations of Space Debris in GEO. In *Advanced Maui Optical and Space Surveillance Technologies Conference*, 2008.

[127] T. Schildknecht, A. Vannanti, H. Krag, and C. Erd. Reflectance Spectra of Space Debris in GEO. In *Advanced Maui Optical and Space Surveillance Technologies Conference*, 2009.

[128] T. Schildknecht, N. Koshkin, E. Korobeinikova, S. Melikiants, L. Shakun, S. Strakhova, E. Linder, J. Silha, and M. Hager. Photometric Monitoring of Non-resolved Space Debris and Databases of Optical Light Curves. In *Advanced Maui Optical and Space Surveillance Technologies Conference*, 2015.

[129] R. Scott and B. Wallace. Satellite Characterization Using Small Aperture Instruments at DRDC Ottawa. In *Advanced Maui Optical and Space Surveillance Technologies Conference*, 2008.

[130] J. T. Armstrong, R. B. Hindsley, S. R. Restaino, J. A. Benson, D. J. Hutter, F. J. Vrba, R. T. Zavala, S. A. Gregory, and H. R. Schmitt. Observations of a Geosynchronous Satellite with Optical Interferometry. In *Adaptive Coded Aperture Imaging, Non-Imaging, and Unconventional Imaging Sensor Systems*, volume 7468, August 2009.

[131] H. Cowardin, K. Abercromby, E. Barker, P. Seitzer, M. Mulrooney, and T. Schildknecht. An Assessment of GEO Orbital Debris Photometric Properties Derived from Laboratory-Based Measurements. In *Advanced Maui Optical and Space Surveillance Technologies Conference*, 2009.

[132] H. Cowardin, S. Lederer, J.-C. Liou, G. Ojakangas, and M. Mulrooney. Optical Signature Analysis of Tumbling Rocket Bodies via Laboratory Measurements. In *Advanced Maui Optical and Space Surveillance Technologies Conference*, September 2012.

[133] M. Hejduk. Specular and Diffuse Components in Spherical Satellite Photometric Modeling. In *Advanced Maui Optical and Space Surveillance Technologies Conference*, September 2011.

[134] D. Hall, K. Hamada, T. Kelecy, and P. Kervin. Satellite Surface Characterization from Non-resolved Multi-band Optical Observations. In *Advanced Maui Optical and Space Surveillance Technologies Conference*, September 2012.

[135] R. Linares, M. K. Jah, and J. L. Crassidis. Inactive Space Object Shape Estimation via Astrometric and Photometric Data Fusion. *Advances in Astronautical Science*, 143:217–232, 2012.

[136] R. Linares, M. K. Jah, J. L. Crassidis, F. A. Leve, and T. Kelecy. Astrometric and Photometric Data Fusion for Inactive Space Object Mass and Area Estimation. *Acta Astronautica*, 99:1–15, 2014.

[137] R. Furfaro, R. Linares, D. Gaylor, M. Jah, and R. Walls. Resident Space Object Characterization and Behavior Understanding via Machine Learning and Ontology-based Bayesian Networks. In *Advanced Maui Optical and Space Surveillance Technologies Conference*, September 2016.

[138] M. Kaasalainen, L. Lamberg, K. Lumme, and E. Bowell. Interpretation of Lightcurves of Atmosphereless Bodies. I - General Theory and New Inversion Schemes. *Astronomy and Astrophysics*, 259:318–332, 06 1992.

[139] J. J. Little. An Iterative Method for Reconstructing Convex Polyhedra from Extended Gaussian Images. In *Proceedings of the Third AAAI Conference on Artificial Intelligence*, AAAI'83, pages 247–250. AAAI Press, 1983.

[140] J. J. Little. *Recovering Shape and Determining Attitude from Extended Gaussian Images*. PhD Thesis, University of British Columbia, 1985.

[141] J. J. Little. Extended gaussian images, mixed volumes, shape reconstruction. In *Proceedings of the First Annual Symposium on Computational Geometry*, SCG '85, pages 15–23, New York, NY, USA, 1985. ACM.

[142] S. Fan and C. Frueh. Direct Light Curve Inversion Scheme and the Influence of Measurement Noise. *Journal of Astronautical Sciences*, 2018.

[143] H. Minkowski. *Volumen und Oberfläche*, pages 146–192. Springer Vienna, 1989.

[144] H. Minkowski. *Allgemeine Lehrsätze über die konvexen Polyeder*, pages 121–139. Springer Vienna, Vienna, 1989.

[145] D. Hilbert and S. Cohn-Vossen. *Geometry and the Imagination*. Chelsea Publishing Co., 1952.

[146] D. A. Smith. Using Enhanced Spherical Images for Object Representation. Technical report, Massachusetts Institute of Technology, Artificial Intelligence Lab, 1979.

[147] B. Horn. *Sequins and Quills, Representations for Surface Topography*. AI memo 536. Massachusetts Institute of Technology, Artificial Intelligence Laboratory, 1979.

[148] B. K. P. Horn. Extended Gaussian Images. *Proceedings of the IEEE*, 72(12):1671–1686, 1984.

[149] R. A. White and S. W. Stemwedel. The Quadrilateralized Spherical Cube and Quad-tree for All Sky Data. In *Astronomical data analysis software and systems I*, volume 25, page 379, 1992.

[150] C. Frueh. Observability of Space Debris Objects. In *Astrodynamics Specialist Conference*. AIAA, 2015.

[151] A. Gelb. *Applied Optimal Estimation*. MIT Press, 1974.

[152] A. Kessy, A. Lewin, and K. Strimmer. Optimal Whitening and Decorrelation. *The American Statistician*, 2017.

[153] T. Schildknecht, A. Vananti, A. Hinze, J. Herzog, and M. Ploner. Long-term Evolution of High Area-to-Mass Ratio Objects in Different Orbital Regions. In *Proceedings of AMOS Conference, Maui, Hawaii*, 2012.

[154] X. R. Li and Z. Zhao. Evaluation of Estimation Algorithms Part I: Incomprehensive Measures of Performance. *IEEE Transactions on Aerospace and Electronic Systems*, 42(4):1340–1358, October 2006.

[155] P. Bajorski. *Fundamentals of Multivariate Statistics*, chapter 5, pages 137–171. John Wiley and Sons, Ltd, 2011.

[156] K. J. DeMars and K. C. Ward. Impact of Considering and Neglecting States on Descent-to-Landing Navigation. In *AIAA Scitech 2020 Forum*, 2020.

[157] K. J. DeMars. Private Communication, 2020.

[158] C. Frueh. *Initial Orbit Determination*, chapter 6. Space Traffic Management (AAE 590), Purdue University, 2019.

[159] U.S. Air Force Research Laboratory, U.S. Air Force Space Command, Space and U.S. Missile Systems Center, and Bluestaq. Unified Data Library, 2020.

[160] B. List. Decomposition of a Covariance Matrix Into Uncorrelated and Correlated Errors. In *Alliance Workshop on Unfolding and Data Correction*, 2010.

[161] T. Kelecy and M. Jah. Analysis of High Area-to-Mass Ratio (HAMR) GEO Space Object Orbit Determination and Prediction Performance: Initial Strategies to Recover and Predict HAMR GEO Trajectories with No A Priori Information. *Acta Astronautica*, 69(7-8):551–558, 2011.

[162] R. Linares, J. L. Crassidis, C. J. Wetterer, K. A. Hill, and M. K. Jah. Astrometric and Photometric Data Fusion for Mass and Surface Material Estimation Using Refined Bidirectional Reflectance Distribution Functions - Solar Radiation Pressure Model. Technical report, Pacific Defense Solutions LLC, Kihei, HI, 2013.

[163] C. J. Wetterer and M. Jah. Attitude Estimation from Light Curves. *Journal of Guidance, Control, and Dynamics*, 32(5):1648–1651, 2009.

[164] F. Santoni, E. Cordelli, and F. Piergentili. Determination of Disposed-Upper-Stage Attitude Motion by Ground-Based Optical Observations. *Journal of Spacecraft and Rockets*, 50(3):701–708, 2013.

[165] P. Koller. Attitude Determination of Cylindrical Rocket Bodies from Optical Light Curves. Bachelor Thesis, Astronomy Institute of the University of Bern, Under the supervision of E. Cordelli and T. Schildknecht, 2016.

[166] F. Piergentili, F. Santoni, and P. Seitzer. Attitude Determination of Orbiting Objects from Lightcurve Measurements. *IEEE Transactions on Aerospace and Electronic Systems*, 53(1):81–90, Feb 2017.

[167] V. Williams. Location of the Rotation Axis of a Tumbling Cylindrical Earth Satellite by Using Visual Observations: Part I: Theory. *Planetary and Space Science*, 27(6):885–890, 1979.

[168] C. A. Markland. Attitude and Orbit Control for Satellite Broadcasting Missions. *Proceedings of the Indian Academy of Sciences Section C: Engineering Sciences*, 3(1):47–65, 1980.

[169] J. M. A. Danby. The Matrizant of Keplerian Motion. *AIAA Journal*, 2(1):16–19, 1964.

[170] D. L. Hitzl. Keplerian Transition Matrices for Elliptical Orbits. *Astronomy and Astrophysics*, 63:429–432, 1978.

[171] G. Der. An Elegant State Transition Matrix. In *Astrodynamics Conference*, page 3660, 1997.

[172] E. C. Bower. Some Formulas and Tables Relating to Orbit Computation and Numeric Integration. *Lick Observatory Bulletin*, 16:34–45, 1932.

APPENDIX A. OBSERVABILITY OF THE ORBIT PROBLEM ADDITIONAL RESULTS

A.1 Impact of Measurement Noise on Orbit Observability

Figures A.1 and A.2 show the impact of measurement noise variance on time to become observable for the ten LEO and GEO objects given in Tables 3.1 and 3.2. The measurement noise variances are specified in Section 3.4 except for these results the declination measurement noise variance is kept fixed and the right ascension measurement noise variance is varied.

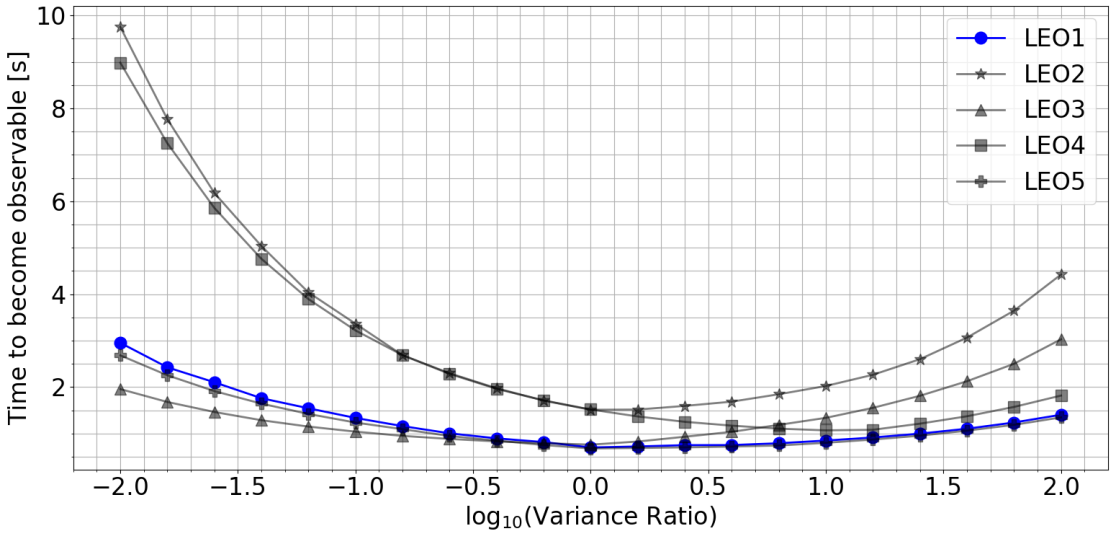

Figure A.1. LEO observability analysis with a range of right ascension measurement noise variance ratios.

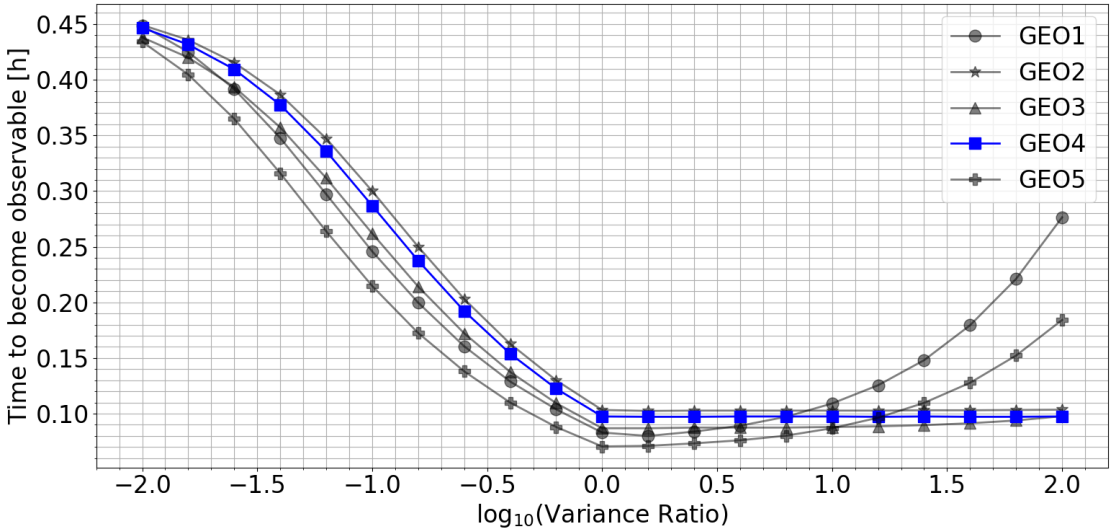

Figure A.2. GEO observability analysis with a range of right ascension measurement noise variance ratios.

A.2 Impact of Propagation Method on Orbit Observability

A.2.1 Numerical Integration versus STM Propagation

The following results compare the singular values of the observability matrix for a state consisting of position and velocity, propagated with two different methods. The linearized measurement matrix is defined with the state at t_k as discussed in Section 3.5. One method propagates the state from t_0 to t_k with the state transition matrix (STM) and the second method propagates the state with numerical integration of the two-body dynamics. The following orbits are defined in Tables 3.1 and 3.2.

Figures A.3 and A.4 show the singular values of the observability matrix with two different propagation methods with short and long propagation times. Figures A.5 and A.6 show similar results for the LEO 2 object. Figures A.7 and A.8 show similar results for the LEO 3 object. Figures A.9 and A.10 show similar results for the LEO 4 object. Figures A.11 and A.12 show similar results for the LEO 5 object.

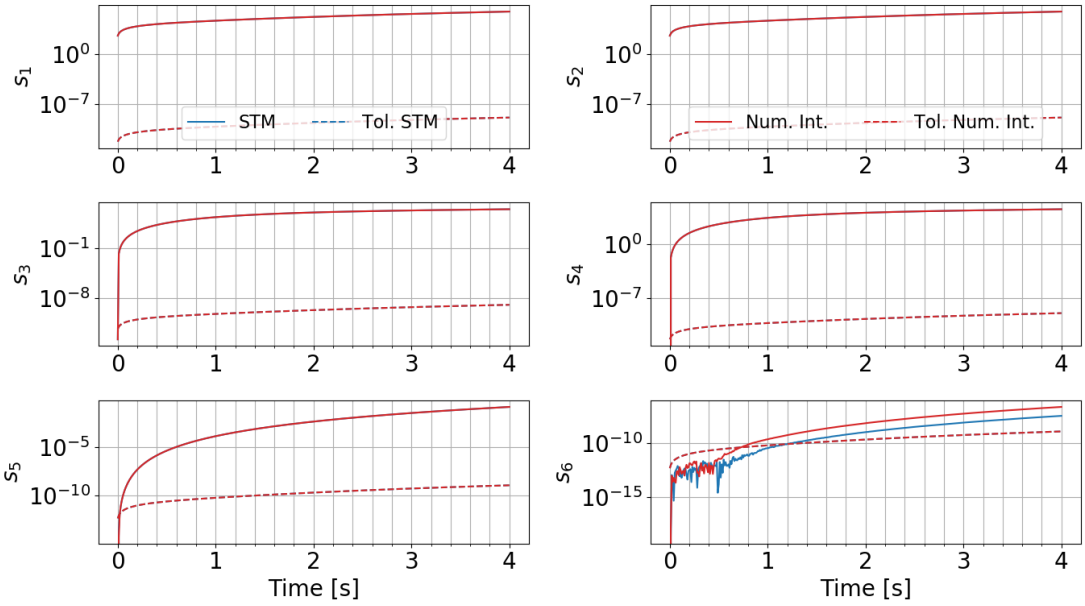

Figure A.3. Singular values of the observability matrix using the STM propagated state versus the numerically integrated state for the LEO 1 object.

Figures A.13 and A.14 show similar results for the GEO 1 object. Figures A.15 and A.16 show similar results for the GEO 2 object. Figures A.17 and A.18 show similar results for the GEO 3 object. Figures A.19 and A.20 show similar results for the GEO 5 object.

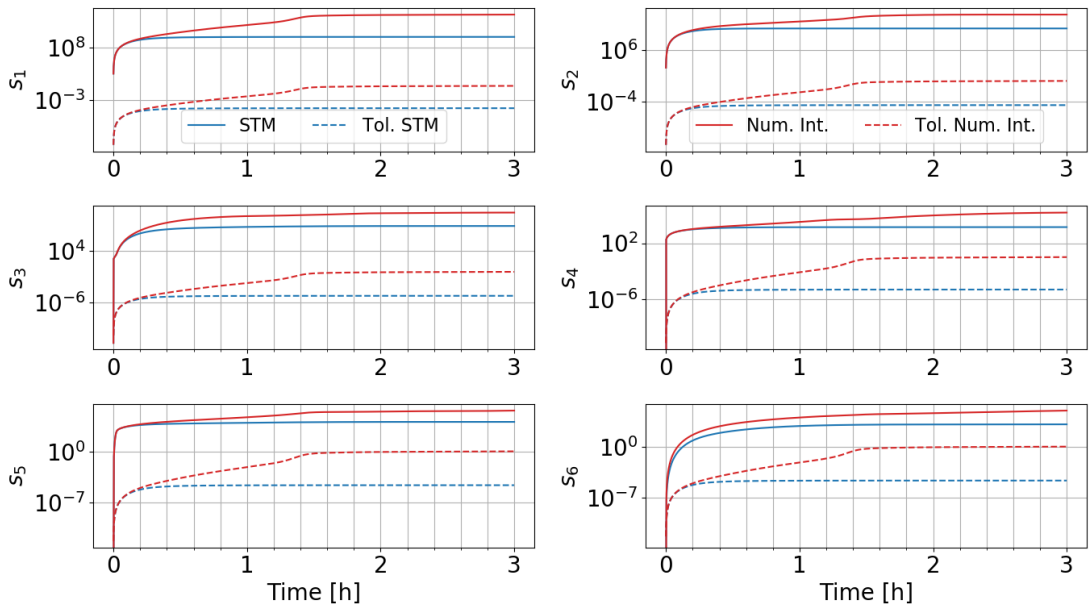

Figure A.4. Singular values of the observability matrix using the STM propagated state versus the numerically integrated state with a longer analysis time for the LEO 1 object.

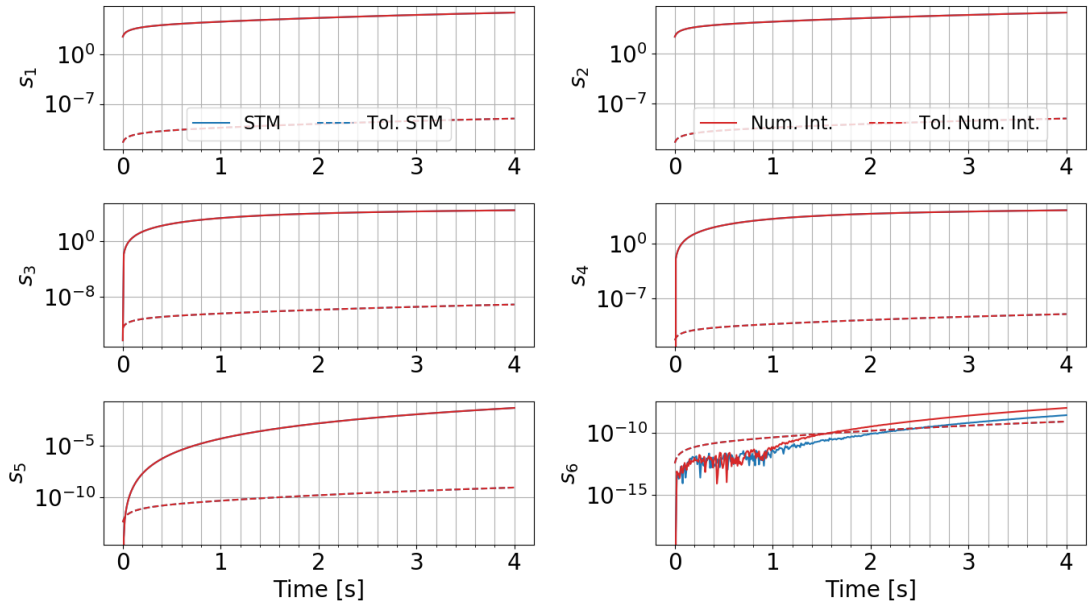

Figure A.5. Singular values of the observability matrix using the STM propagated state versus the numerically integrated state for the LEO 2 object.

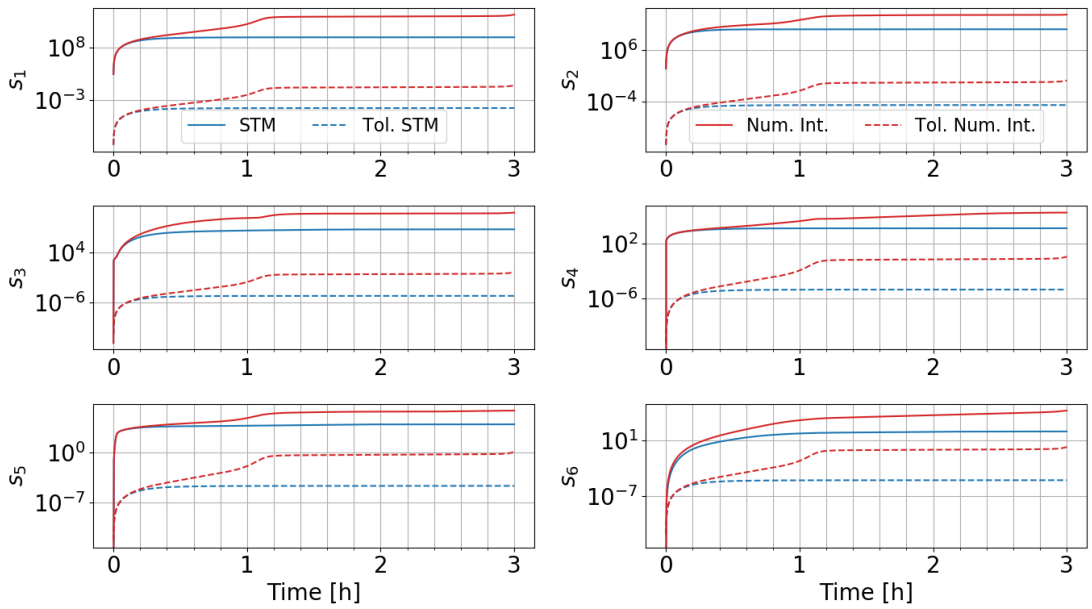

Figure A.6. Singular values of the observability matrix using the STM propagated state versus the numerically integrated state with a longer analysis time for the LEO 2 object.

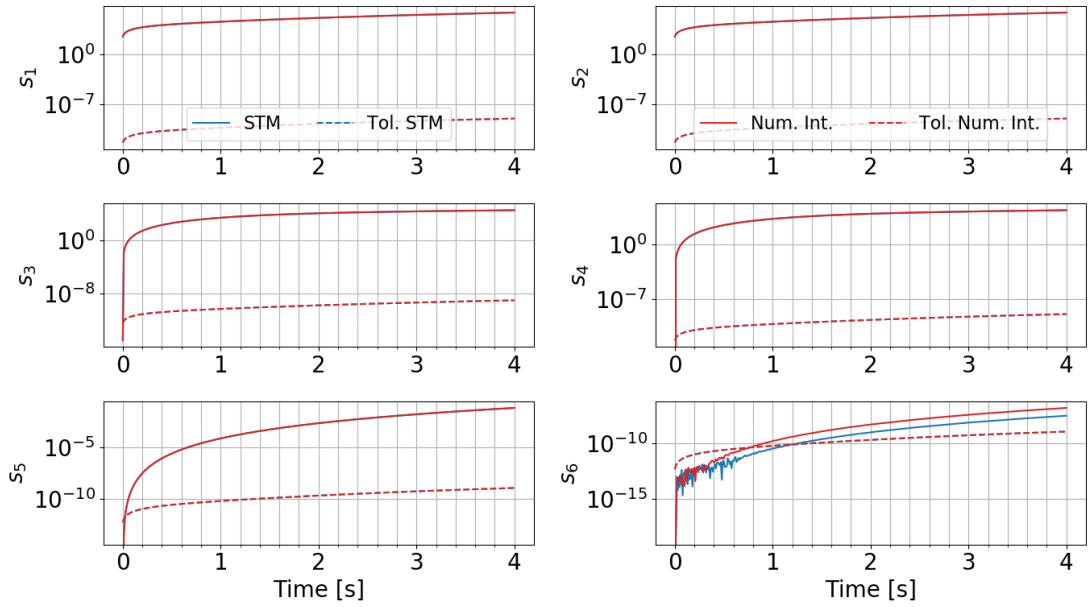

Figure A.7. Singular values of the observability matrix using the STM propagated state versus the numerically integrated state for the LEO 3 object.

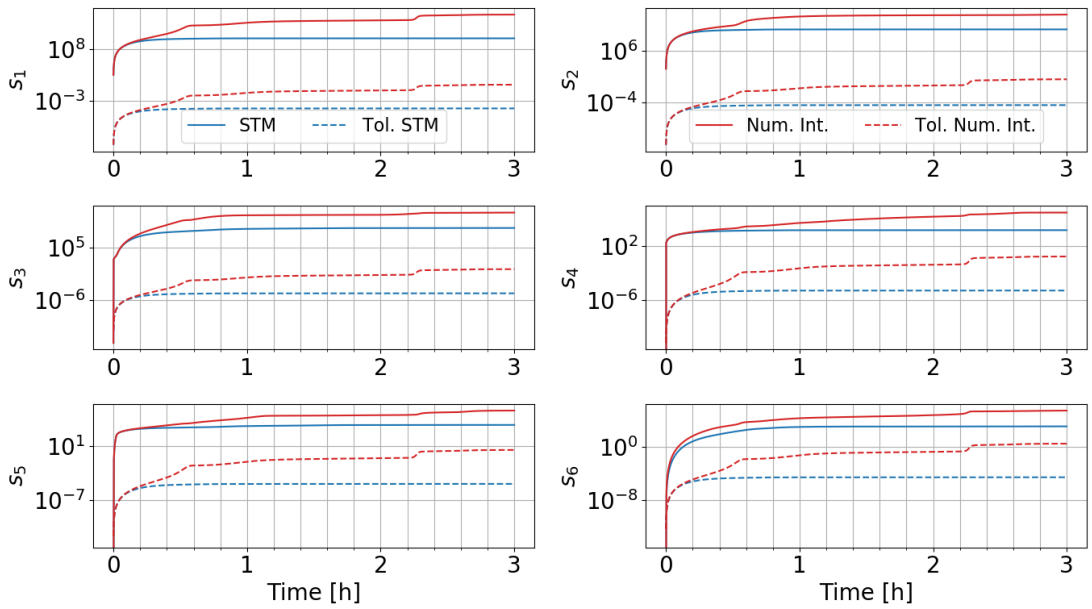

Figure A.8. Singular values of the observability matrix using the STM propagated state versus the numerically integrated state with a longer analysis time for the LEO 3 object.

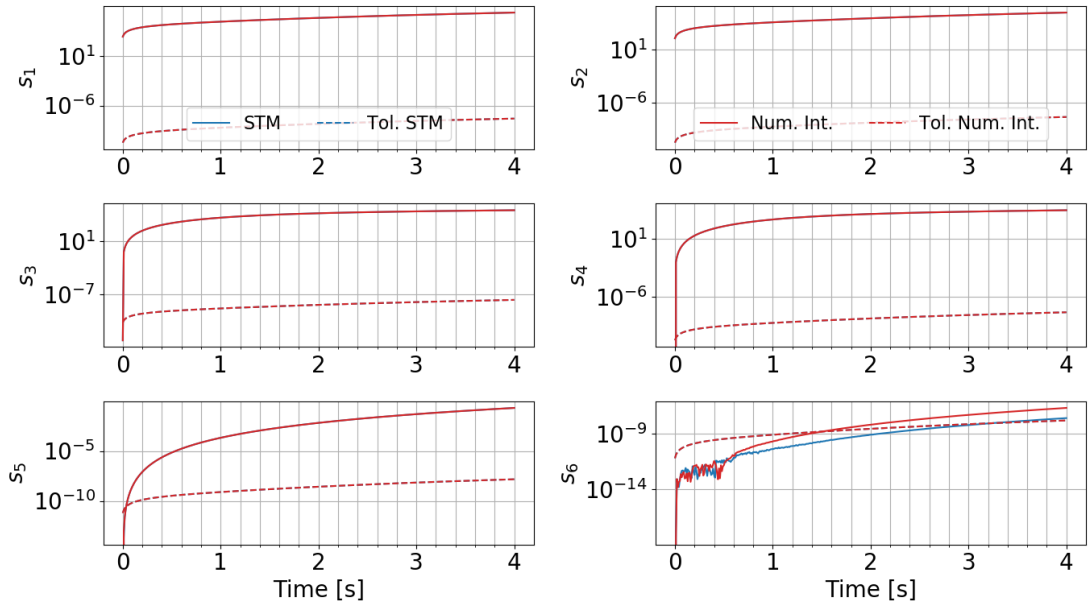

Figure A.9. Singular values of the observability matrix using the STM propagated state versus the numerically integrated state for the LEO 4 object.

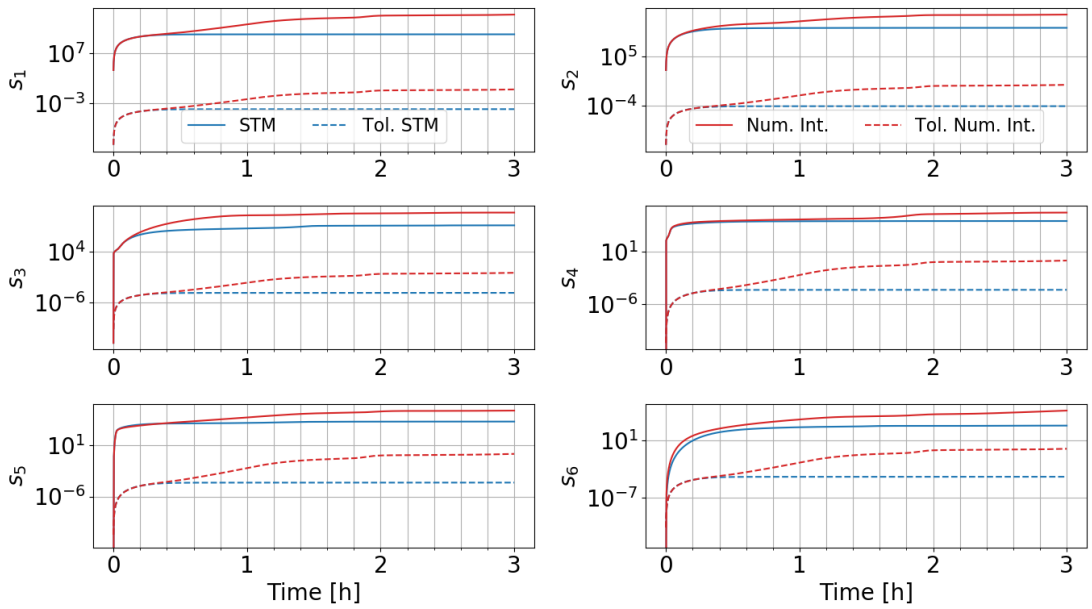

Figure A.10. Singular values of the observability matrix using the STM propagated state versus the numerically integrated state with a longer analysis time for the LEO 4 object.

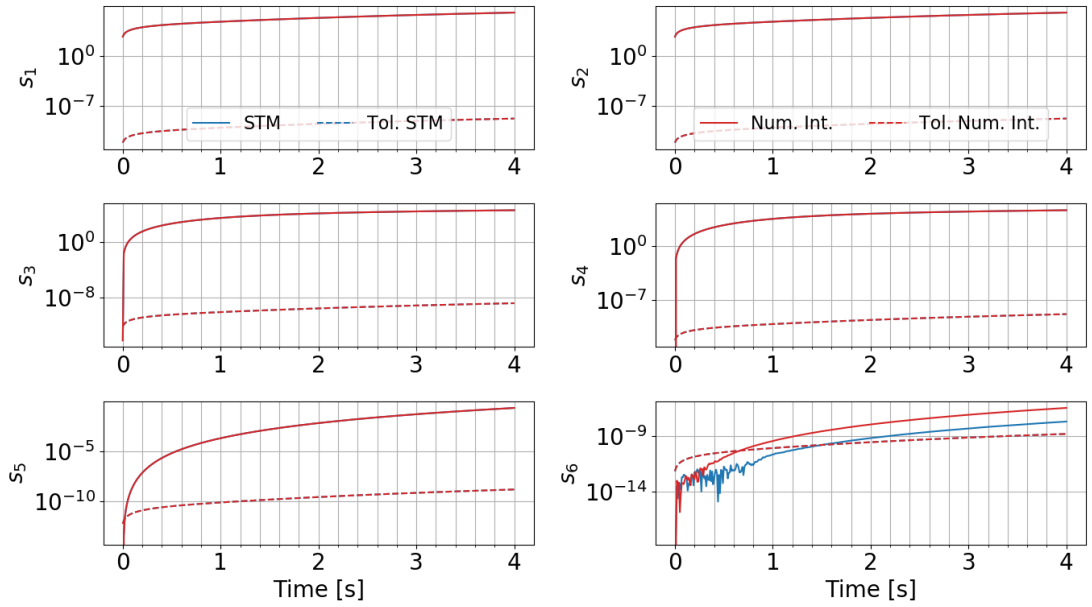

Figure A.11. Singular values of the observability matrix using the STM propagated state versus the numerically integrated state for the LEO 5 object.

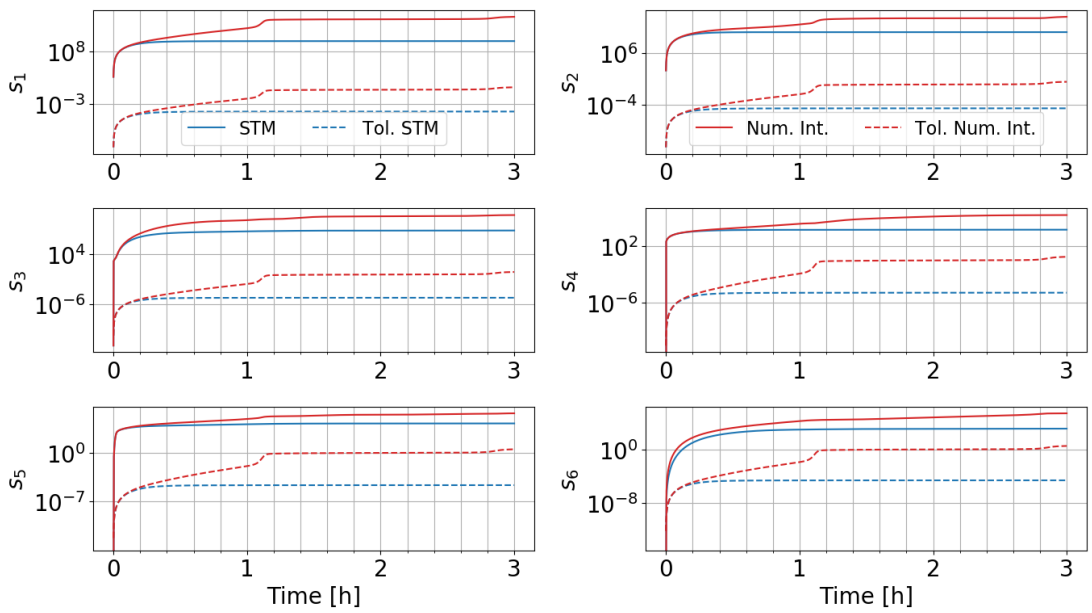

Figure A.12. Singular values of the observability matrix using the STM propagated state versus the numerically integrated state with a longer analysis time for the LEO 5 object.

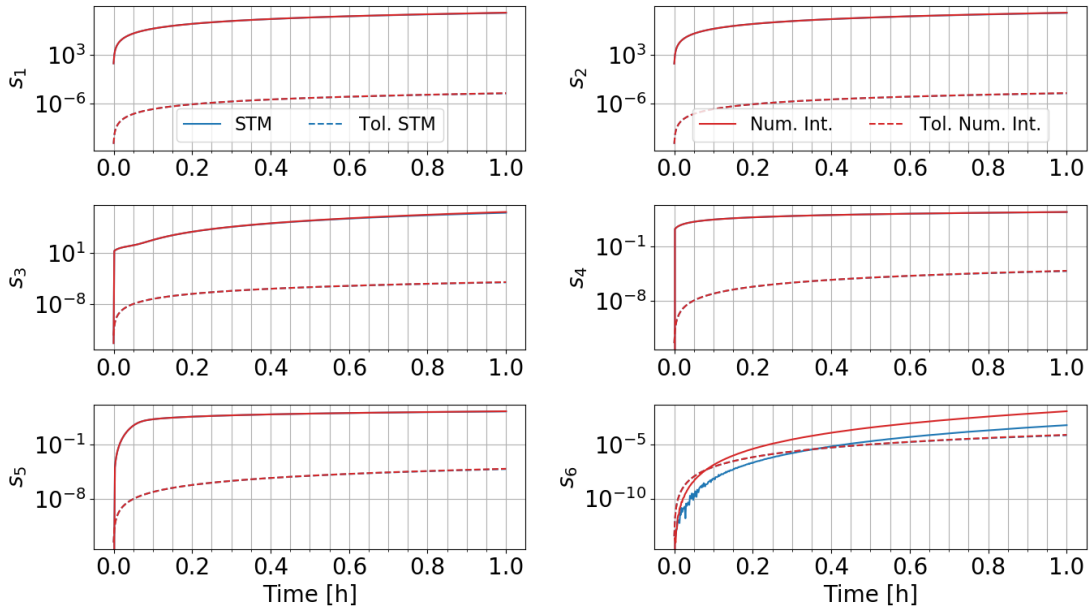

Figure A.13. Singular values of the observability matrix using the STM propagated state versus the numerically integrated state for the GEO 1 object.

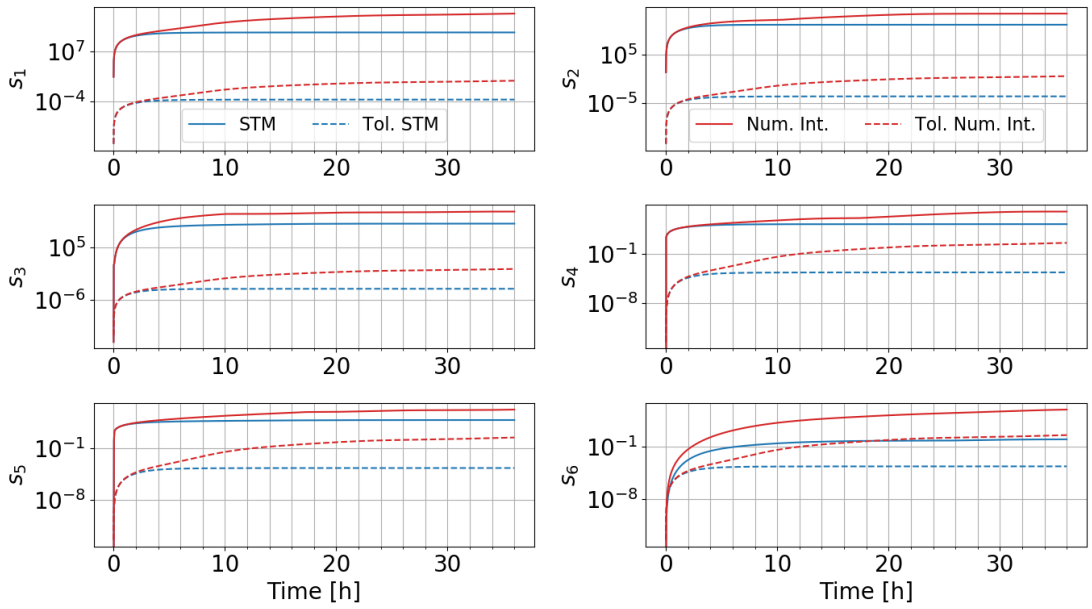

Figure A.14. Singular values of the observability matrix using the STM propagated state versus the numerically integrated state with a longer analysis time for the GEO 1 object.

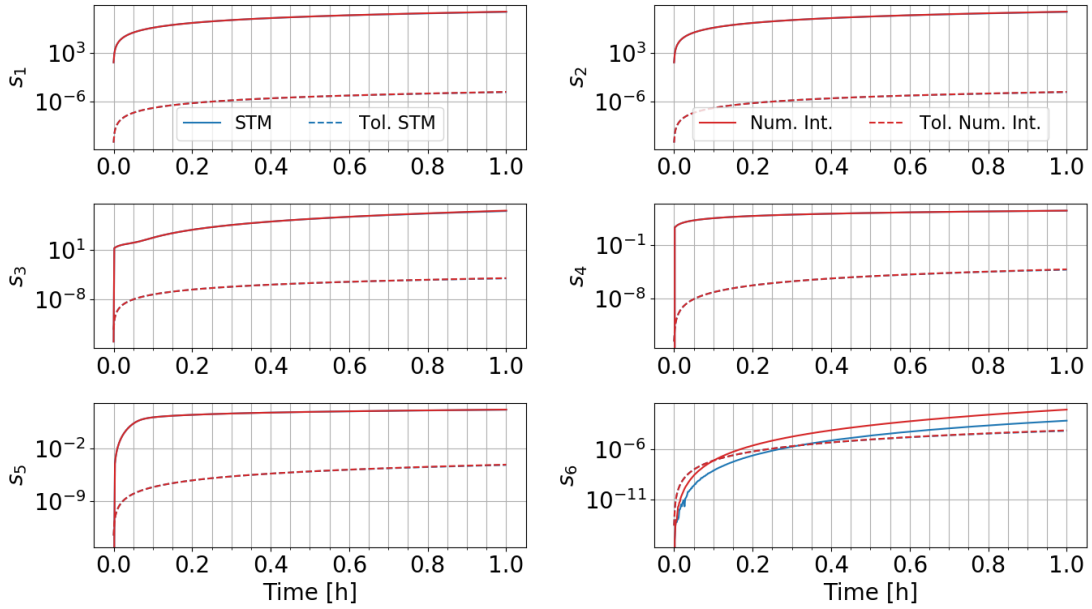

Figure A.15. Singular values of the observability matrix using the STM propagated state versus the numerically integrated state for the GEO 2 object.

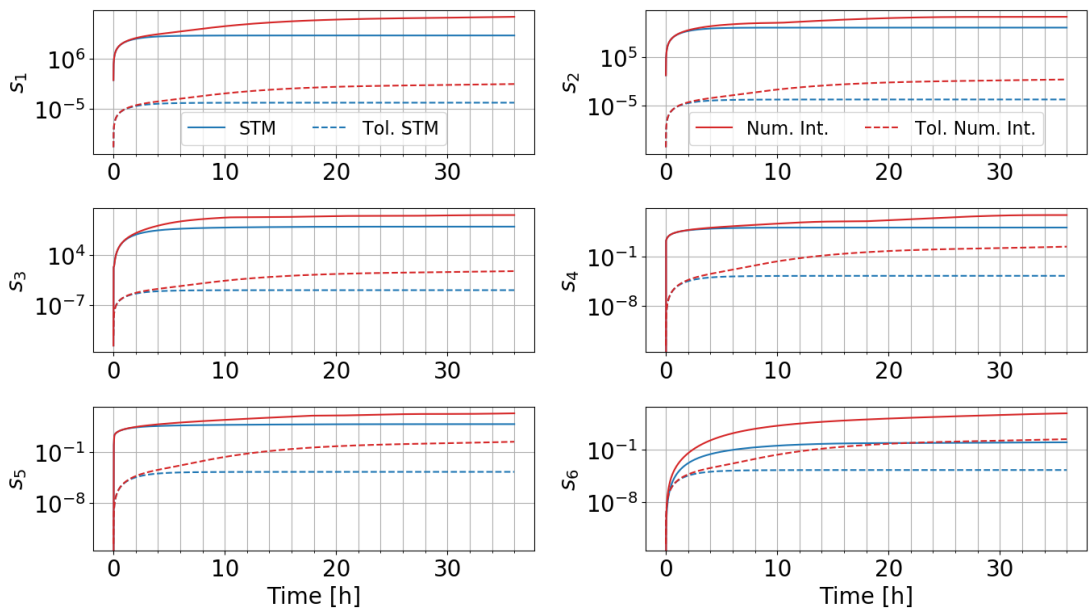

Figure A.16. Singular values of the observability matrix using the STM propagated state versus the numerically integrated state with a longer analysis time for the GEO 2 object.

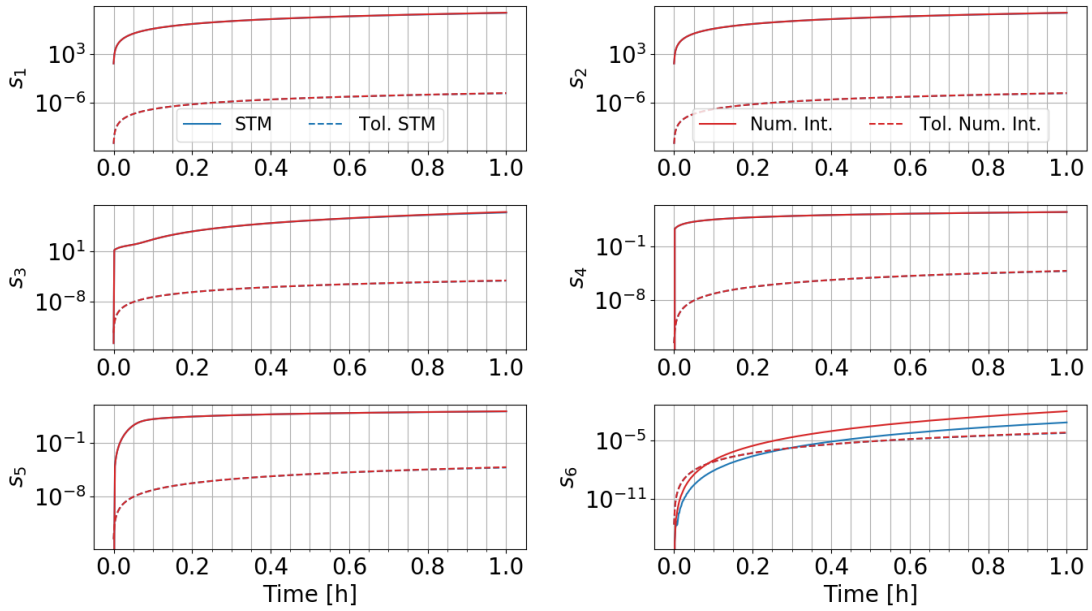

Figure A.17. Singular values of the observability matrix using the STM propagated state versus the numerically integrated state for the GEO 3 object.

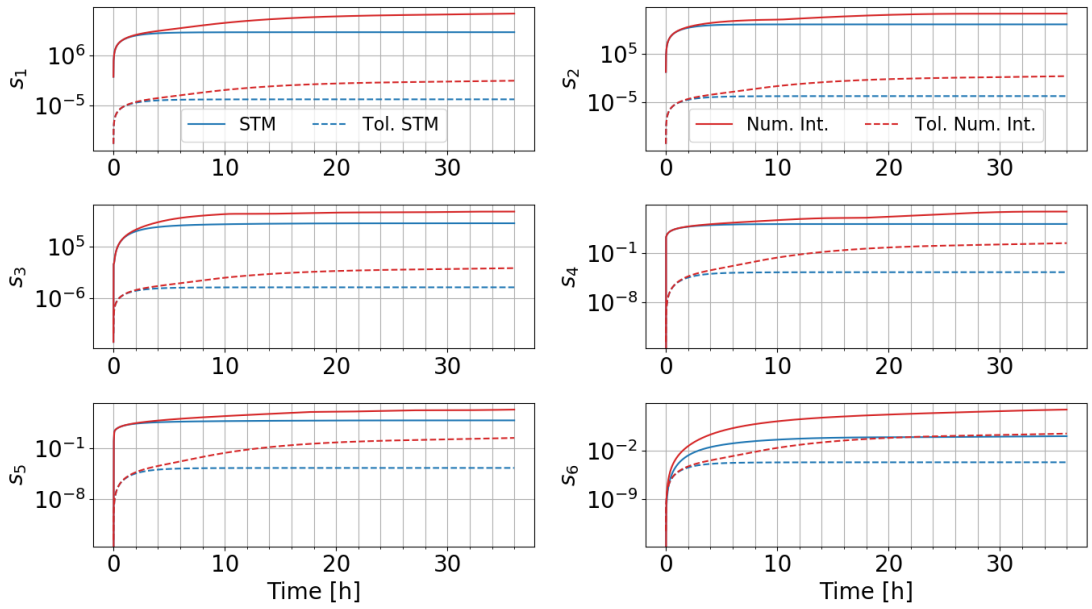

Figure A.18. Singular values of the observability matrix using the STM propagated state versus the numerically integrated state with a longer analysis time for the GEO 3 object.

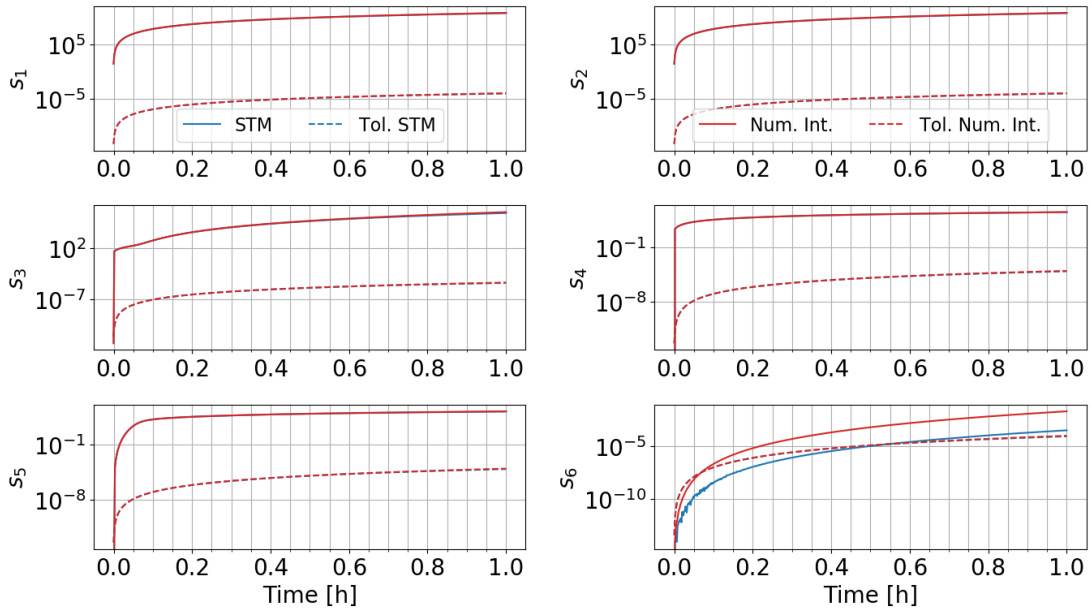

Figure A.19. Singular values of the observability matrix using the STM propagated state versus the numerically integrated state for the GEO 5 object.

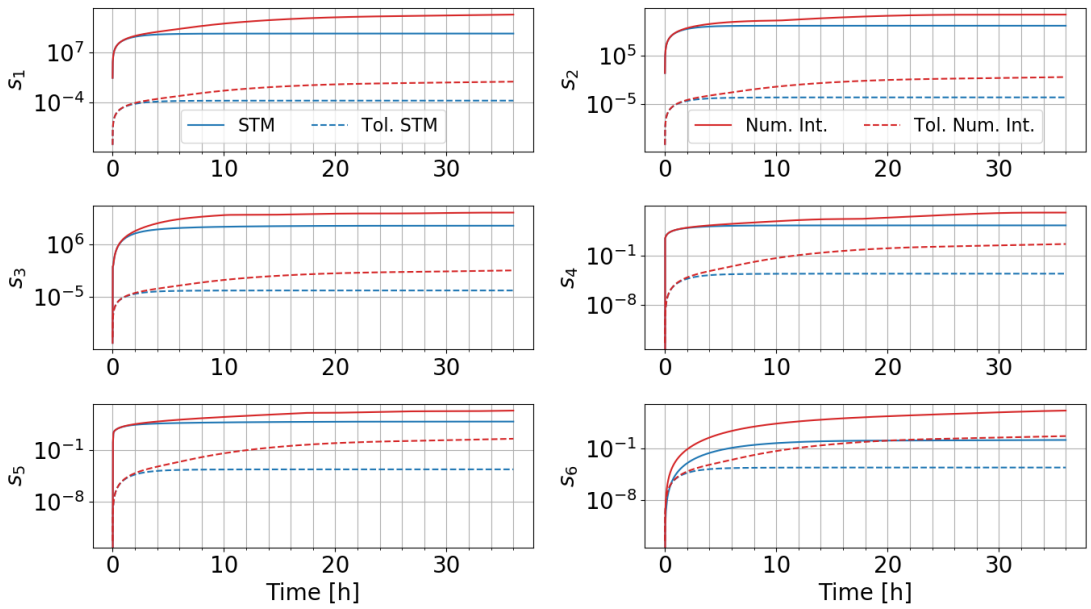

Figure A.20. Singular values of the observability matrix using the STM propagated state versus the numerically integrated state with a longer analysis time for the GEO 5 object.

A.2.2 Comparison of Other Propagators and STMs

Other STM formulations beyond numerical integration of the two-body STM ODE are presented for further comparison of the impact of propagation method on the observability matrix singular values. Three analytic STM formulations from Danby [169], Hitzl [170], and Der [171] are described in the following. In addition to these three analytic STM formulations, SGP4 propagation is implemented in a similar manner to the two-body propagation for observability analysis. Instead of propagation of the state for evaluation of the linearized measurement matrix with a two-body model, SGP4 is used for the propagation. In addition, an STM is formulated by propagating the dynamics with SGP4 and then solving the STM ODE based on the SGP4 propagated dynamics.

Danby STM

Danby develops STMs for several classes of orbits, i.e. elliptic orbits, nearly circular orbits, parabolic orbits, and hyperbolic orbits through modification of Bower's [172] method of differential corrections. The elliptical STM formulations are focused on for this work. Danby's STM formulation is based on an orbital reference system with the x-axis points towards periapsis and the y-axis is in the direction of 90° true anomaly, otherwise known as the perifocal coordinate system. In order to transform a state from a location that is not periapsis to another non-periapsis location, Danby's STM formulation requires a transformation to periapsis first and then a transformation to the final desired time.

Hitzl STM

Hitzl develops a STM with the f & g formulation of orbit propagation. The perifocal coordinate system is also used in this STM formulation. As with Danby's STM,

Hitzl's STM requires an intermediate transformation to periapsis prior to transforming to the final time.

Der STM

Der's STM formulation uses a universal anomaly and using Laguerre's method instead of Newton's method as in the STMs from Danby and Hitzl. However, Der also formulates a STM from the f & g solution, but universal variables are used. The universal variable is defined by

$$x = \frac{\theta}{\sqrt{\alpha}}, \quad a > 0, \alpha > 0, \text{ for ellipses,} \tag{A.1}$$

$$x = \sigma - \sigma_0, \quad a \to \infty, \alpha = 0, \text{ for parabolas,} \tag{A.2}$$

$$x = \frac{\theta}{\sqrt{-\alpha}}, \quad a < 0, \alpha < 0, \text{ for hyperbolas,} \tag{A.3}$$

where θ is the angle between the position vectors $\mathbf{r}_0$ and $\mathbf{r}$, α is the inverse of the semi-major axis, a, and the σ variables are defined by

$$\sigma = \frac{\mathbf{r} \cdot \mathbf{v}}{\sqrt{\mu}} \quad \text{and} \quad \sigma_0 = \frac{\mathbf{r}_0 \cdot \mathbf{v}_0}{\sqrt{\mu}}. \tag{A.4}$$

In Equation A.4, the initial velocity vector and the velocity vector are given by $\mathbf{v}_0$ and $\mathbf{v}$, respectively. Der's STM formulation begins with solving Kepler's equation by using Laguerre's method which is given by the following

$$x_{n+1} = x_n - \frac{5F(x_n)}{F'(x_n) + \frac{F'(x_n)}{|F'(x_n)|}\sqrt{16(F'(x_n))^2 - 20F(x_n)F''(x_n)}}, \tag{A.5}$$

where $n = 0, 1, 2, \ldots$. The F function and derivatives are given by Equations 5, 8, and 9 of Der which use universal functions and are a function of the universal variable, x. An initial guess of $x_0 = \alpha\sqrt{\mu}(t - t_0)$ is used in Equation A.5. Der's STM formulation does not require transition to and from periapsis.

Observability with Various Propagators and STMs

Figures A.21 and A.22 show the observability matrix smallest singular value for each propagation case described above and the GEO 4 object of Table 3.2. Figure

A.22 has a longer propagation time than Figure A.21. The blue line, described by "Num. Int.", corresponds to the case when the state is numerically integrated for evaluation of the linearized measurement matrix. The orange line, described by "STM", corresponds to the case when the state is propagated with an STM evaluated through numerical integration of the STM ODE. The green, red, and purple lines correspond to the Danby, Der, and Hitzl STM propagation methods for the linearized measurement matrix. The brown line, described by "SGP4", corresponds to the propagation of the state with SGP4 for evaluation of the linearized measurement matrix. Finally, the pink line, described by "SGP4 STM", corresponds to the propagation of the state with an STM formulated by solving the STM ODE with a state propagated with SGP4. The tolerance line for each case has the same corresponding color.

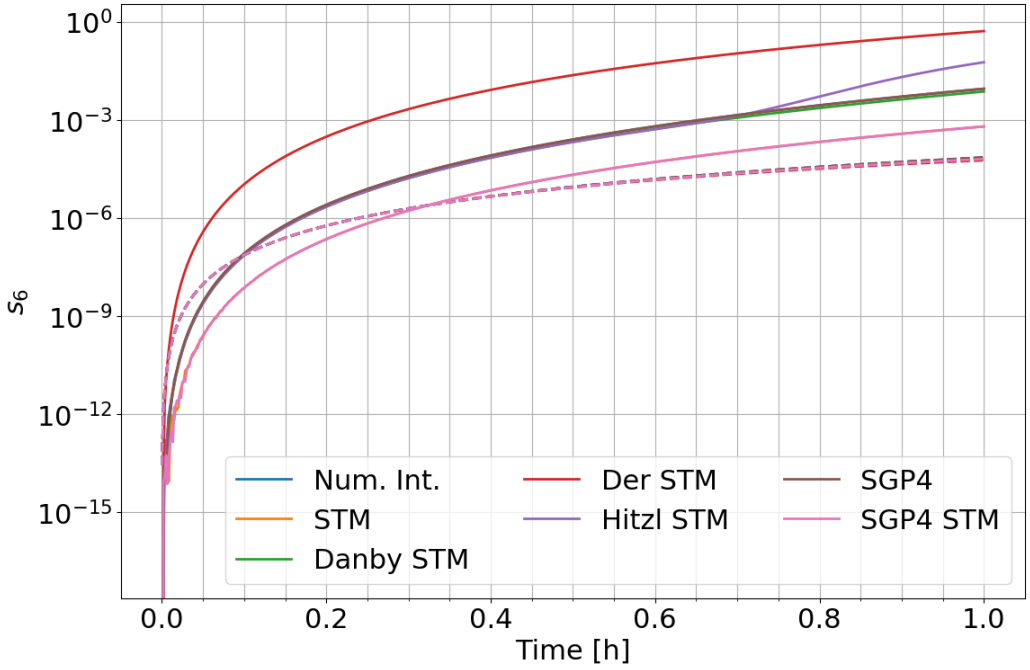

Figure A.21. Smallest singular value of observability matrices defined by several propagation methods and STM formulations over a shorter analysis time. GEO 4 object with a state consisting of position and velocity only.

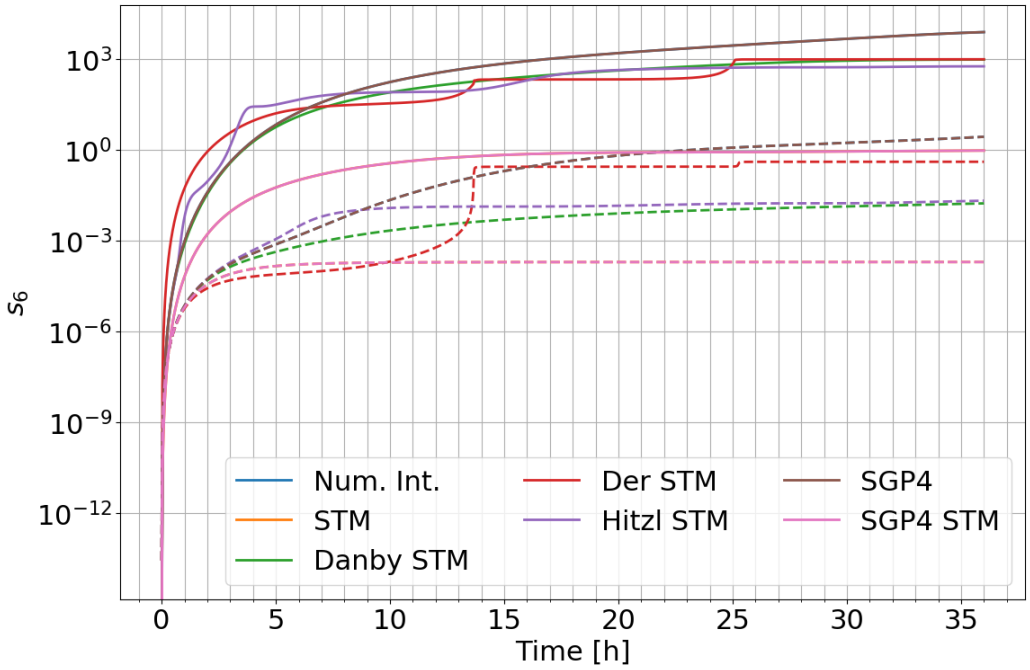

Figure A.22. Smallest singular value of observability matrices defined by several propagation methods and STM formulations. GEO 4 object with a state consisting of position and velocity only.

In Figure A.21, some of the curves are on top of one another, and the "Num. Int." and "SGP4" curves are on top of one another. For short analysis periods, many of the smallest singular value curves are similar, but some of the times for the smallest singular value to cross the tolerance line do differ. In addition, over longer analysis periods, the different STM and propagation methods for evaluation of the linearized measurement matrix vary more significantly. As discussed in Section 3.5, each STM formulation and propagation method has positive and negative attributes for applying observability to the linearized orbit problem.

A.3 Extended State Observability Results Including the C State Extension Case

The following figures reproduce the extended state observability with the extended state case with C as a state variable beyond position and velocity. The orbits implemented in this analysis are given in Tables 3.1 and 3.2.

Figures A.23 and A.24 show the times to become observable for the LEO objects and different extended state cases. For the LEO 2 object in Figures A.23 and A.24, the extended state case with C does not have a value because the observability could not be determined as the six singular value remained below the tolerance line.

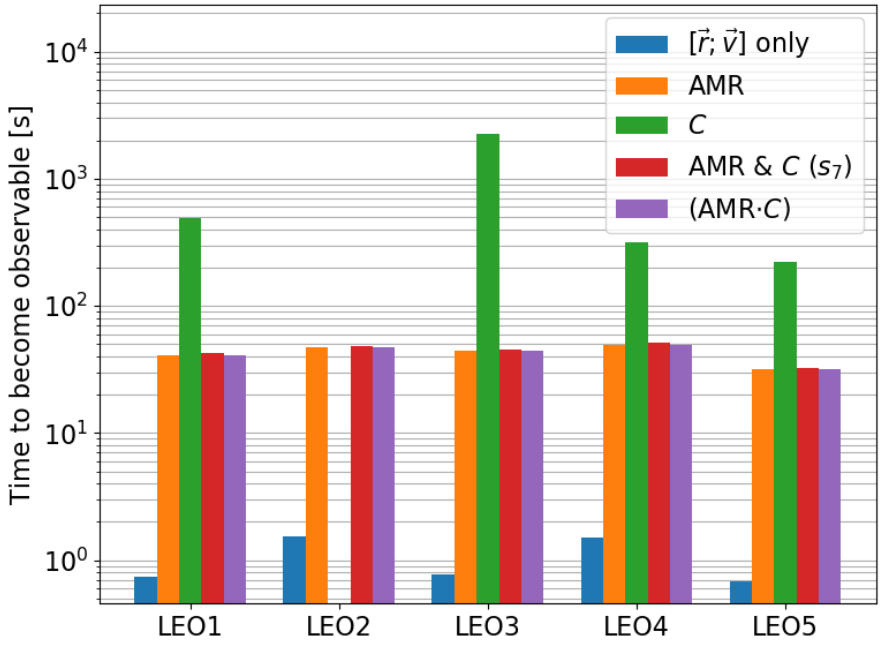

Figure A.23. Time to become observable for the LEO objects, grouped by orbit.

Figures A.26 and A.25 show the times to become observable for the GEO objects and different extended state cases.

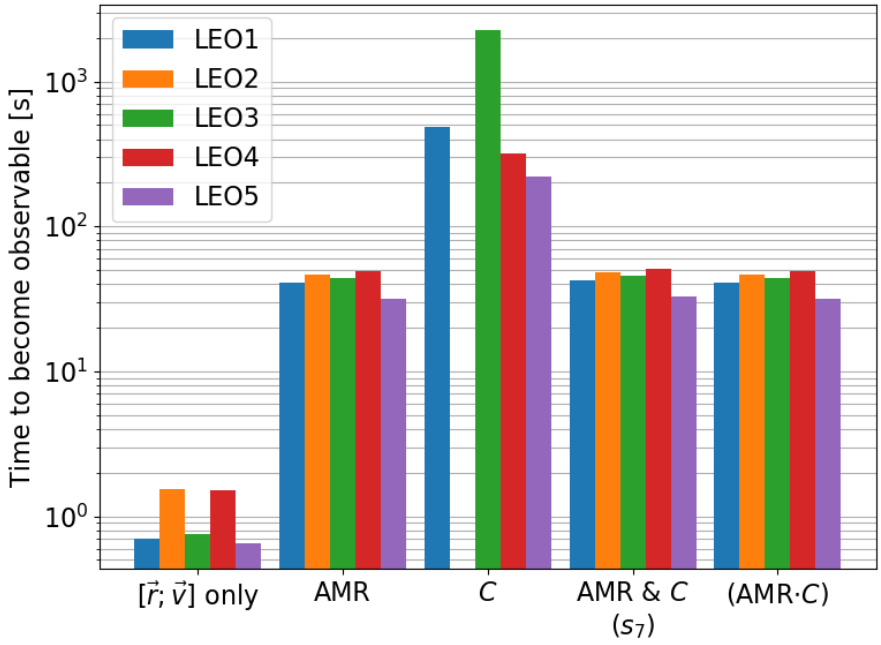

Figure A.24. Time to become observable for the LEO objects, grouped by extended state case.

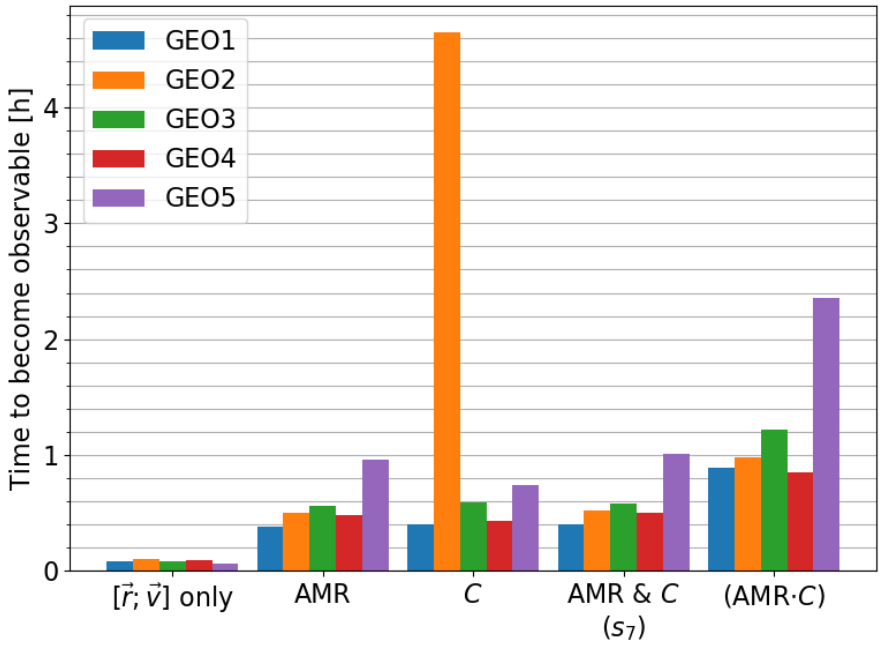

Figure A.25. Time to become observable for the GEO objects, grouped by extended state case.

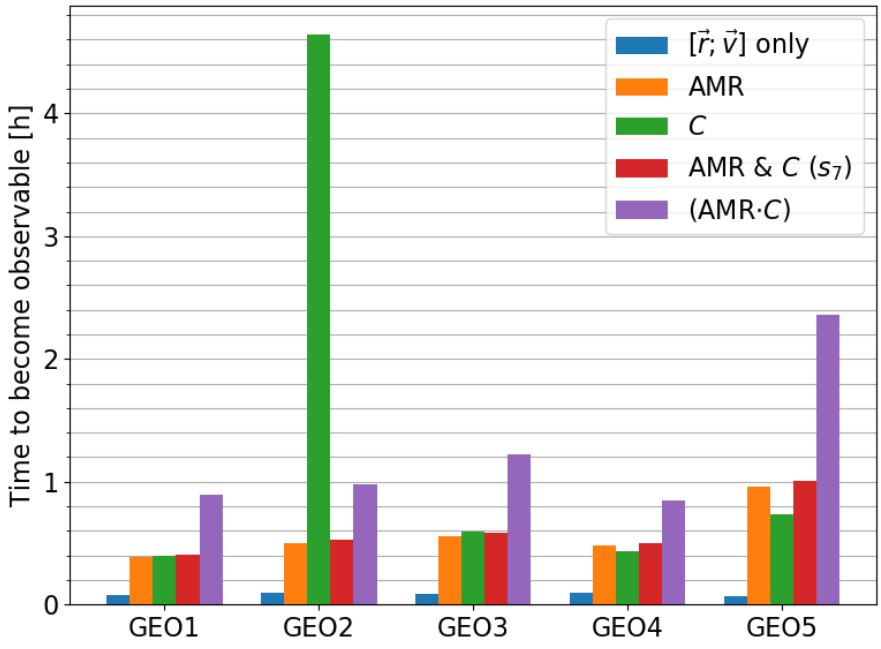

Figure A.26. Time to become observable for the GEO objects, grouped by orbit.

APPENDIX B. OBSERVABILITY-ESTIMABILITY INFORMED CONSIDER FILTER ADDITIONAL RESULTS

B.1 Estimability of the Orbit Problem

The following estimability results expand upon the results of Section 4.3. The GEO 4 object from Table 3.2 is implemented with the EKF and estimability methods from Ham. The eigenvalues and eigenvectors of the normalized state estimation error covariance matrix are shown for the extended state cases in Table 3.3. Initial state uncertainties used in the EKF and estimability analysis are given in Table 3.4.

B.1.1 Constant AMR and C

Figure B.1 show the eigenvalues of the normalized state estimation error covariance matrix for the constant AMR and C extended state case. This figure is repeated from Section B.1.1 to analyze with the eigenvectors of Figure 4.5. Figure 4.5 contains all eight eigenvectors instead of only the first two eigenvectors in Figure 4.5.

B.1.2 Time-Varying AMR and C

Figures B.3 and Figure B.4 show the estimability results for the time-varying AMR and C extended state case. Similar to the Section B.1.1, all eight eigenvectors are shown instead of only the first two eigenvectors.

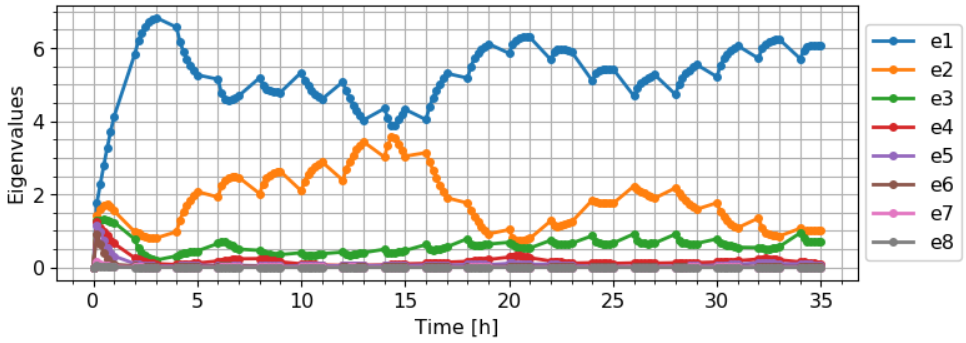

Figure B.1. Estimability eigenvalues for the constant AMR and C case.

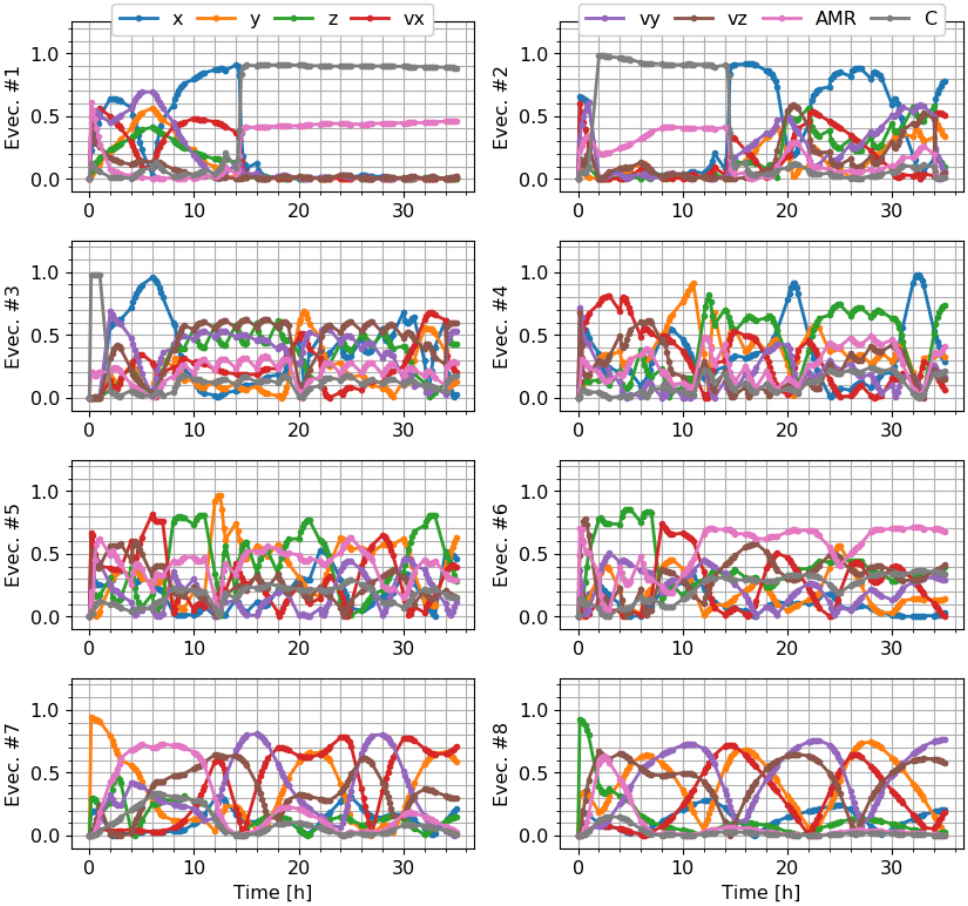

Figure B.2. Estimability eigenvectors for the constant AMR and C case.

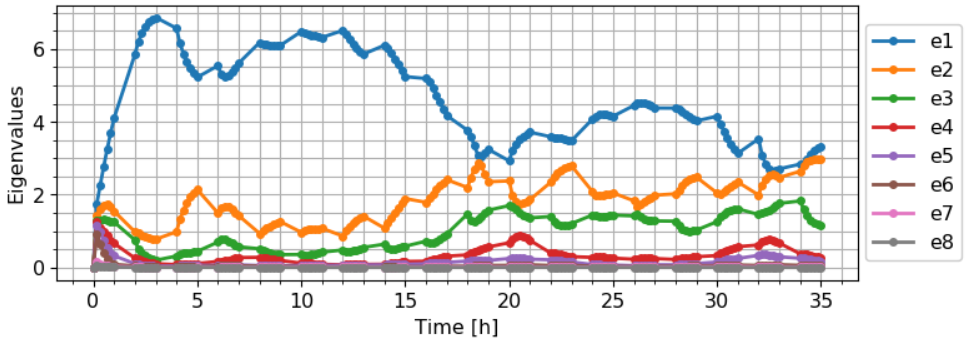

Figure B.3. Estimability eigenvalues for the time-varying AMR and C case.

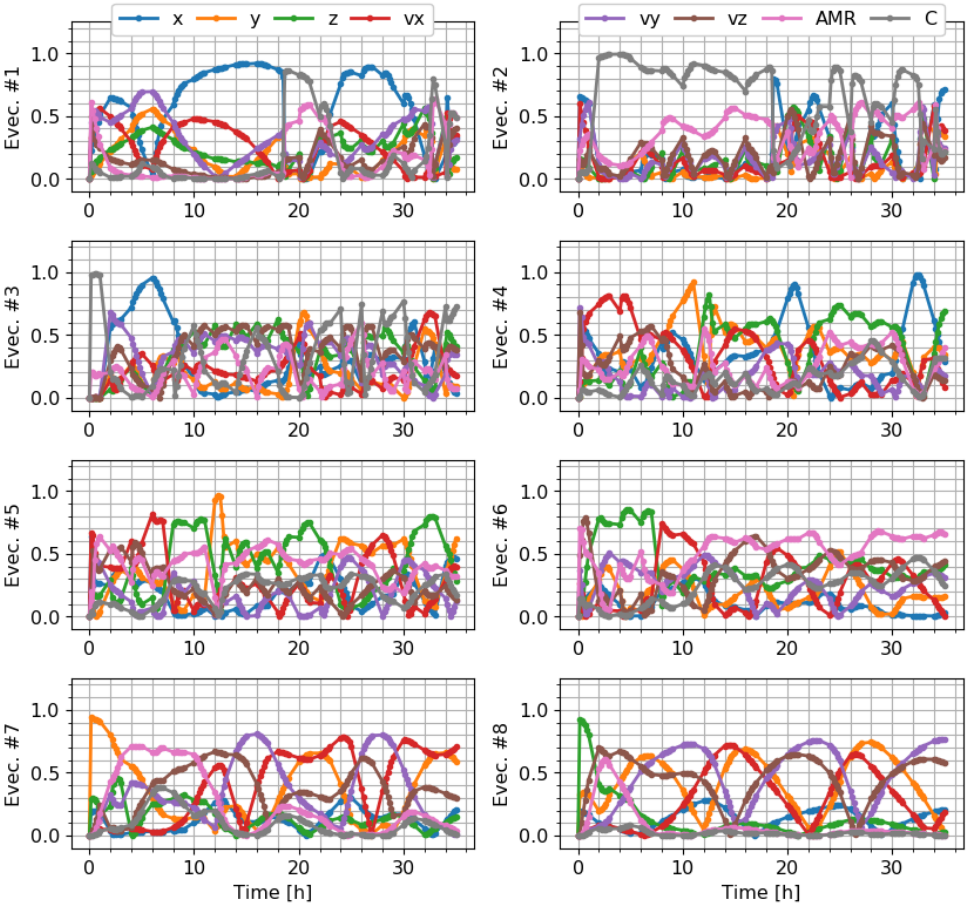

Figure B.4. Estimability eigenvectors for the time-varying AMR and C case.

B.1.3 Time-Varying AMR, Constant C

Figures B.5 and Figure B.6 show the estimability results for the time-varying AMR and constant C extended state case. These estimability results are nearly identical to the time-varying AMR and C extended state estimability results.

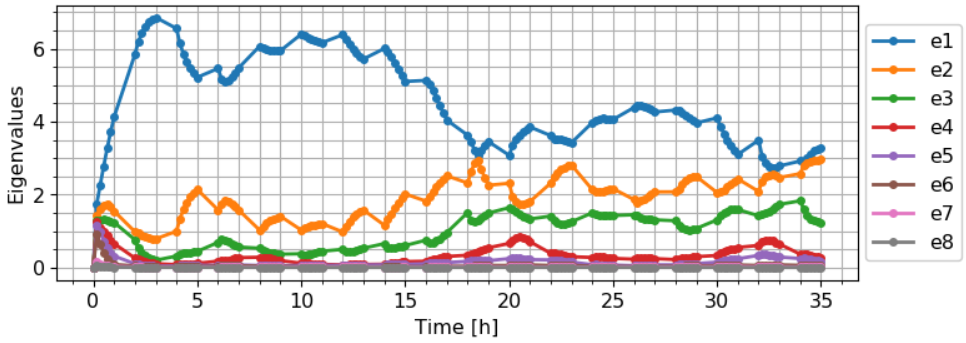

Figure B.5. Estimability eigenvalues for the time-varying AMR and constant C case.

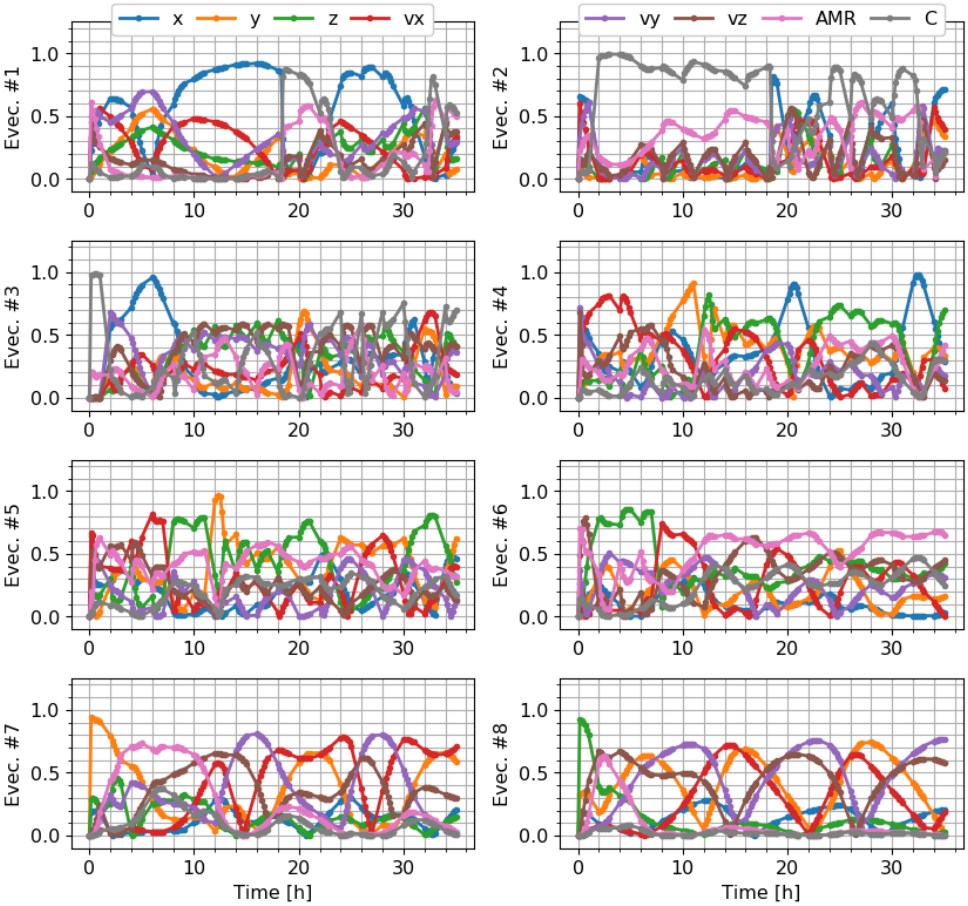

Figure B.6. Estimability eigenvectors for the time-varying AMR and constant C case.

B.1.4 Time-Varying C, Constant AMR

Figures B.7 and Figure B.8 show the estimability results for the time-varying C and constant AMR extended state case. These estimability results are nearly identical to the constant AMR and C extended state estimability results.

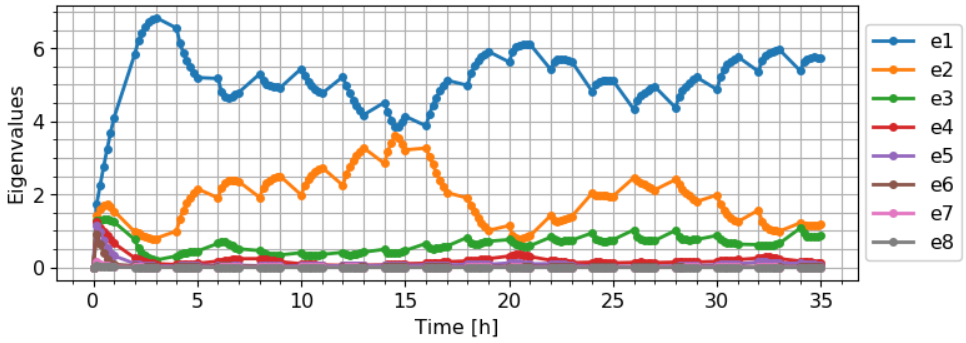

Figure B.7. Estimability eigenvalues for the time-varying C and constant AMR case.

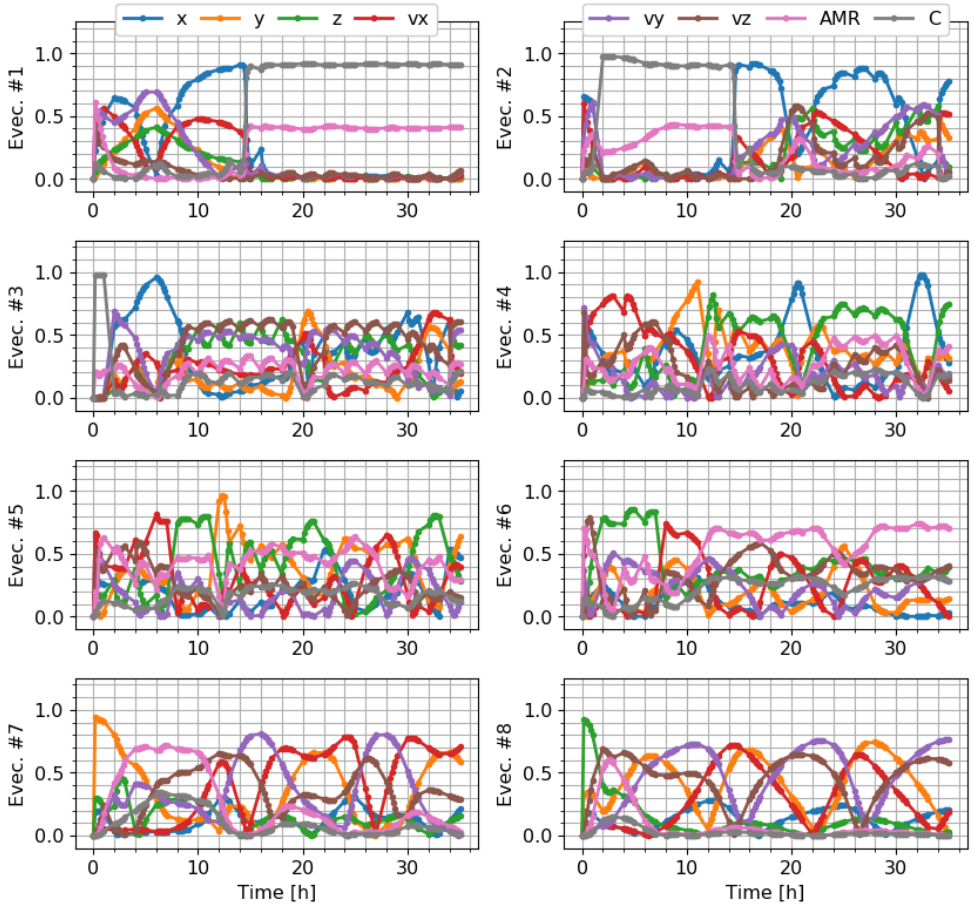

Figure B.8. Estimability eigenvectors for the time-varying C and constant AMR case.

APPENDIX C. OBSERVABILITY OF LIGHT CURVE INVERSION ADDITIONAL RESULTS

C.1 MEO Object with Single-Axis Rotation

Figures C.1 through C.3 show the observability results for the MEO object with single-axis rotation. The orbit and attitude motion are defined in Tables 5.1 and 5.2, respectively. Figure C.1 shows the rank of the observability Gramian versus time, and Figure C.2 shows the rank of the observability Gramian versus number of measurements.

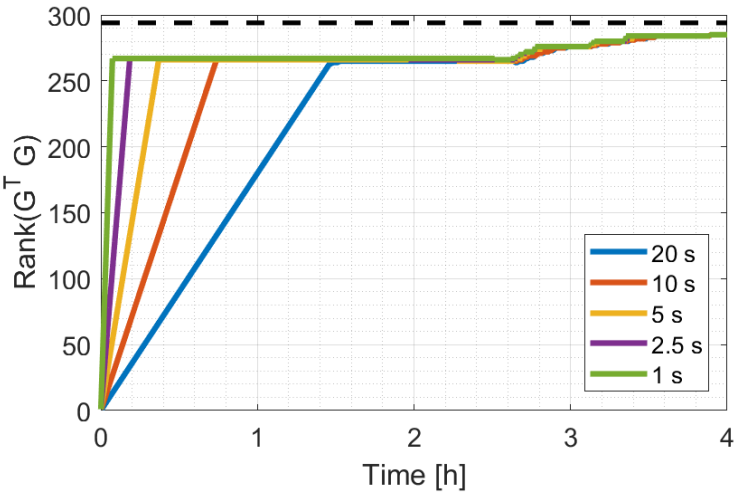

Figure C.1. Rank of the observability Gramian versus time for the MEO object with single-axis rotation and 294 surface normal directions.

Next, the impact of the EGI tessellation number on the observability Gramian is shown in Figure C.3.

Figure C.4 shows the rank deficient regions of the EGI through visualizing the linearly independent columns of the reflection matrix for the MEO object with single-axis

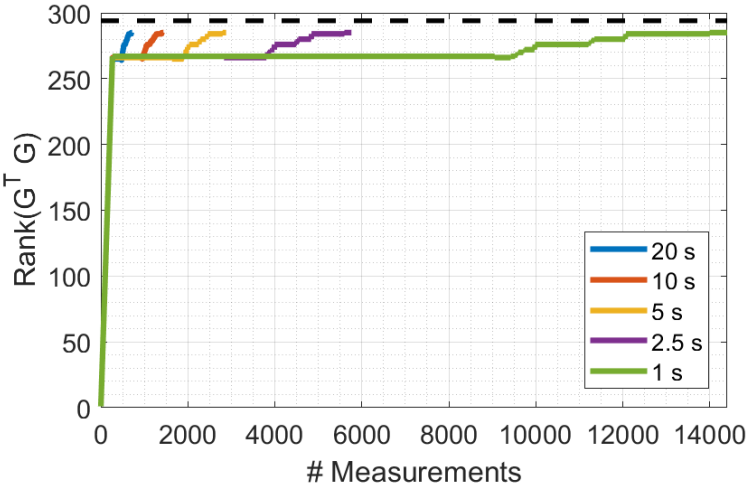

Figure C.2. Rank of the observability Gramian versus number of measurements for the MEO object with single-axis rotation and 294 surface normal directions, zoomed in for detail.

rotation. The top of the EGI corresponds to the slight increase in the observability Gramian rank after approximately 2.5 hours in Figure C.1. In addition, the rank deficiency is apparent in Figure C.4 where the bottom of the EGI is still gray at the end of the analysis time.

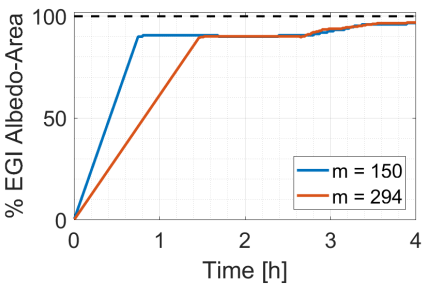

(a) 20 seconds.

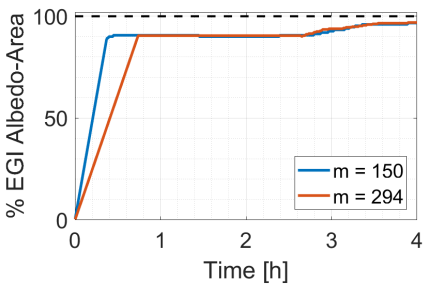

(b) 10 seconds.

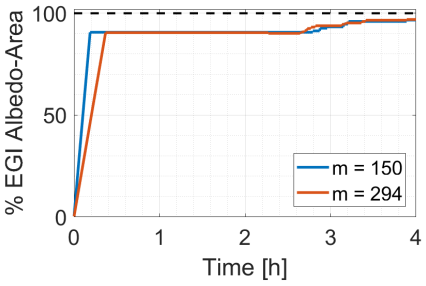

(c) 5 seconds.

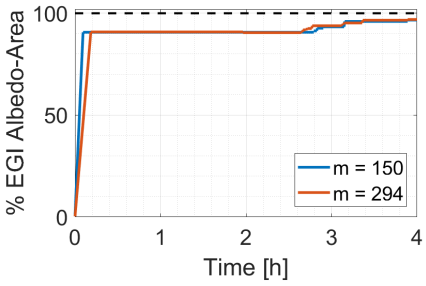

(d) 2.5 seconds.

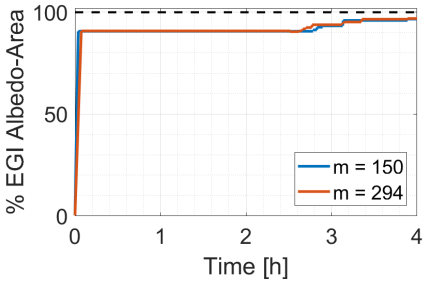

(e) 1 second.

Figure C.3. Comparison of the percentage of the EGI albedo-area which is linearly independent for EGIs with 150 and 294 surface normal directions and the MEO object with single-axis rotation.

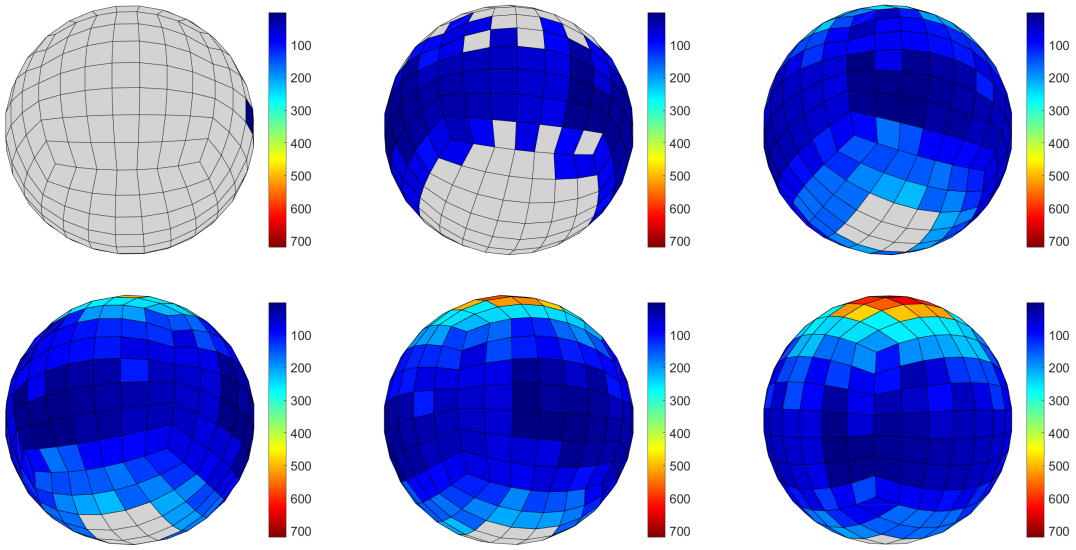

Figure C.4. 3D visualization of the linearly independent columns in the reflection matrix for the MEO object with single-axis rotation, 294 surface normal directions, and 20 seconds between measurements, where the colorbar represents measurement indices.

C.2 LEO Object with Three-Axis Rotation

Figure C.5 shows the comparison of the percentage of EGI albedo-areas for the LEO object with three-axis rotation and different EGI tessellation numbers. The orbit and attitude for the LEO object are defined in Tables 5.1 and 5.2, respectively.

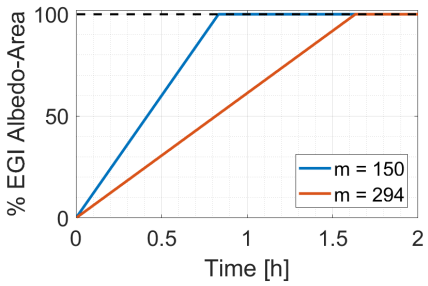

(a) 20 seconds.

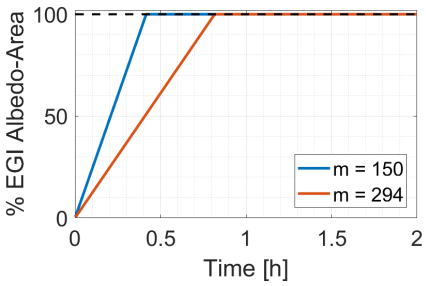

(b) 10 seconds.

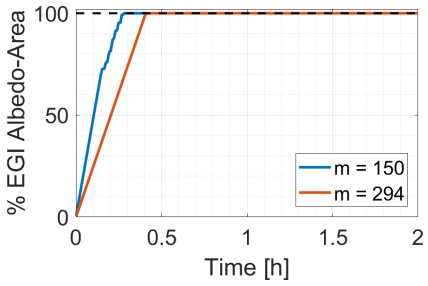

(c) 5 seconds.

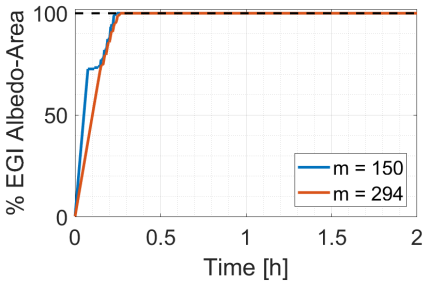

(d) 2.5 seconds.

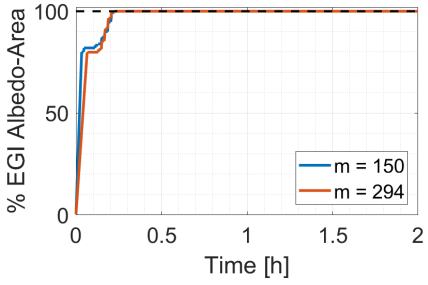

(e) 1 second.

Figure C.5. Comparison of the percentage of the EGI albedo-area which is linearly independent for EGIs with 150 and 294 surface normal directions and the LEO object with three-axis rotation.

C.3 GEO Object with Three-Axis Rotation

Figure C.6 shows the comparison of the percentage of EGI albedo-areas for the GEO object with three-axis rotation and different EGI tessellation numbers. The orbit and attitude for the GEO object are defined in Tables 5.1 and 5.2, respectively.

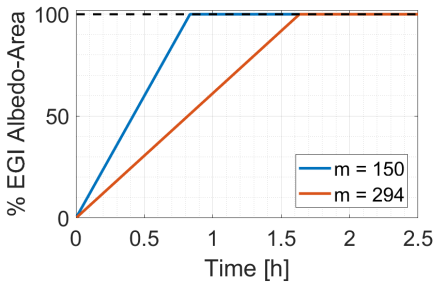

(a) 20 seconds.

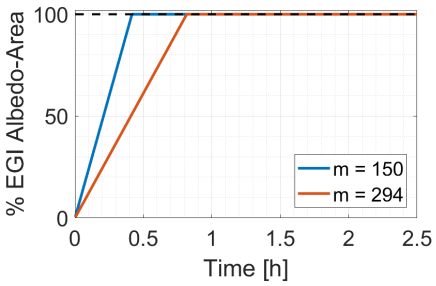

(b) 10 seconds.

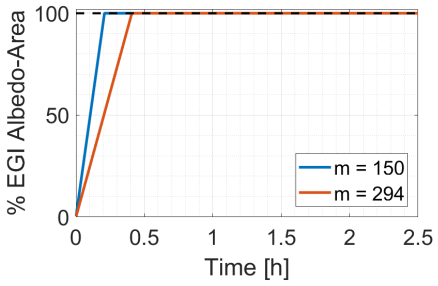

(c) 5 seconds.

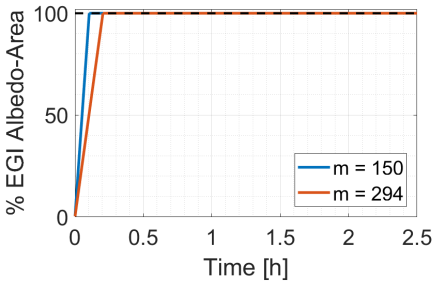

(d) 2.5 seconds.

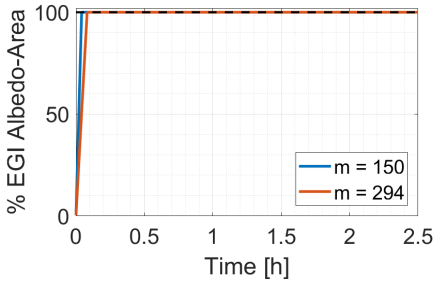

(e) 1 second.

Figure C.6. Comparison of the percentage of the EGI albedo-area which is linearly independent for EGIs with 150 and 294 surface normal directions and the GEO object with three-axis rotation.

C.4 MEO Object with Three-Axis Rotation

Figures C.7 and C.8 show the rank of the observability Gramian over time for the MEO object with three-axis rotation. The EGI tessellation number shown here equals 7, or 294 EGI surface normal directions. The second plot, Figure C.8 shows more detail of the region near full rank.

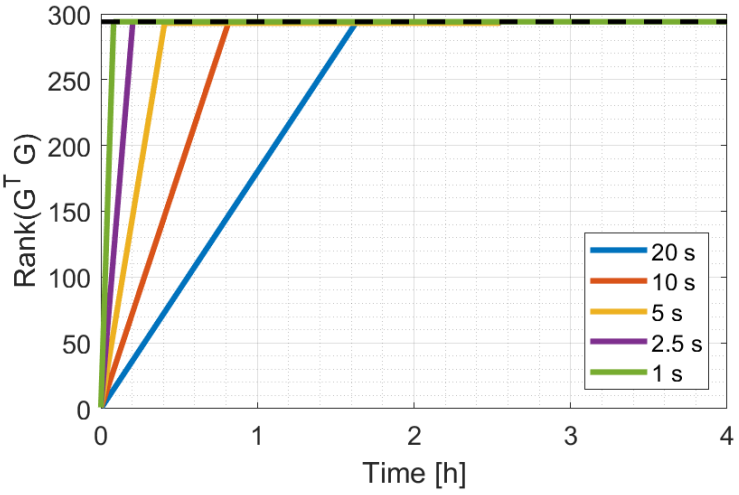

Figure C.7. Rank of the observability Gramian versus time for the MEO object with three-axis rotation and 294 surface normal directions.

Figure C.9 shows the rank of the observability Gramian versus number of measurements for the MEO object with three-axis rotation.

Figure C.10 compares the percentage of the EGI albedo-areas which become linearly independent in the observability Gramian for different EGI tessellation numbers

The 3D visualization of the linearly independent columns of the reflection matrix for the MEO object with three-axis rotation and 10 seconds between measurements is shown in Figure C.11.

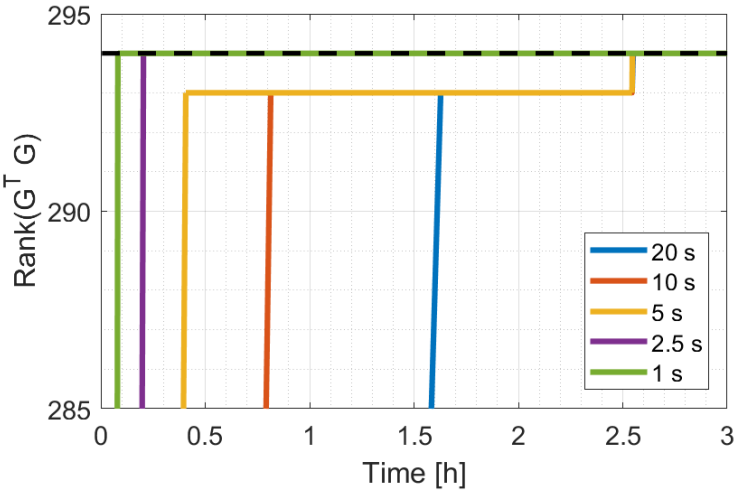

Figure C.8. Rank of the observability Gramian versus time for the MEO object with three-axis rotation and 294 surface normal directions, zoomed in for detail.

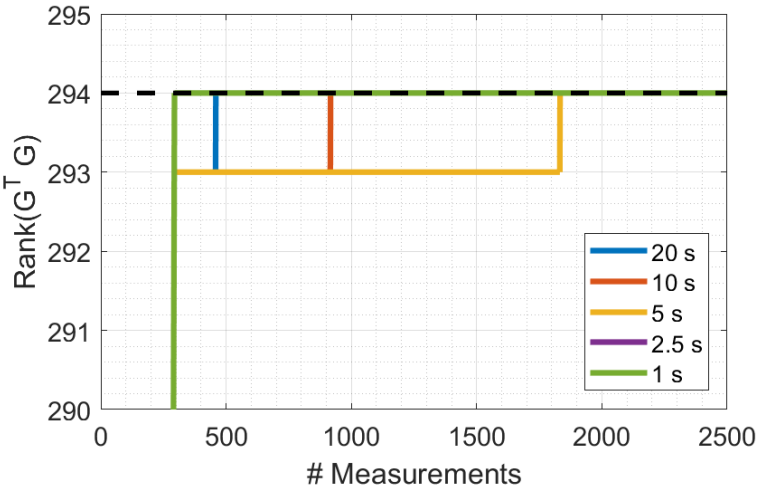

Figure C.9. Rank of the observability Gramian versus number of measurements for the MEO object with three-axis rotation and 294 surface normal directions, zoomed in for detail.

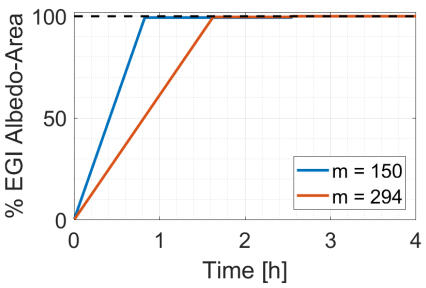

(a) 20 seconds.

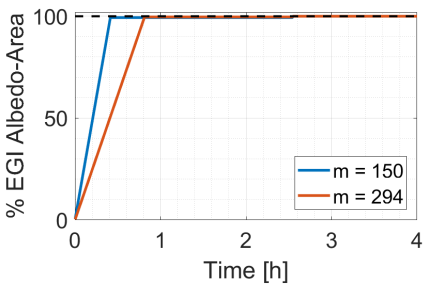

(b) 10 seconds.

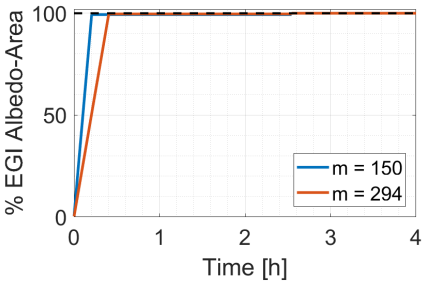

(c) 5 seconds.

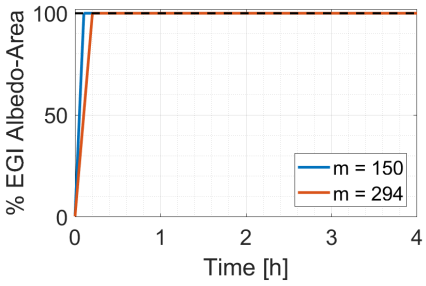

(d) 2.5 seconds.

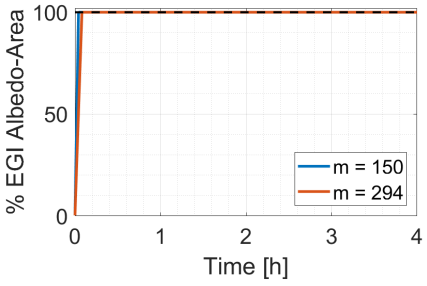

(e) 1 second.

Figure C.10. Comparison of the percentage of the EGI albedo-area which is linearly independent for EGIs with 150 and 294 surface normal directions and the MEO object with three-axis rotation.

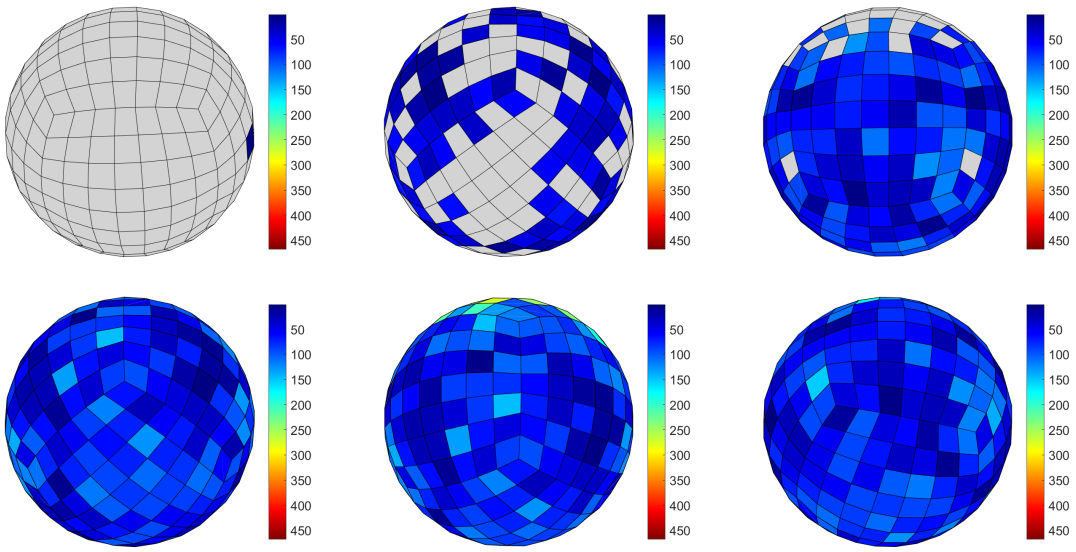

Figure C.11. 3D visualization of the linearly independent columns in the reflection matrix for the MEO object with three-axis rotation, 294 surface normal directions, and 20 seconds between measurements, where the colorbar represents measurement indices.

C.5 Rank Deficiency of Attitude Profile B

More detailed analysis of several unconstrained measurement spacing cases are presented in an attempt to uncover the cause of the rank deficiency with the second attitude profile. Figure C.12 through Figure C.15 show measurement spacing cases with a range of two to ten hours between each batch of measurements, which are comparable to Figure 5.27 through Figure 5.30 with a different attitude profile. All of the unconstrained, equally spaced measurement cases for the second attitude profile do not reach full rank. The two and four hour measurement spacing cases reach a rank of 996, resulting in a rank deficiency of 18. After approximately 17 hours, all of the measurement spacing cases do not increase rank any more with more measurements for this attitude profile. The rank deficiency in this problem indicates that the attitude profile and system geometry changes in a way which excludes a portion of the model from the observer for this analysis time.

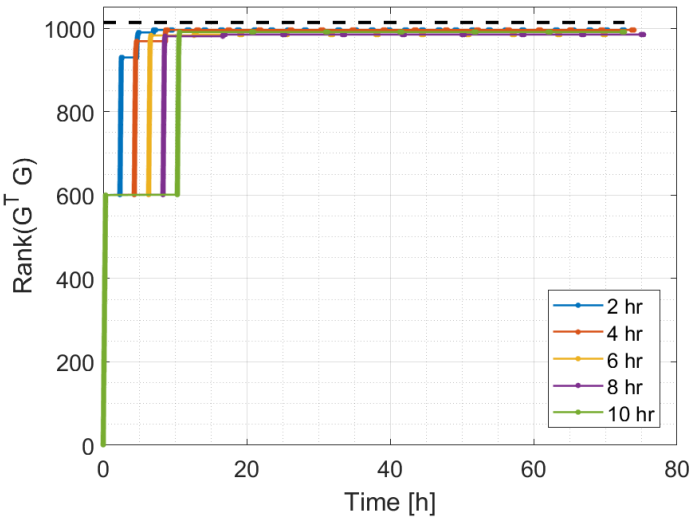

Figure C.12. Rank of the observability Gramian versus time with attitude B and without visibility constraints.

Large computation times resulting from the large number of EGI surface normal directions and the long analysis time resulted in an alternative approach for deter-

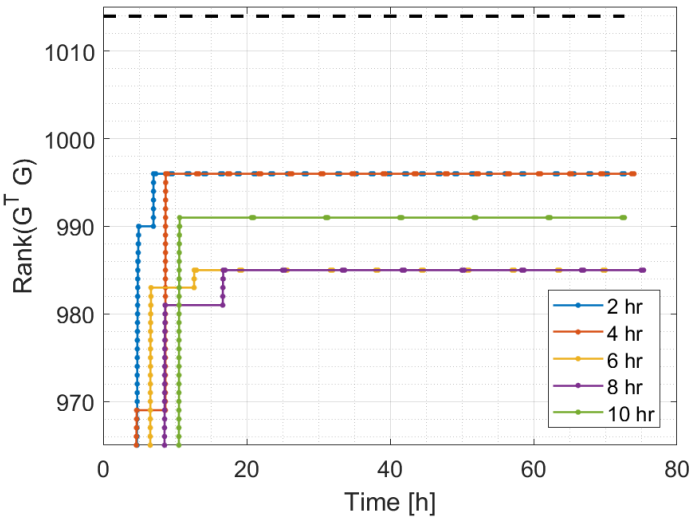

Figure C.13. Rank of the observability Gramian versus time with attitude B and without visibility constraints., zoomed in to show detail.

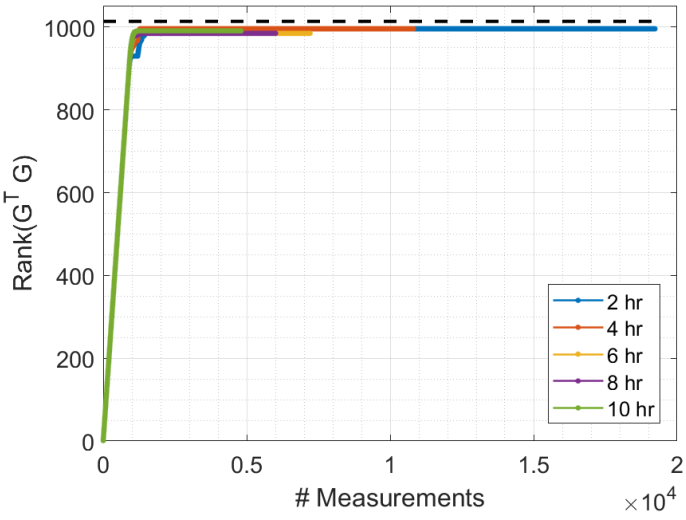

Figure C.14. Rank of the observability Gramian versus number of measurements with attitude B and without visibility constraints.

mining if the geometry changes sufficiently over a long time for observability of the EGI minimization. Instead of equally spaced measurement batches, two sets of two

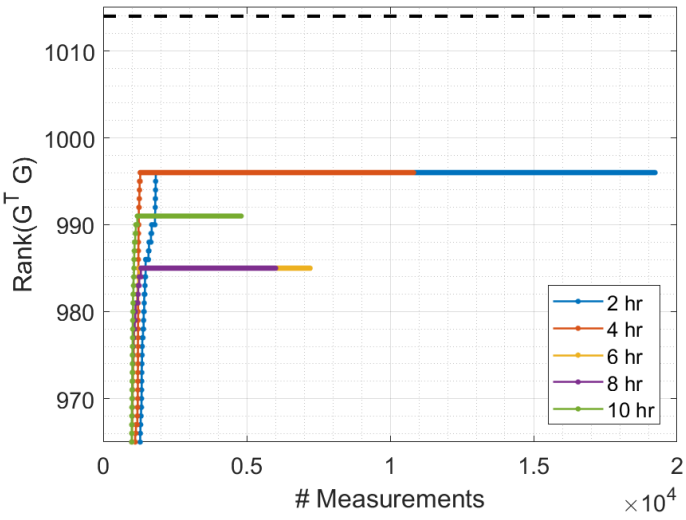

Figure C.15. Rank of the observability Gramian versus number of measurements with attitude B and without visibility constraints, zoomed in to show detail.

measurement batches were placed in visibility windows with varying time between each window. Also, the measurements are placed at the extremes of each visibility window, i.e. the first batch begins at the start of the visibility window and the last measurement of the second batch is at the end of the visibility window. This new arrangement of the measurements keeps the computational time semi-constant as the number of measurements remains the same for each case. The computational time does increase slightly as the time between visibility windows increases, but the observer, object, and Sun propagation is performed prior to analysis of the observability Gramian.

Figures C.16, C.17, and C.18 show the observability results for the new measurement sequence. The time between visibility windows is varied from approximately 5 days to 180 days. Each spacing is approximate because the visibility window of the second set of measurement batches may not be long enough to contain two 20 minute measurement batches, which would result in an earlier visibility window being selected for the second set of measurement batches. Furthermore, the time of the

second set of measurement batches is referenced from epoch, so the spacing between the end of the second and third batches of measurement is one day less than the listed separation.

In Figure C.16, the spacing between visibility windows of 5 days and 180 days have the highest observability Gramian rank at the end of four batches of measurements. Figure C.17 shows the 180 day spacing case in more detail. Figure C.18 shows the rank of the observability Gramian versus the number of measurements. For this system, the 180 day spacing between visibility windows has the highest rank thus far, but full rank is not achieved for the EGI with 1014 surface normal directions.

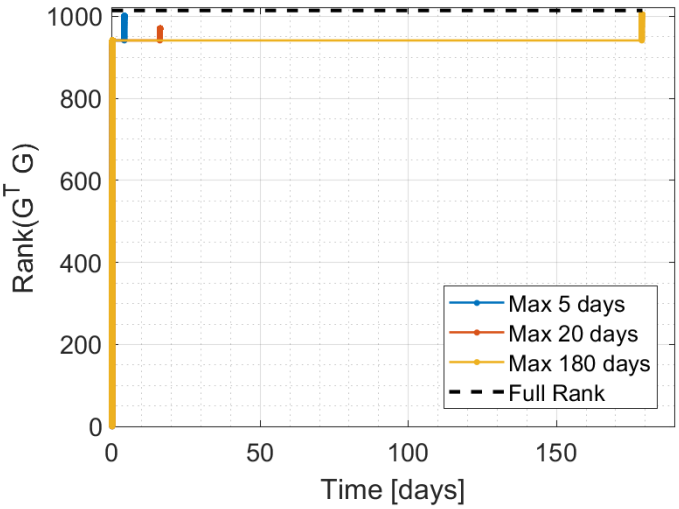

Figure C.16. Rank of the observability Gramian versus time with visibility constraints and attitude B for a range of days between measurement batches.

In order to understand the rank deficiency of this system for EGI minimization, the linear independence of the columns of the reflection matrix is visualized for the 180 day spacing case in Figure C.19. Figure C.19a shows the view from the observer to the object at the end of the last measurement. A second view of the visualization at the same time of the last measurement is given in Figure C.19b which shows a region where the second batch of measurements sufficiently sampled the surface normal directions of the EGI. At first it appears that all surface normal directions

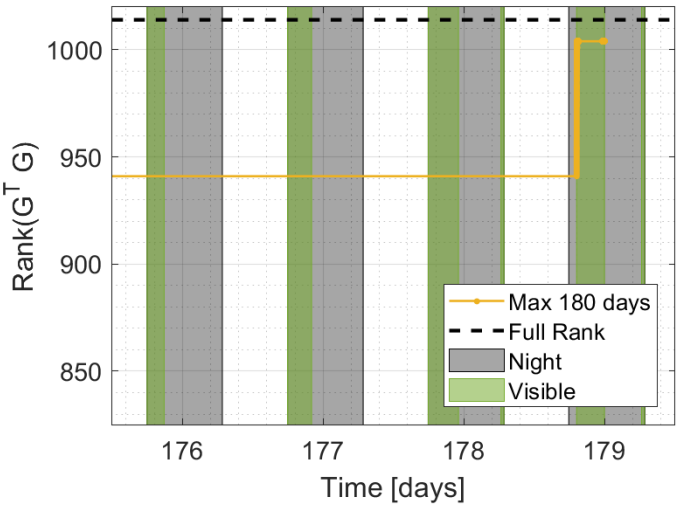

Figure C.17. Rank of the observability Gramian versus time with visibility constraints and attitude B for two sets of measurement batches spaced by approximately 180 days.

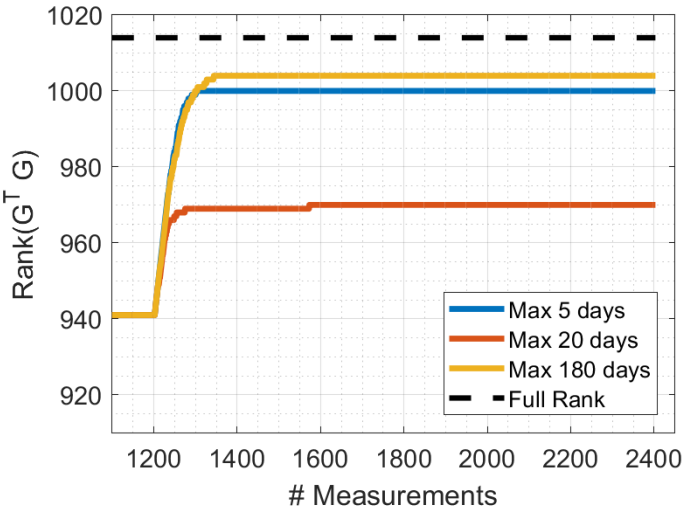

Figure C.18. Rank of the observability Gramian versus number of measurements with visibility constraints and attitude B for a range of days between measurement batches, zoomed in to show detail.

have all been sampled, but Figure C.19c, a different orientation of the visualization at the same time, shows six surface normal directions which were insufficiently sampled.

Therefore, this one region of the EGI was not illuminated and visible to the observer or did not have enough measurements to sufficiently sample the EGI surface normal directions for EGI minimization.

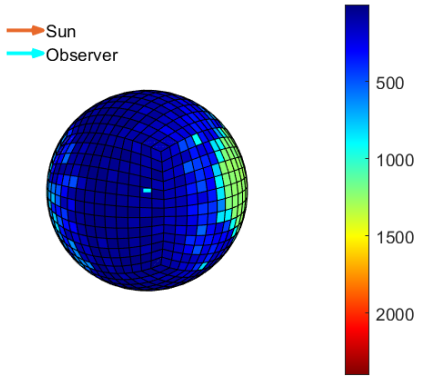

(a) Observer view to the observer after last measurement.

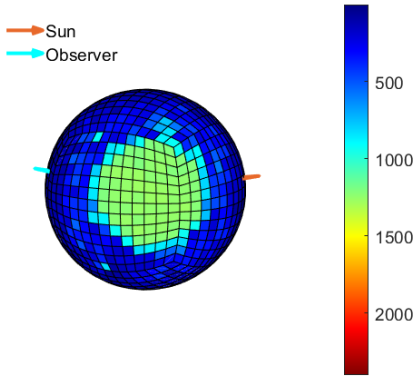

(b) Orientation depicting region sampled during second batch of measurements.

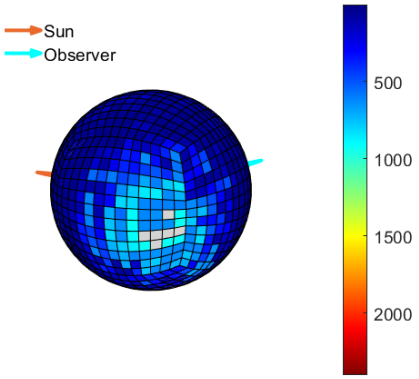

(c) Insufficiently sampled region.

Figure C.19. 3D visualization of the linearly independent columns in the reflection matrix for the Atlas V upper stage with 1014 surface normal directions. Attitude B, two sets of two batches spread over approximately 180 days.

Further analysis of attitude profile B has shown the sensitivity of the EGI minimization to the spin axis orientation. Moreover, the resulting rank deficiency of the observability Gramian for this attitude profile shows the importance of observability analysis for collecting light curve measurements for light curve inversion. More analysis is needed to determine how the Atlas V object with attitude B can be sufficiently sampled. Analysis of alternative observation sites and measurement sequences may aid in sufficient sampling of the system geometry for light curve inversion.

C.6 Propagation Comparison for Constrained Analysis

Observability of the EGI minimization was performed with two orbit propagators, two-body and SGP4, for investigation of the impact of propagation method on observability of this system. The results shown in Figures C.16, C.17, and C.18 implement the SGP4 propagator for orbit propagation. The same measurement spacing cases are repeated with two-body propagation.

Figure C.20 compares the rank of the observability Gramian for the two propagation types. As the three measurement spacing cases have large differences in the time of the third and fourth batches of measurements, the x-axis for the rank comparison is the measurement number in each measurement sequence. Also, the rank difference subtracts the SGP4 results from the two-body propagation results. Therefore, positive values represent times when the rank of the observability Gramian with two-body propagation of the orbit is larger than that of the SGP4 orbit propagation.

Over the first two measurement batches, up to 1200 measurements, the observability Gramian rank is the same for all three measurement spacing cases. There are several points around 1000 measurements where there are differences in the rank for the two propagation methods. However, this rank difference is only one and each measurement spacing case has the same values. The biggest differences in the rank for the two propagation methods occurs for the 180 days measurement spacing case, as expected. Over a long time period, the perturbations in the SGP4 propagator will

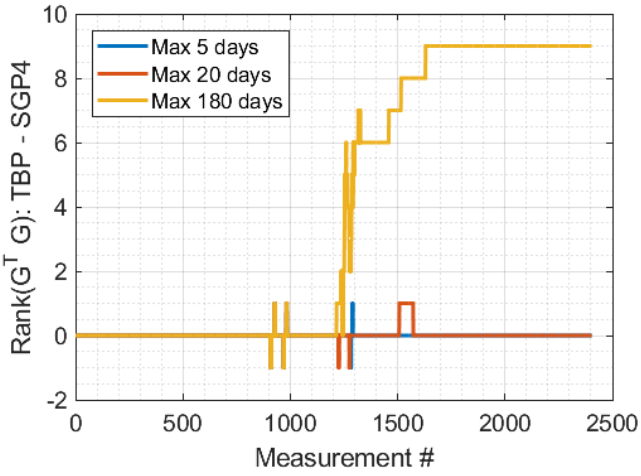

Figure C.20. Difference in the rank of the observability Gramian for two-body and SGP4 propagation of the orbit.

have a large effect on the orbital geometry when compared to a two-body propagated orbit. Note that the SGP4 propagation over 180 days results in an observability Gramian rank which is less than the rank for the two-body propagation. In some cases, more geometric diversity in a system can benefit observability analysis, but for the system of interest here, this is not the case.

Next, Figure C.21 through Figure C.23 compare the orbital elements of the three measurement cases with the two propagation methods. Figure C.21 shows the semi-major axis, eccentricity, and inclination of each measurement spacing case and propagation method. The rows represent the orbit shape defining orbital elements, and the columns represent each measurement spacing case. Figure C.22 presents the same comparison of the propagation methods for the orbit orientation defining orbital elements. For Figures C.21 and C.22, the average orbital element value over each batch of measurements is computed for each propagation method. Moreover, the absolute value of the differences between each propagation method is shown.

In Figures C.21 and C.22, the orbital elements from the orbit propagated with two-body propagation are constant, with the exception of the true anomaly, ν. For

many of the orbital elements, the differences between the SGP4 propagated orbit and two-body propagated orbit are small. The biggest changes in the orbital elements over the analysis time occur in the eccentricity, right ascension of the ascending node, argument of perigee, and true anomaly for the 180 days measurement spacing case. A large change in true anomaly results in a different orbit location at the time of the measurements, and therefore, the orbital geometry which is captured with the measurement is significantly different.

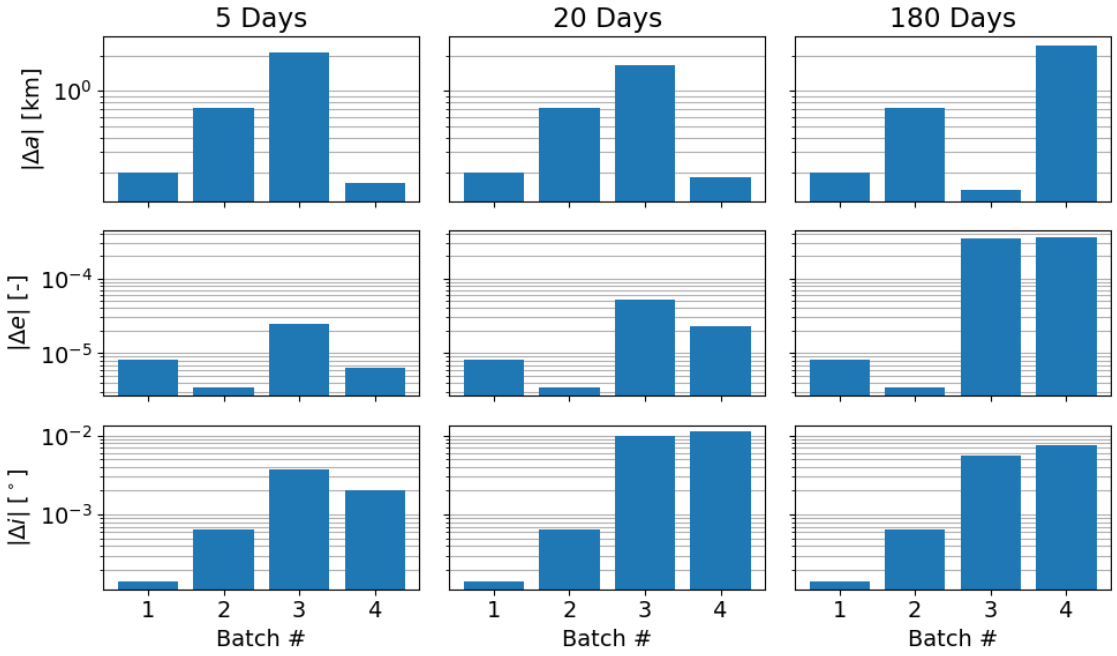

Figure C.21. Comparison of orbital elements defining orbit shape for the three measurement cases and two propagation methods.

Figure C.23 shows the average true anomaly value for each measurement batch, batch spacing case, and propagation method. The two-body propagation results are given in blue and the SGP4 propagation results are given in orange. For the 5 and 20 day batch spacing cases, the true anomaly values are comparable between the two-body propagation and SGP4 propagation. Note that the fourth measurement batch has a similar true anomaly average value as the first measurement batch. As

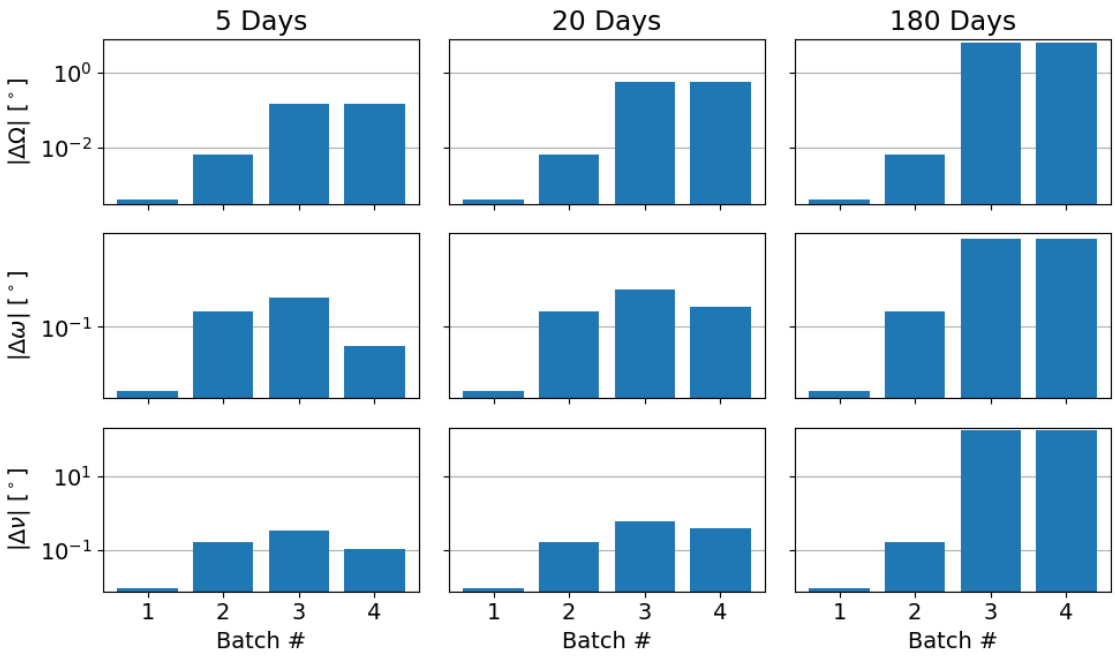

Figure C.22. Comparison of orbital elements defining orbit orientation for the three measurement cases and two propagation methods.

a result, less new information is provided by the third batch of measurements. In the 180 day batch spacing case, the third and fourth average true anomaly values are different from the other cases. The true anomaly for the third batch of the SGP4 propagation is similar to the first batch. However, the true anomaly values of the third and fourth batches using two-body propagation are different from the first and second batches. This uniqueness of the measurement batch true anomaly values for the two-body propagation case resulted in the larger observability Gramian rank in Figure C.20.

Depending on the length of analysis, the orbit propagator implemented for observability of the EGI minimization can have a significant impact on the rank of the observability Gramian. An orbit propagator with perturbations, such as SGP4, will result in more geometric diversity in the system as the orbit shape and orientation may change over time. The greater geometric diversity caused by a propagator with

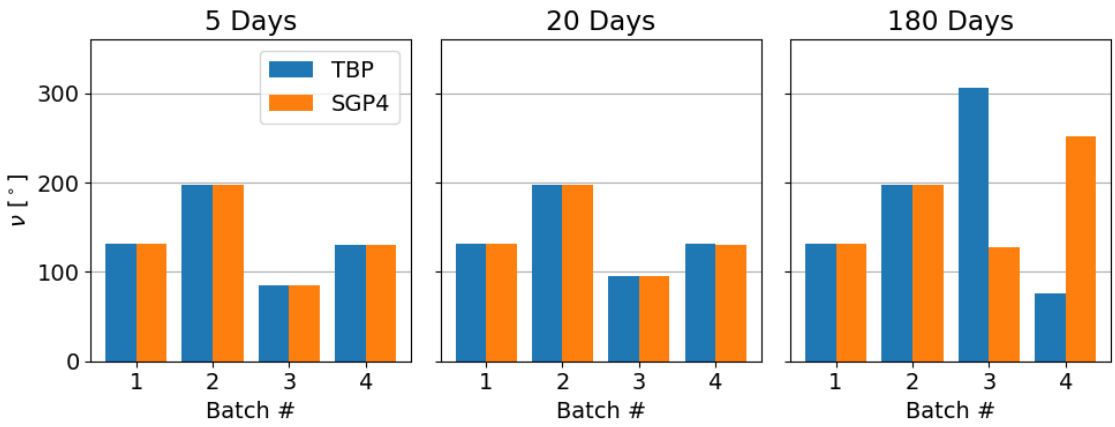

Figure C.23. Comparison of the average true anomaly values per batch of measurements for the three measurement cases and two propagation methods.

perturbations cannot be expected to improve the observability of the EGI minimization. In this analysis, the SGP4 propagation resulted in lower observability Gramian rank values for the 180 day measurement spacing case. Over shorter analysis times, the differences in the rank of the observability Gramian were minimal. Although change in the system geometry due to the SGP4 propagator was detrimental for the rank of the observability Gramian in this system, other systems may benefit from increased geometric diversity. Therefore, depending on the analysis length, this problem is sensitive to the orbit propagator used, and a comparison of the observability Gramian matrix rank with different propagators is important for observability of the EGI minimization.

VITA

Alex attended Virginia Polytechnic Institute and State University (Virginia Tech) from 2009 to 2015. He earned a BS in Engineering Science and Mechanics in 2013 and a MS in Aerospace Engineering in 2015. He joined the Space Information Dynamics group at Purdue University to pursue a PhD in 2015.